Environmental Issues in the Structure and Ultrafast Kinetics of Acids and Hydrated Protons

ISBN 978-94-92323-43-9

Cover design: Oleksandr O. Sofronov

Environmental Issues in the Structure and Ultrafast Kinetics of Acids and Hydrated Protons

UNIVERSITEIT VAN AMSTERDAM

ACADEMISCH PROEFSCHRIFT

ter verkrijging van de graad van doctor
aan de Universiteit van Amsterdam
op gezag van de Rector Magnificus
prof. dr. ir. K.I.J. Maex
ten overstaan van een door het College voor Promoties ingestelde commissie,
in het openbaar te verdedigen in de Aula der Universiteit
op vrijdag 27 november 2020, te 14:00 uur

door

Oleksandr O. Sofronov

geboren te Kharkiv, Oekraïne

Promotor: Prof. dr. H.J.Bakker

Overige leden: Prof. dr. W.J. Buma
Prof. dr. A.M. Brouwer
Prof. dr. P.G. Bolhuis
Prof. dr. P.B. Petersen
Prof. dr. M.S. Pchenitchnikov
Dr. M.A. van der Veen

Faculteit der Natuurwetenschappen, Wiskunde en Informatica

This work is part of the research program of the Netherlands Organization for Scientific Research (NWO) and was performed at the research institute AMOLF, Science Park 104, 1098 XG Amsterdam, The Netherlands. The project has received funding from the European Research Council (ERC) under the European Union's Horizon 2020 research and innovation program (grant agreement No 694386).

Contents

1 Introduction

Protons (H^+) participate in a broad variety of chemical processes as a reactant, a product or a catalyst. In liquid phase solvation and transport of protons is an important and sometimes a rate-limiting step of a reaction. Interestingly, most of the crucial proton-involving processes occur in confined spaces of 0.5 to 100 nanometer length scale, both in living matter and in industrial applications. In living cells protons are transported across the mitochondria membranes through the nanochannels of special proteins, called *proton pumps*, to mediate the synthesis and hydrolysis of adenosine triphosphate (ATP), molecular energy storage. In man-made devices, such as proton-exchange membrane fuel cells or electrolyzers, protons are transported from the anode to the cathode through the nanochannels of a solid electrolyte membrane. In addition, many proton catalyzed chemical syntheses (controlled polymerization, synthesis of self-assemblies or nanoparticles) are carried out in nanoconfinement, such as the pores of solid materials or liquid nanodroplets.

1.1 Proton solvation and proton conduction

In a solution at equilibrium protons do not exist in the form of an H^+ cation. Being a very strong acceptor of electrons, it will always interact either with anions or with the solvent molecules, thus forming a proton solvation structure. Among all of solvents, the solvation of proton in aqueous media is especially interesting, not only because water solutions are ubiquitous, but also because of the special properties of water molecules.

The oxygen atom of a water molecule possesses two lone electron pairs, and there-

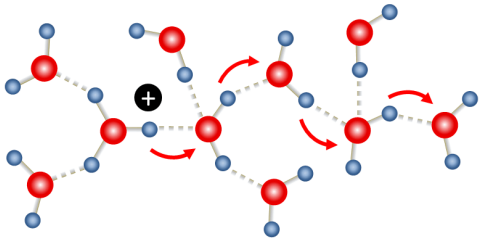

Figure 1.1: Relay mechanism of proton charge transport in liquid water. The blue and red balls represent hydrogen and oxygen atoms, respectively; the solid and dashed lines represent covalent bonds and hydrogen bonds, respectively. The red arrows show the paths of proton hopping.

fore, can accept two hydrogen bonds from other molecules. On the other side, the water molecules has two polar OH-groups which can donate hydrogen bonds to other molecules thus building a branched hydrogen-bond network of liquid water. When an excess proton is introduced into aqueous solution, it can strongly bind to the oxygen atom of a water molecule becoming an H_3O^+ hydronium cation. The H_3O^+ hydronium cation has three polar and strongly hydrogen bonded OH-groups and each of them can dissociate when a proton hops along the hydrogen bond to the neighboring water molecule (Figure 1.1). Subsequently, another proton of the newly created H_3O^+ cation can jump to the next water molecule and so on. In this way the excess proton charge is transported through the hydrogen bond network of water with only small displacements of the proton masses. A similar relay mechanism of proton transport was mentioned first by Theodor von Grotthuss in 1805,[1] and was revived in the beginning of XX century to explain anomalously high mobility of proton in water.[2,3]

In the middle of XX century, Manfred Eigen extensively studied the kinetics of proton transport and its elementary steps with chemical relaxation methods (electric impulse, temperature jump)[4] assuming that in aqueous solution the proton exists in the form of $H_9O_4^+$ - trihydrated H_3O^+ core.[5,6] Later, this assumption was debated by Georg Zundel, who used infrared spectroscopy experiments and proposed $H_5O_2^+$ to be the fundamental structure of the hydrated proton, with a proton tunneling between two water molecules.[7,8] These concepts largely predetermined the following studies of aqueous excess protons. The $H_9O_4^+$ and $H_5O_2^+$ were named Eigen- and Zundel-cations, respectively, and until now are often used to describe the limiting cases of proton hydration structures.

Modern molecular dynamics simulations describe the molecular mechanism of proton transfer as the structural interconversion between Eigen and Zundel hydration structures (Figure 1.2).[9–14] In the first elementary step of this process one of the H_3O^+-H_2O hydrogen bonds of the Eigen-cation shortens due to ultrafast fluctuations of the outer hydration shells. This results in an asymmetry of the Eigen-cation and the creation of a so-called

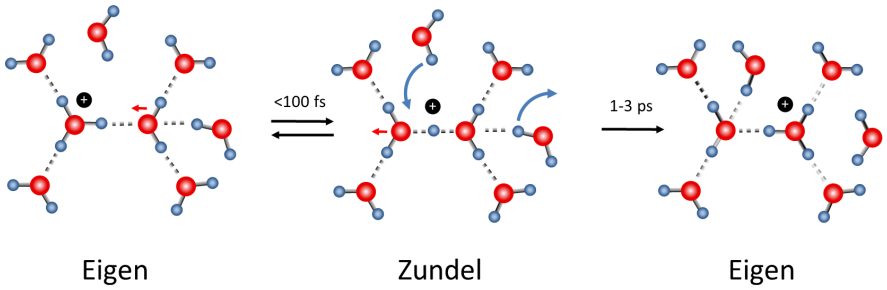

Figure 1.2: Schematic representation of Eigen-Zundel-Eigen structural interconversion.

special pair. Upon the shortening of the O-O distance from 2.5 $\mathring{A}$ to 2.4 $\mathring{A}$, the barrier in the $O \cdots H \cdots O$ potential energy surface strongly decreases. At an O-O distance of 2.4 $\mathring{A}$, proton shuttling between the two oxygens becomes completely barrierless, which results in a completely symmetric Zundel-type structure with the proton being equally shared by the two water molecules. This structure can be converted either into a new Eigen-cation or back to the initial Eigen-cation.

It is still under discussion whether the Eigen- or the Zundel-cation is the more stable proton hydration structure in liquid water.[13,15–18] The conversion between Eigen and Zundel complexes in liquid water is ultrafast and occurs on timescale of 50-100 fs.[12,19,20] It thus makes more sense to define the hydrated proton as an intermediate, highly dynamic structure with Eigen and Zundel being only the limiting geometries.[21–23] Nevertheless, the irreversible proton transfer from one Eigen-cation to another Eigen-cation (or from one Zundel to another Zundel) is estimated to take 1-3 ps.[9,12,24,25] These relatively slow dynamics are explained from the fact that the complete migration of the proton charge from one oxygen atom to another oxygen atom requires the movement of surrounding water molecules and rearrangement of multiple hydrogen bonds.[12,14,26] The central oxygen of the Eigen-cation is a very weak hydrogen bond acceptor, which implies that the hydrogen bond accepted by the oxygen of the newly formed H_3O^+ will dissociate, and a new water molecule has to come in to donate a hydrogen bond to the former H_3O^+ oxygen. The process of the collective rearrangement of the hydrogen bond network around the hydrated proton to facilitate these molecular movements occurs on picosecond timescale.

The hydrogen bond dynamics as well as other properties of water are known to be strongly affected by nanoconfinement.[27–32] Therefore, both the proton solvation structures and the dynamics of their interconversion can be different in nanoconfinement compared to bulk solution.

1.2 Infrared spectroscopy of the hydrated proton

Hydrated protons and water molecules have multiple vibrational modes, which are the oscillations of the O-H bond distances (stretching modes), of the angle between the two O-H bonds (bending mode) and of the position of the molecule with respect to the hydrogen bond network (librations, i.e. hindered rotations). In strongly hydrogen bonded systems, such as liquid water and proton hydration structures, these vibrations (vibrational potential, frequency, transition dipole moment) are very sensitive to the intermolecular interactions and changes of the molecular structures. These vibrations are infrared active, i.e. absorb infrared light at their resonant frequency and can thus be excited by this light. This property makes infrared spectroscopy an ideal tool to study proton solvation, since this method does not perturb the molecular interactions itself, and can provide direct information about the molecules of interest with no need of additional molecular probes. Femtosecond time-resolved infrared spectroscopy, which we use in the experiments presented in this thesis, allows us to capture the picosecond structural dynamics of the hydrated protons described in the previous section.

A drawback of the infrared spectroscopy approach is the relatively low vibrational cross-section of the hydrated proton vibrations, which determines the strength of the infrared absorption signal. Since the absorption features of the hydrated proton overlap with the absorption of water, one has to use relatively concentrated acid solutions ($>$1 mol/L) to have enough contrast between these two signals in infrared spectroscopy experiments. In Figure 1.3 we show the infrared absorption spectrum of an aqueous solution of hydrobromic acid (HBr). Being a superacid, HBr dissociates completely into H^+ and Br^- even at high concentrations. The released protons give rise to a very broad continuous absorption below 3000 cm^{-1} and two broad bands at $\sim$1750 cm^{-1} and $\sim$1200 cm^{-1}. The total spectrum contains contributions from water molecules in the proton hydration shell, bromide hydration shell and of water molecules that interact only with water. The latter can be subtracted using the spectrum of neat water. However, the number of water molecules involved in the hydration of the proton is not well determined which makes the subtraction procedure ambiguous and uncertain in the spectral regions of strong water absorption (HOH-bending mode at 1600-1700 cm^{-1} and OH-stretch vibrations at 3000-3700 cm^{-1}).

Another challenge, which we face when studying hydrated protons with infrared spectroscopy, is the assignment of the infrared spectrum of protons in solution to particular vibrations. Because of the large number of strongly hydrogen bonded water molecules involved in the solvation of the proton, the dynamic nature of the hydrated proton structure, and strong anharmonic effects, it is difficult to model the complex infrared spectrum of

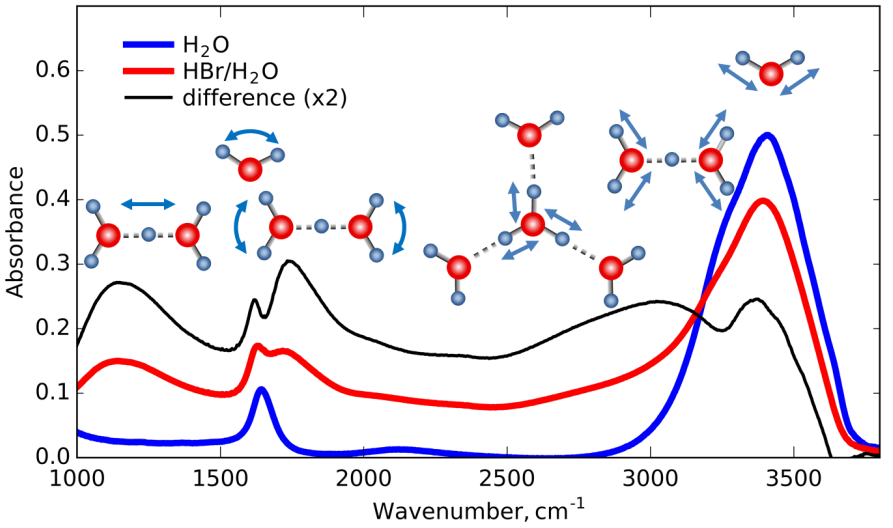

Figure 1.3: Infrared absorption spectra of a hydrobromic acid solution, neat water, and their difference, showing the infrared response of protons in aqueous solution.

aqueous excess proton precisely and to assign the spectral features to particular vibrations of well-defined proton hydration structures. Most of the vibrational assignments reported in the literature are based on semi-empirical molecular dynamics (MD) simulations of protons in aqueous solution[15,22,33–36] or on higher level simulations of small (3-6 molecules) protonated water clusters in the gas phase.[37–40] The latter simulations can be perforemd at a higher level of theory with an improved representation of anharmonic effects. The results of such simulations are always compared to the experimental infrared spectra of small protonated clusters under cryogenic conditions.[41–45] These experiments provide infrared spectra of hydrated protons with well-defined numbers of water molecules and topology, and are used to identify the structure-spectrum relation of hydrated protons. However, the extrapolation of these results to the solution case is not straightforward.

Summarizing (and simplifying) the conclusions of existing theoretical and experimental studies, the infrared absorption spectrum of protons in aqueous solution is assigned as follows. The broad and intense band at 1200 cm^{-1} is assigned to a proton shuttling in a Zundel-configuration[18,36,46], and sometimes to an umbrella mode of H_3O^+ in an Eigen-configuration[22,40,45]. The band at $\sim$1750 cm^{-1} is assigned to bending vibrations of the water molecules flanking the proton in a Zundel-cation.[15,33,47] The extremely broad continuous absorption in the range of 2000-3600 cm^{-1} represents OH-stretch vibrations of the hydrated proton of different configurations. It is believed that the OH-stretch

vibrations of the core of Eigen-cation absorb at 2500-2900 cm^{-1}, and that the OH-stretch vibrations of the two water molecules in the Zundel-cation absorb at 3000-3300 cm^{-1}.[15,33,41,42] Keeping in mind that Eigen and Zundel are limiting proton hydration structures, this assignment is mostly a consequence of the more general concept that states that the stretch vibrations of more polarized OH-bonds appear at lower frequency. A more detailed understanding of the structure-spectrum relation of the hydrated proton, and its specific features (like a small hump at 2400 cm^{-1}, a minimum at 2500 cm^{-1}, a maximum at 3000 cm^{-1}) is not yet present.[21,23,48]

1.3 Protons of carboxyl groups

Proton transport through the nanochannels of proteins is a fundamental process of paramount importance as it enables living cells to create electrochemical potential across their membranes. A disability to maintain the concentration difference of ions between the two sides of the plasma membrane brings the cell to its equilibrium state - death.

Protons are transported across biological membranes by special proteins, so called proton pumps, which are incorporated in the membrane.[49–51] Driven by electron transport, ATP hydrolysis or light, these proteins change their tertiary structure to make it favorable to receive a proton on one side of the membrane, conduct it through the inner channel, and to release it on the other side of the membrane.[52–54] In the inner channels of the pump, protons are transported by a mechanism similar to the proton relay mechanism in water. Here, instead of transfering the proton charge from one water molecule to another water molecule, the proton is transferred between various proton accepting/donating side groups of amino acids. This proton transport can also be assisted by water molecules present in the protein cavities.[55,56] Typical participants of this proton relay are the residues of glutamic and aspartic acids, which possess a side-chain carboxyl group.[56,57] The exact spatial positioning of the involved carboxyl groups is crucial for the molecular interactions between the amino acid residues, and thus for efficient proton transport.

The geometry of the carboxyl group can be different in terms of the position of the hydrogen atom with respect to the C=O group. In general, molecular groups can rotate around every single σ-bond, such as the C-O of the carboxyl group, resulting in different molecular conformations. However, some of molecular conformations are much more stable than other, even at room temperature. For carboxyl group only planar conformations are calculated to be stable (Figure 1.4), with a strong preference for the OH-group to be oriented at 60° with respect to the C=O group (syn conformation) over an anti-parallel orientation with respect to the C=O group (anti conformation).[58–60] In spite of the strong impact of the carboxyl group conformation on the intermolecular interactions and chem-

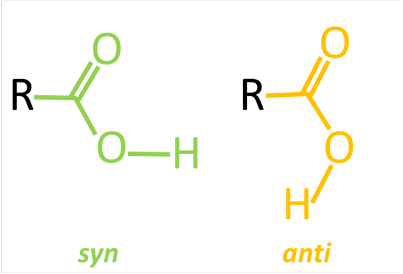

Figure 1.4: Schematic representation of syn- and anti-conformers of carboxyl group.

ical properties, the conformational isomerism of this group is usually overlooked. The conventional method to determine the molecular structure of proteins is X-ray diffractometry. In this method the coordinates of hydrogen atoms are not obtained directly, but they come from additional calculations. Thus, usually conclusions about the geometry of carboxyl group are based on theoretical simulations and not proven experimentally.

1.4 Outline

This thesis focuses on the study of the structure and dynamics of hydrated protons and carboxylic acids in solution using polarization-resolved infrared pump-probe spectroscopy and two-dimensional infrared spectroscopy. In Chapter 2 we present the theoretical background of light-matter interactions and nonlinear infrared spectroscopy. Chapter 3 gives a detailed description of the setups used in the experiments described in the subsequent chapters. In Chapter 4 we present a study of the structure and vibrational dynamics of protons solvated in water/DMSO mixtures. In Chapter 5 we study the vibrational dynamics of small proton hydration clusters in acetonitrile, and we identify the infrared responses of the inner and outer hydration shells of the proton. In Chapter 6 we present an experimental estimation of the proton transfer rate in water nanodroplets and in bulk aqueous solution. In Chapter 7 we discuss the vibrational assignment of the proton continuum absorption, based on polarization-resolved pump-probe experiments on protons solvated in anionic and cationic reverse micelles. In Chapter 8 and Chapter 9 we investigate the conformational isomerism of carboxyl groups of formic acid and aspartic acid, respectively.

2 Theory

In this chapter we introduce the concepts of nonlinear optics underlying the experiments of this thesis. We provide the theory of resonant light-matter interaction and derive an expression for the pump-probe signal. Subsequently we describe a common non-resonant artifact in pump-probe experiments: cross-phase modulation. Finally, we show how the theory relates to the often used phenomenological approach to infrared pump-probe spectroscopy, which is commonly used in the interpration of experiments. This chapter is based on a few textbooks[61–63] and other previous work[64,65].

2.1 Nonlinear optics

An external electric field applied to a material interacts with the charges in the material and induces electric dipole moments. The induced dipole moment per volume of the material is called polarization $\vec{P}$ and can be expressed as a power series in the applied electric field $\vec{E}$:

$$\vec{P} = \vec{P}^{(1)} + \vec{P}^{(2)} + \vec{P}^{(3)} + ... = \epsilon_0(\chi^{(1)}\vec{E} + \chi^{(2)}\vec{E}^2 + \chi^{(3)}\vec{E}^3 + ...) \tag{2.1}$$

where ϵ_0 is the vacuum permittivity and $\chi^{(n)}$ is the n-th order susceptibility. This equation constitutes a general description of light-matter interactions. Here it should be noted that all susceptibilities $\chi^{(n)}$ are $n+1$ rank tensors. The polarization depends on the polarizations of all the mixed waves, and the susceptibility tensor relates directions of n light polarizations with the direction of the induced polarization. The typical values of

$\chi^{(1)}$, $\chi^{(2)}$ and $\chi^{(3)}$ are of the order of 1, 10^{-12} m/V and 10^{-24} m^2/V^2. Thus, when the light field is weak, all the nonlinear terms in Eq. 2.1 can be neglected. This is the case for conventional infrared spectroscopy, which we also call linear infrared spectroscopy, since the linear response of the material under study is measured. However, when intense femtosecond light pulses are used, which correspond to very strong electric fields ($\sim 10^9$ V/m), the nonlinear polarization terms become significant.

The oscillating electric field of incident light induces an oscillating polarization in a material, which subsequently emits an oscillating electric field. This results in multiple effects, which can be observed in spectroscopy. When two monochromatic electromagnetic waves *1* and *2* are mixed in a material, the total electric field can be written as:

$$\vec{E}(\vec{x},t) = \vec{E}_1 e^{i(\vec{k}_1\vec{x}-\omega_1 t)} + \vec{E}_2 e^{i(\vec{k}_2\vec{x}-\omega_2 t)} + c.c. \tag{2.2}$$

where $\vec{k}_i = \vec{n}(\omega_i)\omega_i/c$ is the wave vector for a medium with refractive index $\vec{n}$, ω_i is the frequency and $c.c.$ denotes the complex conjugate. The second order polarization is then given by

$$\begin{aligned}
\vec{P}^{(2)}(t) = \int_{-\infty}^{t}\int_{-\infty}^{\tau_2} & \epsilon_0\chi^{(2)}(\vec{E}_1(\tau_1)\vec{E}_1(\tau_2)e^{i(2\vec{k}_1\vec{x}-\omega_1(\tau_1+\tau_2))} + c.c. && (SHG)\\
& + \vec{E}_2(\tau_1)\vec{E}_2(\tau_2)e^{i(2\vec{k}_2\vec{x}-2\omega_2(\tau_1+\tau_2))} + c.c. && (SHG)\\
& + \vec{E}_1\vec{E}_2 e^{i(\vec{k}_1+\vec{k}_2)\vec{x}}(e^{-i(\omega_1\tau_1+\omega_2\tau_2)} + e^{-i(\omega_2\tau_1+\omega_1\tau_2)}) + c.c. && (SFG)\\
& + \vec{E}_1\vec{E}_2 e^{i((\vec{k}_2-\vec{k}_1)\vec{x}}(e^{-i(\omega_2\tau_2-\omega_1\tau_1)} + e^{-i(\omega_2\tau_1-\omega_1\tau_2)}) + c.c. && (DFG)\\
& + 2(\vec{E}_1^2 + \vec{E}_2^2))d\tau_1 d\tau_2 && (DC)
\end{aligned} \tag{2.3}$$

The polarization will lead to the emission of light, following the Maxwell wave equation. This simple example shows that due to second order polarization the medium will emit light with frequencies different from those of the incident electromagnetic waves. The first two terms correspond to second harmonic generation: production of light at the doubled frequencies $2\omega_1$ and $2\omega_2$, the third and fourth contributions produce electric fields at the sum frequency $\omega_1+\omega_2$ and difference frequency $\omega_1-\omega_2$, and the last contribution represents a DC electric field (optical rectification). In this thesis at certain steps of production of infrared pulses we used second harmonic generation and difference frequency generation. In general these second order processes can occur in all the noncentrosymmetric media. However, only particular crystals are used for efficient frequency conversion. As we can see from Eq. 2.3, the difference frequency wave generated at point $\vec{x}$ of the medium has a phase defined by $\vec{k}_3\vec{x} = (\vec{k}_1 - \vec{k}_2)\vec{x}$. At the exit face of the crystal all the waves generated at different points in the crystal will coherently add up. For the waves generated at points $\vec{x}_1$ and $\vec{x}_2$ there will be a phase mismatch

$\Delta\phi = (\vec{k}_3 - (\vec{k}_1 - \vec{k}_2))(\vec{x}_2 - \vec{x}_1)$. For a certain $(\vec{x}_2 - \vec{x}_1)$ distance the phase mismatch of the two generated waves will be π, and the waves will interfere destructively lowering the efficiency of frequency mixing. To overcome this problem and to make difference frequency generation most efficient and the phase matching condition should be fulfilled: $\vec{k}_3 = \vec{k}_1 - \vec{k}_2$. The latter is called the *"phase matching condition"* and in the collinear geometry, which is oftenly used for frequency mixing, corresponds to:

$$n_3(\omega_3)\omega_3 = n_1(\omega_1)\omega_1 - n_2(\omega_2)\omega_2 \tag{2.4}$$

The refractive index n depends on frequency, thus, this condition is not easy to fulfill in isotropic optical materials. The solution is to use birefringent crystals, for which the refractive index for light polarized perpendicular to the optical axis of the crystal (ordinary index n_o) differs from the refractive index experienced by light polarized parallel to the optical axis (extraordinary index n_e). In type I phase matching the phase matching condition can be fulfilled in a negative uniaxial crystal ($n_e < n_o$) by taking two fundamental beams of ordinary polarization and generating light at the sum frequency with extraordinary polarization. The refractive index of the latter can be tuned by rotating the crystal, thereby obtaining an effective refractive index value between the n_o and n_e. Phase matching can also be achieved with other combinations of polarizations of the interacting beams.

2.2 Molecular vibrations

In a classical picture, chemical bonds between the atoms of a molecule can be seen as springs. The whole molecule then can be represented by a system of anharmonic oscillators, where every atom oscillates around its equilibrium position. This simple representation, however, cannot fully describe the interaction of the molecule with infrared light, since the classical theory does not explain transitions between the states of the oscillator. Therefore, the quantum mechanical approach is needed.

The simplest model to describe a molecular vibration is the quantum harmonic oscillator. In this model the potential of the particle is described by Hooke's law and the Hamiltonian of the system is

$$\hat{H}_0 = \frac{\hat{p}^2}{2\mu} + \frac{1}{2}k\hat{x}^2 \tag{2.5}$$

where $\hat{p}$ is the momentum operator, m is the reduced mass, and $\hat{x}$ is the position operator. The energies E and the wavefunctions $|\psi\rangle$ of the states can be found by solving the time-independent Schrödinger equation:

$$\hat{H}\,|\psi\rangle = E\,|\psi\rangle \tag{2.6}$$

The resulting energy levels are:

$$E_n = \hbar\omega_0(v + \frac{1}{2}) \tag{2.7}$$

where $\omega_0 = \sqrt{k/m}$ is the vibrational frequency and v is the vibrational quantum number. The harmonic potential, energy levels and corresponding wavefunctions are shown in Figure 2.1A. The molecular vibration described by the quantum harmonic oscillator can exist in different states (v=0,1,2,...) and can be transferred between two consecutive states by absorbing or emitting an $\hbar\omega_0$ quantum of light.

The simple harmonic potential is, however, not a good model for real molecules, especially when $v > 1$ vibrational states are considered. For example, for any simple diatomic molecule the potential is already asymmetric. At a large positive displacement the molecule dissociates which corresponds to nearly zero energy difference for further displacement. However, at a large negative displacement , when the distance between the atoms is small, the energy of the system grows with further displacement. To describe molecular vibrations more precisely anharmonic potentials can be used. One of these is the Morse potential (Figure 2.1A):

$$V_0 = D(1 - e^{-\sqrt{k/2D}\hat{x}})^2 \tag{2.8}$$

where D defines the depth of the potential and k is the force constant. A description of a chemical bond with an asymmetric Morse potential is more realistic, since this potential accounts for the dissociation of the bond. The energies of the vibrational states in the Morse potential can also be found analyticaly:

$$E_n = \hbar\omega_0(v + \frac{1}{2}) - \frac{(\hbar\omega_0(v + \frac{1}{2}))^2}{4D} \tag{2.9}$$

where $\omega_0 = \sqrt{k/m}$. As we see, the energy of the transition between two consecutive states decreases with increasing quantum number. This is an important difference between the harmonic and anharmonic potential. The difference in frequencies of v=0→1 and v=1→2 transitions is often used as a measure of the anharmonicity of a vibration. As we will see later, this property is essential for infrared pump-probe spectroscopy.

In specific cases, like proton-hydration structures, other potentials have been used to describe the vibrations. For example, the stretch vibration of a hydrogen-bonded $X - H$ group ($X - H \cdots Y$) can be quite well modeled using the Lippincott-Schroder potential (Figure 2.1B), which accounts for the effect of the $H \cdots Y$ interaction on the effective vibrational potential of the $X - H$ coordinate, and the repulsive and attractive interactions between X and Y.[66,67] The shuttling vibration of proton in the Zundel-cation can be modeled reasonably well with a steep quartic potential (Figure 2.1C).[18,23] This potential supports a "negative anharmonicity" of the vibration: the frequency of the v=1→2

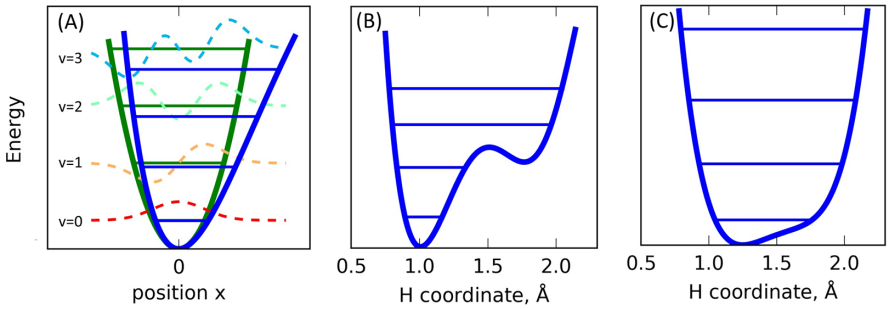

Figure 2.1: (A) Harmonic potential (green) with its energy levels levels and corresponding wavefunctions and Morse potential (blue); (B) Lippincott-Schroder potential and (C) quartic potential, which can be used to model X-H stretch vibrations of strongly hydrogen-bonded molecules.

transition is higher than the frequency of the v=0→1 transition. Schroodinger equations with these more complex potentials can only be solved numerically.

2.3 Resonant nonlinear optics in a density matrix formalism

To describe the interaction of a molecule with light, we consider the Hamiltonian $\hat{H}$ given by the sum of the static Hamiltonian $\hat{H}_0$ and the time-dependent perturbation $\hat{V}(t)$ due to an external electric field:

$$\hat{H} = \hat{H}_0 + \hat{V}(t) = \hat{H}_0 - \hat{\mu}E(t) \tag{2.10}$$

where $\vec{\hat{\mu}}$ is the electric dipole moment interaction. The polarization induced by the incident light is defined as

$$P(t) = N\langle\hat{\mu}\rangle \tag{2.11}$$

where N is the number density of the molecules and $\langle\hat{\mu}\rangle$ the expectation value of the dipole moment operator.

The static Hamiltonian $\hat{H}_0$ has eigenvalues ϵ_n and eigenfunctions $|n\rangle$. The time evolution of the system is described by the time-dependent Schrödinger equation:

$$i\hbar\frac{\partial|\psi(t)\rangle}{\partial t} = \hat{H}_0|\psi(t)\rangle \tag{2.12}$$

and the wavefunction $|\psi(t)\rangle$ written in the basis of eigenfunctions of $\hat{H}_0$

$$|\psi(t)\rangle = \sum_n |n\rangle c_n(t) \tag{2.13}$$

Then we can define the density operator as

$$\hat{\rho}(t) = |\psi(t)\rangle\langle\psi(t)| \tag{2.14}$$

The elements of the density matrix are

$$\rho_{nm} = \langle n|\psi\rangle\langle\psi|m\rangle = \langle n|n\rangle c_n c_m^* \langle m|m\rangle = c_n c_m^* \tag{2.15}$$

The diagonal elements of the density matrix $\rho_{nn} = |c_n|^2$ represent the *population* of the state $|n\rangle$, i.e. the probability to find the molecule in this state. The off-diagonal elements ρ_{nm} describe to which extent the superposition of the states $|n\rangle$ and $|m\rangle$ posseses a well-defined phase relation. In equilibrium state the off-diagonal ρ_{nm} turn to zero.

Using the density matrix we can write the expectation value of the dipole moment operator as:

$$\langle\psi|\,\hat{\mu}\,|\psi\rangle = \sum_{n,m} c_m^* c_n \langle m|\,\hat{\mu}\,|n\rangle = \sum_{n,m} \rho_{nm}\mu_{mn} = Tr(\hat{\rho}\hat{\mu}) \tag{2.16}$$

where Tr denotes the trace of the matrix. Thus, to obtain the polarization induced by the light (Eq. 2.11) we need to find the elements of the density matrix.

It can be shown that the time-dependent Shrödinger equation (Eq. 2.12) is equivalent to

$$\frac{d\hat{\rho}}{dt} = -\frac{i}{\hbar}[\hat{H}, \hat{\rho}] \tag{2.17}$$

where $[\hat{A}, \hat{B}] = \hat{A}\hat{B} - \hat{B}\hat{A}$ is the commutator of two operators. This equation is knows as the Liouville-Von Neumann equation and describes the time evolution of the density operator. Without any perturbation the Liouville-Von Neumann equation yields:

$$\frac{d\rho_{nm}}{dt} = -i\omega_{nm}\rho_{nm} \tag{2.18}$$

where $\omega_{nm} = (\epsilon_n - \epsilon_m)/\hbar$ is the transition frequency between the states $|n\rangle$ and $|m\rangle$. Adding the perturbation induced by the applied electric field, and assuming that without perturbation the density matrix elements decay exponentially to their equilibrium values $\rho_{nm}^{(0)}$ we obtain

$$\frac{d\rho_{nm}}{dt} = -i\omega_{nm}\rho_{nm} - \gamma_{nm}(\rho_{nm} - \rho_{nm}^{(0)}) - \frac{i}{\hbar}E[\hat{\mu}, \hat{\rho}]_{nm} \tag{2.19}$$

where γ_{nm} is a decoherence rate, when $n \neq m$, and a population relaxation rate, when $n = m$. Expanding the density matrix perturbatively in powers of the applied electric field we obtain a set of differential equations in the form:

$$\frac{d\rho_{nm}^{(q)}}{dt} = (-i\omega_{nm} - \gamma_{nm})\rho_{nm}^{(q)} - \frac{i}{\hbar}E[\hat{\mu}, \hat{\rho}^{(q-1)}]_{nm} \tag{2.20}$$

Which after integration gives

$$\rho_{nm}^{(q)}(t) = \frac{i}{\hbar} \int_{-\infty}^{t} e^{(-i\omega_{nm}-\gamma_{nm})(t-t')} E(t')[\hat{\mu}, \hat{\rho}^{(q-1)}]_{nm} dt' \tag{2.21}$$

In pump-probe spectroscopy we are interested in third-order density matrix elements $\rho^{(3)}$, which can be calculated successively by integrating the expressions starting from $\rho^{(1)}$ and $\rho^{(2)}$.

2.3.1 Components of the pump-probe signal

To find the elements of the $\rho^{(3)}$ matrix we need to know *all* the elements of $\rho^{(2)}$ and $\rho^{(1)}$. In general, a consecutive calculation of the third-order density matrix elements of a multilevel system will give an enormous number of components. However, most of these components will be negligibly small. Applying some approximations we can thus significantly reduce the number of contributions and write the pump-probe signal as a sum of only 12 terms.

First, we assume that in the equilibrium state without any perturbation all the molecules are in the ground state. It basically means, that in the $\rho^{(0)}$ matrix only $\rho_{00}^{(0)} \neq 0$.

Second, we apply the harmonic approximation to the transition dipole matrix elements. For the harmonic oscillator the transition dipole moment matrix element μ_{nm} is nonzero only for $m = n \pm 1$, which means that only transitions $|n\rangle \rightarrow |n+1\rangle$ and $|n\rangle \rightarrow |n-1\rangle$ are allowed. This, in combination with the first assumption, allows us to limit the system to only the first three levels $|0\rangle$, $|1\rangle$ and $|2\rangle$ of the vibrational potential. Also, it can be shown that in the harmonic approximation $\mu_{12} = \sqrt{2}\mu_{01}$.

Third, we consider only the polarization with a k vector corresponding to the direction of the probe field. The total electric field can be written as:

$$E = E_1 e^{i(\vec{k}_1\vec{x}-\omega_1 t)} + E_2 e^{i(\vec{k}_2\vec{x}-\omega_2 t)} + c.c. \tag{2.22}$$

where index 1 stands for pump electric field and 2 for the probe. The expression consists of 4 components, which will result in 64 terms when calculating $P(3)$. However, only the terms consisting of E_1, E_1^* and E_2 will give a signal in the direction of probe $\vec{k}_2$ (we neglect the term created by E_2, E_2^* andE_2, as $E_2 \ll E_1$). Hence, we can neglect all the other terms.

The fourth approximation is the rotating wave approximation, which means that we neglect all rapidly oscillating terms. Basically it means that the convolution of the electric field and the exponent in the Eq 2.21 will be nonzero when the frequency under

the exponent is close to the frequency of the electric field, i.e. the light must be resonant with the transition. Note, that, for example, ω_{01} is here defined as $(\epsilon_0 - \epsilon_1)/\hbar$, which is negative. Therefore, transition $|0\rangle \rightarrow |1\rangle$ will be resonant with E_1^*, which has *negative* frequency, and not E_1.

Each term of the final sum for the third order polarization will have a general form of

$$\begin{aligned} P^{(3)}(t) =& N \left(\frac{i}{\hbar}\right)^3 \mu_{db} \int_{-\infty}^{t} E(\tau_3) I_{bd}(t-\tau_3) \mu_{cd} \int_{-\infty}^{\tau_3} E(\tau_2) I_{bc}(\tau_3-\tau_2) \mu_{ac} \\ & \int_{-\infty}^{\tau_2} E(\tau_1) I_{ba}(\tau_2-\tau_1) \mu_{ba} \rho_{00}^{(0)} d\tau_1 d\tau_2 d\tau_3 \end{aligned} \tag{2.23}$$

where $I_{nm}(t) = e^{(-i\omega_{nm} - \gamma_{nm})t}$, and indices $a - d$ can take values 0, 1, 2. Note, that Eq. 2.23 shows only one of the terms contributing to the third order polarization. The relation between the indices of transition dipole moment elements μ and the density matrix evolution functions I comes from the mathematics of the perturbative expansion of the density matrix and from the applied approximations. The detailed derivation of all the $P^{(3)}$ components can be found in ref. 64. Here we will show the $P^{(3)}$ components that are left after the four assumptions and that can be graphically represented with the six Feynman diagrams shown in Figure 2.2.

In these diagrams the arrows represent electric fields and climbing the ladder starting from $\rho_{00}^{(0)}$ we consecutively create elements of $\rho^{(1)}$, $\rho^{(2)}$ and $\rho^{(3)}$. The $\rho^{(1)}$ elements at time τ_2 depend on the interaction of the first electric field with $\rho^{(0)}$ at all times τ_1 before τ_2, which gives us the most inner integral. Then the $\rho^{(2)}$ elements at time τ_3 depend on the interaction of the second electric field with the created $\rho^{(1)}$ at all times τ_2 before τ_3, giving the second integral. Finally, the $\rho^{(3)}$ at time t is obtained from all the interactions of the third electric field with $\rho^{(2)}$ at all times τ_3 before t. The diagrams show which elements of every $\rho^{(n)}$ matrix are build from which elements of $\rho^{(n-1)}$ matrix.

Every integral is build in the following way. Arrows pointing to the right represent an interaction with a certain electric field (wave vector $\vec{k}_i$) and arrows pointing to the left represent its complex conjugate (wave vector $-\vec{k}_i$). It gives us $E(\tau_j)$ in the integral. Interaction with the electric field creates a coherence or a population with the indices written over the arrow. These indices become the indices of $I_{kl}(t)$ in the integral. The field should be "absorbed" to increase the quantum number, and should be "emitted" to decrease the quantum number. The indices of the transition dipole moment in the integral corresponds to indices that are permuted during the interaction. If the indices are permuted on the right, the transition dipole moment should be taken with a "-" sign, and if they are permuted on the left, the sign is "+".

All the possible electric field sequences are presented in the left panel of Figure 2.2.

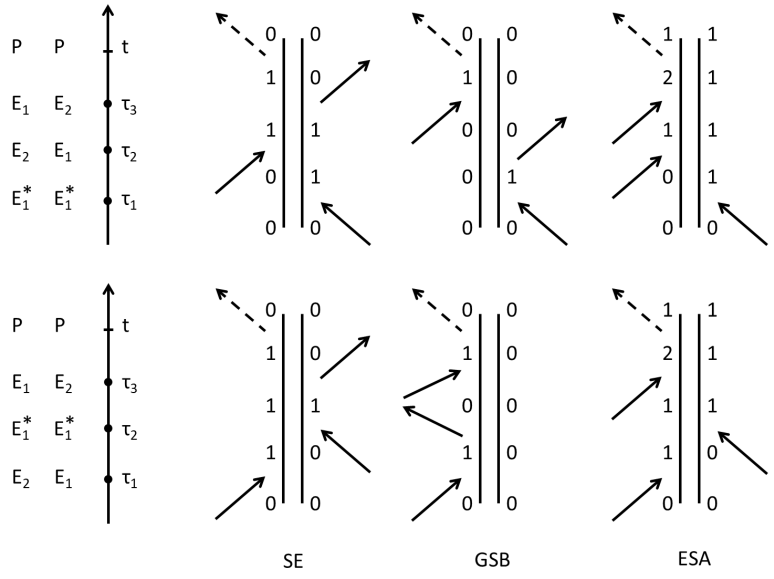

Figure 2.2: Feynman diagrams to calculate third order polarization in pump-probe experiment.

For each diagram there is only one interaction with an E^* field, which must be the pump field E_1^*. The two other interactions must be with E_1 and E_2 to create a third-order polarization with wavevector $\vec{k}_2$, which results in two possible sequences of fields for each diagram. In the first case, when two interactions with pump field (in a sequence E_1^*, E_1 or in a sequence E_1, E_1^*) occurs first, a population is created. The probe field interacts with the population. It gives a conventional pump-probe signal, which can be explained from the vibrational excitation of the molecules by the pump. In the opposite case, when the probe E_2 interacts before the pump E_1, it results in *artifacts*, which cannot be explained so easily (these artifacts are discussed in Section 2.7). This "wrong" sequence of electric fields E_1^*, E_2, E_1 can occur only when the pump and probe pulses overlap in time. Another possible "wrong" sequence E_2, E_1^*, E_1 also results in *artifacts*, which can occur when probe pulse interacts with the material before the pump pulse.

Now we can write all the components of the third order polarization. For example,

the upper left diagram with the "right" electric field sequence will give

$$\begin{aligned} P^{(3)}(t) =& N\left(\frac{i}{\hbar}\right)^3 \mu_{01} \int_{-\infty}^{t} E_2(\tau_3) I_{10}(t-\tau_3)(-\mu_{01}) \int_{-\infty}^{\tau_3} E_1(\tau_2) I_{11}(\tau_3-\tau_2)\mu_{10} \\ & \int_{-\infty}^{\tau_2} E_1^*(\tau_1) I_{01}(\tau_2-\tau_1)(-\mu_{10})\rho_{00}^{(0)} d\tau_1 d\tau_2 d\tau_3 \end{aligned} \tag{2.24}$$

Combining all the six diagrams with the "right" electric field sequence we obtain the total third order polarization for a pump-probe signal:

$$\begin{aligned} & P^{(3)}(t) = N\left(\frac{i}{\hbar}\right)^3 \mu_{01}^2 \\ & \Bigg(\mu_{01}^2 \int_{-\infty}^{t} E_2(\tau_3) I_{10}(t-\tau_3) \int_{-\infty}^{\tau_3} E_1(\tau_2) I_{11}(\tau_3-\tau_2) \int_{-\infty}^{\tau_2} E_1^*(\tau_1) I_{01}(\tau_2-\tau_1) d\tau_1 d\tau_2 d\tau_3 \\ & + \mu_{01}^2 \int_{-\infty}^{t} E_2(\tau_3) I_{10}(t-\tau_3) \int_{-\infty}^{\tau_3} E_1^*(\tau_2) I_{11}(\tau_3-\tau_2) \int_{-\infty}^{\tau_2} E_1(\tau_1) I_{10}(\tau_2-\tau_1) d\tau_1 d\tau_2 d\tau_3 \\ & + \mu_{01}^2 \int_{-\infty}^{t} E_2(\tau_3) I_{10}(t-\tau_3) \int_{-\infty}^{\tau_3} E_1(\tau_2) I_{00}(\tau_3-\tau_2) \int_{-\infty}^{\tau_2} E_1^*(\tau_1) I_{01}(\tau_2-\tau_1) d\tau_1 d\tau_2 d\tau_3 \\ & + \mu_{01}^2 \int_{-\infty}^{t} E_2(\tau_3) I_{10}(t-\tau_3) \int_{-\infty}^{\tau_3} E_1^*(\tau_2) I_{00}(\tau_3-\tau_2) \int_{-\infty}^{\tau_2} E_1(\tau_1) I_{10}(\tau_2-\tau_1) d\tau_1 d\tau_2 d\tau_3 \\ & - \mu_{12}^2 \int_{-\infty}^{t} E_2(\tau_3) I_{21}(t-\tau_3) \int_{-\infty}^{\tau_3} E_1(\tau_2) I_{11}(\tau_3-\tau_2) \int_{-\infty}^{\tau_2} E_1^*(\tau_1) I_{01}(\tau_2-\tau_1) d\tau_1 d\tau_2 d\tau_3 \\ & - \mu_{12}^2 \int_{-\infty}^{t} E_2(\tau_3) I_{21}(t-\tau_3) \int_{-\infty}^{\tau_3} E_1^*(\tau_2) I_{11}(\tau_3-\tau_2) \int_{-\infty}^{\tau_2} E_1(\tau_1) I_{10}(\tau_2-\tau_1) d\tau_1 d\tau_2 d\tau_3 \Bigg) \end{aligned} \tag{2.25}$$

In pump-probe spectroscopy we detect the intensity of light propagating in the probe direction, which basically the interference of the wave emitted by the oscillating third order polarization with the probe electric field. The electric field radiated by the third order polarization is proportional to $iP^{(3)}(t)$, and it can be shown that the measured

absorption change is

$$\Delta\alpha(\omega) = -ln\frac{I_2'(\omega)}{I_2(\omega)} = \frac{2\,\mathrm{Im}\{P^{(3)}(\omega)E_2^*(\omega)\}}{|E_2(\omega)|^2} \tag{2.26}$$

where $P^{(3)}(\omega)$ and $E_2(\omega)$ are the Fourier transforms of the polarization and probe electric field.

2.4 Non-resonant third order response

The third order polarization can be shortly written in a form

$$P^{(3)}(t) = \int_{-\infty}^{t}\int_{-\infty}^{\tau_3}\int_{-\infty}^{\tau_2} \chi^{(3)}(\tau_1,\tau_2,\tau_3)E(\tau_1)E(\tau_2)E(\tau_3)d\tau_1 d\tau_2 d\tau_3 \tag{2.27}$$

where $E = E_1 + E_2$. When the pump and probe frequencies are far from any resonance, the off-diagonal elements given by Eq. 2.21 are only nonzero for $t = t'$. Hence, the integrals in the Eq. 2.25 become nonzero only when $t = \tau_3 = \tau_2 = \tau_1$, i.e. the $\chi^{(3)}$ response is instantaneous. Then combining Eq. ?? and Eq. 2.22 and adding the linear polarization term the polarization can be written as

$$\vec{P}(t) = \epsilon_0(\chi^{(1)} + 6\chi^{(3)}|\vec{E}_1(t)|^2)\vec{E}_2(t)e^{i(\vec{k}_2\vec{x}-\omega_2 t)}) = \epsilon_0\chi_{eff}(t)\vec{E}_2(t)e^{i(\vec{k}_2\vec{x}-\omega_2 t)}) \tag{2.28}$$

Using the relation between the refractive index and susceptibility $n^2 = 1+\chi$ we can write

$$n_{eff}^2 = 1 + \chi^{(1)} + 6\chi^{(3)}|\vec{E}_1|^2 = n_0^2 + 6\chi^{(3)}|\vec{E}_1|^2 \tag{2.29}$$

where n_0 is the linear refractive index. Reorganizing this equation in the form of

$$n_{eff}^2 = (n_0 + \frac{3\chi^{(3)}}{n_0}|\vec{E}_1|^2)^2 - (\frac{3\chi^{(3)}}{n_0}|\vec{E}_1|^2)^2 \tag{2.30}$$

and neglecting the term quadratic in $\chi(3)$, we obtain

$$n_{eff} = n_0 + \frac{3\chi^{(3)}}{n_0}|\vec{E}_1|^2 = n_0 + \overline{n}_2|\vec{E}_1|^2 \tag{2.31}$$

where $\overline{n}_2 = 3\chi^{(3)}/n_0$ is the nonlinear refractive index. The phenomenon described by Eq. 2.31 is called optical Kerr effect (analogously to the DC field dependence of the refractive index). We remember that $\chi^{(n)}$ are tensors, however for the present case of isotropic non-resonant materials we will assume n_0 and n_2 to be isotropic. Substituting

the linear refractive index by the effective refractive index in the expression of the probe wave we obtain:

$$E(x,t) = E_2 e^{i((n_{eff}\omega_2/c)x-\omega_2 t)} + c.c. = E_2 e^{i(k_2 x+(\overline{n}_2\omega_2/c)|E_1|^2 x-\omega_2 t)} + c.c. \quad (2.32)$$

From Eq. 2.32 we see, that due to the optical Kerr effect a time-dependent component is added to the phase of the probe. This pump-induced change of the phase of the probe pulse is called cross-phase modulation (XPM). It depends on the pump field and therefore appears only when pump and probe pulses overlap in time. If the probe pulse is much shorter than the pump, meaning that the derivative of the pump intensity profile with respect to time is constant within the time duration of the probe pulse, the result of this modulation corresponds to a change of the probe frequency:

$$\omega = \frac{d\phi}{dt} = \omega_2(1 - \frac{n_2 x}{c}\frac{d|E_1|^2}{dt}) \quad (2.33)$$

The frequency change will have different sign at positive and negative delay time. At a positive delay time the probe pulse experiences a decreasing intensity of pump (derivative is negative), and as a result the frequency of the probe increases. At a negative delay time the derivative of the pump intensity is positive, and thus the frequency of probe is decreased (Figure 2.3A).

In the experiment we measure the intensity spectrum of the probe, which in this case will be:

$$I_2'(\omega,\tau) \propto |\int_{-\infty}^{+\infty} E_2(t+\tau) e^{i(n_2\omega_2/c)x|E_1(t)|^2} e^{-i\omega t} dt)|^2 \quad (2.34)$$

where τ is the delay time between the pump and probe pulses. Using Eq. 2.34 we can model the absorption change measured in a pump-probe experiment:

$$\Delta\alpha(\omega,\tau) = -ln(I_2'(\omega,\tau)/I_2(\omega)) \quad (2.35)$$

where $I_2'(\omega,\tau)$ is probe intensity measured with *pump on* and $I_2(\omega)$ - with *pump off*. In Figure 2.3 we show the cross-phase modulation signal modelled for ideal Gaussian pump and probe pulses with a spectral full width at half maximum (FWHM) of 150 cm^{-1} and 250 cm^{-1}, respectively (these values are typical for the experiments presented in this thesis).

As we see from Fig. 2.3, the amplitude of the cross-phase modulation artifact is nearly zero at the central frequency of the probe, but strongly increases at the tails. Also, it is almost absent at zero delay time, and steeply grows at very short delays. In pump-probe experiments this artifact can be much more intense than the resonant signal of interest. For the typical measurements presented in this thesis, the resonant pump-probe signal is at its maximum $5\cdot10^{-3} - 5\cdot10^{-2}$ while the cross-phase modulation artifact is at

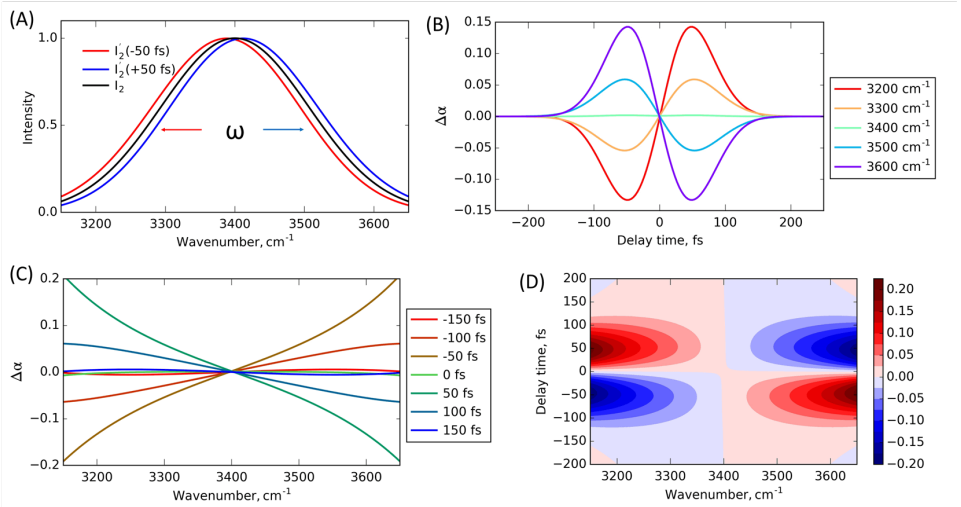

Figure 2.3: Modeling of the cross-phase modulation artifact in pump-probe experiment using Gaussian pump and probe pulses with constant spectral phase. (A) Intensity spectrum of the probe pulse at delay times of -50 fs and +50 fs and with the *pump off* (black line); (B), Cross-phase modulation induced absorption change as a function of delay time; (C) as a funcion of the probe frequency for specific delay times; (D) in a delay-frequency 2D-plot.

its maximum ~ 0.2 (in absorption change units). Since both the resonant pump-probe signal of the sample and the non-resonant XPM signal are third-order optical responses, they scale in the same manner with the intensity of pump pulse. A strong XPM signal overlapping with the resonant signal will add a time-dependent tilt to the signal, which can be misinterpreted as a fast decaying resonant signal. In the used experimental settings, XPM usually limits the time resolution of the pump-probe experiment to 200-400 fs depending on the duration of the pump and probe pulses.

In conventional infrared pump-probe experiments, the XPM artifact is not caused by the sample, but by the windows of the sample cell. A usual sample cell consists of two windows (made of sapphire or calcium fluoride or another salt) of 1-4 mm thickness with a liquid sample of 10-200 μm thickness sandwiched in between. The amplitude of the XPM artifact depends on the path length over which the probe beam overlaps with the pump (coordinate x in Eqs. 2.32-2.34). The total length over which the probe overlaps with the focused pump beam is typically $\sim$1 mm. Therefore, most of the XPM is generated not in the sample itself, but in the windows. By removing the windows we can thus get rid of most of the XPM artifact (the $\overline{n}_2$ of air is 3-5 orders of magnitude lower than that of solids and liquids[61]). Designs of sample cells which overcome this problem are the wire flow cell[68] and cells using thin 200-500 nm silicon nitride membranes as windows.

The latter has been used in some of the experiments of Chapters 5 and 7. However, both these approaches are much less convenient than using CaF_2 windows, especially when studying nonpolar liquids. Additionally, even when XPM from the windows is removed, the resonant $\chi^{(3)}$ "artifacts", which will be discussed later in this Chapter, still limit the pump-probe resolution time to 100-200 fs.

2.5 Characterization of the pulses

Using infrared spectrometer we can measure the spectral intensity of a pulse $I(\omega) = \frac{1}{2}c\epsilon_0|E|^2$. If we also know the spectral phase of the pulse, we can determine the complex electric field as a function of frequency:

$$E(\omega) \propto \sqrt{I} e^{-i\phi(\omega-\omega_0)} + c.c. \tag{2.36}$$

From $E(\omega)$ we can obtain the electric field in time domain $E(t)$ by inverse Fourier transformation, which reveals the pulse duration. The spectral phase can be written as a Taylor expansion around the carrier frequency:

$$\phi(\omega-\omega_0) = \phi_0 + \phi_1 \cdot (\omega-\omega_0) + \phi_2 \cdot \frac{(\omega-\omega_0)^2}{2} + \phi_3 \cdot \frac{(\omega-\omega_0)^3}{6} + ... \tag{2.37}$$

The first term of this expansion is just a constant phase. The second term is linear and upon Fourier transform will not change the shape of the pulse, but will only shift the pulse in time. The second and higher order terms will actually change the shape of the pulse in the time domain. Non-zero values of $\phi_2, \phi_3, ..$ can arise upon propagation through a medium with $d^2k/d\omega^2 \neq 0$, i.e. in which the group velocity of light changes with frequency. The pulse will become chirped: high frequencies lag behind the low frequencies (positive chirp) or the opposite - low frequencies lag behind the high frequencies (negative chirp).

In the previous section we assumed ideal Gaussian pulses, i.e. pulses with only a constant and a linear spectral phase. In this case a Gaussian shape of the pulse in the frequency domain results in Gaussian shape of the pulse in time domain. However, the refractive index of every material is frequency dependent, which implies that a certain group velocity dispersion (GVD) per optical path length is added when a pulse is transmitted through a medium. This effect is undesirable in pump-probe spectroscopy since it broadens the pulses, and decreases the time resolution of experiment. In addition, if the pulse is chirped, this can give wrong results. For example, if the probe is positively chirped, the time delay of the low-frequency components will be shorter than the time delay of the high-frequency components. This will result in a measured spectrum that is tilted as a function of frequency which may be incorrectly interpreted as spectral dynamics of frequency-dependent relaxation of the studied resonance.

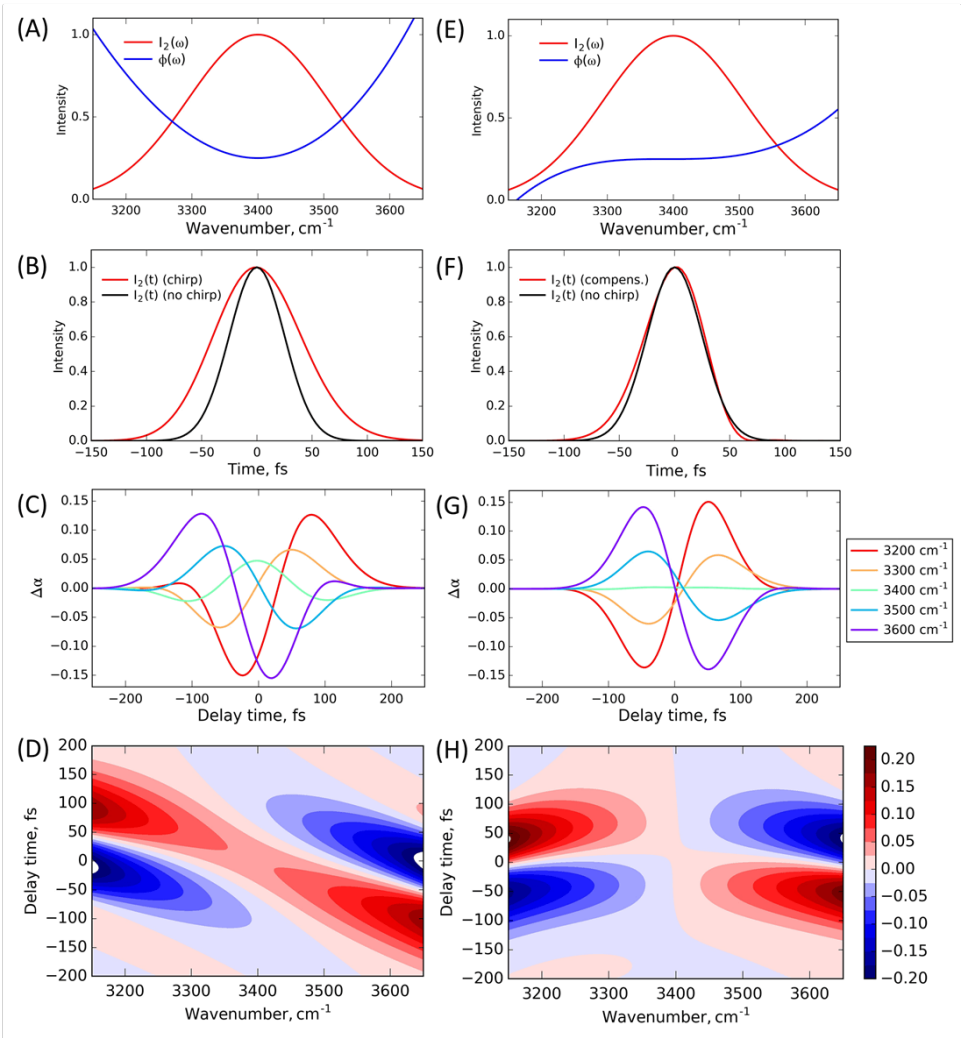

Figure 2.4: Modeling of the cross-phase modulation artifact in pump-probe experiment with a probe pulse transmitted through 1 mm of germanium (left panel) and through 1 mm of germanium plus 15 mm of calcium fluoride (right panel). (A,E) The intensity spectrum and the spectral phase; (B,F) the time profile of the pulse compared to its original profile; (C,G) XPM signal presented as a function of delay time; (D,H) XPM signal in a delay-frequency 2D-plot.

When we combine intensity spectra with a cross-phase modulation effect, we can obtain more information about pump and probe pulses, namely, determine their phase and the time profiles. When pump and probe beams are split from one source, which

means that they are the same, the phase can be retrieved quantitatively by fitting the experimental XPM with Eq.2.34.[69,70] Here we will briefly show how the cross-phase modulation artifact can be used for pulse characterization qualitatively.

In Figure 2.3 we see that when the pulses have a Gaussian shape and linear phase, the XPM signal is completely symmetric and turns zero at zero delay time. However, most of the transmitting optics in a pump-probe setup ($AgGaSe_2$ nonlinear crystal, Ge infrared filter) have a positive group velocity dispersion and thus add a positive chirp to the infrared pulse. In Figure 2.4A we show the same probe pulse used in the calculations before, but now with an additional quadratic spectral phase resulting from the group velocity dispersion in a 1 mm thick germanium plate. The chirp created in such a dispersive medium significantly broadens the pulse in the time domain (Figure 2.4B). A dramatic effect of the chirp is observed in the cross-phase modulation signal (Figure 2.4C,D). Now the signal is broad and asymmetric and does not turn to zero at any delay time between the pump and probe pulses. We also can observe that the high and low frequencies are separated in time. At zero delay time the low frequency component 3200 cm^{-1} will arrive at the sample *before* the pump and experience an XPM effect typical for "negative" delay times, while the high-frequency component 3600 cm^{-1} will arrive *after* the pump and will experience an XPM effect typical for "positive" delay times. In the present case, the difference in timing of the 3200 cm^{-1} and 3400 cm^{-1} frequency components is $\sim$70 fs.

Group velocity dispersion is an additive quantity and therefore a positive chirp created by transmission through a germanium plate can be compensated by transmitting the light through a material with a negative GVD. Calcium fluoride is such a material. In the right panel of Figure 2.4 we show the result of the compensation of the positive chirp created by 1 mm of Ge by the negative chirp created by 15 mm of CaF_2. In Figure 2.4E we see that the spectral phase now becomes almost constant in the frequency range 3300-3500 cm^{-1}, and shows nonlinearity only in the tails of the spectrum. The chirp is not completely removed due to the dependence of GVD on frequency (third and higher order terms in Eq 2.37). Nevertheless, the pulse gets compressed almost to its original shape in the time domain (Figure 2.4F). In Figure 2.4G,H we see that the XPM signal is also brought back to its original symmetric shape with only minor distortions in the tails of the spectrum. Hence by using the XPM effect we can analyze the chirp of the probe pulse and we can test how well we have compensated it by adding additional material in the probe beam path.

In all the experiments presented in this thesis we used XPM in a calcium fluoride window to test the probe pulses for the presence of the chirp and to compensate this chirp if necessary. In the used experimental setups a strong positive chirp usually appears when the probe frequency is $>$2800 cm^{-1}, and then compensation is needed. In addition, the shape of the XPM signal can be used to check for any asymmetry in the time profile

of the pump pulse and the duration of the pulses. In addition, we use the zero-crossing point of the XPM effect to define zero delay time.

2.6 Pump-probe spectroscopy: phenomenological approach

2.6.1 Infrared pump-probe experiment

As we have shown in the previous section, the signal measured in pump-probe experiment can be derived using the theory of nonlinear optics and resonant light-matter interaction. However, in many experiments the dynamics of interest occur at time scales that are long compared to the pulse durations and the decay time constants of the coherences, and a more phenomenological approach suffices. Here we will describe the phenomenological approach to the infrared pump-probe experiment.

First, we consider the pump and probe pulses as infinitely short delta-pulses. The first two terms will result in a negative signal at frequency ω_{01}. From the corresponding Feynamn diagrams we see, that this signal comes from the creation of excited state population, which then emits a photon and converts back to the ground state. This contribution is called stimulated emission (SE) of the excited state. The third and the fourth terms also give a negative signal at frequency ω_{01}. They represent the absorption of the molecules in the ground state, which has decreased due to the fact, that part of the molecules are now in the first excited state. Therefore, this contribution is called ground state bleach (GSB). The last two terms give a positive signal at ω_{12} frequency. This signal is the result of absorption of a photon by the excited state and is called excited state absorption (ESA) or induced absorption.

The first four terms are proportional to μ_{01}^4 and the last two terms are proportional to $\mu_{01}^2\mu_{12}^2$. The absorption change signal can thus be written as

$$\Delta\alpha(\omega) = -2\sigma_{01}(\omega)N + \sigma_{12}(\omega)N \tag{2.38}$$

where N is the excited state population, and $\sigma_{01} \propto \mu_{01}^4$ and $\sigma_{12} \propto \mu_{01}^2\mu_{12}^2$ are the cross-sections of the 0→1 and 1→2 transitions, analogously to the linear infrared spectroscopy. Note, that in the harmonic approximation of the dipole moment $2\sigma_{01} = \sigma_{12}$ since $\mu_{12}^2 = 2\mu_{01}^2$. Thus, for a completely harmonic oscillator, when also $\omega_{01} = \omega_{12}$, there will be no pump-probe signal at all.

In the condensed phase, the pump induced vibrationally excited state decays on a time scale of 0.1-100 ps. The excited molecules relax back to the ground state, which is in many cases a first-order kinetic process, meaning that the excited state population decays exponentially. Note, that this was already included in Eq. 2.25 as I_{00} and I_{11} are exponential functions. Hence, a usual pump-probe experiment will yield a frequency and

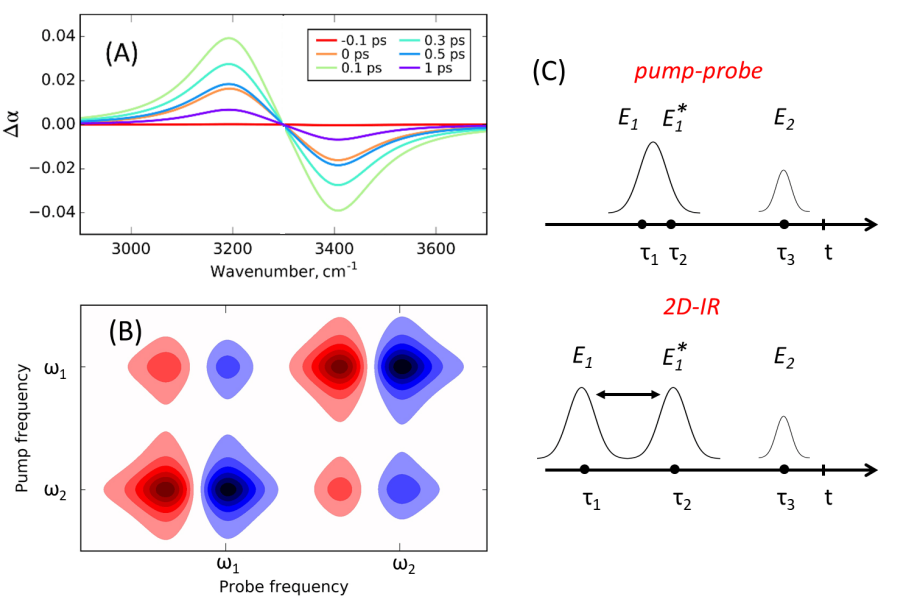

Figure 2.5: (A) Illustration of a pump-probe signal. (B) Illustration of a 2D-IR spectrum of two coupled vibrations, blue color represents negative and red - positive signal. (C) Scheme of the pulse sequence in pump-probe and 2D-IR experiments.

delay time dependent signal shown in Figure 2.5A.

2.6.2 2D-IR EXPERIMENT

An important extension of infrared pump-probe spectroscopy is two-dimensional infrared spectroscopy, which includes the dependence of the transient absorption signals on the pump frequency. There can be two different transitions of very similar frequencies, and in a pump-probe experiment, due to the spectral width of the pump pulse, we may well excite both of them. Measuring the signal as a function of probe frequency only, we cannot judge if the signal of the probed vibration is due to the excitation of that same vibration or due to excitation of the other vibrational that interacts with the probed vibration. This latter situation can, for example, arise if the two vibrations are anharmonically coupled. In this case excitation of one vibration perturbes the potential of the second vibration resulting in a change of the vibrational energy levels. The signal measured in pump-probe experiment will be a sum of the signal due to the direct excitation, and the signal due to the excitation of the coupled vibration (cross-peak). In 2D-IR experiment we can separate these two contributions by resolving the signal on the pump frequency

axis (Figure 2.5B).

We can imagine two spectrally narrow vibrational bands having closely spaced central frequencies ω_1 and ω_2. After the first interaction with the electric field of the pump a coherence of each vibration is created. These two coherences oscillate with frequencies ω_1 and ω_2. If the pump pulse is very short, the second interaction with the pump electric field can occur only at a time when these two coherences still oscillate in phase and thus both will be excited and . To selectively measure the response of one or the other vibration we need to *scan* the second electric field until a time longer than $|\omega_1 - \omega_2|^{-1}$. It can be achieved by using a longer pump pulse, which basically means that the pump spectrum is narrower than the frequency separation between the vibrations, which means that only one of the two vibrations is excited.

The use of a spectrally narrow pump pulse has as a drawback that the time resolution of the experiment defined by the cross-correlation of the pump and probe pulses is lowered. To overcome this effect, in most of 2D-IR experiments a pair of short pump pulses with a variable time delay between them is used instead of one long pulse (Figure 2.5C). This approach was used in all the 2D-IR experiments presented in this thesis. We obtained the pulse pair by splitting the pump pulse in Mach-Zehnder interferometer with one dynamic arm, which scans the delay between the two pulses. Of course, experimentally it is convenient vary the delay of the first pump pulse and to keep the delay between the second pump pulse and the probe pulse constant.

2.6.3 Anisotropy

In the derivation of Eq 2.25 we omitted the fact that both electric fields and transition dipole moments are actually vectors and that within each integral we should take the scalar product $\vec{\mu} \cdot \vec{E} = |\mu||E|cos\Omega$. Hence, the resulting third order polarization is $\vec{P}^{(3)} \propto \vec{\mu} cos\psi cos^2\theta$ and the resulting signal is

$$\Delta\alpha \propto \int cos^2\psi cos^2\theta d\Omega \tag{2.39}$$

where ψ and θ are the angles between the transition dipole moment and the polarization of probe and pump electric field, respectively, and the integral is taken over all the orientations of the molecules in the sample.

Usually in a pump-probe experiment the signal is measured in two polarization configurations: probe parallel to the pump and probe perpendicular to the pump. In this case $cos\psi = sin\theta sin\phi$, where ϕ is the angle between direction of the electric field propagation and the projection of the transition dipole moment on the plane perpendicular to the pump polarization. The signals measured in parallel and perpendicular polarization

configurations are:

$$\begin{aligned}\Delta\alpha_{\parallel}(t) &\propto \int\int \frac{3}{4\pi} p(\theta,\phi,t|\theta_0,\phi_0) cos^2\theta_0 cos^2\theta d\Omega_0 d\Omega \\ \Delta\alpha_{\perp}(t) &\propto \int\int \frac{3}{4\pi} p(\theta,\phi,t|\theta_0,\phi_0) cos^2\theta_0 sin^2\theta sin^2\phi d\Omega_0 d\Omega\end{aligned} \tag{2.40}$$

where $p(\theta,\phi,t|\theta_0,\phi_0)$ is the probability that the transition dipole moment oriented as θ_0,ϕ_0 at zero delay time will be oriented as θ,ϕ at delay time t, and $3/4\pi$ is the normalization factor. Thus, the pump-probe signal actually depends on the initial orientation of the molecules in the sample and on the dynamics of their reorientation. It can be shown[64] that for an isotropic sample (molecular orientation is random) we can construct a quantity

$$\Delta\alpha_{iso}(\omega,t) = \frac{1}{3}(\Delta\alpha_{\parallel}(\omega,t) + 2\Delta\alpha_{\perp}(\omega,t)) \tag{2.41}$$

which is independent of the reorientation of the transition dipoles. Another quantity, called the anisotropy parameter

$$R(\omega,t) = \frac{\Delta\alpha_{\parallel}(\omega,t) - \Delta\alpha_{\perp}(\omega,t))}{\Delta\alpha_{\parallel}(\omega,t) + 2\Delta\alpha_{\perp}(\omega,t))} \tag{2.42}$$

is independent of the vibrational relaxation dynamics and purely represents the average orientation of the transition dipoles at time t with respect to the orientation at time 0. It can be shown[64,71] that the anisotropy parameter is proportional to the second order orienational correlation function:

$$R(t) = \frac{2}{5}C_2(t) = \frac{2}{5}\langle P_2(\vec{\mu}(0)\cdot\vec{\mu}(t))\rangle = \frac{2}{5}\langle(3cos^2\theta(t)-1)/2\rangle \tag{2.43}$$

where $\theta(t)$ is the angle between the transition dipole moment at time zero and at time t.

At zero time $\theta(0) = 0$, which yields R(0)=0.4. At long delay times, when the orientation of the molecules becomes completely random with respect to their orientation upon excitation, $\langle cos^2\theta(t\to\infty)\rangle = \frac{1}{3}$ giving R($t\to\infty$)=0. The anisotropy can also decay due to energy transfer from the originally excited molecule to other molecules of different (random) orientation or as a result of structural changes of the excited molecule. For molecules that possess several degenerate vibrations with different orientations of the transition dipole moment (H_2O, H_3O^+), intramolecular energy transfer or fast structural fluctuations can result in a sub-100 fs (partial) decay of anisotropy.

2.7 Finite pulses and coherent effects

In pump-probe experiments it is usually assumed that the measurement result is independent of the probe pulse. Indeed, if the dynamics of the measured transient signal is

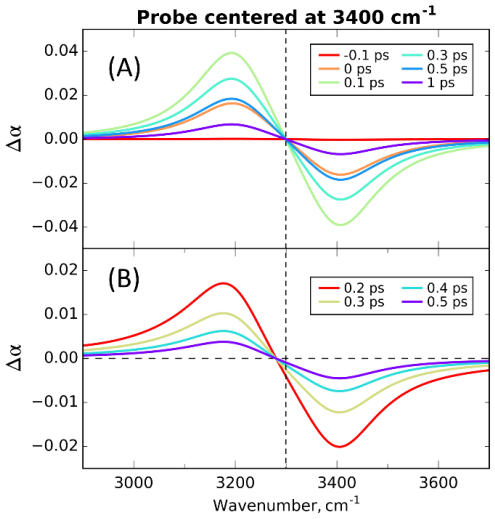

Figure 2.6: Pump-probe spectra modeled with (A) 10 fs broad probe and T_1=0.5 ps; (B) 70 fs broad probe and T_1=0.2 ps.

sufficiently slow, we can assume that the excited state population is constant during the duration of the probe pulse. However, the finite spectral width of the probe pulse and population dynamics occuring during the probe pulse duration can significantly distort the pump-probe signal. Here we will model transient absorption spectra and show how these depend on the properties of the probe pulse.

First we calculate the third order polarization and the "artifact-free" transient absorption signal using Eqs. 2.25-2.26. For the transient absorption signals we set the transition frequencies to ω_{01}=3400 cm^{-1} and ω_{12}=3200 cm^{-1} with the dephasing times T_2 corresponding to 200 cm^{-1} broad (FWHM) Lorentzian shaped absorption bands. The pump was taken to be a 100 fs broad Gaussian pulse centered at 3400 cm^{-1}.

In Figure 2.6 we show the pump-probe spectra of the excited state with vibrational relaxation times T_1=0.5 ps obtained using a 10 fs probe pulse and with T_1=0.2 ps with a 70 fs probe pulse. As we see, the ultrashort probe pulse leads to transient spectra formed by the sum of the negative and positive Lorentzian bands centered at 3400 cm^{-1} and 3200 cm^{-1} respectively. However, in the second case, the the variation of the excited state population during the probe pulse is significant. As a consequence, the pump-probe spectra become distorted, which can be seen from the increased amplitude of the bleaching part and the shift of the zero-crossing frequency. This result shows that only if the population dynamics does not vary significantly during the probe pulse, the relative time dependence of the signal at each frequency will be measured correctly.

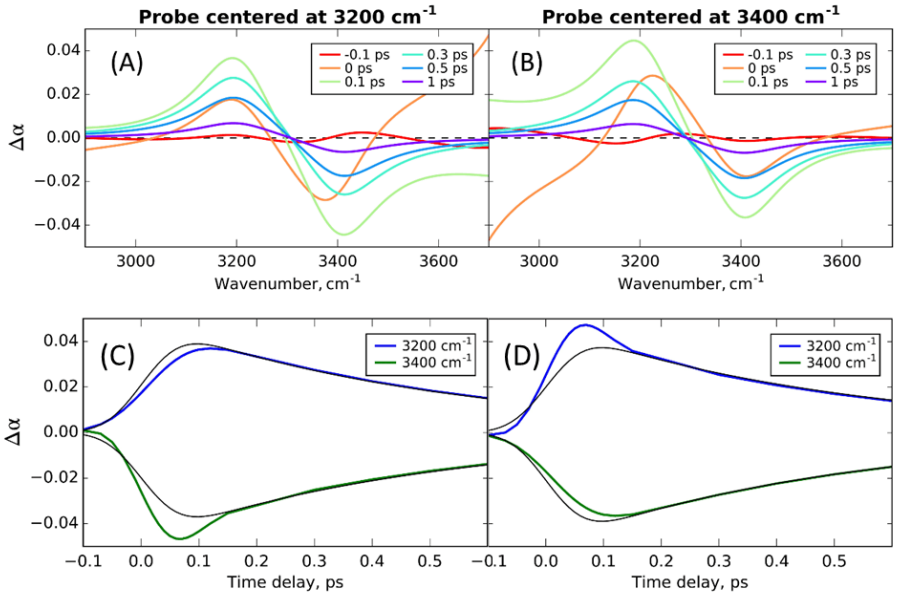

Figure 2.7: Pump-probe spectra modeled with a 70 fs probe pulse centered at (A) 3200 cm^{-1} and (B) 3400 cm^{-1}. Transient absorption signal at 3200 cm^{-1} and 3400 cm^{-1} as a function of delay time for a 70 fs probe pulse centered at (C) 3200 cm^{-1} and (D) 3400 cm^{-1}. The black lines represent the calculated dynamics of the excited state.

We observe that strong distortion of the spectra occurs during the rapid growth of the excited state population around zero delay time (Figure 2.7A,B). This effect can be phenomenologically explained by the fact that, due to a rapid growth of the excited state population, the absorption of the sample changes on a very short time. Thus, part of the probe pulse that arrives to the sample earlier experinces a complex refractive index rather different from the one experienced by the part of the pulse that arrives later. This effect time-dependence of the absorption spectrum and the complex refractive index is similar to the cross-phase modulation effect described before. In the delay time dependence it appears as an enhanced or decreased transient absorption signal around zero delay time (Figure 2.7C,D), which is more pronounced in the tails of the probe spectrum.

In addition to the distortion of transient absorption dynamics resulting from the strong variation of excited state population, a coherent artifact due to a "wrong" electric field sequence can arise around zero delay time. This artifact is a transient grating effect in which the probe and the pump field create a population grating from which the pump diffracts in the direction of the probe. This signal results from interactions illustrated by the the six Feynman diagrams in Figure 2.2, for which the first and second field in-

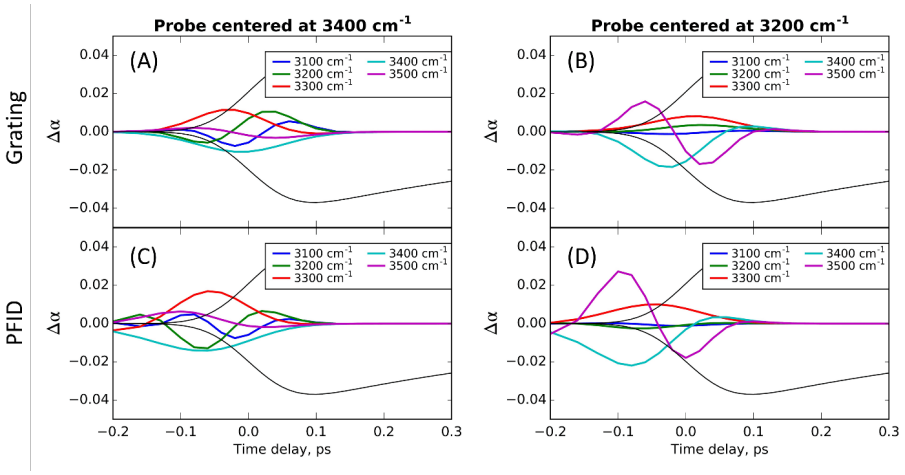

Figure 2.8: Pump-probe signal due to the transient grating effect (A,B) and the perturbed free induction decay (C,D) as a function of delay time. For comparison the black lines represent the signals at 3200 cm^{-1} and 3400 cm^{-1} for the "right" electric field sequence.

teractions are with E_2 and E_1*. The transient grating effect in which E_2 comes first, illustrated by the lower three Feynman diagrams, is also denoted as a perturbed free induction decay. Since this artifact involves the interaction of the probe field before the two field interactions with the pump, this signal is primarily seen at negative delay times (Figure 2.8).

The results of our simple modelling are in qualitative agreement with experimental observations. In Figure 2.9 we show experimental transient absorption signals as a function of delay time for the OH-stretch vibration of HDO molecules in isotopically diluted water. The experiment was performed using a pump pulse centered at the maximum of the OH-stretch absorption band (3400 cm^{-1}) and different probe pulses with a central frequency varied in the range 3250-3400 cm^{-1}. We see that the artifacts discussed and modeled here strongly affect the experimental data, and can be easily mistaken for an ultrafast relaxation processes.[72] The transient absorption signals strongly depend on the pulse characteristics and dephasing rates, parameters that are usually not taken into account in pump-probe experiments. Hence, the analysis of transient absorption signals within the pump-probe cross-correlation time can lead to wrong conclusions.

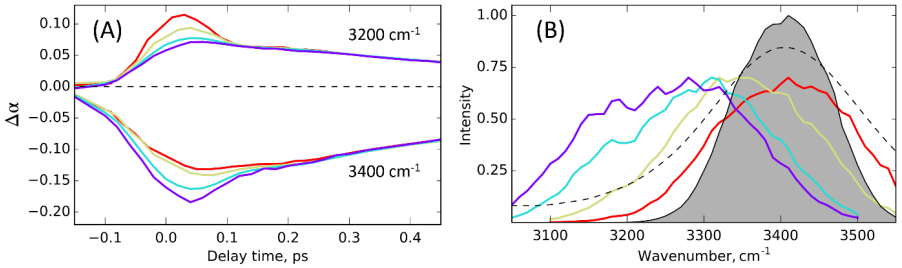

Figure 2.9: (A) Transient absorption change upon the excitation of OH-stretch vibration of HDO measured at 3200 cm^{-1} and 3400 cm^{-1} with different probe pulses. (B) Pump (grey) and probe pulses (color code with respect to part A) used in the experiment; dashed line represents the linear absorption spectrum of HDO (HDO:D_2O=4:96 solution).

3 Experiment

In this thesis we report on studies of the structural and vibrational dynamics of hydrated protons and carboxylic acids using polarization-resolved infrared pump-probe spectroscopy and two-dimensional infrared spectroscopy. For the experiments presented in Chapters 4-9 we used three different setups. A two-color pump-probe setup was used to study the vibrational dynamics of hydrated protons by measuring transient absorption signals over a broad frequency range with varying pump frequencies (Chapters 4-7). A one color pump-probe setup was used to study the structural dynamics of hydrated protons with anisotropy measurements at a particular frequency (Chapters 6, 7). Finally, to resolve the conformations of carboxylic acids (Chapters 8, 9), we used a two-dimensional infrared (2DIR) setup. In this Chapter we present the principal schemes of these setups and provide the experimental details.

3.1 Generation of femtosecond infrared pulses

To perform femtosecond mid-infrared pump-probe experiments we first need to generate femtosecond mid-infrared pulses. This is done by means of frequency conversion of the near infrared pulses from commercially available laser systems (Figure 3.1). In the two-color pump-probe setup and in the two-dimensional infrared setup, a Ti:sapphire oscillator (Mantis, Coherent) generates 800 nm pulses, which are used to seed a Ti:sapphire regenerative amplifier (Legend, Coherent). The crystal of the amplifier is pumped by an internal Nd:YLF diode laser (527 nm). The seed pulse is stretched by a pair of gratings and then coupled into the amplifier's cavity via a Pockels cell. After amplification the

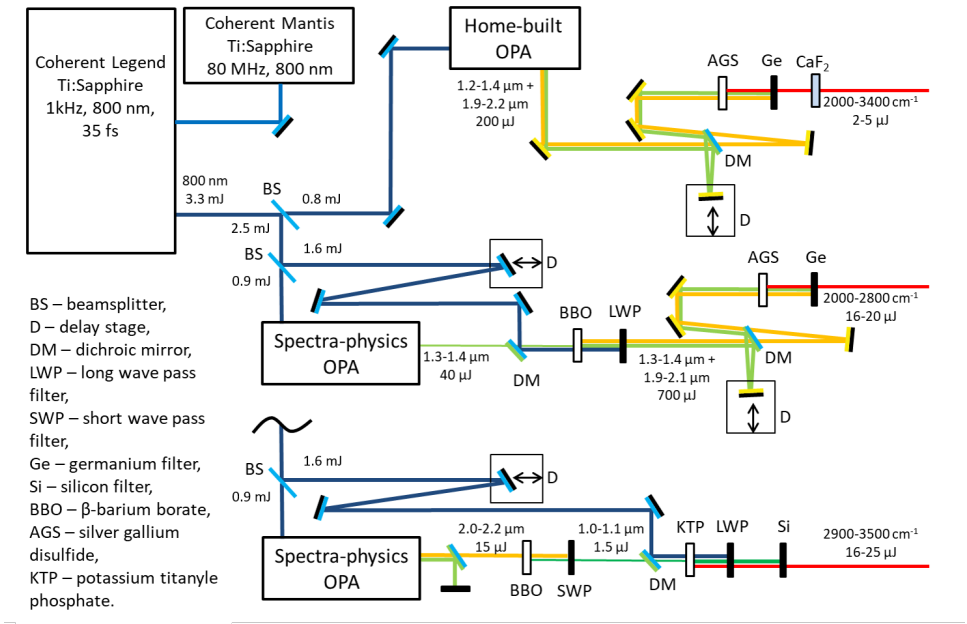

Figure 3.1: Pulse generation scheme in the two-color pump-probe setup.

pulse is coupled out by a second Pockels cell and recompressed. This scheme yields 35 fs 800 nm pulses with a pulse energy of 3.3 mJ (5 mJ in case of the 2DIR setup) at a repetition rate of 1 kHz.

indent 0.8 mJ of the 800 nm light was used to pump a homebuilt optical parametric amplifier (OPA), seeded by the white light that is generated by focusing a small fraction of the 800 nm pulse in a sapphire crystal. A spectral fraction of this white light was amplified by the 800 nm beam in a two-step OPA process using β-barium borate (BBO) crystals. This OPA process yielded signal (1.2-1.4 μm) and idler (1.9-2.2 μm) pulses with a total energy of 200 μJ. The signal and idler pulses were mixed in a silver gallium disulfide (AGS) crystal to generate mid-infrared pulses at their difference frequency. The remainder of the signal and idler was filtered out by a germanium filter. This filter introduces group velocity dispersion (GVD) on the produced infrared pulses. This GVD was compensated by CaF_2 windows. In this way we produced tunable 2000-3400 cm^1 pulses with a pulse duration of $\sim$60 fs, a spectral full width at half-maximum (fwhm) of 250 cm^1 , and an energy between 2 and 5 μJ depending on frequency.

We generated mid-infrared pump pulses with a central frequency of 2000-2800 cm^1 by pumping another OPA with the remaining 2.5 mJ of 800 nm beam. This OPA employs

the same white-light-seeded three-step BBO-based amplification process that we used to generate the probe pulses. The produced signal and idler with a total energy of ∼700 μJ were difference-frequency mixed in an AGS crystal to produce 16-20 μJ pulses with a spectral fwhm of 150 cm^1. In the 2DIR setup the pump and probe pulses were generated in a similar way using two commercial BBO-based OPA's (TOPAS Prime, Coherent) to create signal and idler pulses followed by difference-frequency mixing in AGS crystas. These processes yielded tunable pulses with a central frequency of 1700-2800 cm^{-1} and similar characteristics (pulse duration, pulse energy, spectral fwhm) as in the two-color pump-probe setup.

To generate pump pulses with a central frequency of 2900 cm^1 and higher, the OPA of the two-color pump-probe setup was modified as shown in the bottom panel of Figure 3.1. After two-step BBO-based parametric amplification, we frequency-doubled the idler in another BBO crystal. The resulting second harmonic of the idler was then used to seed an OPA process in a potassium titanyl phosphate (KTP) crystal pumped by the remainder of the 800 nm beam. After filtering out all visible and near-infrared light with a silicon filter, this process yielded 16-25 μJ pulses with a spectral fwhm of 150 cm^1.

In the one-color pump-probe setup the infrared pulses were generated in a different way.[73] An Yb-medium based laser (Pharos, Light Conversion) produced 1028 nm pulses with a pulse energy of 0.4 mJ at a repetition rate of 50 kHz. The repetition rate was reduced by a pulse picker to 1 kHz and the resulting output was used to pump a commercial OPA (Orpheus-ONE-HP, Light Conversion). This OPA yields signal (1350-2060 nm) and idler (2060-4500 nm). The latter pulses (tuned to 2600 cm^{-1}, 12 J, 200 fs) were split by a zinc selenide beamsplitter and used in pump-probe experiments. This setup yielded much better pulse-to-pulse stability than the two-color pump-probe setup (a typical standard deviations measured by the detector for 1000 consecutive pulses was 0.2-0.4% and 0.6-1.2% for one-color and two-color setup, respectively).

3.2 Infrared pump-probe (2DIR) setup

The principal scheme of the pump-probe and 2DIR setups is shown in Figure 3.2. The weak infrared beam (generated in a separate OPA or split from the same source as the pump) was split first by a zinc selenide beamsplitter into probe and reference beams. The probe pulse was sent to a motorized delay stage. Both the probe and reference beams were transmitted through cleaning wire grid polarizers and focused in the sample by a parabolic mirror.

The pump beam is sent through a chopper, a half-wave plate and a wobbler. In the pump-probe experiment the chopper blocks every second pump pulse to measure the transmission of the sample when the pump is *on* and *off*. In the 2DIR experiment the

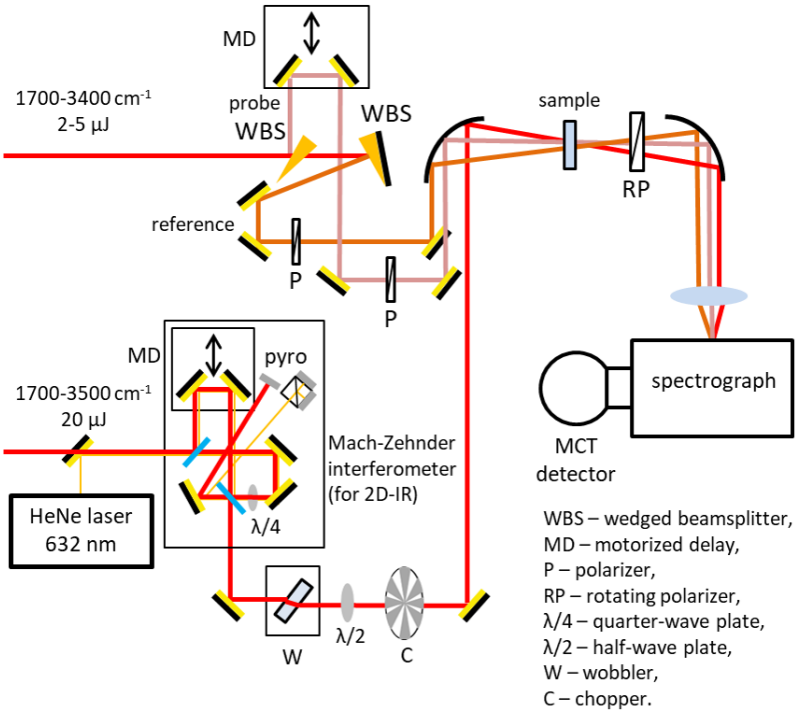

Figure 3.2: The principal scheme of the pump-probe (2DIR) setup.

chopper is not used. The half-wave plate is used to set the polarization of the pump at 45° with respect to the probe polarization. The wobbler is used to suppress the effect of pump scattering from the sample into the direction of the probe. It consists of a 4 mm thick calcium fluoride window, which oscillates with a frequency of 250 Hz and delays the pump pulses performing the phase cycle ($+\pi/2$, 0, -$\pi/2$, 0) in the pump-probe experiment or ($+\pi$, 0, -π, 0) in the 2DIR experiment. In this way, the phase of every two subsequent pulses is different by π (note that in the pump-probe experiment the pulses with 0 phase are chopped). Thus, the interference of the probe and pump light scattered by the sample on the detector cancels out for subsequent shots. In the 2DIR setup the pump beam was sent through a Mach-Zehnder interferometer to produce a pulse pair. One arm of the interferometer had a motorized delay stage to scan the delay time between the pulse pair. The details of this implementation can be found in ref. 74.

The pump beam is focused in the sample in spatial overlap with the probe. After the sample the beams are collimated by a parabolic mirror and sent to a spectrograph

(Oriel MS260, Newport). In the spectrograph the beams are dispersed and detected by a mercury-cadmium-telluride (MCT) detector having three 32 pixel arrays. One of the arrays detects the probe. To account for the pulse-to-pulse fluctuations, the second array detects the reference, which is transmitted through the sample but not overlapped with the pump. The third array can be used to measure the pump spectrum, however, usually the pump is blocked right after the sample to minimize the scattering.

Setting the rotating polarizer after the sample either at 0° or at 90° with respect to the pump polarization allows us to select the probe component of the corresponding polarization and to measure the transient absorption signal in two polarization combinations. In the 2DIR setup this was realized by splitting the probe in two beams by a 50/50 beamsplitter and selecting the corresponding polarization component in each beam. Then the two polarization components of the probe were detected simultaneously by two arrays of the MCT detector.

Published as:

Oleksandr O. Sofronov and Huib J. Bakker. Energy Relaxation and Structural Dynamics of Protons in Water/DMSO Mixtures. The Journal of Physical Chemistry B 2018, 122, pp. 10005-10013

4

Dynamics of Protons in Water/DMSO Mixtures

Abstract

We investigate the structure and dynamics of proton solvation structures in mixed water/dimethyl sulfoxide solvents using two-color mid-infrared femtosecond pump-probe spectroscopy. At a water fraction below 20%, protons are mainly solvated as $(DMSO\text{-}H)^+$ and $(DMSO\text{-}H)^+$-H_2O structures. We find that that excitation of the OH-stretch vibration of the proton in $(DMSO\text{-}H)^+$-H_2O structures leads to an ultrafast contraction of the hydrogen bond between $(DMSO\text{-}H)^+$ and H_2O. This excited state relaxes rapidly with T_1=95$\pm$10 fs, and leads in part to a strong local heating effect and in part to pre-dissociation of the protonated cluster into $(DMSO\text{-}H)^+$ and water monomers.

4.1 Introduction

In the condensed phase, the proton (H^+ ion) strongly interacts with surrounding molecules/ atoms leading to the formation of proton-solvation structures. In liquid water, a large distribution of solvation structures exist, with the Eigen ($H_9O_4^+$) and Zundel ($H_5O_2^+$) structures as limiting cases.[21,48] The transport mechanism of the proton through the solution strongly differs from that of other cations, and strongly relies on the structural dynamics of the solvation structures of the proton.[3,9,13,75]

Aqueous protons give rise to a broad absorption in the mid-infrared region of the spectrum, the so-called Zundel continuum. This continuum can be crudely subdivided into absorption regions of stretch, bend and proton transfer modes.[15,33,47] Although these modes are all of highly mixed character, especially in the liquid phase,[22] infrared predissociation spectroscopy of proton-water clusters in the gas phase allows for a crude assignment of the different regions of the Zundel continuum.[41,42] The blue side of the continuum around 3100 cm^{-1} is thus assigned to water molecules flanking a proton in a ($H_5O_2^+$) Zundel configuration, and the region around $\sim$2600 cm^{-1} is assigned to the OH-stretch modes of the H_3O^+ core of Eigen-like $H_9O_4^+$ structures. The spectral response between 1500 and 2000 cm^{-1} can be assigned to bending vibrations. Finally, the frequency region around 1100 cm^{-1} has been assigned to the shuttling vibration of the proton (proton transfer mode) in between two flanking H_2O molecules.[18] In spite of these assignments, the identification of the different regions of the infrared spectrum of the hydrated proton with particular vibrational modes of solvation structures is still actively debated.[22,35,36]

The dynamics of the proton solvation structures can be studied with time-resolved mid-infrared spectroscopy, as this technique probes the spectral dynamics of the vibrations that in turn report on changes in the covalent and hydrogen bonds.16 In recent years several femtosecond mid-infrared studies on the hydrated proton have been reported.[47,72,76,77] In these experiments the dynamics of proton solvation in different aqueous media (water, water/acetonitrile and hydrated Nafion membranes) was studied by means of excitation of the hydrated proton OH-stretch vibrations. These studies showed that ultrafast structural fluctuations of the hydrated proton result in a sub-100 fs vibrational relaxation of the vibrationally excited state. Only for the H_3O^+-ion strongly bound to a negatively charged sulfonate in Nafion membranes the vibrational relaxation was observed to be significantly slower, with T_1=350$\pm$30 fs.

A challenge in studying the structural dynamics of proton solvation structures in pure water is that the OH-stretch vibrational lifetimes of water molecules and hydrated protons are extremely short ($\sim$0.27 ps[78,79] and $<$100 fs[18,20] respectively). As a result, the time window in which the structural dynamics can be studied in the vibrationally excited state is very much limited. However, previous studies also showed the presence of slower

restructuring and energy dissipation processes following the vibrational relaxation. This observation suggests that the structural lifetime of the proton hydration structures is on the order of picoseconds.[25]

In this chapter we use femtosecond mid-infrared pump-probe spectroscopy to study the structure and dynamics of proton solvation structures in water/dimethyl sulfoxide mixtures. Dimethyl sulfoxide (DMSO) is a polar, aprotic solvent, that solvates water molecules well, but that breaks the hydrogen-bond network. DMSO has a quite strong interaction with water and protons, and for a water fraction below 20%, water molecules primarily exist as monomers solvated by DMSO molecules.[80] This isolation of water molecules can increase the vibrational lifetime up to five times compared to bulk water, as was recently demonstrated in a time-resolved spectroscopy study of the OD stretch vibrations of HDO/H_2O/DMSO solutions.[81] In view of this result, studying the dynamics of protons in a mixed water/DMSO solvent can provide important information on the vibrational energy relaxation and structural dynamics of the solvated proton. We compare the results with recent studies on the structural dynamics of solvated protons in water/acetonitrile studies.[72,76]

4.2 Experiment

Linear mid-infrared absorption spectra were obtained in transmission mode using a commercial Fourier transform spectrometer (Bruker Vertex 80v). The two-color mid-IR pump-probe experiments were performed as described in the section 3.2. The pump pulses with the central frequency of 2550 cm^{-1}, 3200 cm^{-1} and 3450 cm^{-1} were generated as described in the section 3.1. The samples were prepared by dissolving trifluoromethanesulfonic acid (TfOH, 98%, Sigma-Aldrich) in water and deuterated dimethyl sulfoxide (DMSO-d6, 99.9%, Sigma-Aldrich) mixtures under dry air. Trifluromethanesulfonic acid (triflic acid) fully dissociates in water or DMSO, and the triflate anion does not react with the solution components.

4.3 Results

4.3.1 Linear Infrared Spectra

In Figure 4.1 we show linear infrared absorption spectra of triflic acid/water/DMSO-d6 solutions at different acid/water concentration ratios. All spectra contain a water OH-stretch absorption band at 3200–3700 cm^{-1}. We assign the 3430-3500 cm^{-1} doublet to the symmetric and antisymmetric water OH-stretch modes of water molecules and the shoulder at $\sim$3300 cm^{-1} to the overtone of the water bending mode. As the concentrations of water in DMSO are low, water molecules mostly exist as isolated monomers

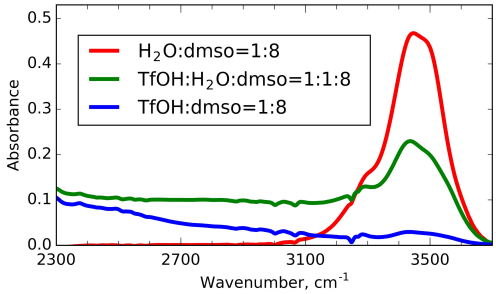

Figure 4.1: Linear absorption spectra of TfOH/DMSO=1:8, TfOH/H_2O/DMSO=1:1:8 and H_2O/DMSO=1:8 (the latter is rescaled with respect to the water concentration in the second solution), the DMSO absorption spectrum is subtracted.

solvated by DMSO.[80] The samples containing triflic acid have an additional broad absorption continuum at lower frequencies.

In a water/DMSO solution the proton will be solvated not only by water, but also by DMSO molecules. To understand the contribution of DMSO solvation to the proton absorption continuum, we also recorded the infrared absorption spectrum of triflic acid in dry DMSO. Triflic acid is a superacid and fully dissociates in DMSO solution (confirmed by the absence of $\nu_{as}(SO_2)$ band around 1400 cm^{-1}).[82] The long absorption tail at 2300–3300 cm^{-1} can thus be assigned to the OH-stretch vibrations of protonated DMSO. When the solution contains both water and triflic acid, the absorption continuum has a more flat shape (contrary to the sloping spectrum of $(DMSO\text{-}H)^+$), and a higher intensity. In this case, the continuum absorption will contain the stretch vibrations of $(DMSO\text{-}H)^+$ and hydrated protons. It has been proposed in the literature that DMSO is more basic than water.[83] Interestingly, even for solutions containing an excess concentration of protons and only trace amounts of water, the water OH-stretch band with its maximum at 3430 cm^{-1} is still observed. On the other hand, the intensity of the water OH-stretch band is significantly reduced in acidic DMSO solutions compared to spectra of water/DMSO mixtures without acid. From this observation we conclude that water and DMSO are similarly basic, so that the protons in solution can be solvated by both DMSO and water molecules. The proton will thus be located in between the oxygen atoms of two DMSO molecules, of a DMSO and a water molecule, or of two water molecules.

4.3.2 Vibrational dynamics of water monomers in DMSO

In Figure 4.2A,B we present experimental results obtained by exciting water/DMSO solutions with a pulse centered at 3450 cm^{-1}, i.e. in the frequency region of the water OH-stretch absorption.

The transient spectrum of the initially excited state consists of a decreased absorption above 3350 cm^{-1} and an enhanced absorption at lower frequencies. The decreased absorption is due to the bleaching of the fundamental v=0→1 transition and the enhanced absorption results from the v=1→2 excited-state absorption. The transient spectrum clearly shows the signature of the doublet of the symmetric and antisymmetric OH-stretch modes at 3430/3500 cm^{-1} and the H_2O bending overtone at 3280 cm^{-1}. The excited v=1 state relaxes with time constant T_1=0.84±0.03 ps. In previous experiments on the vibrational relaxation of the OD-stretch vibration of isotopically dilute HDO/H_2O/DMSO mixtures two distinctly different relaxation times were observed, corresponding to fast-relaxing red-shifted water-bound HDO molecules and slowly-relaxing blue-shifted DMSO-bound HDO molecules.[81,84] The slow component was assigned to the OD groups of HDO molecules forming hydrogen bonds to the oxygen atom of DMSO,

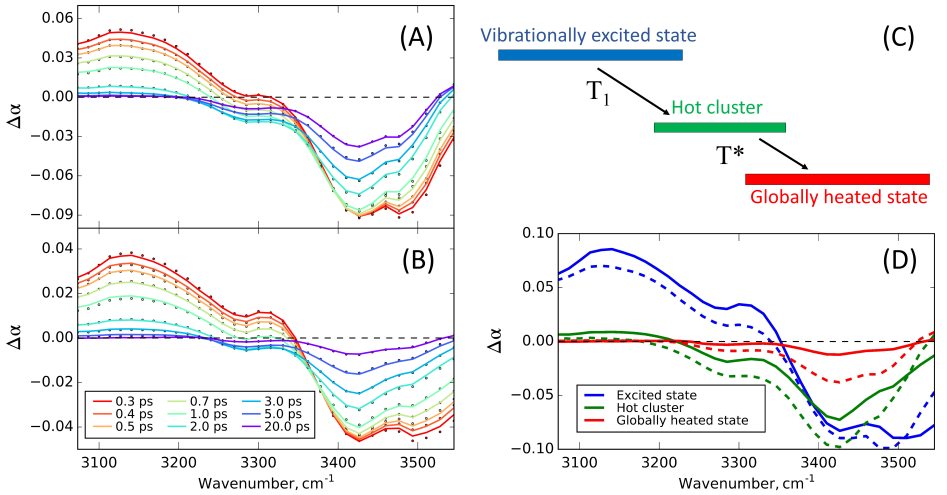

Figure 4.2: Isotropic pump-probe spectra measured after excitation with a pump pulse centered at 3450 cm^{-1}: (A) H_2O/DMSO=1:8, (B) TfOH/H_2O/DMSO=1:1:8. The lines represent the result of the fit of the kinetic model to the data. (C) Kinetic model used to fit the isotropic data. (D) The spectral signatures of the different states of the model obtained from the fit: the solid lines represent the solution containing protons (scaled), the dashed lines represent the solution without protons.

and this component dominated the response for high volume fractions of DMSO. Here we observe a single vibrational relaxation time for the OH-stretch vibrations of a dilute solution of H_2O in DMSO. We assign this single component to H_2O molecules forming hydrogen bonds to the oxygen atoms of DMSO molecules. We thus find that the relaxation time of the OH-stretch vibration of H_2O in DMSO is $\sim$8 times faster than that of the OD stretch vibration of HDO in DMSO, which is in fact a similar ratio as is observed for neat H_2O and HDO:H_2O ($\sim$0.27 ps versus 1.65 ps).

We observe nearly identical transient spectra and relaxation dynamics for solutions with and without added triflic acid, which shows that the excitation pulse excites very little protonated species. We thus conclude that the high frequency part (above $\sim$3350 cm^{-1}) of the linear infrared spectrum represents isolated water molecules, even for solutions that contain equal amounts of water and triflic acid.

The spectral dynamics of TfOH/H_2O/DMSO=1:1:8 and H_2O/DMSO=1:8 solutions are well described by the same kinetic model (Figure 4.2C). According to this model the excited state relaxes to an intermediate state that subsequently decays to a final thermalized state. This model thus accounts for a delay of the global thermalization with respect to the vibrational relaxation. This model has been used before to describe vibrational relaxation in water and other hydrogen-bonded liquids.[85,86] In Figure 4.2D we present the transient spectral components that are obtained from fitting this three-state model to the experimental data.

The transient absorption spectrum of the intermediate state that is reached in the vibrational relaxation, shows a bleaching between 3250 and 3550 cm^{-1}. We explain this bleaching from a strong local heating effect. The vibrational relaxation leads to a local dissipation of energy and thus to a weakening of the hydrogen bonds. As a result, the absorption cross section of the O-H stretch vibrations decreases. The transient absorption spectrum of the final globally heated state is very similar to that of the intermediate, locally hot cluster, only the amplitude is much smaller. The intermediate state relaxes with a time constant of 2.6$\pm$0.3 ps, irrespective whether the solution contains protons or not. The addition of acid does have an effect on the amplitude of the globally heated state spectrum (shown in red). When we scale the spectra with respect to the transient absorption spectrum of the initial excited vibrational state, the amplitude of the final globally heated state has a two times bigger amplitude for a H_2O/DMSO solution than for a H^+/H_2O/DMSO solution. This difference can be explained from the fact that in the presence of H^+, a large fraction of the H_2O molecules will become part of a proton-solvation structure, thus absorbing at lower frequencies. As a result, the solution contains less isolated H_2O molecules of which the absorption will be affected by the same heat energy distributed over the solution after the relaxation. As a result, the transient absorption spectrum of the final globally heated state has a smaller amplitude.

4.3.3 Vibrational dynamics of protonated clusters in water/DMSO solutions

a) Transient spectra

To investigate the structure and dynamics of the solvated proton, we measure transient absorption spectra following excitation of the proton absorption continuum at frequencies $<$3200 cm^{-1}. Figure 4.3 shows isotropic transient spectra of three solutions with different TfOH/H_2O/DMSO ratios obtained with excitation pulses centered at 2550 cm^{-1} for time delays between pump and probe pulses ranging from 0.26 to 20 ps.

For all three solutions the transient absorption spectra show quite similar shapes

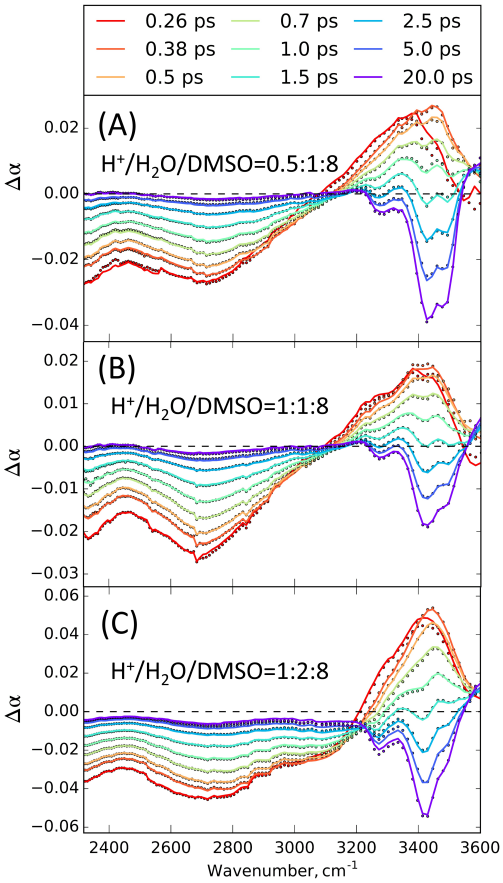

Figure 4.3: Isotropic pump-probe spectra of triflic acid/water/DMSO-d6 solutions with respective concentration ratios: (A) 0.5:1:8, (B)1:1:8, (C) 1:2:8. Pump pulse is centered at 2550 cm^{-1}. Lines represent the result of the fit.

and dynamics. At early delay times, the transient spectrum consists of a broad negative absorption change (bleach) below 3100 cm^{-1} and a positive absorption change (induced absorption) above 3200 cm^{-1}. In all cases the negative absorption signal has its maximum at ~2700 cm^{-1}, and the positive absorption signal is centered at ~3400 cm^{-1}. For solutions containing a larger amount of water we observe a larger negative absorption signal negative shoulder at 3000 cm^{-1} (Figure 4.3C).

The spectral shape observed at early delay times (up to 1 ps) differs from the expected initial shape of a transient absorption spectrum. Usually, the excitation results in a bleach around the frequency of the pump pulse (due to bleaching of the fundamental v=0→1 transition), and an induced absorption at lower frequency due to v=1→2 absorption starting from the excited v=1 vibrational state. Here we observe the induced absorption at higher frequencies than the bleach. Potentially, this could be the result of a positive anharmonicity (frequency of v=1→2 higher than that of v=0→1), but this is not expected for the OH-stretch vibration of water and protonated water molecules. Moreover, the dynamics of the induced absorption are too slow to be caused by vibrational relaxation of the v=1 state of a strongly hydrogen-bonded OH-group. A positive transient absorption signal at higher frequencies is commonly observed after vibrational relaxation of hydrogen-bonded OH-stretch vibrations. In the vibrational relaxation process the excitation energy of the OH-stretch vibration is transferred to the hydrogen-bond network.[79,85] As a result, the hydrogen bonds become longer and weaker, which leads to a blue shift of the OH-stretch absorption spectrum. This blue shift results in a transient spectrum with a bleach in the center and the red wing of the OH-stretch absorption band, and an induced absorption in the blue wing of the OH-stretch absorption band.

We thus conclude that the excited OH-stretch vibration rapidly relax on a time scale of ~100 fs, and that the transient spectra are dominated by the local heating effects resulting from this relaxation. The shape of the broad bleaching signal below 3100 cm^{-1} changes with increasing delay time. This result indicates that the fast vibrational relaxation process not only leads to a local hot state, but that there may be another contributing state with a somewhat different associated transient spectrum and different dynamics.

In Figure 4.4A we show the absorption change as a function of delay time for three different probing frequencies. The transient absorption evolves on a time scale of a few picoseconds to a final bleaching signal (negative absorption change) for frequencies above 3200 cm^{-1} and a near-zero absorption change at lower frequencies. The signals no longer change after 20 ps, which indicates that these signals correspond to the fully thermalized state. In Figure 4.4B we show a zoom-in of the early delay time range. It is seen that the signal at 3500 cm^{-1} starts as a bleaching signal but rapidly evolves into an induced absorption signal on a time scale of ~100 femtoseconds.

We fit the isotropic spectra for all the solutions to the kinetic model presented

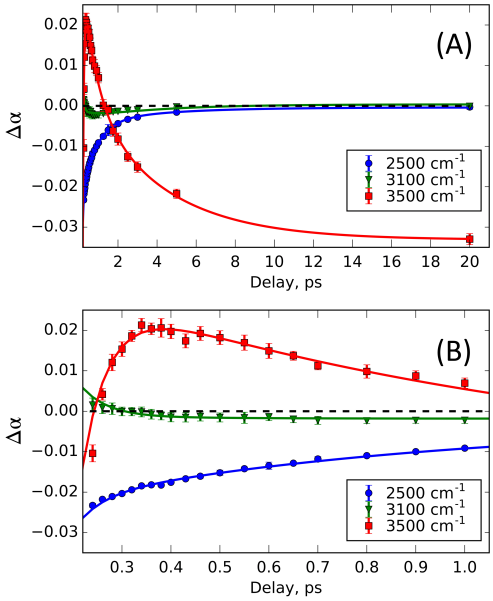

Figure 4.4: (A) Isotropic pump-probe signal of the solution TfOH/H_2O/DMSO=0.5:1:8 at different frequencies as a function of time delay; (B) Zoom-in of the delay time traces of Figure (A) for delay times below 1 ps. The lines are the result of a fit to the kinetic model shown in Figure 4.5.

in Figure 4.5A. Using this kinetic model we obtained the spectral components shown in Figure 4.5B. The actual fits of the model to experimental data are represented by the solid lines in Figures 4.3 and 4.4. The decomposed spectra have similar shapes for all three solutions keeping all the characteristic features (Figure 4.7 in Appendix). The corresponding time constants are T_1=95$\pm$10 fs, T*=0.71$\pm$0.04 ps and τ_r=4.0$\pm$0.4 ps. The nature of the states can be identified from the shape of the associated transient spectra.

b) Vibrationally excited state of the protonated clusters

We assign the first component (shown in blue in Figure 4.5B) to the vibrationally excited state, i.e. the occupation of the v=1 state of an OH-stretch vibration, where the H atom carries (part of) the proton charge. This assignment is supported by several observations. In the first place, the transient spectrum of this state has a bleach signature at the excitation frequency, which is the expected signature following the excitation of the v=1 state of an OH-stretch vibration. Second, the relaxation of this state is ultrafast (95$\pm$10 fs), in agreement with earlier observations that the vibrational relaxation of the

stretch vibrations of strongly hydrogen-bonded OH-groups in protonated species occurs on a time scale of ∼100 fs or even shorter.[20,47] Third, we find this component to be anisotropic (see Appendix), as is indeed expected for the transient absorption signal following excitation of the v=1 state. In the case of a (local) heating effect the anisotropy of the associated spectral change is usually close to zero. Finally, we observe a quite similar transient spectrum at early delay times in pump-probe experiments on a triflic acid/DMSO solution (containing only trace amount of water) with the same pump pulse centered at 2550 cm^{-1} (Figure 4.9 in Appendix). In this case, this spectral component decays somewhat slower (T_1=190±20 fs). As discussed before, in this solution the proton will be solvated completely by DMSO molecules and the broad absorption band is due to the OH-stretch vibrations of $(DMSO\text{-}H)^+$ ions. In these ions the proton attaches to oxygen atoms of DMSO and the positive charge resides in part on the sulfur atoms.[87,88]

The transient spectrum of the vibrationally excited state also shows a strong re-

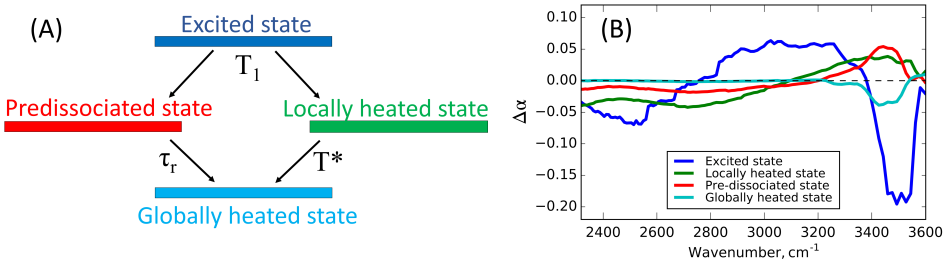

Figure 4.5: (A) Scheme of the kinetic model, describing the spectral dynamics after excitation at ν_{pump}=2550 cm^{-1}; the arrows illustrate population transfer between the states. (B) The corresponding transient spectra of the states for [0.5:1:8] solution.

sponse at frequencies >2800 cm^{-1}. We observe an intense bleach at 3350-3600 cm^{-1} and a broad induced absorption at 2800-3350 cm^{-1}. This response is similar to the transient spectrum that results from the excitation of the v=1 state of water OH-stretch vibrations. However, the excitation pulse at 2550 cm^{-1} is far out of resonance with the OH-stretch vibration of isolated non-protonated water molecules (see H_2O/DMSO spectrum in Figure 4.1). Hence, the high-frequency response following excitation of the OH-stretch vibration of a proton solvation structure at 2500 cm^{-1} likely results from the strong coupling of this mode to the OH-stretch vibrations of neighboring water molecule. These water molecules can be directly hydrogen-bonded to the proton, e.g. forming a $(DMSO\text{-}H)^+$–OH_2 structure, where the proton is primarily bonded to the oxygen atom of the S=O group of the DMSO molecule. Such a structure is reminiscent of an Eigen structure where $(DMSO\text{-}H)^+$ takes the role of the central H_3O^+. Excitation of the OH-stretch vibration of $(DMSO\text{-}H)^+$ to the v=1 state can lead to a contraction of the

hydrogen bond to the H_2O molecule. Such a contraction has been observed before for hydrated protons in aqueous Nafion[77,89] and acetonitrile,[76] and has also been predicted to occur in theoretical studies of infrared induced proton transfer.[75,90] A contraction of the (DMSO-H)$^+$–H_2O hydrogen bond implies that the DMSO-H$^+$–H_2O structure becomes more Zundel-like with the proton more equally shared between the flanking DMSO and H_2O molecules. Such an excitation-induced evolution from Eigen-like to Zundel-like will be accompanied by a redshift of the absorption of the OH-stretch vibrations of the hydrogen-bonded H_2O molecule. The observed induced absorption signal at 2800-3300 cm^{-1} agrees with the reported frequency range of the OH-stretch vibrations of H_2O molecules that flank the Zundel proton in water.[15,33,41]

c) Local heating and vibrational pre-dissociation

The two states of Figure 4.5B indicated in red and green are produced by the relaxation of the v=1 state of the proton vibration. The corresponding spectral shapes reflect the effect of a local dissipation of energy. The green spectrum with a decay time constant of 0.71±0.04 ps consists of a broad negative absorption (bleaching) at frequencies below 3100 cm^{-1} and a positive absorption signal at higher frequencies. We assign this smooth featureless spectrum to the result of a local heating process: as a result of the vibrational relaxation, energy is transferred to the hydrogen bonds of the protonated cluster. The weakening of these hydrogen bonds shifts the absorption spectrum of the OH-stretch vibrations to higher frequencies. This local heating effect decays when the local hydrogen bonds transfer their energy to the solvent surrounding the cluster, leading to an equilibration of the heat with the surrounding DMSO matrix. The spectrum of the locally heated cluster depends on the water concentration. For the [1:2:8] solution we observe a clear rise of a negative shoulder at 3000 cm^{-1} and a larger intensity of the high-frequency induced absorption. We explain this shoulder from the larger fraction of water dimers and trimers present in solution. At this higher water concentration a significant fraction of the protonated DMSO-H$^+$-H_2O clusters is hydrogen-bonded to an additional water molecule. In this case, the local heating of the cluster affects two closely spaced, hydrogen-bonded water molecules of which the OH-stretch vibrations absorb at lower frequencies than H_2O monomers in DMSO.[81,84] The blue shift of the absorption spectrum of this dimer leads to an additional negative absorption change at ∼3100 cm^{-1} and a positive absorption change around 3400 cm^{-1}.

The spectrum of the other intermediate state indicated in red also consists of a negative absorption part below 3200 cm^{-1} that is less structured than the bleaching of the locally heated state, and an induced absorption at high frequencies. The shape of this induced absorption is strikingly similar to the linear infrared spectrum of water monomers in DMSO. This induced absorption shows the double-peak structure of water OH-stretch symmetric and antisymmetric modes, and a shoulder at 3300 cm^{-1} due to the water bending overtone. We conclude that the induced absorption corresponds to the creation

of additional water monomers (solvated only by DMSO molecules), resulting from the dissociation of the originally excited (DMSO-H)$^+$-H_2O cluster. Hence, the energy released by the vibrational relaxation is not only redistributed among several low-frequency modes (hydrogen bonds) of the excited cluster, but in some cases this energy is transferred to a single hydrogen bond between (DMSO-H)$^+$ and H_2O, leading to dissociation of this bond and ejection of a water molecule. The intermediate state reached in this relaxation is thus highly non-thermal, as most of the transferred energy resides in one particular hydrogen bond, leading to vibrational pre-dissociation. In a subsequent relaxation process with time constant τ_r=4.0$\pm$0.4 ps, the energy gets transferred to other local modes, with the result that the (DMSO-H)$^+$–H_2O cluster recombines and the energy distribution becomes thermal.

To corroborate this interpretation, we compared the transient spectrum of the predissociated state (in red) with the difference spectrum of the sum of the H_2O/DMSO and TfOH/DMSO spectra on one hand and the TfOH/H_2O/DMSO spectrum on the other hand (in blue). The H_2O/DMSO and TfOH/DMSO solutions contain H_2O monomers dissolved in DMSO and (DMSO-H)$^+$ structures, but not (DMSO-H)$^+$–H_2O clusters. The TfOH/H_2O/DMSO solution will contain all these three components. If the contributions of the spectra are chosen such that the H_2O/DMSO and TfOH/DMSO solutions together represent an equal amount of H_2O and protons as the TfOH/H_2O/DMSO solution, the difference spectrum S(H_2O/DMSO)+S(TfOH/DMSO)-S(TfOH/H_2O/DMSO) will represent the transfer of (DMSO-H)$^+$–H_2O clusters into water monomers and (DMSO-H)$^+$ structures. In Figure 4.6 this difference spectrum is compared with the red transient spectrum. It is seen that these spectra are highly similar in shape, thus supporting the interpretation of the red transient spectrum as the result of dissociation of the hydrogen bond between (DMSO-H)$^+$ and H_2O clusters of (DMSO-H)$^+$–H_2O clusters.

The good agreement of the transient spectrum of (DMSO-H)$^+$–H_2O pre-dissociation with the corresponding linear difference spectrum implies that among the possible protonated species only (DMSO-H)$^+$ and (DMSO-H)$^+$–H_2O have significant concentrations in the studied solutions. This notion is confirmed by the fact that we can fit the linear infrared spectra of TfOH/H_2O/DMSO solutions of different relative concentrations considering only H_2O, (DMSO-H)$^+$ and (DMSO-H)$^+$–H_2O as the species present in solution (Figure 4.11 in Appendix).

The final state (shown in cyan) is the result of the equilibration of the energy over the pump focus. This globally heated state has a transient spectrum that primarily consists of a bleaching signal in the frequency region of the water-in-DMSO spectrum. This bleaching reflects the decrease of the cross section of the water OH-stretch vibrations resulting from a weakening of the hydrogen bonds. In the frequency region of the protonated species, the absorption change of the globally heated state has almost zero intensity, which differs from what is observed for the steady-state thermal difference spectrum (Figure 4.12).

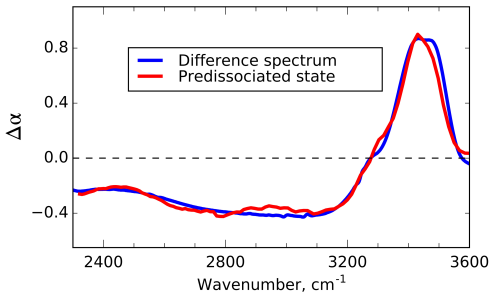

Figure 4.6: Comparison of the red transient spectrum of Figure 4.5B for TfOH/H_2O/DMSO=1:2:8 solution with the difference spectrum (blue) S(H_2O/DMSO)+S(TfOH/DMSO)-S(TfOH/H_2O/DMSO), where S indicates the linear absorption spectrum of the solution in parentheses.

4.4 Discussion

The transient spectrum of the vibrationally excited protonated cluster decays with a time constant of 95±10 fs. This decay time is significantly shorter than the vibrational relaxation time of the OH-stretch vibration of $(DMSO\text{-}H)^+$ in dry DMSO (T_1=190±20 fs). From this we conclude that the H_2O molecule in the $(DMSO\text{-}H)^+$–H_2O cluster provides additional accepting modes for the excited OH-stretch vibration, thus doubling the relaxation rate.

The transient spectrum of the vibrationally excited state of the proton solvated by DMSO and water molecules (blue spectrum of Figure 4.5B) also shows that the excitation leads to a rapid contraction of the hydrogen bond between $(DMSO\text{-}H)^+$ and H_2O within the $(DMSO\text{-}H)^+$–H_2O cluster. Such a rapid contraction of the hydrogen bond within a proton-solvation cluster has been observed before for protonated water in the nanochannels of sulfonated perfluoropolymer Nafion[77,89]. This hydrogen-bond contraction was explained from the fact that the first excited state of the proton vibration possesses a higher energy in the strongly asymmetric potential of the Eigen proton hydration structure than in the more symmetric double-well potential of the Zundel proton hydration structure. Hence, the energy of the v=1 state can be lowered by evolving from an Eigen to a Zundel structure, which corresponds to a contraction and strengthening of the hydrogen bond between the H3O+ core and a water molecule in its hydration shell.

In the present case of $(DMSO\text{-}H)^+$–H_2O cluster we observe a similar vibrational-excitation-induced contraction. Contraction of the hydrogen bond between $(DMSO\text{-}H)^+$ and H_2O molecule leads to a lowering of the energy of the v=1 state, and to a red shift

of the absorption spectrum of the H_2O molecule, thus explaining the observed response in the high-frequency part of the blue transient spectrum of Figure 4.5B. The transient spectrum resulting from the subsequent vibrational pre-dissociation process (red spectrum of Figure 4.5B) indicates that the proton vibrational potential of the contracted (DMSO-H)$^+$–H_2O Zundel-like cluster is not completely symmetric, and still has its lowest well near the oxygen of DMSO. If this potential has been completely symmetric, pre-dissociation of the cluster would likely result in both DMSO and H_3O^+ fragments and in DMSO-H$^+$ and H_2O fragments. The transient spectrum shows that the pre-dissociation results in the production of H_2O molecules, which implies that primarily the H$^+$–H_2O hydrogen bond dissociates, indicating that this bond is weaker than the DMSO-H$^+$ hydrogen bond.

The proton solvation in water/DMSO solutions strongly differs from that in water/acetonitrile solutions that have been studied before.[18,72,76] Acetonitrile is only weakly polar and does not strongly interact with the proton. Hence, in water/acetonitrile solutions the protons are primarily solvated by water molecules leading to larger proton-water clusters that are embedded in an acetonitrile matrix. The high level of hydration of protons in water/acetonitrile mixtures is evident from the linear infrared spectrum that shows the presence of water molecules in the second solvation shell.[72] The larger hydration shell of the proton in acetonitrile solution likely explains the observation that the vibrational relaxation of the OH-stretch vibration of the hydrated proton is significantly faster in acetonitrile (T_1 <65 fs) than in DMSO (T_1=95$\pm$10 fs). The comparison between the relaxation of the OH-stretch vibration of (DMSO-H)$^+$–H_2O and (DMSO-H)$^+$ (T_1=190$\pm$20 fs) shows that already one additional water molecule leads to a significant speed up of the relaxation. Hence, it is to be expected that the further solvation with more water molecules in water/acetonitrile will increase the vibrational relaxation rate of the OH-stretch vibration of the proton even further.

At longer delay times, the transient spectrum of the solvated proton in water/DMSO is quite similar to that of the hydrated proton in acetonitrile. In both cases the isotropic transient spectrum after $\sim$0.5 ps consists of an induced absorption at high frequencies and a broad bleach at lower frequencies. For both systems, this signal is partly due to a local heating effect and partly due to vibrational pre-dissociation of the hydrated proton cluster.[76] A difference is that the induced absorption of the pre-dissociated water monomers in acetonitrile was relatively featureless: the characteristic doublet of the symmetric and antisymmetric OH-stretch modes of water monomers was not observed, in contrast to the present observations for solvated protons in water/DMSO.

4.5 Conclusions

We investigated the vibrational dynamics of different mixtures of water, trifluoromethanesulfonic acid (TfOH), and excess dimethyl sulfoxide (DMSO) using two-color femtosecond mid-infrared spectroscopy. We studied mixtures with compositions of $[H^+]/[H_2O]/[DMSO] = 0.5{:}1{:}8$, 1:1:8, and 1:2:8. The TfOH acid completely dissociates, leading to the formation of $(DMSO\text{-}H)^+$ and $(DMSO\text{-}H)^+$–H_2O clusters. We find that for all studied mixtures the solution contains a significant fraction of water monomers, i.e. H_2O molecules that are solvated by DMSO molecules only and that are not interacting with a proton or with other water molecules. The OH-stretch vibration of these water monomers can be selectively excited with an excitation pulse of 3450 cm^{-1}. The vibrational relaxation dynamics is a two-step process that is independent of the presence of protons in the solution. In the first step, the excited OH-stretch vibration relaxes with a time constant of 0.84 ± 0.03 ps to an intermediate state. This intermediate state represents a strong local heating effect, corresponding to the excitation of low-frequency modes (hydrogen bonds) close to the excited OH-stretch vibration. The intermediate state relaxes with a time constant of 2.6 ± 0.3 ps, leading to a small global heating effect of the sample in the focus of the excitation pulse.

We studied the vibrational dynamics of the protonated structures by exciting the solutions with an excitation pulse centered at 2550 cm^{-1}. Kinetic modeling of the transient spectra shows that this excitation results in a short-living transient absorption spectrum associated with the v=1 state of $(DMSO\text{-}H)^+$ and $(DMSO\text{-}H)^+$–H_2O clusters. This transient spectrum consists of a bleaching of the fundamental transition $v{=}0\rightarrow1$ transition at frequencies $<$2800 cm^{-1}, an induced absorption at 2800-3300 cm^{-1}, and a bleaching signal at frequencies $>$3300 cm^{-1}. We assign the latter two signals to a strong redshift of the OH-stretch vibrations of water molecules that are close to the excited OH-stretch vibration, e.g. in $(DMSO\text{-}H)^+$–H_2O clusters. The excitation to the v=1 state leads to a contraction of the hydrogen bond between $(DMSO\text{-}H)^+$ and H_2O, thus making the $(DMSO\text{-}H)^+$- H_2O cluster more Zundel-like. Due to this contraction, the frequencies of the OH-stretch vibrations of the H_2O molecules flanking the proton shift from 3400-3500 cm^{-1} to 2800-3300 cm^{-1}.

The excited v=1 state relaxes with $T_1{=}95\pm10$ fs. This relaxation leads to two distinctly different intermediate states. One of these states is a locally heated state which is of similar nature as the intermediate state that is created by excitation and relaxation of water monomers in DMSO. The locally hot state relaxes with a time constant of 0.71 ± 0.04 ps. The second intermediate state is a vibrational pre-dissociation state. The vibrational energy of the excited OH-stretch vibration of the solvated proton can also be primarily transferred to the hydrogen bond between $(DMSO\text{-}H)^+$ and H_2O of a $(DMSO\text{-}H)^+$–H_2O cluster, leading to dissociation of this bond. This dissociation leads to

the transient creation of water monomers. The pre-dissociation state relaxes with a time constant of 4.0±0.4 ps, which implies that the hydrogen bond between $(DMSO\text{-}H)^+$ and H_2O reforms with this time constant.

4.6 Appendix

Transient spectral components of protonated clusters

The relaxation model discussed in the main text and illustrated in Figure 4.5A was also used to fit the isotropic transient spectra of the TfOH/H_2O/DMSO=1:1:8 and 1:2:8 solutions. The spectral components obtained from this fit are shown in Figure 4.7. The shape of these spectral components coincide well with the spectral components of TfOH/H_2O/DMSO=0.5:1:8 solution (Figure 4.5B).

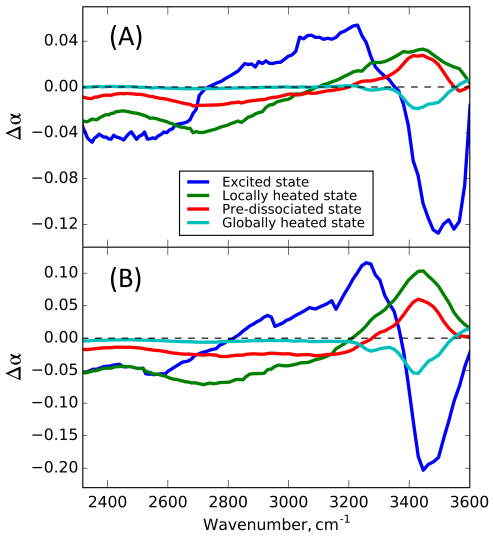

Figure 4.7: Spectral components obtained from fitting the isotropic transient spectra with ν_{pump}=2550 cm^{-1} for solutions of TfOH/H_2O/DMSO=1:1:8 (A), and TfOH/H_2O/DMSO=1:2:8 (B).

Anisotropy dynamics

We measured the transient absorption changes with probe pulses that are polarized parallel and perpendicular to the polarization of the pump pulses. With the resulting signals $\Delta\alpha_{\parallel}(\nu,t)$ and $\Delta\alpha_{\perp}(\nu,t)$ we construct the anisotropy of the transient absorption

change:

$$R(\nu,t) = \frac{\Delta\alpha_{\parallel}(\nu,t) - \Delta\alpha_{\perp}(\nu,t)}{\Delta\alpha_{\parallel}(\nu,t) + 2\Delta\alpha_{\perp}(\nu,t)} \tag{4.1}$$

The dynamics of the anisotropy reflects the reorientation of the excited transition dipoles. If several components contribute to the transient spectrum, the anisotropy can be written as a weighted sum of the anisotropy of each of the components:

$$R(\nu,t) = \frac{\sum R_i \Delta\alpha_i^{iso}}{\sum \Delta\alpha_i^{iso}} \tag{4.2}$$

For an excitation frequency of 2550 cm^{-1} and probe frequencies >3400 cm^{-1} the

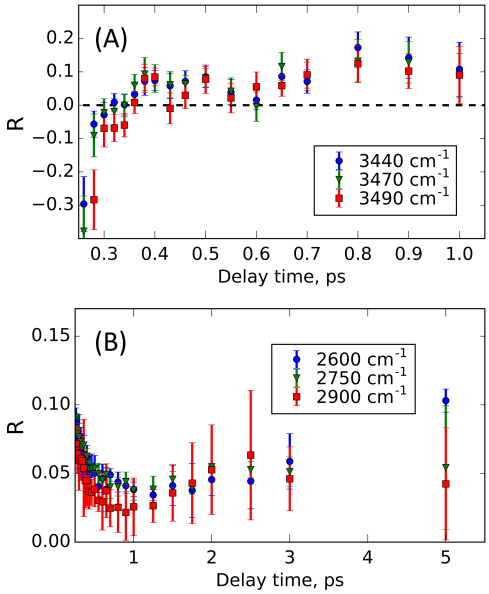

Figure 4.8: Anisotropy of the high-frequency induced absorption signal (A) and of the low frequency bleaching signal (B) as a function of delay time, after excitation with ν_{pump}=2550 cm^{-1} for a solution TfOH/H_2O/DMSO=0.5:1:8.

anisotropy at early delays has a negative value (Figure 4.8A). This negative value results from the presence of several spectral components with different anisotropies. At delay times <0.35 ps and probe frequencies >3400 cm^{-1}, the signal consists of a positive absorption change associated with the locally heated state and the predissociated state, both with a low anisotropy, and a negative absorption change associated with the vibrationally excited state, with a high anisotropy. The high anisotropy of the latter signal

contribution implies that the parallel negative absorption signal is much larger than the perpendicular negative absorption signal. As a result, the total net positive absorption signal is smaller for the parallel polarized probe pulse than for the perpendicular polarized probe pulse, leading to a negative anisotropy value.

The anisotropy at probe frequencies $<$3100 cm^{-1} (Figure 4.8B) is determined by the signals of the locally heated state and the pre-dissociated state. At early delay times, the locally heated state dominates because of its higher initial amplitude. The anisotropy of the locally heated state is relatively low ($\sim$0.1) because local heating affects several OH vibrations within the cluster with different orientations. After 1 ps a re-rise of the anisotropy is observed. This re-rise can be explained from the fact that the pre-dissociated has a longer relaxation time than the locally heated state. As a result, the contribution of the pre-dissociated state becomes increasingly important with increasing time delay. As this state has a higher anisotropy than the locally heated state, the anisotropy of the total signal increases.

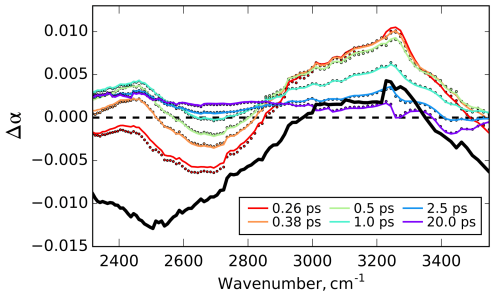

Figure 4.9: Isotropic pump-probe spectra of TfOH/DMSO=1:8 solution, lines are the result of the fit. The initial fast decaying component extracted from the fit is shown in black.

Transient spectra of dry TfOH/DMSO solution

We also measured transient absorption spectra of a TfOH/DMSO=1:8 solution (i.e. without water) measured with a pump pulse centered at 2550 cm^{-1} (Figure 4.9). In this solution the proton is solvated completely by DMSO so we excite only OH stretch vibrations of (DMSO-H)$^+$ ions. We fit the observed spectral dynamics with a kinetic model comprising the initially vibrationally excited state, two intermediate states to account for a nonexponential dissipation of the local heat, and a final globally heated state. The resulting transient spectrum of the initially excited state is shown in black in Figure 4.9. As for the TfOH/H_2O/DMSO solutions this spectrum shows an intense bleach of the OH stretch vibration of (DMSO-H)$^+$ around the excitation frequency. The spectrum also contains a smaller induced absorption and bleaching signal at high frequencies that we

assign to a trace amount of water present in the solution. The excited state spectrum decays with a time constant T_1=190±20 fs, which is somewhat slower than 95±10 fs for the TfOH/H_2O/DMSO solutions.

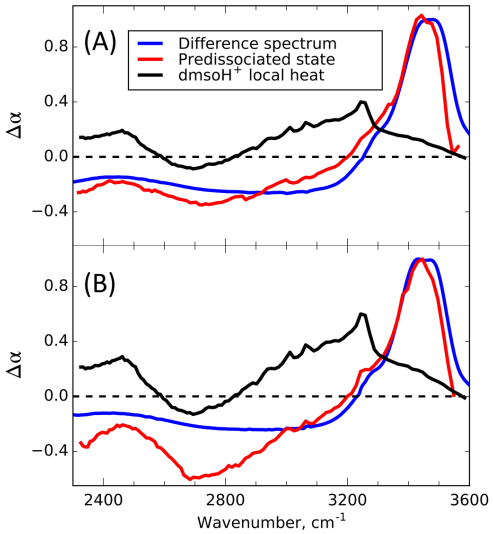

Figure 4.10: Comparison of the linear difference spectrum between the sum of the spectra of TfOH/DMSO and H_2O/DMSO solutions on one hand and the spectrum of a corresponding TfOH/H_2O/DMSO solution on the other hand (in blue), with the transient spectrum of the pre-dissociated state extracted from the kinetic modeling of pump-probe experiments with ν_{pump}=2550 cm^{-1} (in red), for solutions of TfOH/H_2O/DMSO=0.5:1:8 (A) and TfOH/H_2O/DMSO=1:1:8 (B). Also shown is the scaled transient spectrum of locally heated (DMSO-H+) (in black).

The transient spectrum of the pre-dissociated state

In Figure 4.10 we compare the transient spectrum of the pre-dissociated state with the linear absorption difference spectrum for the solutions [0.5:1:8] and [1:1:8]. The difference spectrum between the sum of the spectra of TfOH/DMSO and H_2O/DMSO solutions on one hand and the spectrum of a corresponding TfOH/H_2O/DMSO solution (with an equal total amount of water molecules and protons) on the other hand, represents the effect of the dissociation of $(DMSO\text{-}H\text{-}H_2O)^+$ clusters into $(DMSO\text{-}H)^+$ clusters and

H_2O. We can express this absorption difference as:

$$\Delta\alpha = c(H_2O)\sigma(H_2O) + c(DMSOH^+)\sigma(DMSOH^+) - ([H_2O]\sigma(H_2O) + [DMSOH^+]\sigma(DMSOH^+) + [DMSOH^+(H_2O)_n]\sigma(DMSOH^+(H_2O)_n)) = [DMSOH^+(H_2O)_n](n\sigma(H_2O) + \sigma(DMSOH^+) - \sigma(DMSOH^+(H_2O)_n)) \quad (4.3)$$

where c represents the total concentration, square brackets represent equilibrium concentration and σ is the cross-section of corresponding species. Indeed, the difference spectrum (in blue) is similar to the transient spectrum of the pre-dissociated state, supporting the assignment of this transient spectrum to the result of the dissociation of (DMSO-H-H_2O)$^+$ clusters.

In the solutions [0.5:1:8] and [1:1:8] the concentration of water is not high enough to solvate protons, so that a substantial fraction of protons will exist in the form of (DMSO-H)$^+$ ions. With a pump pulse at 2550 cm^{-1} we will thus also excite a substantial fraction of water-free (DMSO-H)$^+$ clusters. For these solutions, the transient spectrum of the predissociated state will be somewhat distorted by a contribution of locally heated (DMSO-H)$^+$ clusters (shown in black). Indeed, the remaining difference between the linear difference spectrum and the transient spectra of the pre-dissociated state can be well explained from the additional contribution of locally heated (DMSO-H)$^+$ clusters.

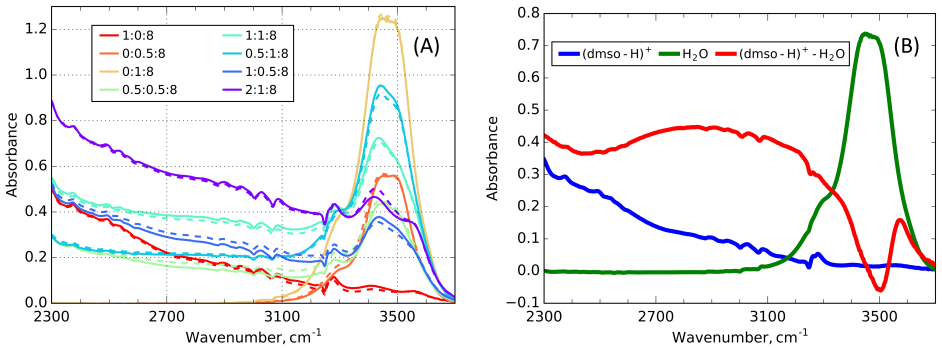

Figure 4.11: (A) FTIR spectra of the TfOH/H_2O/DMSO solutions of different relative concentrations (solid lines, DMSO background is subtracted) and the result of the fit (dashed lines); (B) The decomposed spectral signatures of (DMSO-H)$^+$, H_2O and (DMSO-H)$^+$–H_2O.

To check the potential presence of the species other than H_2O, (DMSO-H)$^+$ and (DMSO-H)$^+$–H_2O, we measured linear infrared spectra of TfOH/H_2O/DMSO solutions with different relative concentrations (Figure 4.11). We fit the spectra taking into account

the chemical equilibrium:

$$(DMSO-H)^+ + H_2O \rightleftharpoons (DMSO-H)^+ - H_2O \tag{4.4}$$

It appears that we only need to consider this equilibrium to obtain an excellent fit of the experimental data. From the fit we obtain an equilibrium constant K=0.8±0.2 L/mol. The good agreement of the calculated spectra with the experimental data confirms that (DMSO-H)$^+$ and (DMSO-H)$^+$–H_2O are the only species containing the solvated proton, which implies that the studied solutions contain negligible amounts of H_3O^+ and $H_5O_2^+$ ions.

The transient spectrum of the globally heated state

In Figure 4.12 we compare the transient spectrum of the globally heated state with the linear thermal difference spectrum for three TfOH/H_2O/DMSO solutions. The linear thermal difference spectrum represents the difference between the spectrum of a heated solution and the same solution at room temperature.

Clearly, the globally heated state spectra obtained from a fit of the transient absorption data to the kinetic model of Figure 4.6A do not correspond exactly to the linear thermal difference spectra. The spectra are especially different in the region of OH stretch vibrations. This result shows that the globally heated state that is reached in the relaxation after ∼10 ps differs from a true thermal equilibrium.

The linear thermal difference spectra show a broad absorption change in the region of the solvated proton (<3200 cm^{-1}), which is hardly present in the transient spectrum of the globally heated state. This difference may be due to the fact that heating of the sample may lead to a different distribution of proton solvation structures. This different distribution is apparently not established on the ∼10 ps time scale of the transient absorption experiment.

High frequency excitation of the proton cluster

We also performed pump-probe experiments with an excitation pulse centered at 3200 cm^{-1}. The isotropic transient spectra of three solution are shown in Figure 4.13. In this experiment we excite the low-frequency part of the OH stretch absorption spectrum of isolated water molecules, and the high-frequency part of the absorption spectrum of solvated protons. The excitation of isolated water molecules explains the observation of a negative absorption change at ν >3200 cm^{-1} due to the bleaching of v=0→1 transition and a positive absorption change at ν <3200 cm^{-1} due to v=1→2 absorption. The simultaneous excitation of proton solvation structures leads to a relatively weak broad bleaching signal at frequencies below 3000 cm^{-1}. With increase of the proton concentration (solutions [1:1:8] and [1:2:8]) this negative signal becomes more dominant and cancels the excited state absorption of the isolated water molecules. The broad negative

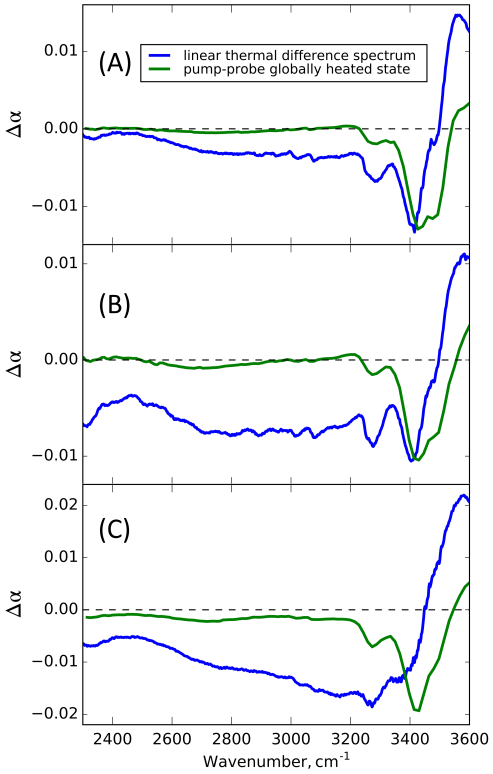

Figure 4.12: Comparison of the linear thermal difference spectrum and the transient spectral component corresponding to the globally heated state (ν_{pump}=2550 cm^{-1}). Linear thermal difference spectrum obtained by subtracting the FTIR absorption spectrum of the sample at 22°C from the spectrum of the sample at 27°C; the transient spectral components are rescaled. Solutions TfOH/H_2O/DMSO=0.5:1:8 (A), TfOH/H_2O/DMSO=1:1:8 (B) and TfOH/H_2O/DMSO=1:2:8 (C).

absorption change is very similar to the characteristic locally heated cluster spectrum observed with a pump centered at 2550 cm^{-1}. This result implies that the absorption spectrum of the solvated protons extends up to 3200 cm^{-1}.

We fit the observed isotropic spectra with two parallel relaxation processes, representing the relaxation of isolated water molecules and the relaxation of solvated protons. We constrained the fitting procedure by modeling the relaxation of the isolated water molecules with the same relaxation time constants and transient spectra as were observed for a H_2O/DMSO solutions (no protons) using the same pump pulse centered at 3200 cm^{-1}. Due to the inhomogeneity of the water OH-stretch absorption spectrum, ex-

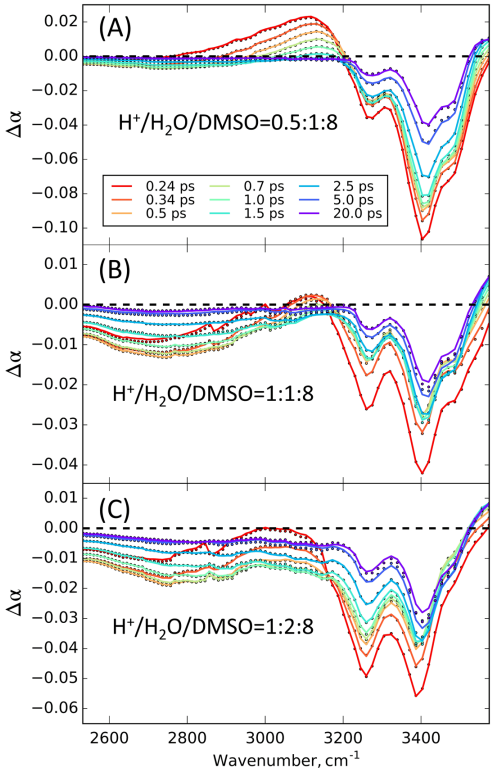

Figure 4.13: Isotropic pump-probe spectra after excitation with pump-pulse centered at 3200 cm^{-1} for $TfOH/H_2O/DMSO$ solutions of different concentrations: (A) [0.5:1:8], (B) [1:1:8], (C) [1:2:8]. The lines are the result of the fit.

citation of the red wing of this band yields a red-shifted transient spectrum of the excited state. This red-shifted spectrum undergoes rapid spectral diffusion, thereby shifting to higher frequencies. We model this spectral diffusion by introducing an initial red-shifted excited state spectrum (blue spectrum in Figure 4.14) that rapidly decays with a time constant of 110 ± 10 fs to a spectrally relaxed excited state spectrum (green spectrum in Figure 4.14). This latter excited state spectrum decays faster than the transient excited-state spectrum that was observed following excitation in the center of the absorption band (0.75 ps versus 0.84 ps). The relaxation of the excited state with a time constant of 0.75 ± 0.03 ps results in a locally hot water cluster (dashed cyan spectrum in Figure 4.14) that subsequently relaxes with a time constant of 2.3 ± 0.2 ps to a globally heated state (dashed purple spectrum in Figure 4.14).

Because of the dominance of the response of the isolated water molecules, the relax-

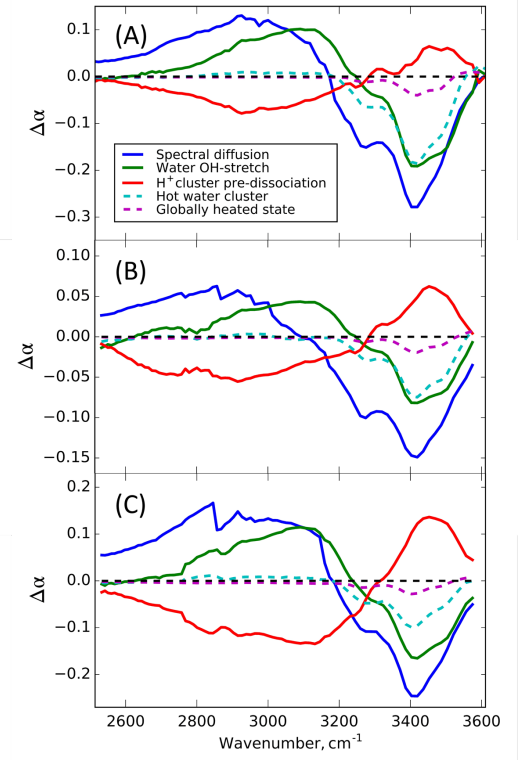

Figure 4.14: Spectral components obtained from the fit of the isotropic transient spectra with ν_{pump}=3200 cm^{-1}; solutions [0.5:1:8] (A), [1:1:8] (B) and [1:2:8] (C).

ation dynamics of the solvated protons can be modeled with a single transient spectral component (red spectrum in Figure 4.14) that is highly similar to that of pre-dissociated (DMSO-H-H_2O)$^+$ clusters following excitation at 2550 cm^{-1}. This spectrum consists of a bleaching signal below 3200 cm^{-1} and an induced absorption at higher frequencies. This transient spectrum decays with a time constant of 1.4$\pm$0.1 ps. The corresponding state relaxes to the same globally heated state as for the isolated water molecules. As was observed for the pre-dissociation spectrum following excitation at 2550 cm^{-1}, the induced high frequency absorption displays the linear absorption doublet of the water OH stretch vibrations at 3450/3500 cm^{-1}. Hence, we conclude that excitation of (DMSO-H-H_2O)$^+$ clusters at 3200 cm^{-1} again (partly) leads to pre-dissociation of the hydrogen bond to H_2O and ejection of a water molecule.

Published as:

Oleksandr O. Sofronov and Huib J. Bakker. Vibrational Relaxation Dynamics of the Core and Outer Part of Proton-Hydration Clusters. The Journal of Physical Chemistry B 2019, 123, pp. 6222-6228

5

Vibrational Dynamics of the Core and Outer Part of Hydrated Proton

Abstract

We study the ultrafast relaxation dynamics of hydrated proton clusters in acetonitrile using femtosecond mid-infrared pump-probe spectroscopy. We observe a strong dependence of transient absorption dynamics on the frequency of excitation. When we excite the OH vibrations with frequencies $\leqslant$3100 cm^{-1} we observe an ultrafast energy relaxation that leads to heating of the local environment of proton. This response is assigned to the OH vibrations of the water molecules in the core of the hydrated proton cluster. When we excite with frequencies $\geqslant$3200 cm^{-1} we observe a relatively slow vibrational relaxation with a T_1 time constant ranging from 0.22$\pm$0.04 ps at ν_{ex}=3200 cm^{-1} to 0.37$\pm$0.02 ps at ν_{ex}=3520 cm^{-1}. We assign this response to water molecules in the outer part of the hydrated proton cluster.

5.1 Introduction

The proton (H^+) plays a key role in various chemical processes in aqueous media.[91–94] For the proton in liquid water different solvation structures have been proposed, including the $H_3O^+(H_2O)_3$ Eigen cation, the $H_5O_2^+$ Zundel cation and the so-called asymmetric Zundel as an intermediate geometry of the first two. These structures are based on cryogenic photodissociation vibrational spectroscopy experiments of small protonated water clusters,[41,42] and molecular dynamics simulations.[10,11,35] In the cluster experiments Eigen and Zundel cation structures have been identified from the central frequencies of the OH-stretch vibrations. However, quantitative infrared spectroscopy[17,21] and photodissociation spectroscopy of large protonated water clusters[41,43,95] as well as molecular dynamics simulations[11,96–98] show that the water molecules in the second solvation shell of the proton also possess different properties from the molecules in bulk water, which implies that the Eigen and Zundel cations only represent the central cores of the proton-hydration structures in liquid water.

Infrared spectroscopy is a powerful technique for studying strongly hydrogen-bonded systems like the hydrated proton, since the vibrational frequency of the stretch vibration of the hydrogen-bond donating group strongly depends on the strength of the donated hydrogen bond.[94,99] A complication is that strong hydrogen bonding leads to extremely broad absorption bands for the OH-stretch vibration. As a result, the hydrated proton in liquid water shows a nearly continuous absorption spanning from 1000 cm^{-1} to 3600 cm^{-1}.[15,22,33] Recent ab initio molecular dynamics simulations show that the large width of the absorption band largely results from the heterogeneity of the hydrogen bonds, in particular the difference in hydrogen-bond strength between the water molecules in the first and the second hydration shells.[100]

Femtosecond infrared (fs-IR) spectroscopy provides information on the relaxation dynamics and can thereby help in the assignment of the different regions of the absorption spectrum of the OH-stretch vibrations of the hydrated proton. Femtosecond IR spectroscopy have recently been used to study the properties of hydrated proton clusters in acetonitrile.[18,72,76] Acetonitrile as a weakly polar solvent is a very suitable matrix for hydrated proton clusters.

In Ref. 23 it was proposed that in a system of acid water in acetonitrile with a ratio $[H^+]$:$[H_2O]$=1:3, the proton is mainly found in between two water molecules (not necessarily in a symmetric configuration), forming a Zundel $H_5O_2^+$ structure. This finding agrees with the results of earlier linear infrared[101] and ^{1}H NMR[102] studies and a fs-IR study of the proton transfer mode.[18] Using excitation pulses centered at 2700 cm^{-1} it was concluded that the excited central OH-stretch vibration of the Zundel-like structure relaxes ultrafast with a time constant T_1 <65 fs.[72] The relaxation following excitation at 3400 cm^{-1} was also observed to be ultrafast with an upper limit for T_1 of 50 fs. This

relaxation behavior was assigned to the OH vibrations of the two H_2O molecules flanking the Zundel proton. It was also shown in this study that the fluctuations of the electrical interactions between the hydrated proton and the surrounding acetonitrile molecules strongly modulate the hydration structure geometry and the vibrational potential of the Zundel proton on an ultrafast scale.[18,72]

Ottosson et al.[76] investigated the picosecond dynamics of hydrated protons in acetonitrile. In this study it was found that the relaxation of the excited proton partly results in the ultrafast creation (<100 fs) of a locally hot proton hydration cluster, and partly in the vibrational predissociation of a hydrogen bond of the cluster and the release of a water molecule. The reassociation of this bond was observed to occur with a time constant of ∼6 ps.

In Chapter 5 we present a comparative femtosecond mid-infrared pump-probe spectroscopic study of the vibrational dynamics of the core and outer parts of hydrated proton clusters in acetonitrile. An important difference between the present study and earlier work is that we resolve the frequency-dependent vibrational relaxation time constants of the OH-stretch vibrations of the outer part of the hydration structure. In the work by Dahms et al.[72] this relaxation was believed to be ultrafast (< 50 fs). We find that for excitation frequencies >3100 cm^{-1} the relaxation is much slower (220-370 fs) and strongly depends on frequency, which implies that the OH-stretch vibrational spectrum of the outer part of the proton hydration structure is strongly inhomogeneously broadened.

5.2 Experiment

The samples are prepared by dissolving trifluoromethanesulfonic acid (TfOH, 99%, Sigma-Aldrich) in water and deuterated acetonitrile (CD_3CN, 99.8%, Sigma-Aldrich) at a ratio TfOH/H_2O/CD3CN=1:3:75. Previous IR pump-probe[76] and FTIR[72,101] studies showed that the nature of the counter-ion ($CF_3SO_3^-$, ClO_4^- or I^-) does not have a significant influence on the structure and dynamics of the hydrated proton in acetonitrile. The solution is put in between two 2 mm thick calcium fluoride windows separated by a 50 μm Teflon spacer. The two-color mid-IR pump-probe experiments were performed as described in the section 3.2. The nonresonant signal due to pump-probe cross-phase modulation in the calcium fluoride windows limits the experimental time resolution to ∼0.2 ps. In some of the experiments we obtained a better time resolution by using 500 nm thick silicon nitride windows instead of calcium fluoride windows.

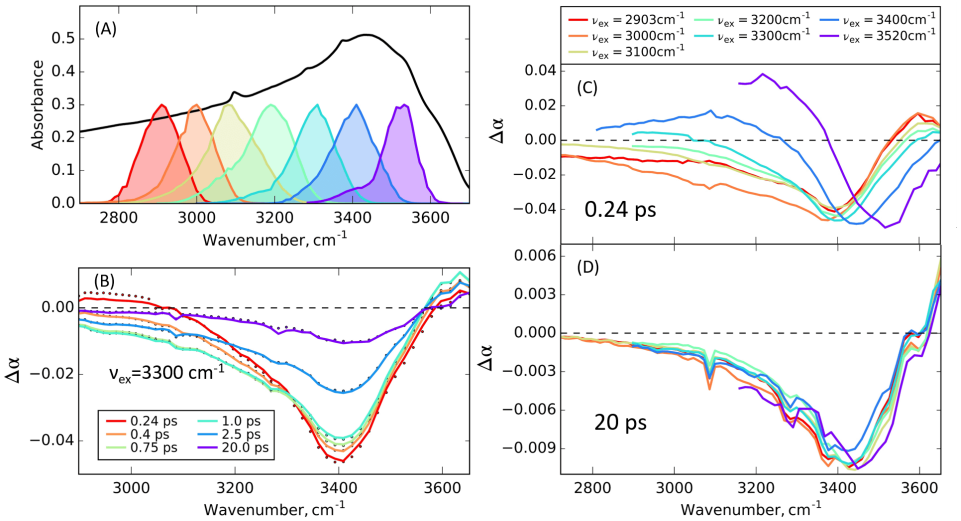

Figure 5.1: Linear infrared absorption spectrum of the TfOH/H2O=1:3 mixture in acetonitrile-d3 (black line, solvent background subtracted) and pump pulses used in the experiments (color lines). (B) Isotropic transient spectra of the hydrated proton in acetonitrile with ν_{ex}=3300 cm^{-1} (lines represent the result of the fit). (C,D) Isotropic pump-probe spectra at the delay times of 0.24 ps (C) and 20 ps (D) with excitation frequency varied.

5.3 Results

5.3.1 Transient spectra and delay time traces

In Figure 5.1B we show transient absorption spectra following excitation with pulses centered at 3300 cm^{-1}. In Figure 5.1C,D we show isotropic transient absorption spectra obtained with different central excitation frequencies at two different delay times (0.24 ps and 20 ps). At an early delay time of 0.24 ps, the transient absorption spectrum strongly depends on the excitation frequency. Excitation with a high-frequency excitation pulse ($\nu_{ex} \geqslant$3300 cm^{-1}) leads to a small positive absorption change at low frequencies. Excitation at frequencies $\leqslant$3200 cm^{-1} leads to a decreased absorption below 3500 cm^{-1} and an enhanced absorption at probe frequencies $>$3500 cm^{-1}. This spectral shape is similar to the transient absorption spectrum observed at long delay times ($>$10 ps) for all different excitation frequencies. This spectrum consists of a positive absorption change at frequencies $>$3600 cm^{-1} and a broad negative absorption change at lower frequencies.

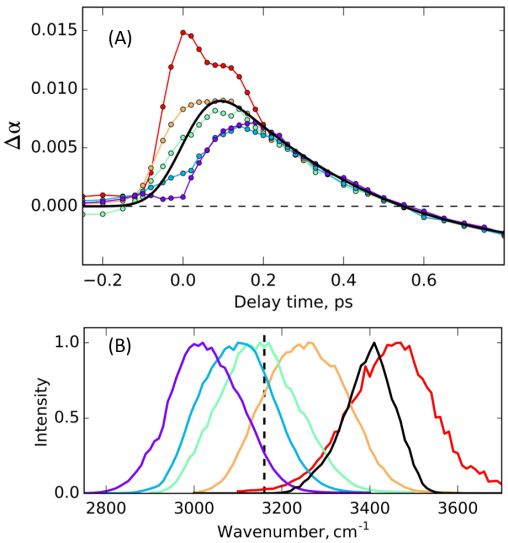

Figure 5.2: (A) The fast transient absorption dynamics at frequency 3160 cm^{-1} measured with various probe pulses; black line represents the fit. (B) Intensity spectra of the probe pulses used (color lines) and the pump pulse (black line).

5.3.2 Coherent coupling effects

In a previous study of hydrated protons in acetonitrile an intense increase of the induced absorption within the pump-probe cross-correlation time was observed.[72] This signal was assigned to Zundel cations excited at 3400 cm^{-1}. Since the observed signal was present only within the cross-correlation of the pump and probe pulses, the authors concluded that the excited state lifetime of these Zundel cations should be below 50 fs. The subsequent slower relaxation was assigned to energy redistribution within the Zundel cation.

In our studies we observed a similar fast signal component within the pump-probe cross-correlation time. However, we found the contribution of this signal component to be strongly dependent on the difference between the central frequency of the probe pulse and the frequency at which the transient absorption signal was detected. In Figure 5.2 we show the early delay time dynamics of the induced absorption signal at 3160 cm^{-1} measured with different probe pulses. After 0.2 ps the transient signal purely consists of the excited state absorption and heating signatures. These signals are independent of the central frequency of the probe pulse. However, in the time interval between -0.1 and 0.2 ps we find that the transient absorption signal becomes increasingly distorted when the detection frequency is shifted further away from the central frequency of the probe pulse. This behavior can be well explained from the additional signal contributions that

arise from coherent coupling effects when the pump and probe pulses overlap in time. The origin and impact of these coherent effects are discussed in detail in the section 3.

When the spectrum of the probe pulse is centered at the frequency of maximum of the linear absorption, i.e. the frequency of the fundamental v=0→1 transition, a strong coherent coupling effect in the region of the excited state absorption (red curve in Figure 5.2A). This coherent-coupling signal has the form of an additional positive signal and can be easily mistaken for the contribution of an ultrafast decaying excited state. We find that this strong additional positive signal vanishes if the spectrum of the probe pulse is centered close to the frequency of interest (green curve in Figure 5.2A). Therefore, we conclude that excitation at 3400 cm^{-1} results only in the excitation of relatively slowly relaxing water OH-stretch vibrations. In view of the frequency of 3400 cm^{-1} these OH vibrations are likely not located in the core of the proton hydration cluster but in the outer part of this structure.

5.3.3 Vibrational relaxation dynamics following excitation $\leqslant$3100 cm^{-1}

When we excite the solution with excitation pulses centered at 2900, 3000 and 3100 cm^{-1}, we observe at early delay times a very broad negative signal (bleaching) extending to lower frequencies (Figure 5.3A). The signal has a zero crossing at 3500 cm^{-1} and a positive sign (induced absorption) at frequencies >3500 cm^{-1}. Following earlier work[72,76] we explain the signal at early delay times from a strong local heating effect that results from the ultrafast relaxation of the excited OH-stretch vibrations.

We model the transient spectra obtained with $\nu_{ex} \leqslant$3100 cm^{-1} with the kinetic model that was used in a previous study of protonated water clusters in acetonitrile.[76] Within this model the excited vibrational state relaxes to an intermediate state with a relaxation time constant that is too short to be resolved. This intermediate state of the relaxation represents the effect on the absorption of the proton hydration complex of the local dissipation of energy to the water molecules that surround the proton. We will denote this state as the local hot state.

In Figure 5.3B we show the transient absorption spectra at early delay times following excitation at 2900, 3000 and 3100 cm^{-1}. The spectral signatures with ν_{ex}=2900 and 3000 cm^{-1} consist of a broad negative absorption change below 3400 cm^{-1} and a positive absorption change around 3500 cm^{-1}. These spectra are similar to the previously obtained spectra with ν_{ex}=2700 and 2800 cm^{-1}.[72,76] The negative part of the spectrum depends on the excitation frequency, which implies that the relaxed energy affects mostly the originally excited vibrations.

The local hot complex relaxes to a second intermediate state that represents the heating of the whole protonated water cluster. The time constant of this relaxation is 0.26±0.04 ps, meaning that the hot proton complex redistributes its energy over the

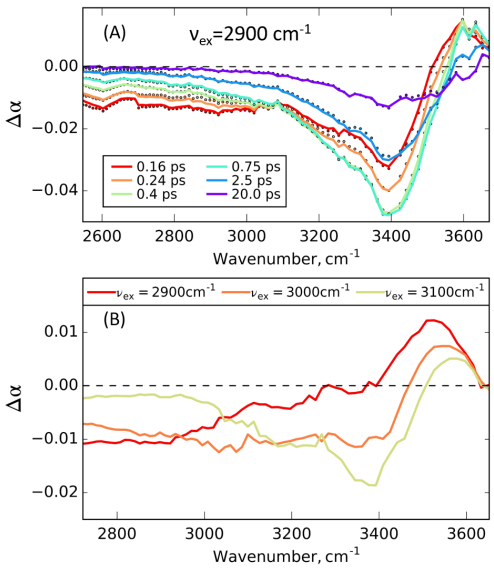

Figure 5.3: (A) Isotropic transient spectra of the hydrated proton in acetonitrile with ν_{ex}=2900 cm^{-1} (lines represent the result of the fit). (B) The transient spectral signatures of the local hot state after the low frequency excitation.

complete protonated water cluster on a time scale of hundreds of femtoseconds. This time constant agrees with the previously reported time constant of 0.32 ps of the energy redistribution following 2800 cm^{-1} excitation.[76] In the hot water cluster the hydrogen bonds are weaker, which induces a decrease of the OH-stretch absorption cross-section and a blue shift of the vibrational frequency. On a longer time scale, the hot cluster dissipates its energy to the acetonitrile solvent, resulting in a significant decrease of the amplitude of the heating signal and the appearance of sharp acetonitrile peaks and OH-stretch absorption features that can be assigned to monomeric water molecules.

5.3.4 Vibrational relaxation dynamics following excitation at frequencies ⩾3200 cm^{-1}

For excitation frequencies ν_{ex} >3300 cm^{-1} we observe a negative absorption change around 3400 cm^{-1} that we assign to the bleaching of the fundamental v=0→1 transition and stimulated v=1→0 emission of the excited OH-stretch vibrations. The positive absorption change below 3200 cm^{-1} is assigned to the corresponding v=1→2 excited state absorption.

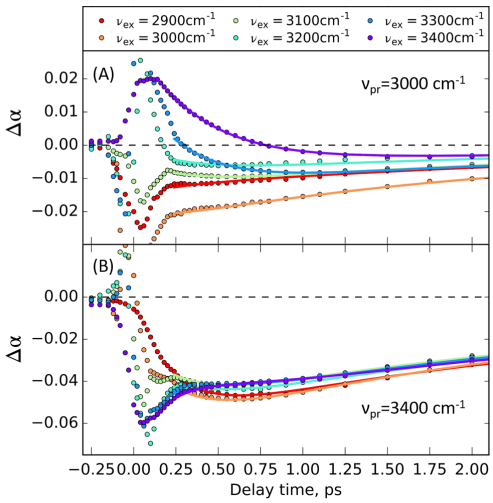

Figure 5.4: Isotropic pump-probe signal of the hydrated proton in acetonitrile at frequencies 3000 cm^{-1} (A) and 3400 cm^{-1} (B) as a function of delay time; excitation frequency varies from 2900 to 3400 cm^{-1}. Lines represent the result of the fit.

The transient absorption spectrum also shows a fast growing spectral component corresponding to the transiently heated hydrated proton cluster. At 1 ps we observe a broad negative signal with a peak at ∼3400 cm^{-1} and a small induced absorption around 3600 cm^{-1} (see Figure 5.1B). This spectrum has a very similar shape as the spectrum that is observed after 1 ps for excitation frequencies ν_{ex} ⩽3100 cm^{-1}, and that is observed at much later delay times, e.g. at 20 ps. Hence, we assign this spectrum to the response of the complete hot protonated water cluster.

Because of its large transient spectral amplitude, the spectral response of the hot protonated water cluster becomes significant already at early delay times and dominates the initial positive absorption signal in the region of the v=1→2 excited state absorption. The transient signal at ν_{pr}=3000 cm^{-1} becomes negative at 0.7 ps for ν_{ex}=3400 cm^{-1}, and already at 0.3 ps for ν_{ex}=3300 cm^{-1} (Figure 5.4A). The transient absorption signal at ν_{pr}=3400 cm^{-1} (Figure 5.4B) shows a much slower decay because at this frequency, the initial signal has a negative sign as it is due to the v=0→1 bleaching and stimulated v=1→0 emission. At this detection frequency the vibrational relaxation process replaces this initial negative signal by the negative absorption change associated with the hot cluster.

We fit the experimental data obtained with excitation frequencies ⩾3300 cm^{-1} with a kinetic model that contains four states. The first state is the v=1 state of the OH-stretch vibration that is excited by the excitation pulse. The relaxation of this state

results in heating of the protonated water cluster. We observe that the rise of this heating is somewhat delayed with respect to the relaxation of the excited v=1 state. It has been observed before in studies of the vibrational relaxation of bulk water that the heating signal grows somewhat slower than the excited vibration relaxes.[79,103] This delay is not observed when we excite low-frequency OH-stretch vibrations with $\nu_{ex} \leqslant$3100 cm^{-1} (the local hot state is observed immediately), which indicates that the low- and high-frequency OH vibration have different relaxation mechanisms. The relaxation of the high-frequency OH vibration likely proceeds through an intermediate state with an associated response that is quite different from a local heating effect. To account for the delay of the heating effect following the relaxation of the high-frequency OH-stretch vibrations, we include in the model an intermediate state in between the excited v=1 state and the hot water cluster state. We did not include the relatively small and long living spectral component of the vibrational predissociation that has been observed before.[76] The hot cluster exchanges heat energy with its surrounding to reach the fourth state in the model which represents the eventual globally heated state of the system.

The relaxation dynamics of the OH-stretch excited state can be well estimated from the low frequency region, where v=1→2 excited state absorption is the dominant spectral component. Comparing the transient absorption dynamics in this frequency region (Figure 5.4A), we observe a strong difference between the results of excitation at 3400 cm^{-1} and at 3300 cm^{-1}. The initial signal value at ν_{pr}=3000 cm^{-1} is much smaller when the oscillators are excited at lower frequency. This observation cannot be explained from a much faster relaxation of OH-stretch excited state, since the dynamics are similar to what is observed in the case of excitation at 3400 cm^{-1}. The observation of a small induced absorption signal at early delay times indicates that the hot cluster state is in part directly populated, i.e. in a separate relaxation channel that is faster than our time resolution. We thus conclude that the excitation pulse centered at 3300 cm^{-1} excites two types of OH oscillators. We find a good description of the transient spectra observed for ν_{ex}=3300 cm^{-1} when 40$\pm$10% of the excited OH vibrations relax very rapidly (T_1 <50 fs) and directly populate the hot cluster state, and 60$\pm$10% relaxes more slowly with a time constant of 270$\pm$30 fs. For ν_{ex}=3200 cm^{-1} we find that 70$\pm$10% relaxes directly to the hot cluster state and 30$\pm$10% relaxes with a time constant of 220$\pm$40 fs.

In figure 5.5A we show the spectral signatures of the excited v=1 state extracted from the fit. The spectrum of the excited state shows a significant dependence on the excitation frequency: the position of the ground state bleach shifts from 3500 to 3380 cm^{-1}, and the excited state lifetime T_1 decreases from 370$\pm$20 fs at ν_{ex}=3520 cm^{-1} to 220$\pm$40 fs at ν_{ex}=3200 cm^{-1} (Figure 5.5B).

The observed frequency dependence of the relaxation time constant indicates that the spectrum of the OH-stretch vibrations is inhomogeneously broadened. The variation of the excited state lifetime T_1 correlates well with the variation in local hydrogen-bond

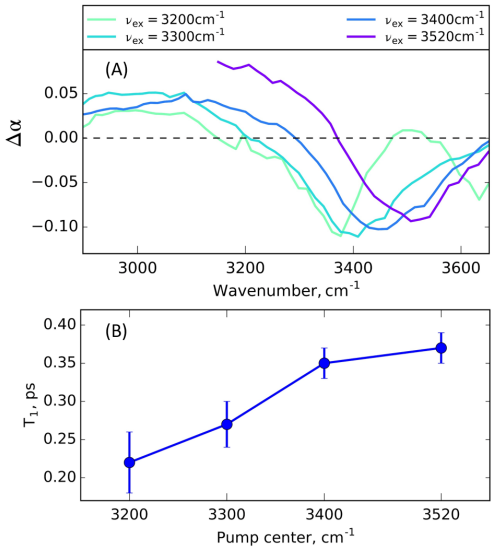

Figure 5.5: (A) Transient spectra associated with the excitation of the v=1 state of the OH-stretch vibration for four different excitation frequencies. (B) Time constant T_1 of the relaxation of the v=1 state as a function of the central excitation frequency.

strength: OH-groups engaged in stronger hydrogen bonds have lower absorption frequencies and show faster relaxation. Interestingly, the dependence of the vibrational lifetime on the excitation frequency is very similar to that observed for bulk liquid water,30 for which T_1 was found to decrease from 0.4 ps for ν_{ex}=3500 cm^{-1} to 0.25 ps for ν_{ex}=3200 cm^{-1}.

5.4 Discussion

We observe strongly different early delay time transient spectra when we shift the excitation frequency from 2900 cm^{-1} to 3520 cm^{-1}. This finding shows that the OH-stretch vibrational spectrum represents OH-groups of highly different character. At frequencies $\leqslant$3100 cm^{-1} we excite OH vibrations located in the core of the proton hydration cluster. For the (distorted) Zundel structure this core is formed by the OH-stretch vibration involving the central H atom in the $H_5O_2^+$ structure, for the Eigen structure the core is formed by the OH vibrations involving the three H atoms of the central H_3O^+ of the $H_9O_4^+$ structure. The main property of these OH vibrations that the H atom carries a significant part of the positive charge, and as a result donates a strong hydrogen bond. As a result, the frequency of these OH vibrations is <3200 cm^{-1} and the vibrational relaxation is ultrafast (<50 fs).

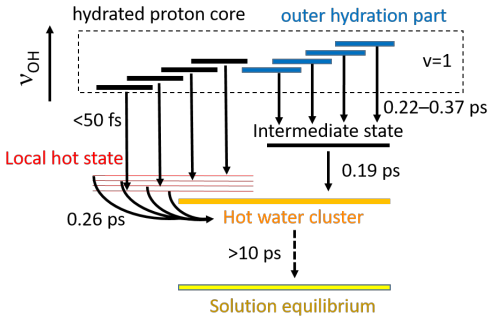

Figure 5.6: Kinetic scheme describing the spectral dynamics after excitation of the hydrated proton OH vibrations.

For excitation frequencies >3200 cm^{-1} the observed transient spectra resemble that of the OH-stretch vibration in neat water and hydrogen-bonded water in other media. The vibrational relaxation of this excited state is about 30 times faster than that of isolated water molecules in acetonitrile (T_1=8 ps),[104] and has a quite similar relaxation rate as the OH-stretch vibrations in bulk water.[78] From this we conclude that the observed high frequency OH-stretch vibrations belong to water molecules that belong to a cluster that contains at least one proton, but that are not in the center of the proton hydration structure, i.e. the H atoms involved in these OH vibrations do not carry a significant of the positive proton charge. At a concentration ratio of $[H^+]/[H_2O]$=1:3 the hydrated proton clusters in acetonitrile contain 2 to 6 water molecules.[102] The OH vibrations giving rise to this response can thus belong to the two H_2O molecules flanking the Zundel proton, or the OH vibrations of the three outer H_2O molecules of the Eigen $H_9O_4^+$ structure, or water molecules even further away from the core of the proton hydration structure. All these OH vibrations have in common that the partial positive charge on the H atom is small and that they absorb at frequencies $\geqslant$3200 cm^{-1}.

Excitation at intermediate frequencies of 3100-3200 cm^{-1} yields spectral dynamics of intermediate character. We observe OH-stretch vibrations showing a fast but resolvable vibrational relaxation, and the direct creation of a local hot state. It thus follows that we observe quite distinct vibrational relaxation behavior of the core and the outer part of the proton hydration cluster, even in the spectral region where the spectra of the corresponding OH vibrations overlap.

Interestingly, the transient spectrum observed at long delay times and that we assign to the response of the entire hot water cluster, is the same irrespective of the original excitation frequency. This finding shows that all OH-stretch vibrations absorbing in the region from 3520 cm^{-1} to 2900 cm^{-1} belong to protonated water clusters that have similar absorption spectra and that are thus likely of similar composition.

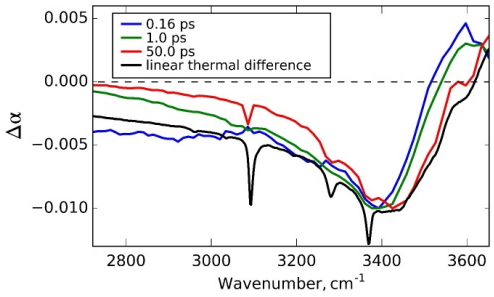

Figure 5.7: Isotropic pump-probe spectra at different delay times (ν_{ex}=2900 cm^{-1}) and a linear thermal difference spectrum of the studied solution. All the spectra are scaled with respect to the pump-probe spectrum at 50 ps.

Combining the results of all different excitation pulses we summarize the relaxation processes of the different OH-stretch vibrations in the protonated water cluster with the kinetic scheme shown in Figure 5.6. In this scheme, the v=1 state relaxes to a local hot state with a time constant T_1 that decreases with decreasing excitation frequency. The high frequency part ($\geqslant$3200 cm^{-1}) of the spectrum corresponds to the OH-stretch vibrations of the water molecules in the outer part of the proton hydration cluster, which display the vibrational relaxation dynamics similar to that of bulk water. The lower frequency absorption of the protonated cluster is due to the vibrations of the core of the cluster, the excited state of which relaxes much faster. The absorption spectra of these two types of vibrations overlap in the frequency region of 3100-3300 cm^{-1}, and excitation pulses in this frequency region will thus excite both the core and the outer part of the proton hydration cluster. As a result, we observe mixed vibrational relaxation dynamics. For all OH vibrations the relaxation results in a local hot state with a spectrum that depends on the excitation frequency. At lower frequencies this spectrum will primarily reflect the effect of local heat dissipation on the core of the proton hydration structure. At higher frequencies the spectrum of the local hot state is blueshifted and is very similar to that of the complete hot water cluster, i.e. the state that results after the heat has been equilibrated over the entire proton hydration cluster.

We note that the transient hot states observed in our experiments are very local in nature and differ from a true thermal state of the whole sample. As a result, these transient hot spectra differ from the linear thermal difference spectrum of the hydrated proton in acetonitrile. This latter spectrum shows a much broader negative absorption change than observed in the femtosecond experiments at delay time >10 ps.[76] An increase in the equilibrium temperature is observed to lead to a similar decrease of the cross-section for all OH-stretch vibrations (Figure 5.7). In contrast, the pump-probe spectrum at 1 ps

shows predominant absorption changes in the frequency region of the outer part of the cluster even when the core of the cluster was initially excited. Apparently, the studied system does not reach complete thermal equilibrium within the picosecond time frame of the pump-probe experiment. Similar observations were done for pump-probe experiments on the hydrated proton in DMSO (see Chapter 4) and in bulk water.[25,47] This discrepancy between the final thermal difference spectrum of the pump-probe experiment and the fully equilibrated response to heating of the sample can be explained from the fact that complete equilibration includes a change of the composition of the clusters. This change in composition involves diffusion and exchange of molecules between different clusters. These processes occur on much longer time scales than the picosecond times scale of the time-resolved experiments.

5.5 Conclusions

We studied the vibrational relaxation and energy dissipation of small protonated water clusters in acetonitrile using femtosecond mid-IR pump-probe spectroscopy. We find that the relaxation dynamics strongly depend on the excitation frequency. Excitation of the low frequency part of the OH-stretch band (3100 cm^{-1}) is followed by ultrafast vibrational relaxation (T_1 <50 fs), resulting in a local energy dissipation that affects mostly the originally excited vibrations. The transient spectrum of this local hot state shows a broad negative absorption change around the excitation frequency. After the fast vibrational relaxation of these OH groups the energy equilibrates over the complete protonated water cluster with a time constant of 0.26$\pm$0.04 ps.

Excitation of the high-frequency part of the OH-stretch band (3200 cm^{-1}) is followed by vibrational relaxation of the OH-stretch vibration with a time constant ranging from T_1=0.22$\pm$0.04 ps for an excitation pulse centered at 3200 cm^{-1} to T_1=0.37$\pm$0.02 ps for an excitation pulse centered at 3520 cm^{-1}. We found that the signal previously assigned to the relaxation of the Zundel cation excited at 3400 cm^{-1} strongly depends on the probe pulse and originates from the coherent coupling of pump and probe pulses. The vibrational relaxation results in a somewhat delayed heating of the complete protonated water cluster, which indicates that the high-frequency OH-stretch vibrations have a different relaxation mechanism, i.e. proceed through a different intermediate state in comparison with the low-frequency OH-stretch vibrations.

The spectrum of the hot protonated water cluster that results after relaxation of the high-frequency OH vibrations is the same as is observed after excitation of the low-frequency OH-stretch vibrations. This result shows that the high- and low-frequency OH vibrations belong to the same type of protonated water clusters. We thus assign the low-frequency part of the OH spectrum to the core of the proton hydration cluster and the high-frequency part of this spectrum to the outer part of this cluster. At intermediate

excitation frequencies between 3100 cm^{-1} and 3300 cm^{-1} we do not observe average or intermediate behavior but two distinct relaxation components. Part of the OH vibrations show the ultrafast relaxation behavior of the core while the other part shows the relatively slower relaxation dynamics of the outer part. This latter fraction increases with increasing excitation frequency. We conclude that the core shows quite distinct vibrational relaxation behavior from the outer part, even in the spectral region where the spectra of the corresponding OH vibrations overlap.

Published as:

Oleksandr O. Sofronov and Huib J. Bakker. Slow proton transfer in nanoconfined water ACS Central Science 2020, 6, pp. 1150–1158

6

Slow ProtonTtransfer in Nanoconfined Water

Abstract

The transport of protons in nanoconfined environments, such as in nanochannels of biological or artificial proton conductive membranes, is essential to chemistry, biology and nanotechnology. In water proton diffusion occurs by hopping of protons between water molecules. This process involves the rearrangement of many hydrogen bonds, and as such can be strongly affected by nanoconfinement. In this Chapter we study the vibrational and structural dynamics of hydrated protons in water nanodroplets stabilized by cationic surfactant using polarization-resolved femtosecond infrared transient absorption spectroscopy. We determine the time scale of proton hopping in the center of the water nanodroplets from the dynamics of the anisotropy of the transient absorption signals. We find that in small nanodroplets with a diameter $<$4 nm proton hopping is more than 10 times slower than in bulk water. Even in relatively large nanodroplets with a diameter of $\sim$7 nm, we find that the rate of proton hopping is slowed down by 4 times compared to bulk water.

6.1 Introduction

Proton transfer in nanoconfined water is a process of paramount importance in biological and man-made systems, in particular in the generation and storage of energy.[52,105–107] Energy is stored in cells by proton transfer through the nanochannels of mitochondrial membranes and the flow-back through these channels is coupled to the generation of ATP. In bulk liquid water, proton diffusion occurs through the so-called Grotthuss mechanism, which implies that the proton does not move as a particle, but that rather its charge is being transferred between hydrogen atoms located on different water molecules.

In several theoretical studies it was found that the transfer of the proton charge in liquid water results from the interconversion between $H_9O_4^+$ Eigen proton-hydration structures located at different positions in the liquid, with Zundel $H_5O_2^+$ proton hydration structures acting as short-living intermediates.[10,11,13,98] However, recent ab initio molecular dynamics (AIMD) simulations of the vibrational spectrum of acid water indicated that the Zundel species is in fact quite prominently present in acid water.[18,22,35,36] This notion was confirmed in a two-dimensional infrared spectroscopy study by Fournier et al.[23], in which it was shown that the proton in aqueous solution forms a single spectroscopically distinct species, which can best be described as an asymmetric Zundel structure.

Proton transfer in liquid water is intimately connected to the reorganization of the hydrogen-bonded network of the water solvent. As the properties of water in nanoconfinement such as the polarity and self-diffusion are different from bulk,[29,108] it is to be expected that nanoconfinement of the water matrix will strongly affect the rate and mechanism of aqueous proton transfer. Very suitable systems to study the effect of nanoconfinement on the dynamics of water and aqueous protons are reverse micelles: water nanodroplets in an apolar matrix that are stabilized by surfactant molecules with a polar head and an apolar tail. The diameter of the water nanodroplet (d_w) can often be varied over a quite large range by varying the hydration ratio w_0=[H_2O]/[surfactant]. Reverse micelles have thus been used to study the effect of nanoconfinement on the release and solvation of protons by photoacid molecules.[32,109–112] In these studies it was found that the proton release occurs much slower in nanoconfined water than in bulk. These results indicate that nanoconfinement strongly affects aqueous proton transfer. Unfortunately, a detailed understanding of the effect of nanoconfinement on proton transfer is complicated by the fact that the observed proton-release dynamics also rely on the water solvation dynamics of a relatively large conjugate photobase, and that the photoacid molecules are often not uniformly distributed over the water nanodroplet.[113]

The anionic Aerosol OT (dioctyl sulfosuccinate, AOT) is an ideal surfactant to create reverse micelles over a wide range of sizes. AOT reverse micelles have thus been widely used to study the effect of nanoconfinement on the dynamics of liquid water.[114–116] For the study of nanoconfinement on aqueous proton transfer AOT reverse micelles are less

suitable because the protons will strongly interact with the negatively charged sulfonate groups of the surfactant molecules.[117–119]

Here we study the vibrational and structural dynamics of hydrated protons in water nanodroplets of cationic reverse micelles using polarization-resolved femtosecond infrared (fs-IR) transient absorption spectroscopy. We use a positively charged surfactant system consisting of CTAB (cetyltrimethylammonium bromide) and hexanol, where the addition of hexanol as a co-surfactant allows to prepare much more stable and monodisperse nanodroplets.[120?] Recent small-angle neutron scattering (SANS) studies[120] showed that water nanodroplets stabilized by these surfactants in an apolar solvent have an ellipsoid shape with an axial ratio between 1.7 for small nanodroplets (w_0 <17) and 1.1-1.3 for large nanodroplets (w_0 >20). Since the shape is near-spherical, we will further use the diameter d_w of a sphere of equal volume to refer to the size of the studied nanodroplet (for the details see the Experimental section). In microemulsions the reverse micelles move and collide, which can result in intermicellar exchange. However, these processes take place on a much slower time scale (typically microseconds) than the time frame of our experiments (picoseconds). Hence, in our experiment, the emulsion of reverse micelles can be considered to be a static system.

In cationic reverse micelles excess protons will not bind to the positively charged surfactants, which implies that the protons will be well embedded and hydrated in the core of the nanodroplet. We can thus measure the "pure" effect of nanoconfinement, with very little influence of the surface of the nanoconfined region. We observe that nanoconfinement leads to a very strong slowing down effect on the rate of aqueous proton transfer. Even for relatively large nanodroplets with a water pool diameter of 7.4 nm, proton transfer occurs at least 4 times slower than in bulk water, which indicates that solvent properties in the core of water nanodroplet are different from water properties in bulk.

6.2 Experiment

Linear mid-infrared absorption spectra were obtained in transmission mode using a commercial Fourier transform spectrometer (Bruker Vertex 80v). The two-color mid-IR pump-probe experiments and one-color pump-probe anisotropy measurements were performed as described in the section 3.2. Nanodroplets were prepared by mixing n-hexane, 1-hexanol, cetyltrimethylammonium bromide (CTAB), water and hydrobromic acid solution (48%) and stirring for 5 minutes. All the chemicals were purchased from Sigma-Aldrich. The concentrations of CTAB (0.11 M) and 1-hexanol (0.61 M) were the same for all microemulsions and yielded a ratio [hexanol]:[CTAB]=3:1 in micellar phase.[121,122] Water and hydrobromic acid were added to obtain the desired w_0=([H_2O]+[HBr])/[CTAB] ratio

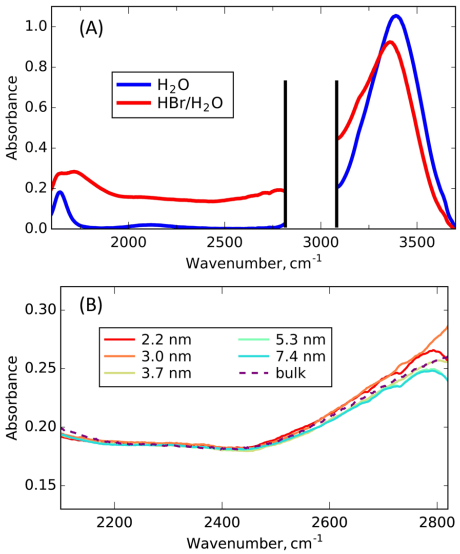

Figure 6.1: (A) Linear infrared absorption spectrum of the water nanodroplets (dw=2.2 nm) with (red) and without (blue) protons. The 2800-3100 cm^{-1} spectral region is not accessible because of the strong absorption of CH-stretch vibrations. The dashed box highlights the part of the spectrum that corresponds to the response of water molecules in the outer hydration shells of the proton. (B) Comparison of OH-stretch continuous absorption of the hydrated proton in nanodroplets of different diameters and in bulk water. In these spectra the neat water contribution is subtracted.

and a concentration of HBr of 7 M in the nanodroplets. Without HBr this procedure yields nearly spherical monodisperse nanodroplets with a water pool diameter $d_w = 0.26 \times w_0$ (nm).[120–122] We estimate the size of the water nanodroplets with a particular w_0 to become 1.4$\pm$0.2 times smaller when the water is replaced by an aqueous 7 M HBr solution, which implies that $d_w = 0.29 \times w_0$ (nm). (see Appendix, Section 6.6.1). The samples were contained in a sample cell consisting of two 2 mm thick calcium fluoride windows separated by a 50-200 μm spacer.

6.3 Results

In Figure 6.1A we show Fourier transform infrared (FTIR) absorption spectra of neat water nanodroplets and nanodroplets containing a 7 M HBr solution. We vary the ratio w_0=[H_2O]/[surfactant] between w_0=12 and w_0=40, corresponding to a variation in nanodroplet diameter of 2.2-7.4 nm. The presence of excess protons in the nanodroplets is

observed to yield a broad continuous absorption at frequencies below 2800 cm^{-1}, similarly as has been observed for bulk liquid water. The broad featureless absorption at 2000-3000 cm^{-1} has been assigned to the OH-stretch vibrations of different proton hydration structures, whereas the absorption band observed at 1750 cm^{-1} is usually assigned to the bending vibrations of these structures.[15,22,33]

In Figure 6.1B we zoom in on the absorption continuum of the hydrated proton OH-stretch vibrations. The spectrum is nearly flat below 2500 cm^{-1} and increases in amplitude for frequencies above 2500 cm^{-1}. The absorption spectrum of the nanodroplets is quite similar to the absorption spectrum of bulk acid water.

To study the dynamics of the hydrated proton we measure transient absorption spectra following the excitation of the proton OH-stretch continuum with an intense 100 femtosecond infrared pulse centered at 2600 cm^{-1}. Figure 6.2A shows the resulting isotropic transient absorption spectra of hydrated protons in d_w=2.2 nm nanodroplets at different time delays between the excitation and detection pulses, ranging from 0.26 to 5 ps. At all delay times the spectra consist of a weak and broad negative signal below 2800 cm^{-1}, a much more intense negative signal centered at $\sim$3300 cm^{-1} and a positive absorption change above 3500 cm^{-1}. This shape of the transient absorption spectrum is observed for all studied nanodroplet sizes. The 2800-3000 cm^{-1} region is not accessible due to the high absorbance of the alkyl chains of the surfactant molecules.

First, we focus on the high frequency part of the transient spectrum (highlighted in Figure 6.2A, Figure 6.6). The observed strong negative absorption change and smaller positive absorption change at higher frequency is a typical signature of the hot ground state of the OH-stretch vibration of water that results from the transfer of vibrational energy into low-frequency degrees of freedoms (e.g. hydrogen bonds) following the relaxation of the excited OH stretch vibration.[79,85,123] This process results in a blue shift of the OH-stretch absorption spectrum, which is similar to the effect of increasing the temperature of the sample.

In the first picosecond after the excitation the hot ground state spectrum grows in amplitude and shifts to higher frequency. After 1 ps the signal slowly decays reaching a constant level after $\sim$50 ps. We fit these spectral dynamics with a cascade kinetic model consisting of three states. From the fit we obtain the spectral components shown in Figure 6.2B. The first state has a red-shifted transient spectrum with a minimum at $\sim$3200 cm^{-1} and decays with a time constant of 280$\pm$50 fs to the second state. The second state has a transient spectrum with a minimum at $\sim$3300 cm^{-1} and slowly decays to the third state with a transient spectrum of similar shape but with a reduced amplitude. The time constant of the latter relaxation process depends on the nanodroplet size.

A pump pulse centered at 2600 cm^{-1} cannot excite water OH-stretch vibrations near 3300 cm^{-1}. The observed early-time transient spectral response near 3300 cm^{-1} (red spectrum in Figure 6.2B) is thus the result of ultrafast energy relaxation of the initially

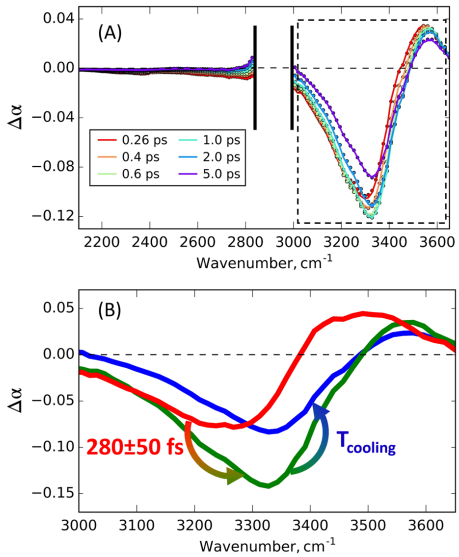

Figure 6.2: (A) Isotropic transient spectra of the acid water nanodroplets (d_w=2.2 nm) following the excitation at 2600 cm^{-1}; lines are the result of the fit. (B) Spectral components obtained from the fit of the transient spectral dynamics.

excited OH stretch vibration of hydrated protons, leading to heating of water molecules that are close to the excited OH stretch vibration. These water molecules are close to the positive proton charge and thus will have relatively strong hydrogen bonds and a redshifted absorption spectrum compared to water molecules in bulk liquid water. The subsequent transition from the red to the green transient spectrum can be assigned to energy transfer from water molecules close to the initially excited core of the hydrated proton, to water molecules further away. These latter water molecules will have weaker hydrogen bonds and thus a more blueshifted absorption spectrum. The final slow decay of the green to the blue transient spectrum corresponds to the dissipation of the heat to surfactant molecules and the oil phase, i.e. cooling of the water nanodroplet. This process leads to a decrease of the amplitude of the transient absorption spectrum. The dynamics of this latter process are non-exponential and depend on the nanodroplet diameter.[124,125]

In Figure 6.3 we show transient absorption spectra at frequencies <2800 cm^{-1} for different nanodroplet sizes. This part of the spectrum corresponds to the OH-stretch vibrations of the core of the proton hydration structures, i.e. OH-vibrations for which the H atom carries a significant fraction of the excess positive proton charge.

Since at very short delay times we already observe a strong heating signal from

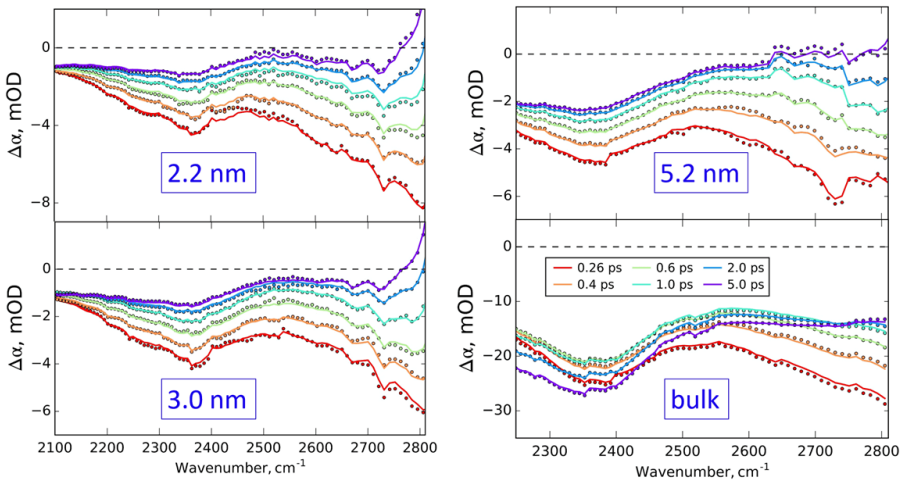

Figure 6.3: Isotropic transient spectra of acidic CTAB reverse micelles of different diameters and a bulk solution of HBr in water following excitation at 2600 cm^{-1}. The lines are the result of a fit of the kinetic model described in the text.

water molecules (Figure 6.2), we conclude that excited OH-stretch vibrations at 2600 cm^{-1} relax ultrafast within the time resolution ($\sim$100 fs) of the experiment. This means that the transient spectra at frequencies $<$2800 cm^{-1} are not due to the population of the excited v=1 state of the OH vibrations but rather reflect a local heating effect on the absorption spectrum of the proton hydration structure. The spectral dynamics are observed to be nonexponential, showing a fast and a slow processes. We fit these dynamics with the same three-level model used to fit the high frequency part of the spectrum shown in Figure 6.2. The first decay with a time constant of 280$\pm$50 fs again reflects the energy equilibration with the proton hydration structure and the second much slower decay the cooling of the whole nanodroplet.

The amplitude of the transient absorption spectra increases for frequencies $>$2500 cm^{-1}, an effect that is also observed in the linear infrared absorption spectra (Figure 6.1B). Interestingly, the lower-frequency region of the transient spectra is not as featureless as the corresponding frequency region in the linear absorption spectrum. The transient absorption spectra show a distinct band at 2350 cm^{-1} region. This band is not the result of nanoconfinement, as it is also present in the transient spectrum of the hydrated proton in bulk liquid water.

The response of the hydrated proton is anisotropic: the absorption change measured with a probe pulse that is polarized parallel to the polarization of the pump is larger than the absorption change measured with a probe pulse that has a perpendicular polarization.

To quantify these observations we calculate the anisotropy value, which is the normalized difference between the absorption change in parallel and perpendicular polarizations.

In Figure 6.4A we show the anisotropy dynamics of the transient absorption signal at 2600 cm^{-1} following excitation with a pump pulse centered at 2600 cm^{-1}, for acidic water nanodroplets of different sizes and for acidic bulk water. The dynamics of the anisotropy of the signal measured with the same excitation and detection frequencies represents the reorientation of the transition dipole moments of vibrations absorbing at that frequency.

For bulk water we observe a decay of the anisotropy with a time constant of 1.6$\pm$0.2 ps, which is in excellent agreement with the proton hopping time derived from NMR experiments[126] (see Appendix, Figure 6.7). The anisotropy decay is much slower for the nanodroplets and strongly slows down with decreasing size of the nanodroplet. For the smallest nanodroplets (d_w=2.2 nm), the anisotropy does not decay at all within the accessible time window. For this nanodroplet size even a small rise of the anisotropy is observed, which we can explain from the contribution of protonated hexanol molecules that have a slightly higher anisotropy and of which the transient absorption signal decays somewhat slower than that of hydrated protons (see Appendix, Section 6.6.3). For the larger nanodroplets ($d_w \geqslant$3.0 nm), the contribution of protonated hexanol is too small to significantly affect the anisotropy dynamics. For the large nanodroplets (5.2 nm and 7.4 nm) we extracted effective decay times of anisotropy of 14$\pm$3 ps and 7$\pm$1 ps respectively. In Figure 6.4B, we present the anisotropy decay time constant as a function of the inverse nanodroplet diameter.

6.4 Discussion

The anisotropy represents the average relative orientation of the transition dipole moment of the probed vibration with respect to the transition dipole moment of the excited vibration. For a single, well-localized vibration the initial value R0 of the anisotropy is expected to be 0.4. When the absorption bands of strongly coupled vibrations with different orientation of their transition dipole moment overlap, the anisotropy rapidly decays, often even within the time resolution of the experiment. This is for instance observed for the symmetric and antisymmetric OH-stretch vibrations of water molecules in acetonitrile.[104] In the case of rapid randomization of the vibrational excitation in a planar symmetric molecular structure like H_3O^+ cation, the value of R_0 is thus expected to be 0.1. The initial value of anisotropy R_0 can thus be interpreted as the level of degeneracy of the vibration. The observed R_0 values of 0.2-0.25 (Figure 6.4A) are below 0.4, which indicates, that the OH-stretch vibrations of the hydrated proton have a certain degree of degeneracy. These values are also higher than 0.1, which indicates that the probed

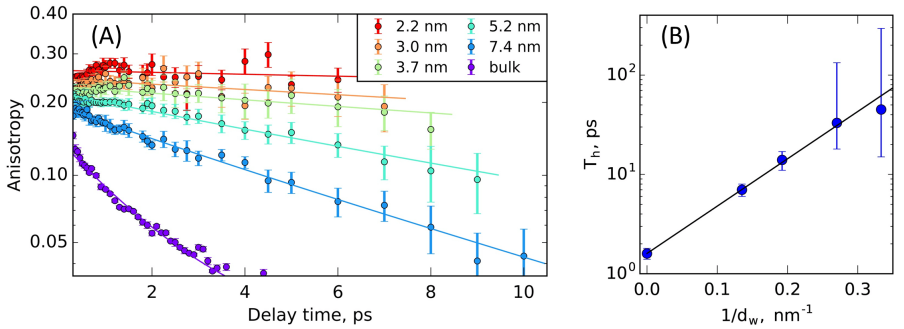

Figure 6.4: (A) Anisotropy of the transient signal at 2600 cm^{-1} as a function of delay time for acidic CTAB reverse micelles of different sizes and a bulk HBr (7 M) solution, plotted on a logarithmic scale. The straight lines represent exponential fits to the anisotropy decays. (B) Proton hopping time extracted from anisotropy dynamics as a function of the inverse water nanodroplet diameter. The straight solid line serves as a guide to the eye.

OH-vibrations are more restricted in orientation than in an ideal planar symmetric H_3O^+. Thus, in line with previous experimental[23] and theoretical[10,11,13] works, we conclude that the proton hydration structure can be described as an asymmetric Eigen or Zundel structure.

The decay of the anisotropy reflects the randomization of the orientation of the transition dipole moment of the probed vibration. In the measurements of Figure 6.4A, the anisotropy is due to a local heating effect on the OH-stretch vibrations absorbing at 2600 cm^{-1}. This anisotropy can potentially decay as a result of three different processes: 1) diffusion of the locally dissipated heat to other proton hydration structures that were not excited and that have OH vibrations absorbing at 2600 cm^{-1} with a random orientation; 2) molecular rotation of the OH groups of the hydrated proton structure absorbing at 2600 cm^{-1}; 3) structural reorganization of the proton hydration structure as a result of which other, nearby O-H stretch vibrations with different orientations acquire absorption at 2600 cm^{-1}. This latter process would imply a transfer of the proton charge to another position in the liquid, i.e. a proton jump.

Heat diffusion does not require a restructuring of the hydrogen bonds of the proton hydration structure. For the hydration shells of hydroxide ions it was found that heat diffusion constituted the dominant mechanism leading to decay of the anisotropy of the signal of the hydration shell of the hydroxide.[127] The importance of heat diffusion was evident from the fact that the rate of anisotropy decay was observed to increase with increasing hydroxide concentration, i.e. decreasing average distance between the hydroxide solvation complexes. We find that for bulk acid solutions the anisotropy dynamics does

not depend on the proton concentration (see Appendix, Figure 6.7), which shows that heat diffusion does not form a significant contribution to the decay of the anisotropy. This finding agrees with the results of a previous study by Carpenter et al.[25] of the anisotropy dynamics of hydrated protons in bulk water. It should also be noted that the global thermalization of the excitation energy (second relaxation process), that is the result of heat diffusion, leads to a nearly zero transient absorption signal at 2600 cm^{-1} (Figure 6.3). This means that for the nanodroplets the signal resulting from heat diffusion forms a negligible (isotropic) contribution to the observed total transient absorption signal at 2600 cm^{-1}. Hence, heat diffusion leads to a decay of the total transient absorption signal at 2600 cm^{-1}, but as this decay leads to an almost complete vanishing of the transient absorption signal, it will have very little effect on the dynamics of the anisotropy of the remaining signal at 2600 cm^{-1}.

In bulk liquid water the molecular reorientation of OH groups occurs with a time constant of $\sim$2.5 ps.[128,129] This reorientation involves a reorganization of the hydrogen-bond network as a result of which the hydrogen bond of the probed OH group is broken and transferred via an intermediate state consisting of a bifurcated hydrogen bond to a hydrogen bond to another water molecule. For strongly hydrogen-bonded OH groups absorbing at 2600 cm^{-1} this process is expected to be much slower than for the OH groups in bulk liquid water. It should further be noted that reorientation of the originally excited OH group at 2600 cm^{-1} results in a new hydrogen-bonded structure in which the rotated OH group likely absorbs at a different (higher) frequency and in which other OH groups acquire absorption at 2600 cm^{-1}. In this case molecular reorientation is the same process as structural reorganization of the hydrogen-bond network in which the absorption at 2600 cm^{-1} is transferred to OH stretch vibrations different from the originally excited OH stretch vibration.

The reorganization of the hydrogen-bond structure can thus lead to proton transfer and a decay of the anisotropy. A prerequisite for the latter is that the net orientation of the new OH stretch vibrations absorbing at 2600 cm^{-1} differs from the orientation of the excited OH group. These new OH stretch vibrations are the water-like OH groups that before the hydrogen-bond reorganization absorb at frequencies 3000-3700 cm^{-1} (Figure 6.2), and that are directly affected by the vibrational energy relaxation and dissipation of the excited OH stretch vibration at 2600 cm^{-1}. We observe the anisotropy of the transient absorption signal of these OH groups to be zero (Figure 6.6), which means that these OH groups have no net orientation with respect to the excited OH vibration at 2600 cm^{-1}. Hence, irreversible transfer of the proton charge to other, nearby OH groups will convert the initial anisotropic signal at 2600 cm^{-1} into an isotropic signal at this frequency, and thus will lead to a decay of anisotropy.

The assignment of the anisotropy decay to the structural reorganization of the hydrogen-bond network, leading to irreversible proton transfer, agrees with the results of a recent

fs-IR spectroscopy study by Carpenter et al.[25] In this latter study the transient signal of the OH-bending vibration of proton hydration structures following its excitation at 1750 cm^{-1} was measured. The observed anisotropy dynamics yielded an upper limit for the proton hopping time of 2-2.5 ps. This time constant agrees quite well with the time constant of 1.6$\pm$0.2 ps that we observe for the decay of the anisotropy for bulk water, and is consistent with previous experimental and theoretical works.[9,12,24] An experimental difference with the study of Carpenter et al.[25] is that we measure the anisotropy dynamics of the response of the OH-stretch vibrations of the hydrated protons. This has as an advantage that the observed transient absorption response does not show any contribution of ordinary water molecules, as the OH vibrations of these molecules absorb at frequencies >2900 cm^{-1}. For the bending region there is not such a clear separation of the bending modes of the proton hydration structures (centered at 1750 cm^{-1}) and water molecules (centered at 1650 cm^{-1}).

For the 5.2 nm and 7.4 nm nanodroplets we extracted the decay times of the anisotropy of 14$\pm$3 ps and 7$\pm$1 ps respectively. Thus, even in large nanodroplets with a water pool diameter d_w=7.4 nm, the proton hopping occurs at least 4 times slower than in bulk water. We observe the clear increase of the proton hopping time when decreasing the nanodroplet diameter (Figure 6.4B), however, the uncertainty of the values for d_w¡4 nm does not allow us to quantify this dependence. The lack of decay of the anisotropy of the smaller nanodroplets (d_w=2.2 nm; 3.0 nm) in our time window of $\sim$6 ps, shows that for these water nanodroplets the proton transfer is slowed down by more than a factor of 10 in comparison to bulk liquid water. This slowing down of proton transfer in nanoconfined water is in qualitative agreement with the results of previous studies of photoacid dissociation in reverse micelles that were stabilized with anionic (AOT=sodium dioctyl sulfosuccinate) and non-ionic (BRIJ-30=polyoxyethylene(4)lauryl ether) surfactants. In these studies a strong slowing down of the proton release with decreasing nanodroplet size was observed.[32,109–112] However, the strong dependence of the photodissociation on the dynamics of solvation of the photoacid and the conjugated base does not allow for a quantitative comparison of these results to the proton hopping dynamics studied here.

The effect of nanoconfinement on the proton transfer rate depends on the dimensionality of the nanoconfinement. Recent studies of proton transfer in water nanotubes[130,131] (two-dimensional confinement) and water layers[132] (one-dimensional confinement) showed that the proton mobility is not very different from bulk water in the dimensions that are not confined. Apparently, the fact that the hydrogen-bond network of water is still extended in one or two dimensions allows for a relatively high mobility of the proton in those dimensions. In the case of water nanodroplets (three-dimensional confinement) the proton can only move in dimensions that are confined, and the effect on the proton mobility in these dimensions is much higher than in the unconfined dimensions of water layers and water nanochannels.

An interesting question is how the observed strong decrease of the proton transfer rate upon three-dimensional nanoconfinement in CTAB reverse micelles can be explained. This slowing down cannot be explained from surface effects. It was shown with small-angle neutron scattering (SANS) experiments that the shape of the studied nanodroplets is nearly spherical or only slightly ellipsoidal.[120] For such a shape only a small part of the water molecules will be in close contact with the surface effects (20% of the volume for a droplet with a diameter of 7.4 nm). The limited effect of the surface is further confirmed by the low fraction of water molecules showing a slower vibrational relaxation as a result of their location near the surface of the reverse micelle (see Appendix, Section 6.6.1).

The strong slowing down of the proton transfer can also not be explained from ordering of water molecules by the field of the electric double layer at the charged surface of the nanodroplets. Vibrational sum-frequency generation experiments have shown that the effect of water ordering near charged surfaces is strongly suppressed for salt solutions.[133–135] Already at a bulk concentration of 0.5 M NaBr the ordering of water near a CTAB monolayer is suppressed by an order of magnitude.[133] Thus, having an even higher ionic strength in the HBr containing reverse micelles, we do not expect significant ordering of water molecules beyond one molecular layer from the interface. This notion is confirmed by molecular dynamics simulations of nanodroplets stabilized by charged surfactants, which show that the fraction of water molecules whose motion is restricted by the electric dipole moment alignment corresponds to an interfacial layer of only $\sim$0.3 nm thickness (one molecular layer).[30,136]

The slow proton transfer can also not result from the high concentration of bromide ions. To study the potential effect of bromide ions on the rate of proton transfer, we measured the proton hopping rate for different concentration of HBr in reverse micelles of two different sizes, and in bulk solutions (see Appendix, Figure 6.7). In neither case we observed a significant effect of the concentration of HBr on the proton-transfer rate, which demonstrates that the slowing down of the proton transfer in water nanodroplets is not due to the high concentration of counter ions.

Reverse micelles have also been used to study the effect of nanoconfinement on the reorientation dynamics of water molecules.[31,116,137,138] In these studies it was found that nanoconfinement slows down the average reorientation of the water molecules, but not to the extent that we observe here for the proton transfer. For 7.4 nm nanodroplets the reorientation time is expected to increase by $\sim$25% only, while the proton transfer time is observed to increase by a factor of 4.

The large difference in the effect of nanoconfinement on aqueous proton transfer in comparison to water molecular reorientation may be explained from the fact that proton transfer involves a much larger reorganization of the hydrogen-bond network than molecular reorientation.[130,139] Proton transfer involves an extended reorganization of the hydrogen-bond structure in which many water molecules and ions have to reorganize to

allow for stabilization of the charges. This highly collective process will get frustrated if there is not enough space. In a recent molecular dynamics simulations study it was found that the proton transfer in non-ionic reverse micelles slows down primarily because the dynamics of the water hydrogen-bond network are significantly hindered.[140] An additional effect may be a long-range disruption of the hydrogen-bond network. Cringus et al.[125] found that intermolecular vibrational coupling between the water molecules in the core of AOT-stabilized water nanodroplets is strongly suppressed because of a disrupted hydrogen bond network. Car-Parinello molecular dynamics simulations[141,142] show that water molecules that donate only one hydrogen bond or no hydrogen bond at all cannot efficiently accept the proton due to their reduced basicity. As a result, the number of possible proton transfer pathways decreases and the average residence time of the proton at each water molecule increases.

6.5 Conclusions

In this Chapter, we studied the vibrational and structural dynamics of proton hydration structures in bulk water and water nanodroplets that are stabilized with the cationic surfactant CTAB (cetyltrimethylammonium bromide) and hexanol, using polarization-resolved fs-IR spectroscopy. We observe that excitation of the OH-stretch vibrations of the hydrated proton at 2600 cm^{-1} results in long-living anisotropic absorption changes that largely decay as a result of proton hopping. For bulk acidic water proton hopping occurs with a time constant of 1.6 ps, in agreement with previous results. We observe the proton hopping to be 4 times slower for nanodroplets with a diameter of 7.4 nm, and more than 10 times slower for nanodroplets with a diameter $<$4 nm. We thus find that nanoconfinement of liquid water strongly affects the rate of aqueous proton transfer, in contrast to other properties of water like the reorientation of the water molecules. We hope that these results will stimulate new theoretical work to explain the exceptionally strong effect of nanoconfinement on the rate of aqueous proton transfer.

6.6 Appendix

6.6.1 Size of the nanodroplets

To investigate the influence of high concentration of protons on the properties of the nanodroplets we record the isotropic transient absorption spectra of neat water nanodroplets and acidic water nanodroplets following the excitation at 3400 cm^{-1} (Figure 6.5A,B). These spectra represent the vibrational dynamics of water molecules which are not bound to proton and therefore absorb at high frequency. At short delay times the spectra we

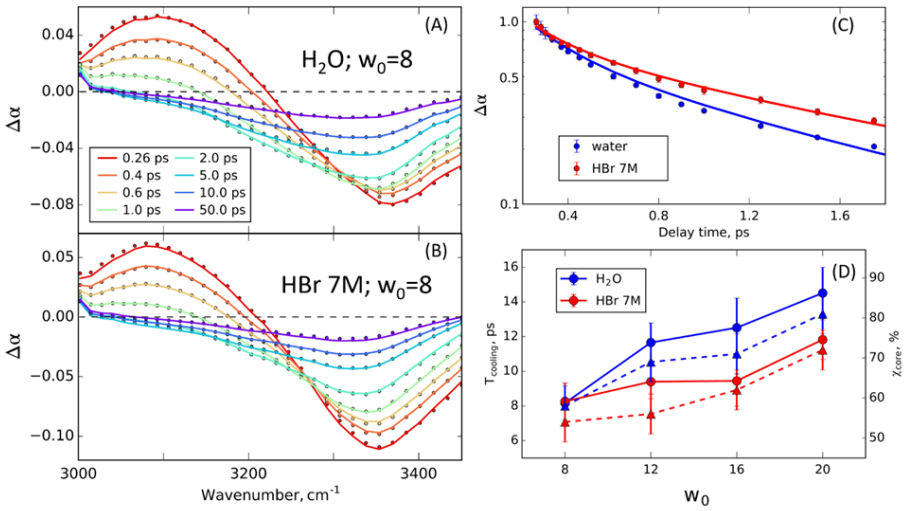

Figure 6.5: Isotropic pump-probe spectra of neat water nanodroplets (A) and acidic water nanodroplets (B) following the excitation at 3400 cm^{-1}; lines are the result of the fit. (C) Normalized delay time dynamics of the signal dominated by the excited state relaxation in logarithmic scale; lines are the result of the fit. (D) Dependence of the effective nanodroplet cooling time (circles) and the fraction of the core water molecules (triangles) on w_0.

observe a negative absorption change above 3200 cm^{-1} due to bleaching of fundamental v=0→1 transition and a positive absorption change at lower frequency corresponding to v=1→2 excited state absorption.

After 2 ps the low frequency positive absorption change disappears indicating the complete vibrational relaxation of the excited water molecules. From this delay time the vibrational energy is completely transferred to heat energy and the transient spectrum represents the so-called hot ground state of water molecules. In this state the water molecules' hydrogen bonds weaken, that decreases the OH-stretch cross-section and blueshifts the absorption spectrum. The hot ground state spectrum slowly decays due to the dissipation of heat to the surfactant molecules and the oil phase. After 50 ps the transient spectrum stays constant due to the equilibrium heat distribution over the phases.

In Figure 6.5C we show the dynamics of the transient signal at the frequency 3450 cm^{-1}, where the hot ground state contribution is nearly zero. This signal directly represents the excited state relaxation dynamics. We observe that the decay of the signal is clearly non-exponential and requires at least two components to fit. This non-exponential relaxation dynamics have been widely studied for neat[125,137] and isotopically

diluted[27,28,116] water nanodroplets stabilized by different surfactants. It originates from the difference of water properties in the central core of the nanodroplet and in its surface. Due to the incredibly large concentration of bromide ions the excited water molecules in and near the Stern layer of the reverse micelle relax much slower. It was shown that the excited OH-stretch vibrations of anion-bound HDO molecules in the interface of the CTAB reverse micelle relax 5 times slower than the vibrations of the molecules in the central core.[137]

To fit the vibrational relaxation dynamics, taking into account the two types of water molecules in the nanodroplet, we employed the kinetic model developed by Cringus et al.[125] for AOT reverse micelles. In this model the excited core water molecules relax with the time constant close to that of bulk water (0.27 ps) to the dark intermediate state, which subsequently populates the hot ground state. The heat is then dissipated to the surfactant and the oil phase with an effective cooling time constant $T_{cooling}$. The excited interface water molecules relax slower (T_1=0.85 ps). Following the relaxation the heat energy is transferred directly to the surfactant molecules. The latter was reasoned by the independence of the heat growth dynamics on the size of the nanodroplet and, therefore, the fraction of interfacial water, which is also observed in the present case.

For both the neat and acidic water nanodroplets of different size we find the vibrational relaxation time constants of 0.24$\pm$0.03 ps and 1.0$\pm$0.1 ps for core and interfacial water molecules respectively. The identical vibrational relaxation rates in the neat water and acidic water nanodroplets indicate, that even with a high concentration of the strong acid the microemulsion consists of nanodroplets of the same nature and the properties of water confined in nanodroplets are the same.

Together with the relaxation time constants, we also extract from the fit the effective cooling time constants and the fractions of the core water (Figure 6.5D). These parameters are known to be well correlated with the size of the water nanodroplets.[115,124,125] Both the cooling time and the core water fraction increase with increase of the nanodroplet size.

First, we obtain the relation between w_0 and the reverse micelle diameter for the system without HBr using the formula[121]

$$d_w = \frac{6v_w}{a_{CTAB} + a_{ROH} \cdot P_0 P_{mic}} w_0 \tag{6.1}$$

where v_w is the molecular volume of water, a_{CTAB} and a_{ROH} – the headgroups' surface area of CTAB and alcohol molecules, respectively, P_0 is alcohol/CTAB total mole ratio and P_{mic} is the alcohol partition constant between the micellar phase and the continuous phase (the product $P_0 P_{mic}$ gives the alcohol/CTAB ratio in the micelle). The molecular parameters for CTAB, hexanol and water were taken from ref. 121 and the value of the partition constant for n-hexanol was obtained from ref. 122. It results in a relation $d_w = 0.26 \times w_0$ (nm).

Relating the fraction of the core water molecules to the known diameters of the correspondent nanodroplets we calculate the thickness of the interfacial water layer of 0.19±0.03 nm (assuming spherical shape of the nanodroplets). Using this value we obtain the diameters of the acidic water nanodroplets d_w=2.0; 2.1; 2.6; 3.6 (versus 2.1; 3.1; 4.2; 5.2 for neat water) for w_0=8; 12; 16; 20. Thus, with addition of a high concentration of strong acid to water/CTAB/hexanol/hexane microemulsion we apparently create smaller nanodroplets.

The ratio between the core and interfacial water is not a very reliable parameter when we compare the nanodroplets of different content. Protons added to the nanodroplet with positively charged interface will mostly locate in the center of the water pool.[143,144] This will reduce the number of water molecules in the core which absorb at 3400 cm^{-1}, therefore, resulting in underestimation of the core fraction. On the other hand, increased ionic strength in the water pool due to H^+ and Br^- ions can make the interfacial Stern layer thinner with higher density of bromide-ions.[145] In the estimation of the nanodroplet radius these two factors counteract and may cancel out, however, precise calculation of these two contributions requires radial distribution functions of all the components of the nanodroplet.

A complementary parameter to estimate the size of the nanodroplet is its cooling time.5,10,15 This parameter depends mostly on the thermal diffusivity of the non-polar phase, which remains constant. Approximating $T_{cooling}(d_w)$ dependence for the neat water nanodroplets with a linear function and applying it to the acidic water nanodroplets we obtain the diameters of 1.7; 2.3; 2.3; 3.8 nm. Thus, from the two parameters (core fraction and cooling time) we estimate the diameter of the acidic water nanodroplets to be 1.4±0.2 times smaller than the diameter of the neat water nanodroplets of the same w_0.

6.6.2 Additional anisotropy measurements

In Figure 6.6 the anisotropy dynamics measured around 3400 cm^{-1}. This anisotropy is nearly zero, which indicates that the OH groups in the outer hydration shell of proton have no net orientation with respect to the excited OH vibration in the core of the proton hydration structure.

In Figure 6.7A we show the anisotropy dynamics of the signal at 2600 cm^{-1} signal measured for bulk HBr solutions with concentrations varied from 0.5 to 7 M. The anisotropy dynamics is nonexponential, but can be well fitted with an exponent with a small offset of 10-20% from the initial value. From the fit we extract an effective time constant of 1.6±0.2 ps independent of the proton concentration (Figure 6.7B). This value is consistent with the previously found ∼2 ps time constant for the anisotropy decay of the hydrated proton bending vibration in HCl solutions.[25]

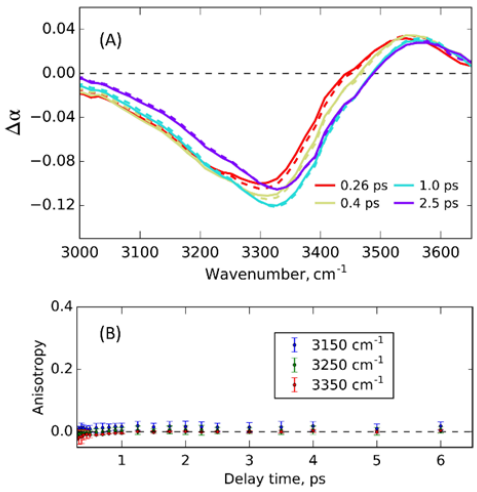

Figure 6.6: (A) Transient spectra of reverse micelles with w_0=12 system following excitation at 2600 cm^{-1}, recorded with parallel (solid) and perpendicular (dashed) polarizations of the detection pulse with respect to the excitation pulse. (B) The resulting anisotropy measured at frequencies 3150-3350 cm^{-1}.

In Figure 6.7C,D we compare the anisotropy dynamics measured for nanodroplets with 3 M HBr. The results of these experiments are similar to those of the 7 M solution, but with a smaller signal-to-noise ratio. It implies that the proton hopping rate in CTAB reverse micelles is independent of HBr concentration (as it is also found for bulk solutions).

6.6.3 Impact of the protonated hexanol molecules on the measured anisotropy

The anisotropy measured for the smallest nanodroplets with w_0=8 and w_0=12 does not show any decay within the accessible time window of ∼6 picoseconds (Figure 6.8). For w_0=8 nanodroplets we even observe a small increase of the anisotropy, which indicates the presence of at least two anisotropic components of the signal, of which the longer living component has higher anisotropy. The fact that this rise is observed only for reverse micelles with little water content, indicates that it may be the result of partial protonation of hexanol molecules.

In Figure 6.9A we show the linear infrared absorption spectrum of protonated hexanol molecules in the frequency region of interest. It is seen that protonated hexanol can

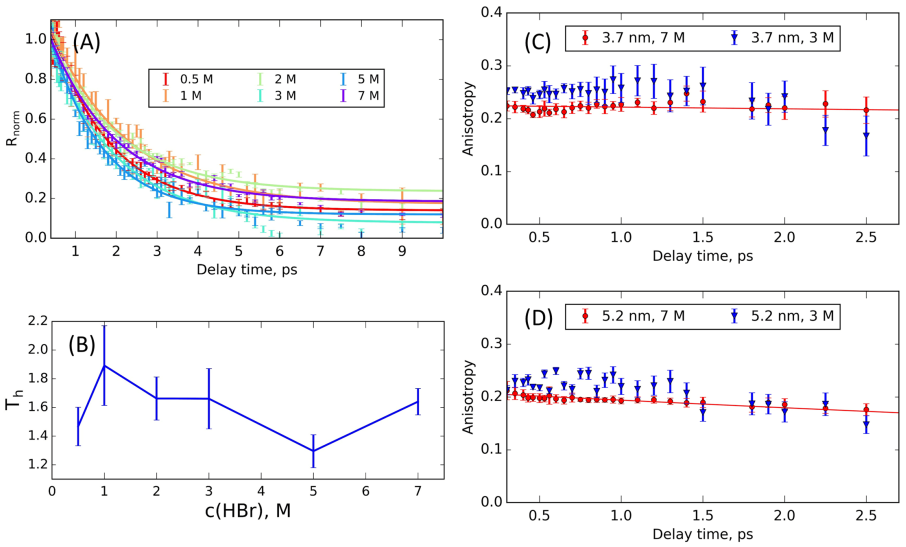

Figure 6.7: (A) Normalized anisotropy of the transient signal at 2600 cm^{-1} as a function of delay time for different concentrations of HBr. (B) Proton hopping times as a function of concentration HBr extracted from the fit of the anisotropy dynamics. (C, D) Comparison of the anisotropy measured for nanodroplets with diameter 3.7 nm (C) and 5.3 nm (D) containing 7 M HBr and 3 M HBr solution.

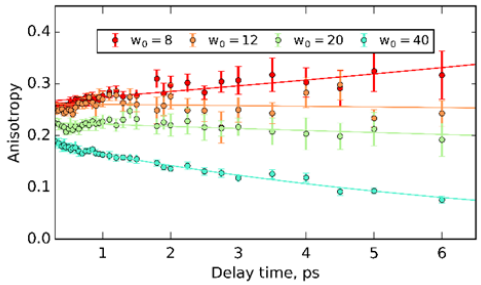

Figure 6.8: Comparison of anisotropy dynamics for acidic water nanodroplets with w_0=8, 12, 20 and 40.

indeed absorb in this frequency region and, therefore, can be excited by the pump pulse.

In general, presence of protons at the positively charged surface of CTAB-stabilized nanodroplets is highly unlikely.[119,143,144] Nevertheless, in the smallest micelles, which contain only about twice more water molecules than hexanol, a significant fraction of protons can be attached to hexanol. Comparing the normalized transient absorption spectra for

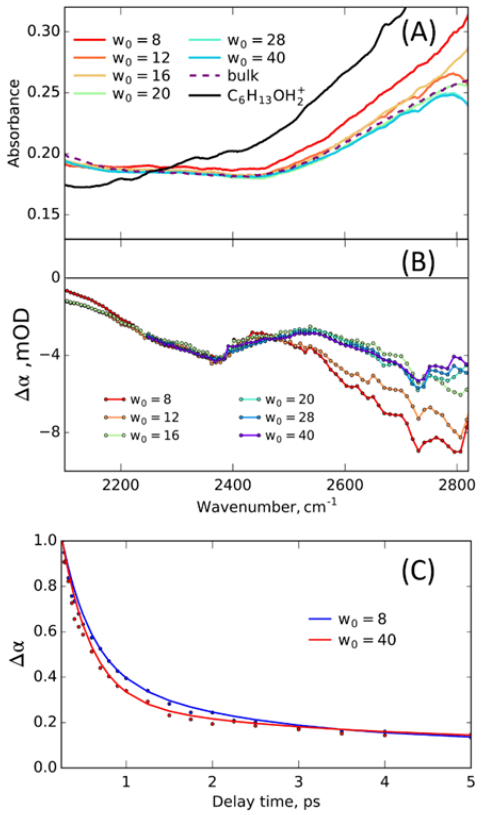

Figure 6.9: (A) Comparison of the linear infrared spectrum of protonated hexanol in mixture with triflic acid. (B) Transient absorption spectra at 0.26 ps delay time following the excitation at 2600 cm^{-1} for different nanodroplets; spectra are normalized with respect to 2350 cm^{-1} band. (C) Normalized transient absorption dynamics of the signal at 2600 cm^{-1} for w_0=8 and w_0=40 nanodroplets.

different nanodroplets (Figure 6.9B) we find that the slope above 2500 cm^{-1} becomes steeper for small nanodroplets with w_0=8 and w_0=12, similar to what is observed in the linear absorption spectra. We do not observe any difference between the transient spectra for the larger nanodroplets. Thus, we assign the additional rise of the transient absorption signal and the absorption of the linear spectrum of w_0=8 nanodroplets to a contribution of protonated hexanol molecules.

For the protonated hexanol molecules to create a rise of the anisotropy of the overall transient absorption signal, their contribution to the signal should relax slower and possess a higher associated anisotropy. As we see from the dynamics of the isotropic signal

at 2600 cm^{-1} (Figure 6.9C), the signal indeed decays slower for the small nanodroplet, for which a significant part originates from protonated hexanol. Since protonated hexanol $C_6H_{13}OH_2^+$ possesses only two OH groups that donate strong hydrogen bonds, whereas H_3O^+ possesses three of these OH groups, the OH-stretch vibrations of protonated hexanol are expected to be less degenerate than those of the hydrated proton. As a result, the anisotropy of the signal of protonated hexanol molecules will be higher than that of the hydrated protons in the core of the nanodroplet and can create a rise of the total anisotropy, provided that this signal also lives longer. Apparently, already at w_0=16, when the number of water molecules in the nanodroplet is about 5 times larger than the number of hexanol molecules, the contribution and effect of protonated hexanol molecules becomes negligible.

Published as:

O.O. Sofronov, H.J. Bakker. Nature of hydrated proton vibrations revealed by nonlinear spectroscopy of acid water nanodroplets. Physical Chemistry Chemical Physics 2020, 22, pp. 21334 - 21339

7

Vibrations of Hydrated Protons in Reverse Micelles

Abstract

We use polarization-resolved femtosecond pump-probe spectroscopy to investigate the vibrations of hydrated protons in anionic (AOT) and cationic (CTAB/hexanol) reverse micelles in the frequency range 2000-3500 cm^{-1}. For small AOT micelles the dominant proton hydration structure consists of H_3O^+ with two OH groups donating hydrogen bonds to water molecules, and one OH group donating a weaker hydrogen bond to sulfonate. For cationic reverse micelles, we find that the absorption at frequencies >2500 cm^{-1} is dominated by asymmetric proton-hydration structures in which one of the OH groups of H_3O^+ is more weakly hydrogen-bonded to water than the other two OH groups.

7.1 Introduction

In aqueous solution, the proton (H^+) exists in the form of extended dynamic hydration structures. These hydration structures rapidly interconvert, thus facilitating fast diffusion of the proton charge.[9,11,13] Multiple experimental and theoretical studies conclude that the preferential proton hydration structure is a distorted $H_3O^+(H_2O)_3$ Eigen[11,13,15,16] or $H_5O_2^+$ Zundel[17,18,23,146] cation, or an intermediate structure showing both Eigen and Zundel character[21,22,37,38,48]. Which of these hydration structures is predominantly present in aqueous media, is still under debate.

To obtain the pure spectrum of the hydrated proton in aqueous solution one would have to subtract the spectral response of water molecules that are not participating in proton hydration. Unfortunately, it is not possible to determine the absorption spectrum of the hydrated proton without any ambiguity because the fraction of water molecules that is not affected by proton charge is not precisely known. By subtracting the maximum possible amplitude of the water spectrum without the appearance of negative signals, we obtain the infrared spectrum shown in Figure 7.1A, that forms an approximation of the infrared spectrum of the hydrated proton.

The infrared absorption spectrum of the hydrated proton in aqueous solution (black line in Figure 7.1A) shows a broad absorption continuum at frequencies $<$3000 cm^{-1}. Most of the studies assign the high frequency part ($>$2000 cm^{-1}) of this continuum to the OH-stretch vibrations of the hydrated proton, the band centered at $\sim$1750 cm^{-1} to the bending vibrations of the hydrated proton, and the broad band at 1200 cm^{-1} to the proton transfer mode – i.e. the shuttling vibration of the central proton in a Zundel-type $H_5O_2^+$ configuration.[15,18,22,33]

The OH-stretch absorption appears as a nearly flat signal in the frequency range of 2000-2500 cm^{-1} and a broad band at higher frequency with a maximum at $\sim$3000 cm^{-1}. Studies of small protonated water clusters show that the OH-stretch vibrations of strongly hydrogen bonded OH-groups are shifted to lower frequencies with respect to the OH stretch vibrations of water molecules.[40,42,45] When the positive charge resides on a hydrogen atom, the corresponding OH-group becomes more polar, which increases the hydrogen-bond interaction and leads to a shift of the OH-stretch vibration to lower frequency. Hence, one of the possible interpretations of the extremely broad OH-stretch spectrum of hydrated protons is that this spectrum results from the existence of a large variety of (transient) structures with different geometries and charge distributions.

In this Chapter we study the vibrational spectrum and the structure of hydrated protons in water nanodroplets of reverse micelles. Reverse micelles are widely used as nanoreactors for proton-mediated processes, such as acid catalyzed polymerization.[147–149] Besides this, reverse micelles have important advantages for a femtosecond infrared spectroscopic study of proton solvation in liquid water. First, they allow the preparation of

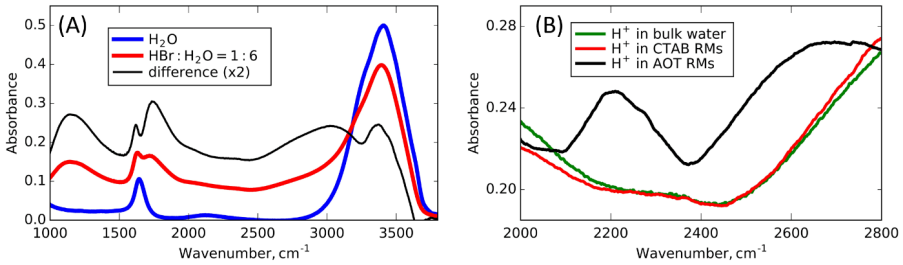

Figure 7.1: (A) Fourier-transform infrared spectra of neat water (blue), HBr solution (red) and their weighted difference (black). (B) Zoomed in spectra of the hydrated proton in bulk aqueous solution (green) and in CTAB (red) and AOT (black) reverse micelles.

samples with an overall low water concentration, which is useful in view of the strong absorption of the molecular vibrations of water. At the same time, the spectroscopic properties of water in nanodroplets are more similar to those in bulk water, than the properties of isolated water molecules or small water clusters. Second, the nonpolar solvent, which forms the continuous phase of the microemulsion, can act as a heat bath that accepts the energy dumped in the sample by exciting the water molecules in the reverse micelles with a laser pulse. This energy uptake by the nonpolar solvent reduces the signal contribution of the isotropic response of the heating of water. All these factors make reverse micelles a favorable system to study the vibrational spectrum of hydrated protons.

The drawback of reverse micelles as a model system to study the vibrational response of hydrated protons is that the solvation of chemical species and the dynamics of chemical processes can be different from bulk solutions. This difference can originate either from the special solvent properties of the confined water or from specific interactions with the molecular groups of the surfactant molecules located at the surface of the water nanodroplet.[29,150]

In Figure 7.1B we show the linear infrared absorption spectrum of hydrated protons in anionic (AOT as surfactant) and cationic (CTAB as surfactant) reverse micelles, in the frequency range 2000-2800 cm^{-1}. The infrared spectrum of hydrated protons in cationic reverse micelles resembles closely the spectrum of hydrated protons in bulk water, probably because the protons are repelled by the positive charges of the surfactant, with the result that the protons reside predominantly in the bulk-like core of the water nanodroplet. For the anionic reverse micelles we observe a strong additional absorption band at $\sim$2200 cm^{-1}. Interestingly, the absorption spectrum of the cationic reverse micelles and bulk water also shows the presence of a weak absorption band at $\sim$2350 cm^{-1}. This band is not an artifact of the subtraction procedure. In fact, a strong band near this frequency

has been observed by Fournier et al. in a two-dimensional infrared (2D-IR) spectroscopic study of aqueous HCl solutions.[23]

A highly suitable technique to study the structure and dynamics of hydrated protons in different environments is femtosecond nonlinear vibrational spectroscopy. This technique has been used to study the vibrational relaxation dynamics of the bending and OH-stretch vibrations of small protonated water clusters in polar solvents (acetonitrile[72,76,151] and dimethyl sulfoxide[152]). These studies showed that the vibrationally excited states of proton hydration structures relax with a time constant T_1 <100 fs, leading to ultrafast heating of the direct environment of the proton. The vibrational relaxation is followed by a slower process in which the heat is redistributed over the solution.

Femtosecond nonlinear vibrational spectroscopy has also been used to study the OH-stretch vibrations of the asymmetric Zundel-cation in water, in particular to investigate the properties of the proton transfer mode.[18,23] It was shown that the experimental data can be well explained with an asymmetric quartic potential for this vibration. Fournier et al.[23] used polarization-resolved femtosecond nonlinear vibrational spectroscopy to study the orientation of hydrated proton bending modes with respect to the proton transfer mode and the OH-stretch modes. In another study[25] the anisotropy dynamics of the bending modes of the hydrated proton were measured, and used to estimate the proton transfer time in water. Recently, we used single-color polarization-resolved femtosecond nonlinear vibrational spectroscopy to study the OH-stretch vibrations of hydrated protons in nanoconfined aqueous environments[153] We observed that nanoconfinement leads to a strong slowing down of aqueous proton transfer.

Here we use two-color polarization-resolved femtosecond nonlinear vibrational spectroscopy infrared (fs-IR) pump-probe spectroscopy to investigate the structure-spectrum relation of the OH-stretch vibrations of proton solvation structures in liquid water. We perform these experiments for protons in reverse micelles (microemulsions), i.e. water nanodroplets in an apolar solvent that are stabilized by anionic (AOT) and cationic (CTAB/hexanol) surfactants.

7.2 Experiment

Linear mid-infrared absorption spectra were obtained in transmission mode using a commercial Fourier transform spectrometer (Bruker Vertex 80v). The two-color mid-IR pump-probe experiments were performed as described in the section 3.2. To perform anisotropy analysis we average the data measured at different frequencies around 2250, 2300 or 2600 cm^{-1} (15 pixels, $\pm$50 cm^{-1} from the central frequency, the error bars of the datapoints represent the standard deviation of the anisotropy over different pixels). The averaged data were fit by exponential functions from 0.4 ps to 2.5 ps (AOT reverse micelles) or to

5 ps (CTAB reverse micelles). From the fits we also extract the anisotropy value R_0 at zero delay time.

All used chemicals were purchased from Sigma-Aldrich. Cationic nanodroplets were prepared as described in Chapter 6. Cetyltrimethylammonium bromide (CTAB) and 1-hexanol (99%, anhydrous) were dissolved in n-hexane (99%, anhydrous) at concentrations of 0.11 M and 0.61 M, which yields a ratio [hexanol]:[CTAB]=3:1 in the micellar phase. By adding water (ultrapure milli-Q grade) and hydrobromic acid (HBr, 48%) we varied the hydration ratio w_0=([H_2O]+[HBr])/[CTAB] from 8 to 40 with a constant HBr concentration of 7 M in the aqueous phase. This procedure yields nearly spherical nanodroplets with a water pool diameter $d_w = 0.19 \times w_0$. Anionic microemulsions were prepared by dissolving sodium dioctylsulfosuccinate (AOT, 99%) in carbon tetrachloride (CCl_4, 99.5%, anhydrous) at a concentration of 0.5 M. Water and perchloric acid ($HClO_4$, 70%) were added to achieve a ratio w_0=([H_2O]+[$HClO_4$])/[AOT] ranging from 1 to 3 and a $HClO_4$ concentrations in aqueous phase of 7.2 M (w_0=1; 1.5; 2) or 4.8 M (w_0=2; 2.5; 3). These mixtures were kept in an ultrasonic bath for 1.5 hour to completely equilibrate the microemulsions, as evidenced by their complete transparency. We could not equilibrate anionic microemulsions with w_0 >3 or containing other acids (HBr, HCl, CF_3SO_3H), even when the acid concentrations was lowered to 3 M. In Chapter 6 we investigated the effect of the acid concentration on the anisotropy dynamics of the hydrated proton for solutions of HBr in water, and found that the concentration does not lead to significant changes in these dynamics within a concentration range 0.5-7 M. This finding implies that in this concentration range the anion Br^- has very little effect on the spectral response and transfer dynamics of the hydrated protons. Because of the relatively low vibrational cross-sections of hydrated protons, it is not possible to measure the vibrational spectrum of hydrated protons in aqueous solution at much lower concentrations.

The AOT microemulsions were stable for 4-7 days after preparation. After that time the nanodroplets were observed to aggregate and the mixtures became opaque. All the measurements on AOT microemulsions were thus done within two days after their preparation. In both the FTIR and the pump-probe measurements, the samples were kept between two 2 mm thick calcium fluoride (CaF_2) windows, separated by a 50-200 m PTFE spacer.

We estimated the diameter of the AOT-stabilized nanodroplets by measuring the vibrational relaxation of the water OH-stretch vibrations. It yielded the diameters 1.1, 1.5 and 1.8 nm for w_0=1, 2 and 3, respectively (for details see Appendix, section 7.6.1).

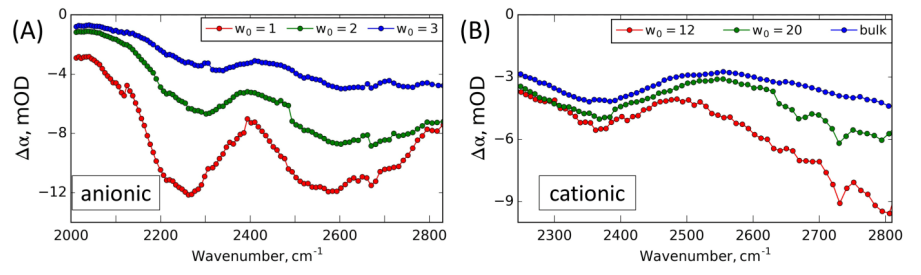

Figure 7.2: Isotropic transient absorption spectra of hydrated protons (A) in anionic reverse micelles and (B) in cationic reverse micelles and in bulk aqueous solution. Excitation frequency ν_{ex}=2600 cm^{-1}, pump-probe delay time T$_w$=0.3 ps; the spectra are scaled for better comparison.

7.3 Results

In our pump-probe experiments we excite OH-stretch vibrations of the proton hydration structures with an intense mid-infrared pulse. The excited stretch vibrations of OH-groups that carry a significant amount of the proton charge relax on sub-100 fs time scale by transferring the vibrational energy to the adjacent hydrogen bonds.[25,72,76,151] This process results in a "locally hot state", in which the hydrogen bonds in the local proton hydration structure are weakened due to the dumped energy, similarly to the effect of thermal heating. This non-equilibrium state typically persists for picoseconds before the excess energy is equilibrated over a bigger volume. The locally hot state has an absorption spectrum different from that of the hydrated protons in the equilibrium state. We measure this absorption change with a weaker probe pulse delayed in time.

In Figure 7.2 we show the isotropic transient absorption spectra for hydrated protons in anionic (A) and cationic (B) reverse micelles of different size following the excitation at 2600 cm^{-1}. At this frequency we only excite OH-stretch vibrations in the core of the hydrated proton and not those of water molecules outside this core. In the frequency region of 2000-2800 cm^{-1} the transient spectra consist of a broad negative absorption change (for the details see Figures 7.6-7.8 of Appendix).

The transient spectrum of the hydrated protons confined in anionic micelles shows two strong bands centered at ∼2250 cm^{-1} and ∼2600 cm^{-1}, which resemble the structure of the linear infrared spectrum of anionic micelles (Figure 7.1B). For the hydrated protons in cationic micelles we observe a similar absorption spectrum. It can be also subdivided into two signatures: a band at ∼2350 cm^{-1} and a slope at higher frequency (>2500 cm^{-1}), which is the low-frequency tail of an intense band at frequency >2800 cm^{-1}.

For hydrated protons in anionic reverse micelles there is a clear gradual change in the

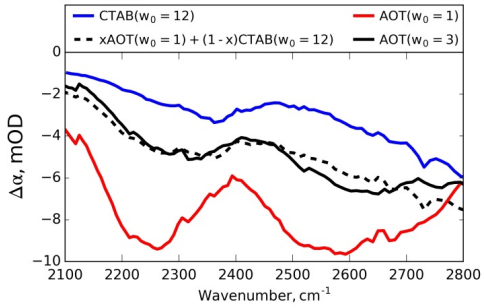

Figure 7.3: Transient spectra of hydrated protons in small anionic reverse micelles (red line) and in cationic reverse micelles (blue line), the weighted sum of these two spectra (black dashed line) and the transient spectrum of hydrated protons in large anionic reverse micelles (black solid line).

transient spectra with the increase of water content. The low-frequency band shifts from $\sim$2250 cm^{-1} to $\sim$2350 cm^{-1}, and the high-frequency band grows with respect to the low-frequency band. These spectral changes can result from different possible localization of the hydrated protons in the water pool.

In AOT-stabilized water nanodroplets protons can be solvated both in the core of the water pool and at the water-AOT interface. The sulfonate group of the AOT surfactant is negatively charged and thus a substantial fraction of the protons will be solvated in the vicinity of the sulfonate groups and/or substitute the sodium cations in the Stern layer.[117,119] For small micelles (w_0=1) all protons are inevitably located close to sulfonate groups of the AOT surfactant. With increasing micelle size the probability for protons to be hydrated in the center core of the nanodroplet increases.

We find that the transient spectrum of the larger anionic reverse micelles (w_0=3) can be constructed as a weighted sum of the transient spectrum of the smallest anionic reverse micelles with w_0=1 and that of the cationic reverse micelles of similar size (Figure 7.3), reflecting that in large anionic micelles a fraction of the protons is close to, and strongly interacting with the AOT surfactants, while another fraction is located in the center core of the water nanodroplet. This result demonstrates that the spectroscopic response of hydrated protons in the center of the anionic reverse micelles resembles that of hydrated protons in cationic reverse micelles.

The transient absorption spectrum of small AOT reverse micelles shows great similarity with the linear infrared spectra of concentrated solutions of ethanesulfonic acid (Figure 7.9). From this similarity we conclude that the two bands at 2250 cm^{-1} and 2600 cm^{-1} can be assigned to a heteromolecular proton solvation complex. This complex can be seen as a contact ion pair [RSO_3^-–$H_3O^+(H_2O)_n$], in which the proton charge is shared by water molecules and an anionic sulfonate group. Raman[154] and NMR[155] exper-

iments suggest that the basicity of alkanesulfonates in solution is similar to that of water. Hence, we expect that in the solvation complex [RSO_3^-–$H_3O^+(H_2O)_n$] the proton will be delocalized over the water molecules and the sulfonate group. The infrared spectra of concentrated ethanesulfonic acid solutions (Figure 7.10) show that at a concentration ratio $EtSO_3H$:H_2O=1:1 about 85% of the acid is deprotonated, which indicates that the water molecules have a slightly stronger basicity than the ethanesulfonate anion. Thus, we expect that in [RSO_3^-–$H_3O^+(H_2O)_n$] complexes the proton charge is mostly delocalized over the water molecules.

In Figure 7.4 we present the anisotropy of the transient absorption signal for anionic and cationic reverse micelles as a function of micelle size. For cationic reverse micelles the anisotropy at 2300 and 2600 cm^{-1} becomes lower with increasing micelle size. This trend agrees with the facts that for bulk acid solutions the anisotropy value is lower ($\sim$0.15 at 2600 cm^{-1} [153]), and that the core of the nanodroplet is expected to become increasingly bulk-like with increasing micelle size. For the anionic reverse micelles the anisotropy is low for the smallest reverse micelle with w_0=1, and increases with the size of the nanodroplet. This latter trend can be explained from the increasing contribution of the signal from the protons in the center core of the nanodroplet. As illustrated in Figure 7.3, the signal of the anionic reversed micelles becomes increasingly similar to that of cationic reverse micelles with increase reverse micelle size.

The anisotropy represents the average relative orientation of the probed vibration with respect to the excited vibration. Here we see that the excitation at $\sim$2600 cm^{-1} results in different anisotropy values at 2300 and 2600 cm^{-1}, both in anionic and cationic reverse micelles, which implies that different vibrations with differently oriented transition dipole moments are being probed.

When pumping and probing at the same frequency, the initial anisotropy value R_0 represents the degeneracy of the vibration. For a non-degenerate vibration, the initial anisotropy value is 0.4. The fact that we observe lower initial anisotropy values indicates that the probed vibrations possess a certain degree of degeneracy.[153] The anisotropy is observed to be lower for low-frequency vibrations, indicating that the lower-frequency vibrations are more degenerate than the higher-frequency vibrations.

For the cationic reverse micelles the anisotropy is independent of the excitation frequency and is determined only by the degeneracy of the probed vibration. This is a consequence of the very weak absorption of the 2350 cm^{-1} band in the infrared spectrum. A pump pulse centered at 2300 cm^{-1} thus mostly excites higher frequency vibrations centered at 2800-3000 cm^{-1}. The relatively high anisotropy value of the transient absorption signal probed at 2600 cm^{-1} indicates that a large fraction of these high-frequency vibrations is quite well localized on a single OH-group.

For the anionic reverse micelles (Figure 7.4B) we observe the lowest anisotropy for ν_{ex}=2250 cm^{-1} and ν_{pr}=2250 cm^{-1}, and the highest anisotropy for ν_{ex}=2600 cm^{-1} and

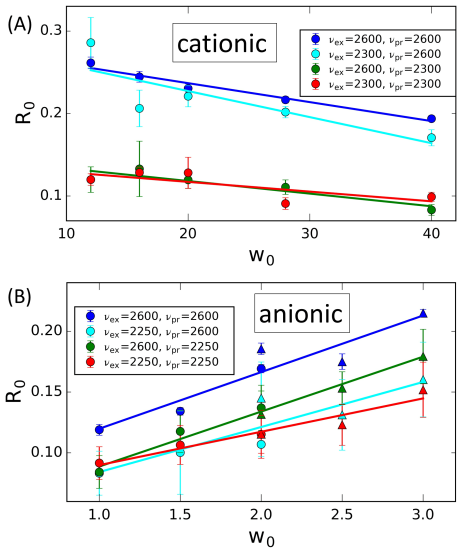

Figure 7.4: Anisotropy of the low frequency band and the high frequency band following the excitation of each of them measured for cationic (A) and anionic (B) reverse micelles. The size of a CTAB cationic micelle with w_0=12 is approximately the same as that of an AOT anionic micelle with w_0=3.

ν_{pr}=2600 cm^{-1}. In this case the absorption bands of the low- and high-frequency vibration are of approximately equal strength, and the signal at each of the excitation/probing frequencies of 2250 and 2600 cm^{-1} will contain contributions of both bands. The highest anisotropy is thus observed when the less degenerate vibration with its absorption band centered at 2600 cm^{-1} is both excited and probed.

7.4 Discussion

The interpretation of the transient spectra of protons in cationic and anionic reverse micelles is aided by the comparison with infrared photodisocciation (IRPD) spectra of small hydrated proton clusters at low temperatures. This comparison should be carried out with some care, as the vibrational frequencies of hydrated protons in liquid water are subject to fast fluctuations of significant amplitude that result in a strong broadening of the vibrational bands compared to what is observed for small clusters at low temperatures. However, it has been observed that the vibrational spectra of hydrated proton clusters show distinct structures that strongly depend on the hydrogen-bond structure of the first

hydration shell.[42] Hence, if the liquid phase spectrum shows characteristic features that agree with the observations for particular hydrated proton clusters, it appears quite likely that the first hydration shell in the liquid phase possesses a similar structure as those clusters.

IRPD experiments on protonated water clusters showed that in a perfectly symmetric $D_3O^+(D_2O)_3$ structure, the absorption bands of the three OD-stretch vibrations of the central D_3O^+ moiety overlap, constituting a single broad absorption band.[42] Addition of a hydrogen-bond accepting molecule to one of the D_2O molecules of the cluster makes this molecule a stronger hydrogen bond acceptor, thus distorting the C_{3v} symmetrical structure and resulting in a split of the single broad OD-stretch band of D_3O^+.[42,44,45,95]

A similar split of the OH absorption band of the H_3O^+ core is observed if one of the OH groups is more weakly hydrogen bonded than the other two OH groups. The limiting case of such an asymmetric structure is the protonated water trimer H_2O–H_3O^+–H_2O, in which two OH-groups of the H_3O^+ core are hydrogen bonded to H_2O molecules and one OH-group is non bonded. Such $H_7O_3^+$ structures were observed for hydrated super acids in crystals and in nonpolar solvents.[156–159]

These properties of asymmetric hydrated proton structures have been studied in detail in IRPD experiments on the protonated water trimer ($H_3O^+(H_2O)_2$),[40,160] pentamer ($H_3O^+(H_2O)_4$),[38,95] and hexamer ($H_3O^+(H_2O)_5$)[45]. For the pentamer $H_3O^+(H_2O)_4$ bands at $\sim$2600 cm^{-1} and $\sim$2800 cm^{-1} where the band at 2600 cm^{-1} is assigned to the near-degenerate symmetric and antisymmetric vibrations of the two relatively strongly hydrogen bonded OH-groups of H_3O^+, and the band at 2800 cm^{-1} is assigned to the stretch vibration of the less strongly hydrogen-bonded OH group.[?] Furthermore, it is observed that with increasing difference in hydrogen-bond strengths of the three OH groups of the central H_3O^+ ion, the band at 2600 cm^{-1} shifts to lower frequencies ($\sim$2400 cm^{-1} for $H_3O^+(H_2O)_5$ and 1900-2300 cm^{-1} for the extremely asymmetric $H_3O^+(H_2O)_2$), and the band at 2800 cm^{-1} shifts to higher frequencies ($\sim$3000 cm^{-1} for $H_3O^+(H_2O)_5$ and $\sim$3600 cm^{-1} for the free OH-group of $H_3O^+(H_2O)_2$).

The spectra of acid water in anionic and cationic micelles show similar spectral characteristics as the clusters. The spectra of protons in AOT reverse micelles contain two bands at 2250 cm^{-1} and 2600 cm^{-1}. The band at 2250 cm^{-1}, that the anisotropy measurements show to represent a more degenerate vibration, matches well with the bands at 1900-2600 cm^{-1} observed in IRPD experiments. Therefore, we assign this band to the degenerate symmetric and antisymmetric OH-stretch vibrations of two strongly hydrogen-bonded OH groups of the central H_3O^+ ion of the proton hydration structure. The band at 2600 cm^{-1}, that the anisotropy measurements show to represent a less degenerate vibration, can be assigned to the stretch vibration of the third, less strongly hydrogen-bonded OH group of the central H_3O^+ ion of the proton hydration structure.

For AOT micelles with low water content (low w_0), the asymmetry in the proton

hydration structures likely results from the interaction of the central H_3O^+ ion with sulfonate (SO_3^-) groups. In several theoretical calculations it was shown that the most favorable hydration structure of sulfonic acids is formed by the [RSO_3^-–$H_3O^+(H_2O)_2$] motif.[161–164] In this complex, the sulfonate group is a weaker hydrogen bond acceptor than the two H_2O molecules. Hence, the band at 2600 cm^{-1} can be assigned to the OH groups that is more weakly hydrogen bonded to sulfonate, and the band at 2250 cm^{-1} can be assigned to the two other OH-groups that are more strongly hydrogen bonded to water molecules. The degeneracy of the stretch vibrations of the strongly hydrogen-bonded OH groups results in a low anisotropy value of $\sim$0.1, in agreement with our observations for the low-frequency band. Due to the relatively high concentration of AOT molecules, most of which interact with sodium cations, the two water molecules accepting the two stronger hydrogen bonds from H_3O^+ most likely donate hydrogen bonds to sulfonate groups of other AOT molecules.

The proton hydration structures in cationic reverse micelles are also largely asymmetric, which is demonstrated by the relatively high anisotropy value of $\sim$0.25 observed at 2600 cm^{-1}. This high anisotropy value indicates that the absorption at frequencies $>$2500cm^{-1} is dominated by proton-hydration structures for which one of the three OH groups of the H_3O^+ core is more weakly hydrogen bonded than the other two OH groups.

We propose that the weak absorption band at 2350 cm^{-1} observed for acid cationic reverse micelles and acid bulk water originates from a (near-)symmetric [$H_3O^+(H_2O)_3$] complex. Replacing the SO_3^- group in the asymmetric [RSO_3^-–$H_3O^+(H_2O)_2$] complex by H_2O is thus proposed to lead to the merging of the two bands at 2250 cm^{-1} and 2600 cm^{-1} into a single band at 2350 cm^{-1}. This interpretation is supported by the observation that the anisotropy of the transient absorption signal at 2350 cm^{-1} has a value of $\sim$0.1 (Figure 7.4A), which is the value that would result from the complete randomization of a vibrational excitation in a plane. Hence, an anisotropy value of $\sim$0.1 corresponds well to the case of 3 near-degenate OH vibrations of a planar, symmetrically hydrogen-bonded H_3O^+ core.

It is clear from the linear infrared spectrum of acid cationic reverse micelles and acid bulk water that the band at 2350 cm^{-1} is relatively weak, which implies that only a small fraction of the proton hydration structures will be symmetric. Most of the proton-hydration structures in acid cationic reverse micelles and acid bulk water will thus be asymmetric, as illustrated by the strong absorption near 2800 cm^{-1}. The large abundance of asymmetric proton hydration structures can be explained from the fact that in the studied cationic reverse micelles and bulk water the proton hydration structures are surrounded by a large number of water molecules and counterions (second and third solvation shells), that show a large variation in composition and hydrogen-bond structure, thus inducing a large variation in the strengths of the hydrogen bonds of the three OH groups of the central H_3O^+ core.

7.5 Conclusions

In summary, we investigated the OH-stretch absorption spectrum of hydrated protons in cationic and anionic reverse micelles with linear infrared absorption spectroscopy and femtosecond transient absorption spectroscopy. The vibrational spectrum of hydrated protons in small anionic AOT reverse micelles shows two distinct bands at 2250 and 2600 cm^{-1}. These two bands correspond to two different vibrations of the same proton hydration structure. The anisotropy of the bands shows that the low-frequency vibration is more degenerate than the high frequency vibration. Comparing our results with the results of studies of small hydrated proton clusters and studies of hydrated sulfonic acids, we assign the two bands to OH stretch vibrations of the H_3O^+ core of a [RSO_3^-–$H_3O^+(H_2O)_2$] complex. The band at 2600 cm^{-1} is assigned to the stretch vibration of the OH group that is more weakly hydrogen bonded to sulfonate, and the band at band at 2250 cm^{-1} is assigned to the two other OH-groups that are more strongly hydrogen bonded to water molecules.

For acid cationic reverse micelles and acid bulk water we observe a weak band at 2350 cm^{-1}. We propose that this band corresponds to a symmetric [$H_3O^+(H_2O)_3$]. Hence, replacing the SO_3^- group by H_2O leads to the merging of the two bands at 2250 cm^{-1} and 2600 cm^{-1} into a single band at 2350 cm^{-1}. The symmetric complex constitutes only a minor fraction of the proton-hydration complexes in acid cationic reverse micelles and acid bulk water. Most of the complexes are asymmetric proton-hydration structures for which one of the three OH groups of the H_3O^+ core is more weakly hydrogen bonded than the other two OH groups.

7.6 Appendix

7.6.1 Size of the nanodroplets

The size of anionic reverse micelles may change upon the addition of acid, as we observed before for cationic reverse micelles (Chapter 6). To test this we performed pump-probe experiments for neat water nanodroplets and acidic water nanodroplets measuring the excited state relaxation dynamics of the water OH-stretch vibrations. The OH-stretch relaxation rate was shown to be dependent on the size of water/AOT reverse micelles and can thus be used to estimate the diameter of the nanodroplets.[104] In Figure 7.5A we show the transient absorption spectra for acidic water nanodroplet (w_0=1) following excitation at 3470 cm^{-1} (frequency of the maximum of the water OH-stretch absorption). At short delay times the spectra consist of a negative absorption change above ~3350

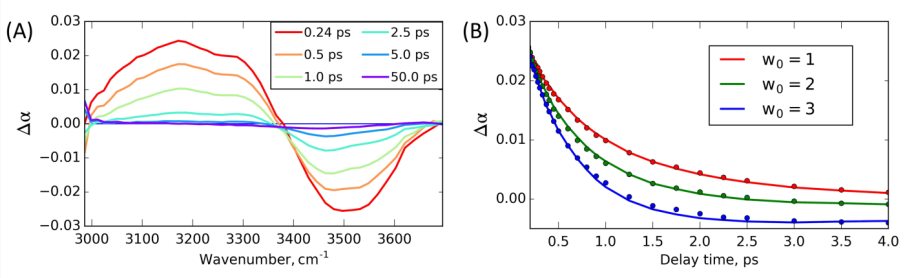

Figure 7.5: (A) Transient absorption spectra measured for the HClO4/water/AOT system with w_0=1 following the excitation at 3470 cm^{-1}. (B) Transient absorption dynamics probed at 3200 cm^{-1} for different acidic (dots) and neat water (lines) AOT reverse micelles.

cm^{-1} due to bleaching of the fundamental v=0→1 transition and a positive absorption change at lower frequency due to v=1→2 excited state absorption. At long delay times (>5 ps) the spectrum consists only of a negative absorption change at high frequency due to heating of water molecules following the vibrational relaxation. Subsequently, the heat is transferred to the surfactant molecules and oil phase, which results in a decrease of this heating signal.

The spectral dynamics at frequencies <3300 cm^{-1} is determined only by the vibrational relaxation of the excited OH-stretch vibrations, i.e. it represents the vibrational relaxation rate. In Figure 7.5B we compare the transient absorption dynamics at 3200 cm^{-1} for neat (lines) and acidic (dots) water nanodroplets of different w_0. We see that the vibrational relaxation becomes faster with increasing water content, which indicates that the size of the nanodroplets increases.[104] Also we observe that the relaxation rate in the acidic water nanodroplets is exactly the same as in the neat water nanodroplets of the same w_0. From this we conclude that the size of the nanodroplets does not change with the addition of acid. Using the results of earlier studies,[104,165] the diameters d_w of the water nanodroplets contained in AOT reverse micelles with w_0=1, 2, and 3, are 1.1, 1.5, and 1.8 nm, respectively. For cationic CTAB reverse micelles we have found that d_w=0.19×w_0, which implies that the CTAB/hexanol reverse micelle with w_0=12 will have approximately the same size (d_w=2.2 nm) as an AOT micelle with w_0=3.

7.6.2 Transient spectra of the hydrated protons in the anionic reverse micelles

In Figure 7.6 we show isotropic transient spectra at different pump-probe delay times following excitation the of OH-stretch vibrations of proton solvation structures at 2600 cm^{-1} for three different sizes of AOT reverse micelles. At all delay times the spectra

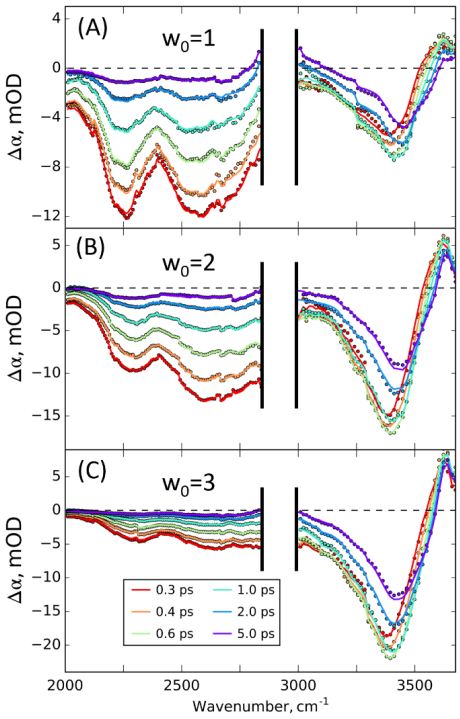

Figure 7.6: Isotropic transient spectra of acidic water AOT nanodroplets of different sizes following excitation with an intense mid-infrared pump pulse centered at 2600 cm^{-1}. The lines represent results of fits to the kinetic model described in the text.

show a broad negative absorption change in the frequency range from 2000 cm^{-1} to 3500 cm^{-1} and a small positive absorption change in the frequency range from 3500 cm^{-1} to 3600 cm^{-1}. The spectral region 2850-3000 cm^{-1} is not accessible due to strong absorption of the CH-stretch vibrations of the surfactant. The spectrum can be subdivided into two frequency regions: 2000-2850 cm^{-1} and 3000-3600 cm^{-1}. The low-frequency part of the spectrum represents the OH-stretch vibrations in the core of the hydrated proton, and the high-frequency part represents the response of the OH stretch vibrations of water molecules in the outer solvation shells of the proton, and of water molecules not interacting with protons.[151]

Due to nonresonant artifacts from the CaF_2 windows, we cannot determine the response of the OH vibrations at delay times <0.3 ps. To check if other transient spectral components appear at short delay times, we also measured pump-probe spectra of $HClO_4/H_2O/AOT/CCl_4$ systems using a sample cell with 500 nm thick silicon nitride

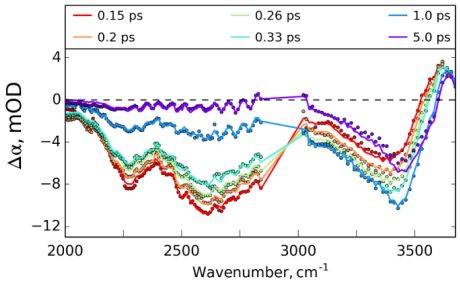

Figure 7.7: Isotropic transient spectra of acidic water AOT nanodroplets (w_0=2) following excitation with an intense mid-infrared pump pulse centered at 2600 cm^{-1} measured with silicon nitride sample cell.

membranes instead of calcium fluoride windows. Because of their small thickness, the nonresonant signal of these silicon nitride membrane at short delay times is negligibly small. Hence, the signal at early delay times will only show coherent artifacts due to the sample itself. This allows us to measure transient spectra at delay times down to 150 fs. As we see in Figure 7.7, the transient spectra in the range of 0.15-0.3 ps are qualitatively the same as the spectra shortly after 0.3 ps. The spectra contain oscillatory components between 2400 and 2800 cm^{-1} which are the result of the interference of the probe with probe light that is two times reflected by the ultrathin Si_3N_4 membrane of the sample cell.

In the 3000-3600 cm^{-1} spectral region we observe a fast growth of a negative band (until ∼0.6 ps) and a shift of this band to higher frequencies. These spectral dynamics can be explained from energy transfer from the core of the excited proton hydration structure to its outer shells. The OH-stretch vibrations of the hydrated proton excited by the pump pulse relax to the ground state within 100 fs by transferring their vibrational energy to low-frequency hydrogen-bond modes.[20,72] This process can corresponds to a strong heating of the local environment of the initially excited vibration. Subsequently, the excess energy equilibrates between the inner and outer solvation shells, which leads to the rise of a signal corresponding to the creation of hot water molecules in the outer hydration shells. These latter water molecules absorb at 3000-3600 cm^{-1} and due to the heating effect their absorption decreases, thus explaining the observation of a negative transient absorption signal in this frequency region.

We model the isotropic spectral dynamics with a three-level cascade model. The first state relaxes exponentially and populates the second state, which also relaxes exponentially to populate the third state. The extracted spectral components and the time constants are shown in Figure 7.8. The result of the fit is shown by the lines in Figure 7.6.

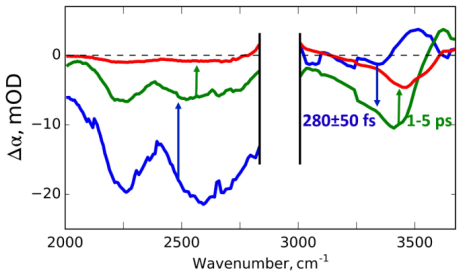

Figure 7.8: Transient spectral components extracted from the fit of transient spectra of w_0=1 nanodroplets. The component shown in blue converts into the component shown in green with time constant 280±50 fs, and the green subsequently converts into the spectrum shown in red with nonexponential picosecond dynamics.

We find that in the range of 0.3-5 ps the transient spectra can be well fit with this three state model. The dynamics of both the low- and high-frequency regions of the spectrum consist of fast and slow processes. In the high-frequency region we observe the growth of a negative absorption change with a time constant 280±50 fs. This signal also shifts to higher frequencies, which is captured by the positive band at 3500 cm^{-1} in the spectrum of the first state (blue). This fast frequency shift represents the energy equilibration between the inner and outer hydration shells of the hydrated proton. The time constant is very similar to the previously found time constant of energy equilibration in small protonated clusters (260±40 fs).[151] The second state (green) decays more slowly to the final thermal state. This decay is due to heat energy transfer from the water phase of the nanodroplet to the surfactant molecules and the oil phase. These dynamics are non-exponential and therefore cannot be precisely fitted with our model (see discrepancy between the fit and experimental data at 5 ps in Figure 7.6). The time constant of this slow process depends on the size of nanodroplet and the delay time range considered (up to 5 ps or 20 ps) and is typically in the range of 1-5 ps. Similar energy equilibration dynamics have also been observed for proton hydration structures in cationic reverse micelles (Chapter 6).

7.6.3 Proton solvation in solutions of ethanesulfonic acid

To further investigate the nature of the bands at 2250 and 2600 cm^{-1} in the transient spectra of anionic reverse micelles, we also studied concentrated solutions of ethanesulfonic acid ($EtSO_3H$) in water. Concentrated solutions of ethanesulfonic acid resemble the interface of AOT-stabilized nanodroplets having a high concentration of sulfonate groups, protons and hydrophobic groups. In Figure 7.9 we show FTIR spectra of solutions with

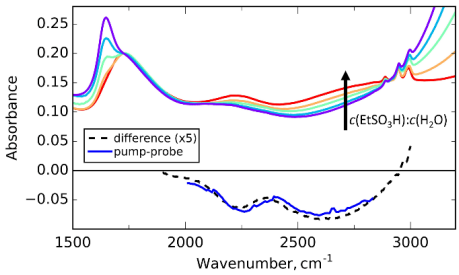

Figure 7.9: FTIR spectra of EtSO3H aqueous solutions with molar ratio c($EtSO_3H$) : c(H_2O) of 1:10; 1:8; 1:5; 1:3; 1:2 (colors from purple to red). The spectra are normalized with respect to the absorption of the bending vibration of hydrated proton at 1750 cm^{-1}. . The black dashed line represents the difference between the FTIR spectra of [1:3] and [1:2] solutions, and the blue line compare represents the early delay time pump-probe spectrum of protons solvated in w_0=1 AOT microemulsion.

different concentrations of $EtSO_3H$ normalized to the absorption at 1725 cm^{-1}, which is attributed to the OH-bending vibration of hydrated protons.

In these spectra we observe for all studied concentrations a broad continuous absorption in the 2000-3000 cm^{-1} frequency range. On top of this broad absorption we observe a band centered at ∼2250 cm^{-1} which disappears upon dilution of the acid. Already at a molar ratio $EtSO_3H$:H2O=1:2, ethanesulfonic acid is completely dissociated, as demonstrated by the vanishing of the $\nu_{as}(SO_2)$ and ν(S-O) absorption peaks at 1344 cm^{-1} and 904 cm^{-1} respectively6 (Figure 7.10). Hence, the 2250 cm^{-1} band cannot be assigned to the OH-stretch vibration of undissociated ethanesulfonic acid. This band cannot also be the result of hydrogen-bonded dimer formation, since dimers of $EtSO_3H$ would likely also be present in neat $EtSO_3H$, and the spectrum of neat $EtSO_3H$ does not contain this band. Instead, this band can be assigned to the OH stretch vibration of a hydrogen-bonded proton solvation structure involving a sulfonate group. The gradual decrease of the 2250 cm^{-1} absorption band with increasing acid dilution indicates that the proton solvation environment changes. At the lowest studied molar fraction of ethanesulfonic acid (1:10), the 2250 cm^{-1} absorption is strongly suppressed resulting in a flat and broad absorption in the 2000-3000 cm^{-1} frequency range. At this concentration, due to the high excess of water, protons are fully solvated by water molecules and are well separated from the ethanesulfonate anions. Conversely, at high ethanesulfonate concentrations the formation of ion pairs is highly probable.

The 2250 cm^{-1} absorption band does not represent undissociated $EtSO_3H$ or fully hydrated $H^+(H_2O)_n$, but a heteromolecular proton solvation complex [RSO_3^-–$H_3O^+(H_2O)_n$]. Interestingly, from the amplitudes $\nu_{as}(SO_2)$ and ν(S-O) absorption peaks at low water

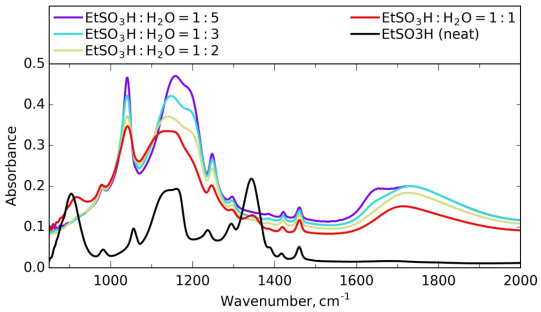

Figure 7.10: Infrared absorption spectra of ethanesulfonic acid solutions of different $EtSO_3H/H_2O$ molar ratio and of neat $EtSO_3H$. The spectra are normalized with respect to the absorption of the CH_2-bending vibration of ethanesulfonic acid at 1460 cm^{-1}.

content ($EtSO_3H$:H_2O=1:1) we can conclude that only ∼15% of the sulfonic acid remains undissociated. The 85% degree of ionization of ethanesulfonic acid also correlates with the concentration dependence of the characteristic hydrated proton bending absorption at 1750 cm^{-1}. This high degree of dissociation is in qualitative agreement with the results of an earlier 1H NMR study of methanesulfonic acid, in which 50% deprotonation at a 1:1 ratio was observed.[155] To facilitate sulfonic acid dissociation the water molecule accepting the proton has to be hydrogen bonded to two water molecules in order to become polarized and therefore to be basic enough.[158,161,162] It is possible that at low water content, the role of the two additional polarizing water molecules fulfilled by SO-groups of other sulfonate groups. In this case the proton solvation structure can be an asymmetric H_3O^+ ion with two or even three OH-groups strongly hydrogen bonded to sulfonate SO-groups.[158]

It is remarkable, that the transient absorption spectrum following excitation of the OH-vibrations of solvated proton structures in small AOT reverse micelles closely resembles the difference between FTIR spectra of ethanesulfonic acid solutions with low and high concentrations of the acid (Figure 7.9). This indicates that the excitation of small AOT nanodroplets results in a similar change of the proton-solvation structures as the dilution of ethanesulfonic acid solutions. This change is likely a bleaching of the OH stretch aborption bands of $[RSO_3^-–H_3O^+(H_2O)_n]$ solvation complexes, in the case of excitation of the AOT micelles as a result of weakening or partial dissociation of the hydrogen bonds due to local heating, in the case of dilution of the ethanesulfonic acid solutions by replacing the $EtSO_3^-$ group by H_2O.

Published as:

Giulia Giubertoni, Oleksandr O. Sofronov and Huib J. Bakker, Observation of Distinct Carboxylic acid Conformers in Aqueous Solution, *The Journal of Physical Chemistry Letters 2019, 10, pp. 3217-3222*

8

Observation of Distinct Carboxylic Acid Conformers in Aqueous Solution

Abstract

We investigate the molecular geometry of the carboxyl group of formic acid in acetonitrile and aqueous solutions at room temperature with two-dimensional infrared spectroscopy (2DIR). We found that the carboxyl group adopts two distinct configurations: a configuration in which the carbonyl group is oriented anti-parallel to the hydroxyl (anti-conformer), and a configuration in which the carbonyl group is oriented at an angle of $\sim 60^{\circ}$ with respect to the hydroxyl (syn-conformer). These results constitute the first experimental evidence that carboxyl groups exist as two distinct and long-living conformational isomers in aqueous solution at room temperature.

8.1 Introduction

The chemical impact of conformational isomerism has been recognized for a long time.[166–171] The conformation change of a relatively small molecular group can have a large impact on the macromolecular structure. For example, the cis/trans-isomerization of the amino-acid proline can have a strong effect on the conformation of proteins.[172–176] Carboxyl groups play an important role in this respect, as they form strong inter- and intramolecular hydrogen bonds that govern and stabilize macromolecular structures.[177,178] As a consequence, the conformational isomerism of carboxylic acids has been intensely studied with different molecular simulations techniques.[58,59,179,180] These studies predicted the existence of distinct conformational isomers of the carboxyl group, both in the gas phase and in aqueous solution.

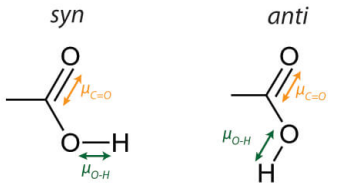

Figure 8.1: Schematic picture of syn- and anti-conformers. Orange and green arrows indicate the transition dipole moment of the carbonyl and hydroxyl vibrations,respectively.

Up to now, distinct carboxyl group conformers have only been experimentally observed in rare-gas matrices under cryogenic conditions.[181–183] The carboxyl group adopts two distinct planar geometries in rare gas matrices at low temperatures, as illustrated in Figure 8.1.[181,182,184,185] In the syn-conformer, the O-H group is oriented at $\sim 60^{\circ}$ with respect to the C=O, while in the anti-conformer the O-H is anti-parallel to the C=O. The anti-conformer is less stable than the syn-conformer, with the result that the chemical reactivity depends on the conformation.[186] Molecular dynamics simulations showed that the equilibrium concentration of the high energy anti-conformer is negligible in the gas phase at room temperature, but that this conformer stabilizes upon hydration.[58–60]

In a rare-gas matrix at extremely low temperatures, the anti- and syn- configurations were identified with linear infrared spectroscopy, which was enabled by the fact that the carbonyl and hydroxyl stretch vibrations of the carboxyl group have narrow absorption lines in these conditions. In room-temperature solutions, in particular in water, the carbonyl and hydroxyl stretch vibrations are strongly affected by the interactions with the surrounding solvent molecules, leading to a strong broadening of the absorption bands. In addition, at acid concentrations above ~ 3 M, the vibrations will also be affected by

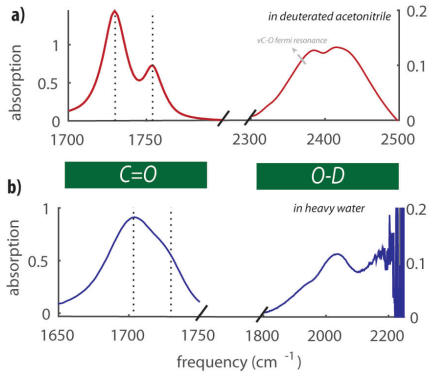

Figure 8.2: a) Linear infrared absorption spectrum of a 0.5 M solution of formic acid in deuterated acetonitrile. The spectrum shows two distinct narrow bands at 1730 cm^{-1} and 1754 cm^{-1}, and a broad band around 2430 cm^{-1} with a shoulder at 2380 cm^{-1}. b) Linear infrared absorption spectrum of a 0.3 M solution of formic acid in D_2O. The spectrum shows a C=O stretch band around 1700 cm^{-1} with a shoulder at 1724 cm^{-1}, and a band at 2030 cm^{-1} that is part of the broad and structured absorption spectrum of the OD-stretch vibration of formic acid. The solvent background absorption is subtracted in both cases.

dimer formation.[187–189] These effects preclude the study of conformational isomerism of carboxylic acids in aqueous media at room temperature with conventional linear infrared spectroscopy.

Here we use two-dimensional infrared (2DIR) spectroscopy to study the conformations of carboxyl group of formic acid molecules in room temperature solutions. We study the coupling between the carbonyl (C=O) and hydroxyl (O-D) stretch vibrations for deuterated formic acid dissolved in different solvents, including water. We found that the measurement of this coupling reveals the relative orientation of the carbonyl and the hydroxyl groups, and thus forms a unique experimental test of the existence of conformational isomerism of carboxylic acids under bio-relevant conditions.

8.2 Experiment

The details of our 2DIR setup are reported in Chapter 3. In all experiments the excitation pulses are centred at 1720 cm^{-1} with a bandwidth of 200 cm^{-1}, in resonance with the carbonyl vibrations. The probe pulse is centred at 2450 cm^{-1} to measure the response of the OD-stretch vibrations in deuterated acenotrile, and at 2050 cm^{-1} to measure the response of the OD-stretch vibrations in heavy water solutions. The 2DIR signal is

recorded simultaneously with the probe in parallel and perpendicular polarizations with respect to the pump, which allows us to extract information on the relative orientation of the excited C=O vibration and the probed OD-vibration.

The samples were prepared in a glass vial by adding formic acid to deuterated acetonitrile, heavy water, and dimethyl sulfoxide to reach the desired concentration. All the solvents were provided by Sigma Aldrich. Formic acid OD was purchased from Cambridge Isotope Laboratories.

8.3 Results and Discussion

In Figure 8.2a and Figure 8.2b we show the linear infrared spectra of formic acid dissolved in deuterated acetonitrile and heavy water (0.5 and 0.3 M, respectively) in the frequency regions of the C=O ($\sim$1750 cm^{-1}) and the O-D ($\sim$2430 cm^{-1}) stretching vibrations. Acetonitrile is a weakly polar and aprotic solvent, and the measured response of formic acid in this solvent may be similar to that in an inert gas matrix, which was used in previous experiments.[181,184,185] Comparison of the response of formic acid in acetonitrile with the response in (heavy) water will reveal the effect of hydration on the carbonyl and hydroxyl stretch vibrations, and on the potential presence and relative abundance of different conformers.

For formic acid in acetonitrile the absorption spectrum shows two distinct bands at 1730 cm^{-1} and 1754 cm^{-1}. The similarity of this spectrum with that of a more dilute solution (see Figure 8.7a in Appendix) indicates that the bands are unlikely to be the result of dimer formation. In the OD-stretch region we observe a broad band around 2430 cm^{-1} with an additional peak at 2380 cm^{-1}. The latter can be assigned to a Fermi resonance of the OD-stretch vibration with the overtone of the C-O stretch vibration.[182,184,190] For formic acid in water (Figure 8.2b), we observe a broad band for the carbonyl vibration around 1700 cm^{-1} with a shoulder around 1724 cm^{-1}. The absorption of the OD-vibrations is redshifted in heavy water[191] compared to acetonitrile solution. The band is broad and shows different subbands. Because of the strong absorption of the OD-stretch vibrations of D_2O, we cannot resolve the full OD-stretch spectrum of formic acid. However, the spectrum shows a distinct band at 2050 cm^{-1} corresponding to the OD-stretch vibration. The full OD-stretch absorption spectrum of formic acid can be seen in dimethyl sulfoxide (DMSO) solution (Figure 8.7c in Appendix). The observed spectrum is broad (1900-2300 cm^{-1}) and has multiple peaks due to combined excitations of the OD-stretch vibration and the O-D...O hydrogen bond. Since DMSO and water are hydrogen-bond acceptors of similar strength, the part of the formic OD-stretch absorption that we can observe in D_2O corresponds to the low-frequency part of

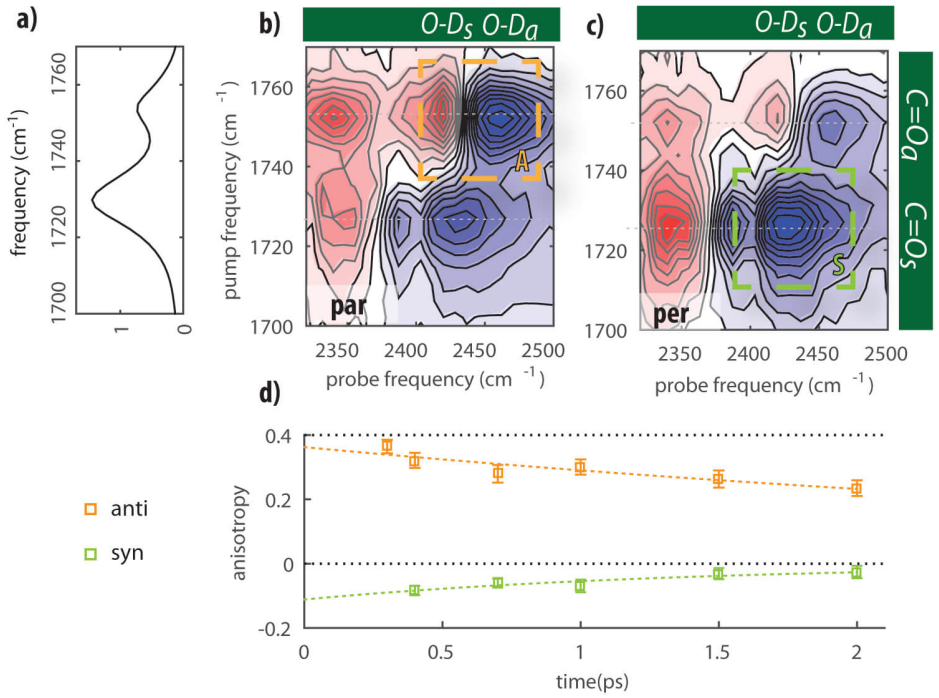

Figure 8.3: a) Linear spectrum of a 0.5 M solution of formic acid in deuterated acetonitrile in the region of the carbonyl stretch vibration. b) and c) 2DIR spectra at T_w=1 ps of the same solution when exciting the carbonyl stretching modes and probing the OD-stretching modes in parallel and perpendicular polarization configuration, respectively. d) Anisotropy of the A (anti) and S (syn) cross-peaks as a function of delay time between the excitation and detection pulses. The dashed lines are single exponential fits.

the formic OD-stretch absorption spectrum observed in DMSO.

In Figure 8.3b and Figure 8.3c we show 2DIR spectra of formic acid in acetonitrile. The blue colored regions correspond to negative transient absorption changes (bleaching) and the red colored regions to positive transient absorption changes. The spectra contain several cross-peak signals corresponding to frequency shifts of the OD-stretch vibration that are induced by the excitation of the carbonyl vibration. In both the parallel and the perpendicular 2DIR spectra, we observe cross-peak bleachings at 2380, 2423, and 2463 cm^{-1}. We observe additional structure in the 2DIR spectrum at probe frequencies below 2400 cm^{-1}, namely a decreased absorption near 2380 cm^{-1}, and an enhanced absorption at 2340 cm^{-1}. These signals result from the frequency shift and/or bleaching of the aforementioned Fermi resonance of the OD-stretch vibration and the overtone of

the C-O vibration, following the excitation of the carbonyl vibrations. The 2423 cm^{-1} and the 2463 cm^{-1} represent OD-stretching modes. It is clearly seen that the low-frequency carbonyl vibration at 1754 cm^{-1} shows a more intense cross-peak (which we denote as A) with the 2463 cm^{-1} OD-stretch mode in parallel polarization (Figure 8.3b). Similarly, the low frequency carbonyl vibration at 1730 cm^{-1} shows a more intense cross-peak (which we denote as S) with the 2423 cm^{-1} OD-stretch mode in perpendicular polarization (Figure 8.3c).

To better illustrate the polarization dependence of the signals, we plot the anisotropy of the two cross-peaks as a function of the time delay between the excitation and probing pulses. Figure 8.3d shows that at all time delays between 0.3 and 2 ps the anisotropy of the S-cross-peak is negative, indicating that the C=O at 1725 cm^{-1} is oriented at a large angle with respect to the OD-stretch vibration at 2423 cm^{-1}. The A-cross-peak shows a positive anisotropy, indicating that the C=O vibration at 1754 cm^{-1} is oriented almost parallel to the OD-stretching vibrating at 2463 cm^{-1}. The relative orientations indicate that there are two distinct species of formic acid in deuterated acetonitrile solution, with different relative orientations of the carbonyl and the OD-stretch modes.

The anisotropy signals of Figure 8.3d decay, probably as a result of the reorientation of the formic acid molecule. To extract the angle between the carbonyl and hydroxyl groups, we fit the anisotropy decays (Figure 8.3d) with a single exponential decay function. By extrapolating the fit to time delay zero, we determine the initial anisotropy R_0, from which we calculate the angle with the following expression: $\theta = \arccos\left(\sqrt{\frac{5R+1}{3}}\right)$. The two angles extracted from the anisotropy values (15$\pm$5° and 65$\pm$10 $^\circ$) match well with the molecular geometries of the anti and syn configurations, respectively (Figure 8.1). Thereby these results demonstrate that formic acid exists in distinct anti and syn configurations in room temperature solution. The extracted angles are affected by the fast inertial (librational) motion of O-D bond,[192] which explains why the extracted angle for the anti-conformer is somewhat larger than expected (15° vs 0°).

We find that the syn-conformation of formic acid in deuterated acetonitrile has a low-frequency carbonyl vibration and a low frequency hydroxyl vibration, while the anti-conformation has high-frequency carbonyl and high-frequency hydroxyl vibrations. This finding agrees with the properties of formic acid in a low-temperature rare-gas matrix.[183] By comparing the linear infrared and 2DIR spectra (Figure 8.8 in Appendix), we find that the anti species accounts for 30%$\pm$5% of the total amount of carboxyl groups present in solution. The absence of a cross-peak signal between the different hydroxyl vibrations, which would indicate the transformation from syn to anti or viceversa, shows that the two species do not exchange within the lifetime of the vibrationally excited state ($\sim$6-8 ps). This finding is supported by the results of an experiment in which we excite and probe the carbonyl vibrations, and in which we also do not observe a cross-peak signal of the two carbonyl vibrations (Figure 8.4). This outcome agrees with the results of

molecular dynamics simulations that showed the presence of a large energy barrier ($\sim$11 kcal/mol)[60,183] between the two species.

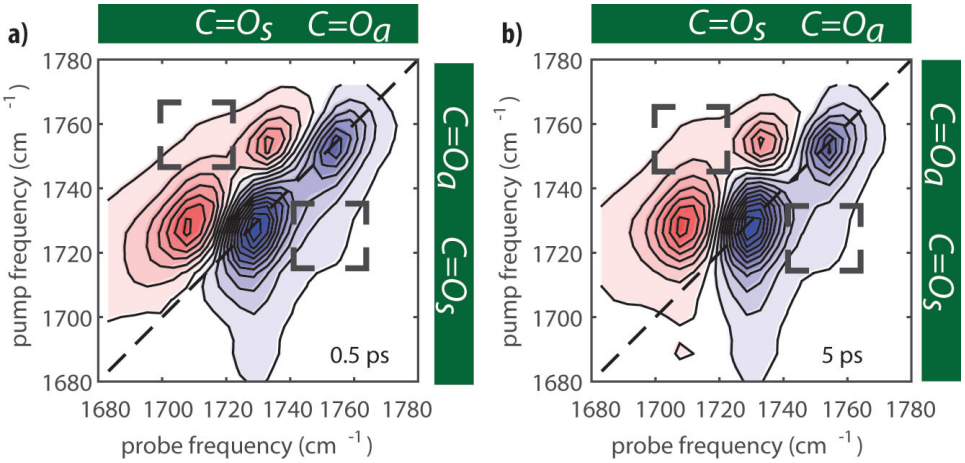

Figure 8.4: a) and b) isotropic degenerate 2DIR spectra of formic acid in deuterated acetonitrile at 0.5 and 5 ps, respectively. The dashed squares indicate the upward and downward cross-peak regions, where we do not observe any ingrowing spectral signatures.

In Figure 8.5b-8.5c we show 2DIR spectra of formic acid in heavy water solution in the cross-peak region where the carbonyl stretching modes are excited and the OD-stretch modes around 2050 cm^{-1} are detected in a parallel and perpendicular polarization configuration with respect to the pump. The spectral features are much broader and not as distinct as in acetonitrile solution. However, we observe again that the cross-peak of the high-frequency shoulder of the carbonyl at 1724 cm^{-1} is stronger in parallel polarization (Figure 8.5b), while the cross-peak of the low-frequency carbonyl at 1694 cm^{-1} is stronger in perpendicular polarization (Figure 8.5c).

An interesting observation is that the high-frequency carbonyl vibration now has a cross-peak with a lower frequency OD-vibration while the low-frequency carbonyl vibration has a cross-peak with a higher frequency OD-vibration. In Figure 8.5d we plot the anisotropy of the A and S cross-peaks in water, and we observe that the A cross-peak corresponds to a positive anisotropy value while the S cross-peak corresponds to a negative anisotropy. We thus find strong evidence of the existence of two molecular geometries of formic acid in aqueous solution: a configuration in which the carbonyl makes a small angle with the OD-vibration (A-cross-peak and anti configuration), and a configuration where the carbonyl vibration makes a large angle with the OD-vibration (S-cross-peak and syn configuration).

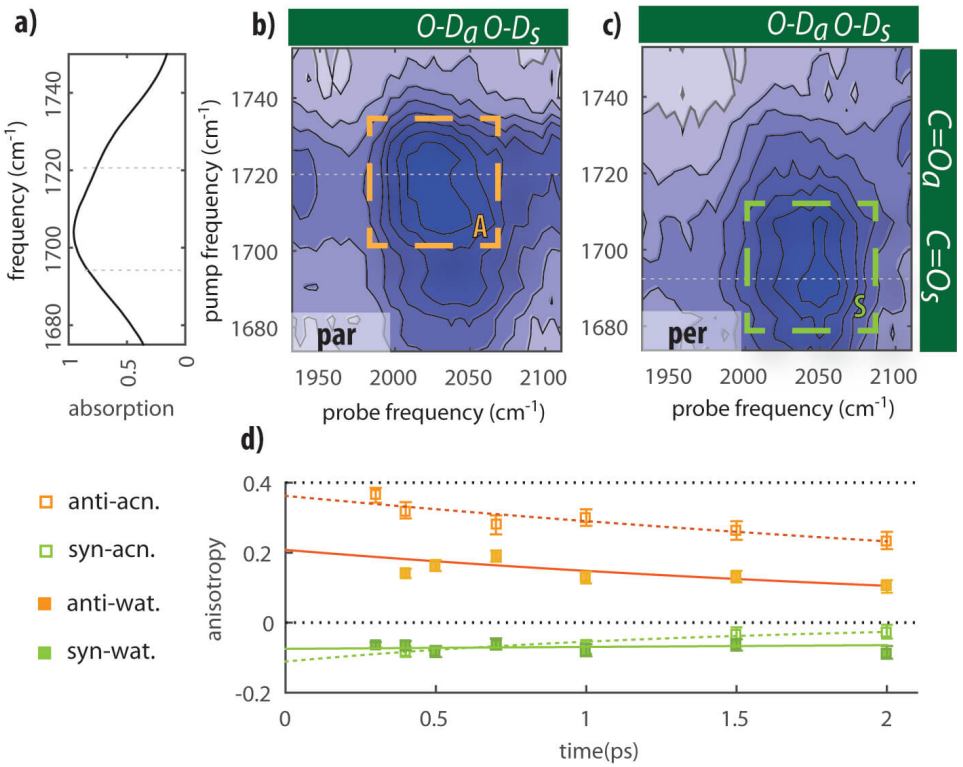

Figure 8.5: a) Linear spectrum of a 0.3 M solution of formic acid in D_2O in the region of the carbonyl stretch vibration. b) and c) 2DIR spectra at T_w=1 ps of the same solution when exciting the carbonyl stretching modes and probing the OD-stretching modes in parallel and perpendicular polarization configuration, respectively. d) Anisotropy of the A- and S-cross-peaks as a function of delay time between the excitation and detection pulses. For comparison for formic acid in acetonitrile also the results of Figure 8.3d are shown. Dashed and continuous lines are single exponential fits.

An interesting question is why the 1724 cm^{-1} carbonyl vibration shows a cross-peak with a lower frequency OD-stretch vibration, and the 1694 cm^{-1} carbonyl vibration with a higher frequency OD-stretch vibration. This finding clearly deviates from what was observed for formic acid in acetonitrile (Figure 8.3) and in a rare-gas matrix at low temperature.[183] This observation can be explained from the difference in the strength of the hydrogen bonds between the O-D group of formic acid and the surrounding water molecules in the two configurations. In the anti configuration these hydrogen bonds are stronger than in the syn configuration. As a result, the OD-vibration undergoes a stronger

red-shift in the anti configuration than in the syn configuration, which overcompensates the intrinsically higher frequency of the OD-stretch in the anti configuration that was observed for formic acid in deuterated acetonitrile and in a rare gas matrix. A similar reversal of the OD-stretch vibrational frequency is observed for a solution of formic acid in DMSO (which is a similarly strong hydrogen bond acceptor as water), as shown in Figure 8.9 in Appendix. This explanation is also supported by molecular dynamics simulations of acetic acid hydrates, which show that the anti-conformer is more strongly hydrated than the syn-conformer.[60]

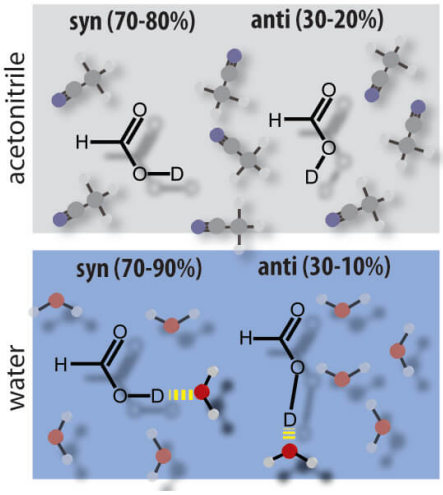

Figure 8.6: Illustration of the syn- and anti-conformers of formic acid in acetonitrile and in liquid water.

In Figure 8.5d we compare the anisotropy values obtained for formic acid in heavy water with the results obtained for formic acid in deuterated acetonitrile. We observe that the negative anisotropy of the S-cross-peak does not show a significant change by changing the solvent while the positive anistropy of the A-cross-peak is somewhat lower in heavy water than in deuterated acetonitrile. This difference likely results from the fact that the spectral features are much broader in heavy water than in deuterated acetonitrile. Hence, the signal observed in the region of the A cross-peak has some contribution of the stronger S cross-peak for which the anisotropy has a negative value. An additional effect may be that the stronger hydrogen bonding of the anti configuration to surrounding water molecules leads to a larger net deviation from a perfect parallel arrangement of the carbonyl and O-D groups.

We estimate from the amplitudes of the cross peaks that $25\pm10\%$ of formic acid adopts an anti configuration in heavy water. Unfortunately, the precision of this estima-

tion is low as a result of the strong broadening of the carbonyl absorption band. The analysis of the more narrow carbonyl spectrum of formic acid in DMSO yields a similar fraction for the anti configuration of 30±5%. It thus appears that the character of the solvent does not significantly change the concentration, and thus the relative stability of the two formic acid conformers. This result indicates that the stronger hydrogen bond donated by the formic acid O-D group in the anti configuration constitutes only a small contribution to the overall stabilization of this conformer, or that this contribution is compensated by counteracting solvation effects of the remainder parts of the molecule.

8.4 Conclusion

In summary, using femtosecond 2DIR spectroscopy we demonstrate that formic acid adopts two distinct, long-living conformations in deuterated acetonitrile and heavy water solutions, denoted as syn and anti (Figure 8.6). We observed that for formic acid in heavy water the frequency of the OD-stretch vibration is at a lower frequency in the anti configuration than in the syn configuration, which is opposite to what is observed for formic acid in deuterated acetonitrile. This difference indicates that the OD group of formic acid forms a stronger hydrogen bond to surrounding water molecules in the anti-conformer than in the syn-conformer. We observe that the fractions of anti-conformer syn-conformer are 20-30% and 80-70 %, respectively, both in deuterated acetonitrile and in heavy water solution. The observation of distinct conformers of the carboxylic acid and their slow exchange at room temperature shows that these conformers are separated by high energy barriers. As a result, the presence of these conformers can have a large effect on the structure and dynamics of (bio)molecular systems.

8.5 Appendix

8.5.1 Assignment of absorption peaks to carbonyl and O-H/OD-vibrations

Solutions of formic acid in d-acetonitrile show two absorption peaks in the carbonyl vibrational region. The most intense is around 1730 cm^{-1}, while the second is at 1760 cm^{-1}. To discard the possibility that one of the peak is due to dimer formation, we measure the linear spectra of formic acid at 0.05 M and 0.5 M. Figure 8.7a shows the spectra normalized to the absorption of the 1730 cm^{-1} peak. We observe that the relative intensity between the two peaks does not change by increasing the concentration, strongly suggesting that these two peaks are associated to two structurally different monomers.

The spectrum of D_2O strongly absorbs between 2200 to 2600 cm^{-1}, partially overlapping with the vibrational region of the acid O-D modes around 2100 cm^{-1}. To corroborate the assignment of the absorption peaks at 2050 cm^{-1} to the O-D modes of the acid and

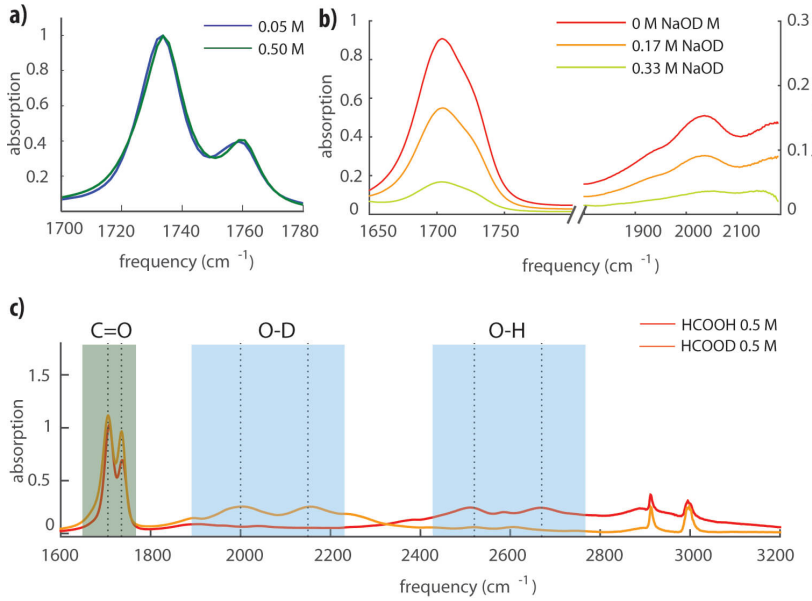

Figure 8.7: a) Scaled linear infrared spectra of 50 and 500 mM solution of formic acid in acetonitrile-d3.b) Linear infrared spectra of 0.5 M formic acid in heavy water with different amounts of added NaOD (D2O background is subtracted). We observe a strong decrease in absorption at 2050 cm^{-1}, which supports the assignment of this band to the OD-stretch vibration of formic acid. c) Linear infrared spectra of 0.5 M solutions of deuterated and non-deuterated formic acid in DMSO (solvent background is subtracted). In both solutions the double-peak structure of the carbonyl band is clearly observed. The broad structured bands at 1900-2300 cm^{-1} and 2400-2800 cm^{-1} are assigned to OD- and OH-stretch vibrations of deuterated and non-deuterated formic acid, respectively.

not of the D_2O, we add different concentrations of NaOD to formic acid solutions. By gradually deprotonating the -COOD groups, we observe that the intensities of the absorption peaks at 2050 cm^{-1} decrease (Figure 8.7b). This indicates that the peaks observed at 2050 cm^{-1} are due to the absorption of the vibrational modes of the acid O-D. This assignment is corroborated by measuring the vibrational spectrum of formic acid in dimethyl sulfoxide. In Figure 8.7c we observe that the spectrum of HCOOD in dimethyl sulfoxide contains a broad structured band around 2100 cm^{-1}. In the case of HCOOH this broad band is shifted to higher frequency (2600 cm^{-1}), confirming that the broad band at 2100 cm^{-1} HCOOD is due to the absorption of the acid O-D modes.

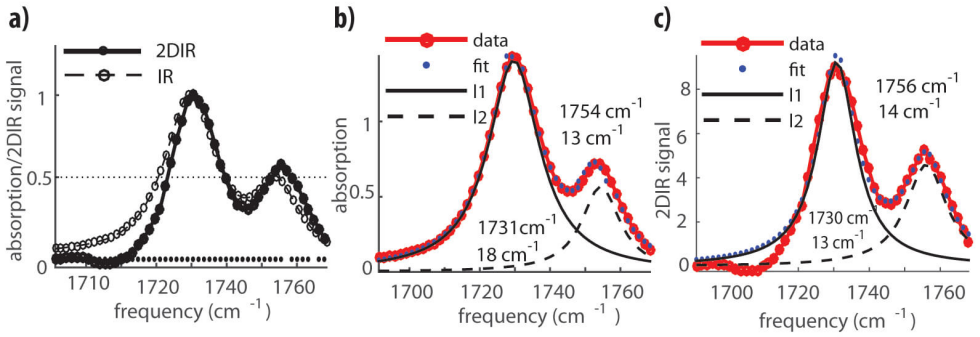

Figure 8.8: a) Linear infrared spectrum and a diagonal slice of the 2DIR spectrum of formic acid in acetonitrile-d3. The similar shapes of the spectra indicate that the carbonyl stretch vibration has a similar absorption cross section for the syn- and anti-conformers. b) and c) Decomposition of the linear infrared spectrum (b) and 2DIR diagonal slice (c) of formic acid in acetonitrile-d3 into two Lorentzian-shaped bands, corresponding to two formic acid conformers.

8.5.2 Relative concentration of syn- and anti- conformers

The relative concentration of the conformers cannot be determined from the linear infrared spectrum, as the cross-sections of the carbonyl vibrations of the two conformers are not known. However, we can make use of the fact that the linear infrared absorption spectrum scales as μ^2 (where μ is the vibrational transition dipole moment), while the 2DIR spectrum scales as μ^4, thus providing an additional relation between the measured signals, cross-sections and relative concentrations of the conformers. The linear IR spectrum and the diagonal 2DIR spectrum (pump frequency = probe frequency) are shown together in Figure 8.8a.

The diagonal 2DIR spectrum (and in fact all presented 2DIR spectra) is normalized with respect to the pump spectrum. We observe a very similar ratio of the two bands in the linear IR spectrum and the diagonal 2DIR spectrum, which indicates that the two bands have similar cross-sections. To obtain the precise ratio between the cross-sections of the peaks, we fit the linear spectrum and the 2DIR slice with two Lorentzian-shaped bands (Figure 8.8b-c). We find that the ratio of the two cross-sections is close to 1. We then calculate the areas under the bands of the two carbonyl vibrations by fitting the linear spectrum. The ratio of these areas represents the fractions of the two conformers.

8.5.3 Syn- and anti- conformers in DMSO solution

Figure 8.9a-b show the parallel and perpendicular 2DIR spectra obtained by exciting the carbonyl modes at 1730 cm^{-1}, and probing the OD-vibrational modes around 2100 cm^{-1}.

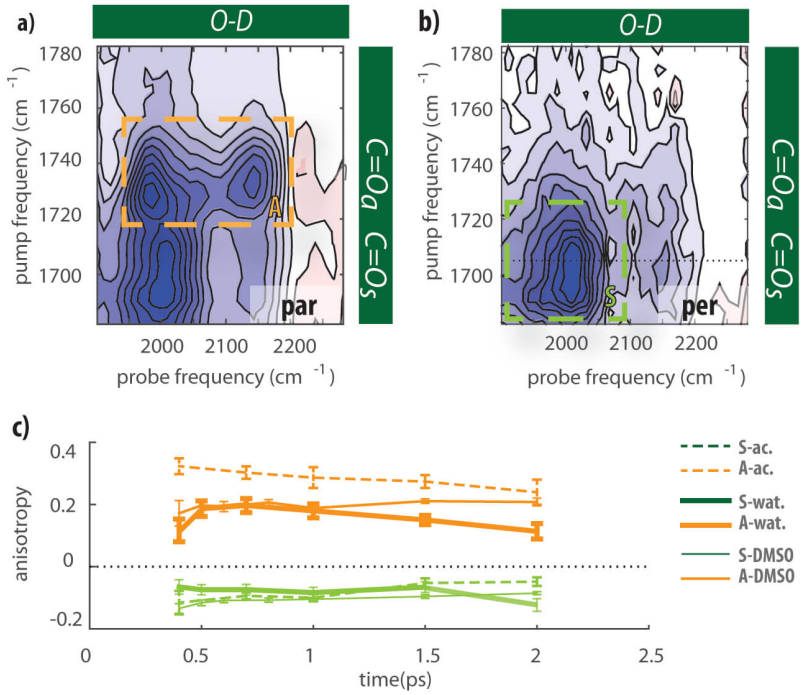

Figure 8.9: 2DIR spectra of 0.5 M of formic acid in DMSO obtained by excitation of the carbonyl stretch vibration and probing of the OD-stretch modes with a) parallel and b) perpendicular probe polarization; c) Comparison of the anisotropy values of the O-D/C=O cross-peaks of formic acid in acetonitrile-d3, heavy water, and DMSO solution.

Similarly to formic acid in heavy water and in acetonitrile, we notice that in parallel polarization configuration the strongest cross-peak signal is observed when pumping the carbonyl vibration at 1730 cm^{-1}, while in perpendicular polarization configuration the strongest cross-peak signal is obtained when pumping at 1710 cm^{-1}. The dependence of the amplitude of the cross-peak signal on the probe polarization suggests that in DMSO two different species of formic acid are present. We find that the anisotropy of the cross-peak obtained by exciting at 1730 cm^{-1} is around 0.2, similar to the value that we observe when exciting the higher frequency carbonyl mode of formic acid dissolved we find in water. This anisotropy value corresponds to an angle between the transition dipole moments of the O-D and C=O vibrations of $\sim 35^{\circ}$. The anisotropy of the cross-peak at lower pump frequency is -0.1, corresponding to an angle of $\sim 70^{\circ}$.

Published as:

Oleksandr O. Sofronov, Giulia Giubertoni, Alberto Pérez de Alba Ortíz, Bernd Ensing, Huib J. Bakker, Peptide side-COOH groups have two distinct conformations under bio-relevant conditions, The Journal of Physical Chemistry Letters 2020, 11, pp. 3466–3472

9

Conformations of Peptide Side-COOH Groups Under Bio-relevant Conditions

Abstract

The carboxyl (COOH) side-chain groups of amino acids, such as aspartic acid, play an important role in biochemical processes, including enzymatic proton transport. In many theoretical studies it was found that the (bio)chemical reactivity of the carboxyl group strongly depends on the conformation of this group. Interestingly, up to now there has been no experimental investigation of the geometry and the stability of different COOH conformers under bio-relevant conditions. Here, we investigate the conformational isomerism of the sidechain COOH-group of N-acetyl aspartic acid amide using polarization-resolved two-dimensional infrared spectroscopy. We find that the carboxyl group shows two distinct near-planar conformers (syn and anti) when dissolved in water at room temperature. Both conformers are significantly populated in aqueous solution (75$\pm$10% and 25$\pm$10% for syn and anti, respectively). Molecular dynamics simulations show that the anti-conformer interacts more strongly with water molecules than the syn-conformer, explaining why this conformer is significantly present in aqueous solution.

9.1 Introduction

Carboxyl groups and carboxylate anions are widely present in proteins, both as part of the side chain of amino acids glutamic and aspartic acid, and as C-terminal groups. Under physiological conditions, the carboxyl groups are usually deprotonated, but in specific microenvironments they can still be found in protonated form.[193–196] The side-chain carboxyl groups of aspartic acid and glutamic acid residues are essential for enzymatic catalysis, protein folding,[197,198] proton conduction in protein nanochannels,[52,199] and gating of pH-sensing ion channels[200,201].

For simple carboxylic acids (formic, acetic and propionic acid) dissolved in rare-gas matrices under cryogenic conditions, the carboxyl group can adopt two distinctly different conformations with a planar structure.[181,202,203] In the so-called syn-conformer, the hydroxyl group is at an angle of $\sim 60^\circ$ with respect to the carbonyl group, while in the so-called anti-conformer the hydroxyl group is oriented anti-parallel to the carboxyl group. In Chapter 8 we showed for formic acid that distinct long-living syn and anti carboxyl conformers exist also in aqueous solutions at room temperature, with relative abundances of 70-80% and 20-30%.

The conformational isomerism of carboxyl groups in molecules that are more complex than propionic acid has not been studied yet.[183] The potential presence of the anti conformer is often neglected, especially in X-ray diffraction studies in which proton positions cannot be determined accurately. As a consequence, only 2% of the carboxyl groups found in the Cambridge Structural Database are depicted in an anti-conformation.[204] Nevertheless, the presence of side-chain COOH-groups of aspartic and glutamic acid residues in an anti-conformation is expected to play an important role in enzymatic reactions and polypeptide structure stabilization.[204–211]

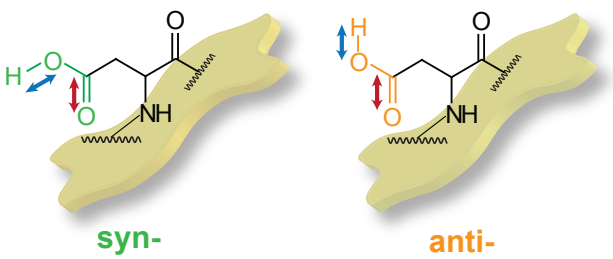

Figure 9.1: Syn and anti conformers of N-acetylaspartic acid amide. Red and blue arrows indicate the transition dipole moments of the carbonyl and of the hydroxyl vibrations, respectively.

Here we use polarization-resolved two-dimensional infrared (2DIR) spectroscopy and molecular dynamics simulations to study the conformational isomerism of the side-chain

carboxyl group of N-acetylaspartic acid amide (Figure 9.1), as a model for the aspartic acid residue. In the 2DIR experiments we measure the response of the hydroxyl vibration upon the excitation of the carbonyl vibration of the same carboxyl group. The polarization dependence of this signal provides unique information on the molecular geometry of the carboxyl group. We observe two distinct conformations of the carboxyl group with different orientations of the hydroxyl group with respect to the carbonyl group. We also determine the fractions of the two conformers in dimethyl sulfoxide (DMSO) solution and in aqueous solution. Finally, we use molecular dynamics simulations to explain the structures and relative abundances of the two conformers from their intermolecular interactions with the solvent molecules.

9.2 Experiment

The details of our 2DIR setup are reported in Chapter 3. In all experiments the excitation pulses are centred at $\sim$1730 cm^{-1}, in resonance with the carbonyl vibrations, and the probe pulses are centered either at 2700 cm^{-1} or 1730 cm^{-1} to measure the response of OH- or CO-stretch vibrations. N-acetylaspartic acid amide (>95%, Enamine Ltd.) was dissolved in either deuterated dimethyl sulfoxide (DMSO-d6, anhydrous, 99.8% D, Sigma-Aldrich) or in ultrapure water to reach the desired concentration. For the infrared absorption measurements (Bruker Vertex 80v FTIR spectrometer) and the two dimensional infrared experiments the solution was held between two calcium fluoride windows separated by a PTFE spacer of 10-50 μm thickness.

9.3 Results and Discussion

9.3.1 Geometry of the carboxyl group conformers

First, we measure the 2DIR spectra of N-acetylaspartic acid amide in DMSO solution (0.4 M) obtained by exciting the carbonyl stretch vibration and probing the hydroxyl stretch vibration (Figure 9.2a). The good solubility of this amino acid in DMSO and the absence of solvent absorption bands in the spectral regions of the carbonyl and hydroxyl groups allow for an accurate measurement of the 2DIR cross-peak signals of these two groups. The carbonyl vibration has an absorption band centered at 1720-1730 cm^{-1}. Upon excitation of this vibration, cross-peak signals appear at 2500-2800 cm^{-1} resulting from the excitation-induced frequency shift of the hydroxyl vibration (see Chapter 8). In the probed frequency region 2500-2800 cm^{-1} this shift results in a negative absorption change (colored in blue). The cross-peak signal has the form of a series of subbands, which is typical for OH-stretch vibrations of strongly hydrogen bonded systems, and results from

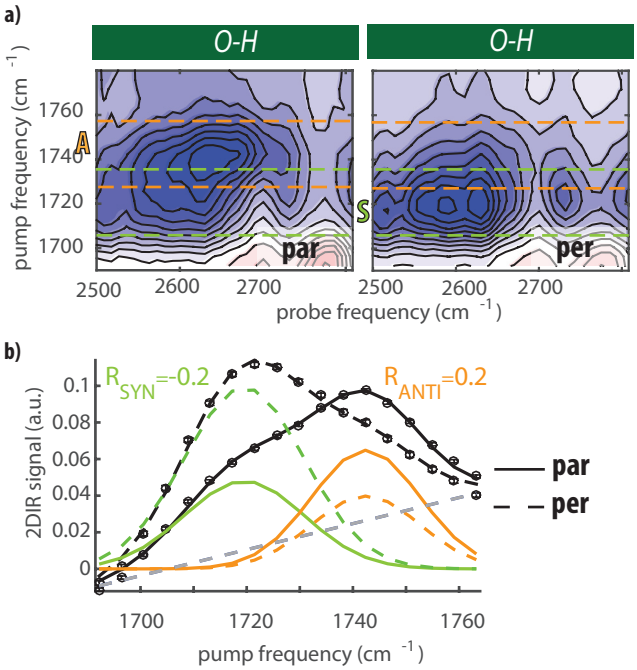

Figure 9.2: a) 2DIR spectra in the C=O/O-H cross-peak region measured in parallel and perpendicular polarization configuration at a time delay T_w=0.5 ps. The green and the orange bars highlight the responses of the syn- and anti-conformers, respectively. b) Parallel (solid) and perpendicular (dashed) transient absorption signals obtained by integrating the corresponding 2DIR signal over the probe frequency in the range between 2500 and 2750 cm^{-1}. The green and the orange colours indicate, respectively, the vibrational responses of the syn and anti conformers. The grey dashed line represents the correction for the isotropic background (see Methods).

the strong coupling of the OH-stretch vibration to the low-frequency vibrations of the hydrogen bonds.[212,213] These subbands are also observed in the linear infrared absorption spectrum of the hydroxyl vibration (see Appendix Sec.9.5.1 and Figure 9.7).

The amplitude of the cross-peak signal is observed to depend on the excitation frequency and the polarization configuration. Excitation of the low-frequency part of the carbonyl vibration (~1720 cm^{-1}) results in a stronger hydroxyl cross-peak signal in perpendicular polarization, whereas excitation of the high frequency part of the carbonyl peak (~1745 cm^{-1}) yields a cross-peak signal that is more pronounced in parallel polarization.

In Figure 9.2b we show the 2DIR signals in parallel and perpendicular polarizations

integrated over probe frequency range 2500-2750 cm^{-1} as a function of the carbonyl excitation frequency. We fit this integrated cross-peak signal with two Gaussian-shaped bands. For each band we calculate the anisotropy $R = \frac{\Delta\alpha_{\parallel} - \Delta\alpha_{\perp}}{\Delta\alpha_{\parallel} + 2\Delta\alpha_{\perp}}$, where $\Delta\alpha_{\parallel}$ and $\Delta\alpha_{\perp}$ are the transient absorption changes (cross-peak signals) measured in parallel and in perpendicular polarization configuration, respectively. The anisotropy represents the relative orientation of the hydroxyl transition dipole moment with respect to the carbonyl transition dipole moment, and can be used to calculate the angle between the carbonyl and the hydroxyl groups following $\theta = \arccos\sqrt{\frac{5R_0+1}{3}}$.

We find that the cross-peak of the higher carbonyl vibration has a positive anisotropy of ∼0.2 (35°) and the lower carbonyl peak has a negative anisotropy of ∼-0.2 (90°). These anisotropy values clearly indicate that the two carboxyl group species comprise distinctly different relative orientations of the O-H group and C=O group. Based on the found angles, we assign the cross-peak signal with positive anisotropy and a high frequency of the carbonyl vibration to the anti-conformer, and the cross-peak signal with a negative anisotropy and a low frequency of the carbonyl vibration to the syn-conformer. This result demonstrates that the carboxyl group shows distinct syn- and anti-conformers, not only for simple carboxylic acids, but also for more complex molecules like amino acids. We observe these distinct conformers also for the terminal carboxyl groups of other amino acids in DMSO solution (see Appendix Sec.9.5.2).

The obtained angles between the carbonyl and hydroxyl groups differ from the ideal values of 0° (for a perfect in-plane anti-parallel configuration) and 60° (for an in-plane syn configuration). Similar deviations have been observed for formic acid in DMSO solution (see Chapter 8). These deviations can be explained from the fact that the extracted anisotropy values can be affected by out-of-plane rotations of the O-H or C=O group. Such a rotational distortion can explain an increase of the ideal angle of the anti-configuration from 0° to 35°, and an increase of the ideal angle of the syn configuration from 60° to ∼90°. Indeed, analysis of the Cambrige Structural Database shows that the O-C-O-H dihedral angle can deviate by 10-30° from the ideal value for both the syn and anti conformers.[214] In addition, the anisotropy values may be affected by fast inertial (librational) motion of O-H bond, which leads to an ultrafast or even pulse-width limited partial decrease of anisotropy.[192]

9.3.2 Carboxyl group conformers in aqueous solution

To mimic the properties of aspartic acid residues under biological conditions, we study the conformational isomerism of N-acetylaspartic acid amide in aqueous solution. In Figure 9.3 we show 2DIR spectra of N-acetylaspartic acid amide dissolved in water, obtained by exciting the carbonyl vibration at ∼1730 cm^{-1} and probing the O-H stretching vibra-

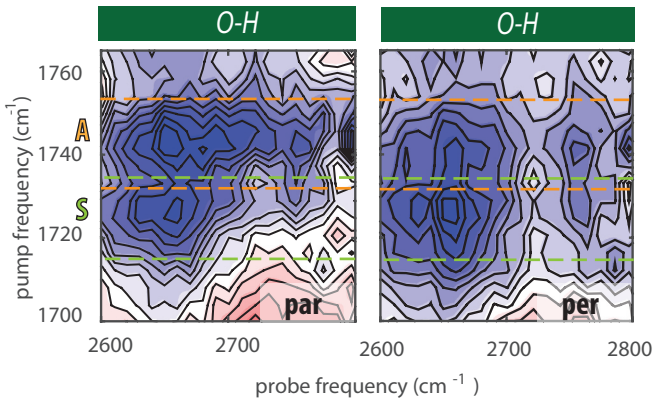

Figure 9.3: Cross-peak 2DIR spectra of N-acetylaspartic acid amide in aqueous solution. 2DIR spectra of N-acetyl aspartic acid amide in the C=O/O-H cross-peak region measured in perpendicular and parallel polarization configuration at T_w=0.3 ps. The green and the orange bars highlight the responses of the syn- and anti-conformers, respectively.

tion at ∼2700 cm^{-1}. For this solution, a strong absorption band of the solvent, i.e. the water HOH-bending vibration, overlaps with the carbonyl band of the acid. Therefore, to increase the contrast between the carbonyl and the water absorption, and to obtain a significant carbonyl-hydroxyl cross-peak signal, we used a 1 M aqueous solution of N-acetylaspartic acid amide. The cross-peak signals that we observe in parallel and perpendicular polarization configurations for this solution are qualitatively the same as those measured for N-acetylaspartic acid amide dissolved in DMSO. Again we observe a stronger cross-peak signal in perpendicular polarization at a low excitation frequency of 1725 cm^{-1} of the carbonyl vibration. At this excitation frequency, we extract an anisotropy of ∼-0.1, from which we derive an angle between the O-H and C=O groups of ∼65°. In parallel polarization we observe a stronger cross-peak signal at a relatively high frequency of the carbonyl vibration. We find that in parallel polarization the maximum of the cross-peak intensity is at 1745 cm^{-1}. At this excitation frequency we extract an anisotropy of ∼0.25, corresponding to an angle between O-H and carbonyl of ∼30°.

In order to quantify the populations of the anti- and syn-conformers, we also measured degenerate 2DIR spectra, in which the carbonyl vibrations are both excited and probed. The 2DIR signal is proportional to the concentration and the square of the vibrational cross-section, whereas the linear IR absorption scales with the concentration and the vibrational cross-section. Hence, from the combination of the degenerate 2DIR spectrum and the linear IR absorption spectrum we can determine the ratio of the vibrational cross-sections and the relative concentrations of the two carboxylic acid conformers. Figure 9.4a shows the 2DIR spectrum of N-acetylaspartic acid amide in aqueous solution at

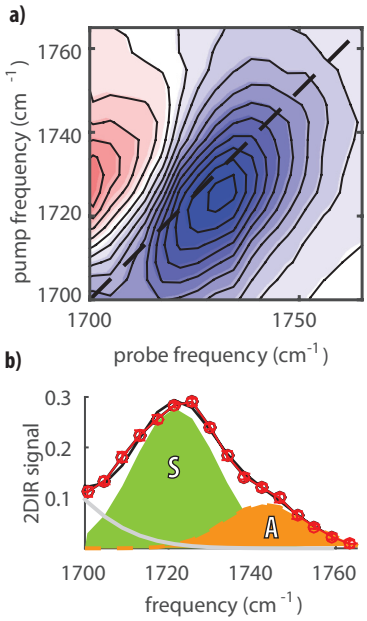

Figure 9.4: Degenerate 2DIR spectrum of N-acetylaspartic acid amide in aqueous solution. a) Isotropic degenerate 2DIR spectrum of a solution of 1 M N-acetylaspartic acid amide in water, measured at T_w=0.3 ps. b) Transient absorption signal obtained by taking the diagonal slice of the bleach signal of the 2DIR spectrum plotted as a function of pump frequency. The green and orange coloured bands represent the 2DIR signals of the syn and anti conformers obtained from a fit of the measured spectrum with Voigt profiles.

a concentration of 1 M. Because of the low cross-section of the water bending vibration and its fast relaxation dynamics, its impact to the 2DIR signal at delay time 0.3 ps is negligible.[215] We observe that the diagonal peak is centered at 1725 cm^{-1} and is elongated at the high frequency side.

In Figure 9.4b we plot a diagonal cut (probe=pump frequency) of the degenerate 2DIR spectrum as a function of the pump frequency. The resulting transient absorption spectrum shows a peak centered at 1725 cm^{-1}, and a shoulder around 1745 cm^{-1}. These two vibrational frequencies match with the excitation frequencies found in Figure 9.3 for the syn- and anti-conformers. We fit the 2DIR signal with two Voigt profiles, representing the carbonyl stretching vibrations of the syn- and anti-conformers. A third Voigt-shaped band centered at 1680 cm^{-1} was added to account for the contribution of the amide vibration (grey line). We find that the relative area of the anti-conformer band in the diagonal 2DIR signal amounts to ∼25%. Unfortunately, we cannot determine the

relative area of the absorption band of the anti-conformer in the linear infrared absorption spectrum, because of the strong overlap with the bending mode of the water. However, for N-acetylaspartic acid amide dissolved in DMSO we can analyze both the diagonal negative absorption change of the degenerate 2DIR spectrum and the linear infrared absorption spectrum (see Appendix Sec.9.5.3 and in Figure 9.10). We find similar areas for the bands of the syn- and anti-conformers in the linear spectrum and the 2DIR spectrum, which implies that the vibrational cross-sections of syn- and anti- carbonyls are similar, as was found before for formic acid (see Chapter 8). Based on this quite general result, we assume that the cross-section ratio of the carbonyl vibrations of the two conformers is also similar in water solution, which implies that the relative area of the anti-conformer in the 2DIR spectrum directly represents the relative fraction of this conformer. We thus find the populations of the syn- and anti-conformer to be 75$\pm$10% and 25$\pm$10%, respectively. These populations are similar to those found for formic acid in water (see Chapter 8). Hence, we conclude that the relative abundances of the syn- and anti-conformers of carboxyl groups in polar solvents such as DMSO or water depend only weakly on the rest of the molecule.

9.3.3 Hydration of the carboxyl group conformers

A.Pérez de Alba Ortíz et al.[216] performed molecular dynamics (MD) simulations to study the intermolecular interactions of the syn- and anti-conformers of N-acetylaspartic acid amide in water. The MD simulations are done with full atomistic resolution and at the force field level of theory. Two MD simulations of aqueous solvated N-acetylaspartic acid amide have been performed in the two different planar configurations of the –COOH group, syn and anti. The angles between C-O and O-H, and the dihedral C-O-C-H, are not restrained in these simulations.

From the simulations of both conformers, they obtained the density histograms of the hydrogen and oxygen atoms of water molecules closest to the hydrogen and oxygen atoms of the carboxyl group as a function of the hydrogen bond distance and the angle between the hydrogen bond and the corresponding covalent O-H bond (Figure 9.5). We see that in all cases for distances larger than 2.45 Å the angle becomes ill-defined. Thus, we define 2.45 Å as a cut-off distance for hydrogen-bond formation between the carboxyl group and the water molecules.

The radial distribution functions of water oxygens forming a hydrogen bond with the acid hydrogen of the two conformers (Figure 9.6a) show clear differences. We find that the strongly polar OH-group of the carboxylic acid donates $\sim$1.0 hydrogen bonds for both conformers. However, the density of water oxygen atoms at a short distance ($\sim$1.8 Å) is about 10% higher for the anti-conformer than for the syn-conformer. This result shows that the hydrogen bonds donated by the carboxyl group of the anti-conformer are shorter

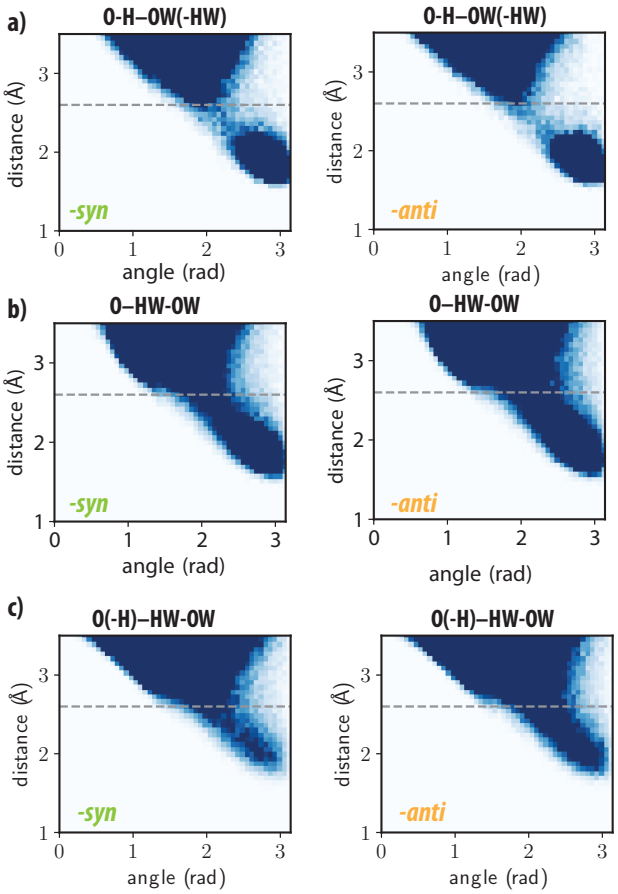

Figure 9.5: Density histograms of the water oxygen and hydrogen atoms closest to the hydrogen and oxygen atoms of the carboxyl group of N-acetylaspartic acid. a) Density of water oxygens closest to the hydrogen atom of the carboxyl group as a function of the $H_c \cdots O_w$ distance and O_c–$H_c \cdots O_w$ angle. b, c) Densities of the water hydrogens closest to the carbonyl (b) and hydroxyl (c) oxygen atoms of the carboxyl group as a function of the $O_c \cdots H_w$ distance and $O_c \cdots H_w$–O_w angle. The index c stands for the carboxyl group and the index w for a water molecule.

and stronger than those of the syn-conformer. This finding reflects that the hydroxyl group is more polar for the anti-conformer than for the syn-conformer, in accordance with earlier theoretical work.[60,214]

The hydration number of the oxygen atoms is rather different for the two carboxyl group conformers (Figure 9.6b,c). The oxygen atom of the carbonyl group accepts $\sim$1.7

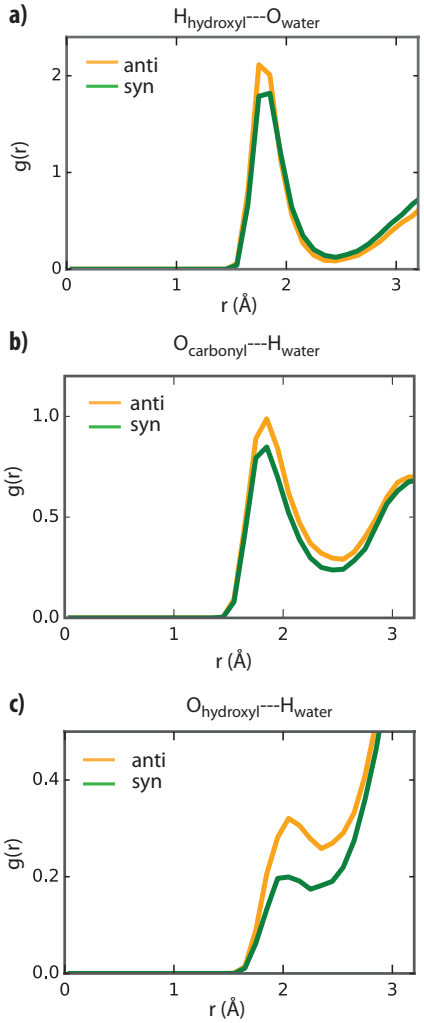

Figure 9.6: Molecular dynamics simulations of the interaction of the carboxyl group of N-acetylaspartic acid amide in syn- and anti-conformation with water. a) Radial density function of the water oxygens closest to the hydrogen atom of the carboxyl group. b,c) Radial density functions of the water hydrogens closest to the carbonyl (b) and hydroxyl (c) oxygen atoms of the carboxyl group.

hydrogen bonds from water molecules for the anti-conformer, and only ∼1.4 hydrogen bonds for the syn-conformer. The same trend is observed for the hydroxyl group, its oxygen atom accepts ∼0.7 hydrogen bonds from water molecules for the anti-conformer

and $\sim$0.5 hydrogen bonds for the syn-conformer. The anti-conformer is thus much better hydrated than the syn-conformer. These differences are captured at the classical level of MD simulations, which means that they are due to exposure and steric effects and not the result of differences in the basicities of the oxygen atoms in the syn- and anti-conformers.

The better hydration of the anti-conformer explains why we observe this conformer to be significantly present in aqueous solution while it is nearly absent in the gas phase. The $25\pm10\%$ fraction of anti-conformer in aqueous solution suggests a free energy difference between the anti- and syn-conformer of 0.6 ± 0.3 kcal/mol. This value will also determine the difference in equilibrium constants of chemical reactions involving the carboxyl group such as acid dissociation. We calculate a difference in acidity of syn- and anti-conformers of $\Delta pK_a=0.5\pm0.3$. Hence, in spite of its better hydration, the anti-conformer of the carboxyl group is still more acidic than the syn-conformer, which can play an important role in intermolecular interactions and protolytic equilibria inside polypeptide structures. The difference in acidity between the two conformers is much smaller than the $\Delta pK_a=4$ that was obtained in calculations of the two conformers without any solvent present[205,217,218] This latter value for ΔpK_a is widely accepted in enzyme studies.[206,208,210,219] The energy gap we estimate from our experiment is in fact even smaller than the 1.5-1.7 kcal/mol that has been calculated for acetic acid conformers in aqueous solution.[58–60] Hence, the anti-conformer of the side-chain carboxyl group of N-acetylaspartic acid amide is more acidic than the syn-conformer, but this difference in acidity could strongly depend on the degree of solvation. Variation of the local environment of the amino acid, i.e. within a protein, can thus lead to a strong change of the acidity of the aspartic acid side group.

9.4 Conclusion

We showed with polarization-resolved two-dimensional infrared spectroscopy that the side-chain carboxyl group of N-acetylaspartic acid amide exists in two distinctly different conformations, both in DMSO solution and in aqueous solution. In one of these conformations the carbonyl stretch vibration has a relatively low frequency of $\sim$1720 cm^{-1}, and the angle between the carbonyl and hydroxyl groups of the carboxylic acid side group amounts to $\sim90^\circ$. For the other conformer the carbonyl stretch vibration has a relatively high frequency of $\sim$1745 cm^{-1}, and the angle between the carbonyl and hydroxyl groups of the carboxylic acid side group is $\sim35^\circ$. In line with earlier work we assign these conformers to nearly-planar syn- and anti-conformers, where we explain the deviations from the ideal values of 60° (syn) and 0° (anti) from small angle out-of-plane rotations of the hydroxyl and carbonyl groups.

We find that the anti-conformer of N-acetylaspartic acid amide has a relative abundance of $\sim25\%$, both when dissolved in DMSO and in water, which is significantly higher

than the <1% observed in gas-phase studies. Molecular dynamics simulations show that the increase of the relative abundance of the anti-conformer upon dissolution in water can be explained by the more favourable hydration of this conformer in comparison to the syn-conformer. The lower relative abundance of the anti-conformer in comparison to the syn-conformer implies that this conformer is more acidic in water than the syn-conformer, corresponding to a ΔpK_a of 0.5 ± 0.3. The acid dissociation is only one of the chemical properties of the carboxyl group that depends on the molecular conformation. Hence, the fact that both the syn- and the anti-conformers are present under biological conditions must be carefully taken into account when studying biochemical processes of polypeptides.

9.5 Appendix

9.5.1 Infrared spectra of N-acetylAspartic acid amide

The linear spectra of N-acetylaspartic acid in DMSO and water solutions are shown in Figure 9.7. For our purpose, we focus on the carbonyl and hydroxyl regions around 1700 cm^{-1} and 2700 cm^{-1}, respectively. In the carbonyl region, we observe the carbonyl stretching modes at 1720 cm^{-1}, and the amide I vibrations at 1680 cm^{-1}. We observe that in water the amide I and C=O vibrations are broader with respect to in DMSO solutions because of the strong interactions with the water molecules. In the hydroxyl region, we observe both in DMSO and in water solutions the broad structured band of the stretching mode of the hydroxyl group.

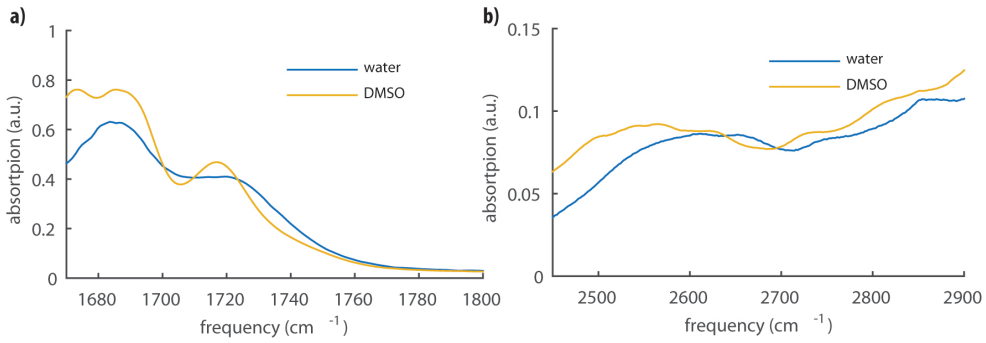

Figure 9.7: Linear infrared spectra of N-acetylaspartic acid amide in dimethyl sulfoxide and in aqueous solution in the frequency regions of the carbonyl a) and the hydroxyl b) vibrations. The absorption background of the solvent has been subtracted.

9.5.2 Syn- and anti- conformers in terminal –COOH groups of N-AcetylLeucine and N-AcetylPhenylalanine

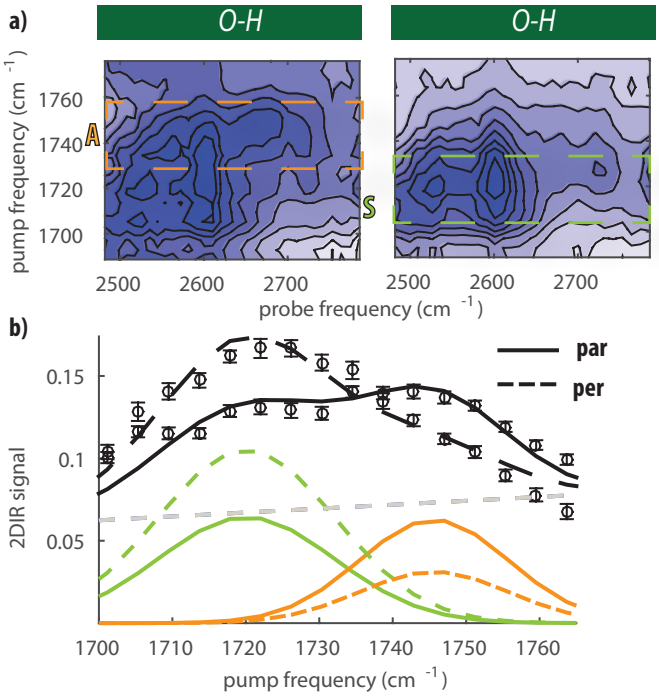

Figure 9.8: a) 2D-IR spectra in the C=O/O-H cross-peak region measured in parallel (left) and perpendicular (right) polarization configuration at a time delay T_w=0.5 ps. b) Parallel (solid) and perpendicular (dashed) transient absorption signal obtained by averaging the corresponding 2DIR signal over the probe frequency in the range between 2550 and 2750 cm^{-1}. The green and the orange colours indicate, respectively, the vibrational responses of the syn- and anti-conformers. The extracted anisotropy values are 0.25 and -0.15 for the anti- and syn-conformers, respectively.

To investigate the existence of distinct conformers of the –COOH groups of amino acids, we studied N-acetylleucine and N-acetylphenylalanine. For N-acetylphenylalanine the sidechain is a benzyl group, and for N-acetylleucine an isobutyl group. In Figure 9.8a we show 2DIR spectra obtained by exciting the carbonyl vibrations and probing the hydroxyl vibration of the–COOH group of N-acetylleucine, measured in parallel and perpendicular polarization configuration. We observe that in parallel polarization configuration the cross-peak is more intense at an excitation frequency of 1740 cm^{-1}, while in perpendicular polarization configuration the signal is most intense at an excitation

frequency of 1720 cm^{-1}. To extract the anisotropy of the signals, we average over the probe region between 2500 and 2700 cm^{-1}. Figure 9.8b shows the averaged parallel and perpendicular 2DIR signals as a function of the pump frequency. We fit the spectra with two Gaussian-shaped bands to extract their anisotropy values. We find that the cross-peak at the higher excitation frequency has a positive anisotropy ($R = 0.25$), while the one at the lower excitation frequency has a negative anisotropy ($R = -0.15$). Similar results are obtained for N-acetylphenylalanine (Figure 9.9). We assign the cross-peak signal with an excitation frequency of 1740 cm^{-1} and a positive anisotropy value to the anti-conformer, and the cross-peak signal with with an excitation frequency of 1720 cm^{-1} and a negative anisotropy to the syn-conformer.

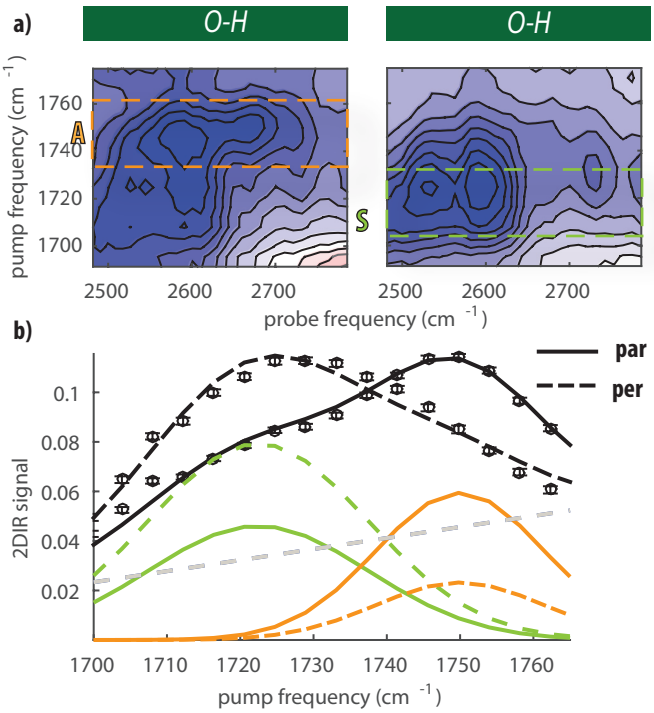

Figure 9.9: a) 2D-IR spectra of N-acetylphenylalanine in DMSO solution in the C=O/O-H cross-peak region measured in parallel (left) and perpendicular (right) polarization configuration at a time delay T_w=0.5 ps. b) Parallel (solid) and perpendicular (dashed) transient absorption signals obtained by averaging the 2DIR signals of Figure a) over the probe frequency in the range between 2550 and 2750 cm^{-1}. The green and the orange colours indicate, respectively, the vibrational responses of the syn- and anti-conformers. The extracted anisotropy values are 0.25 and -0.15 for the anti- and syn-conformers, respectively.

9.5.3 Concentration of syn- and anti-conformers in DMSO

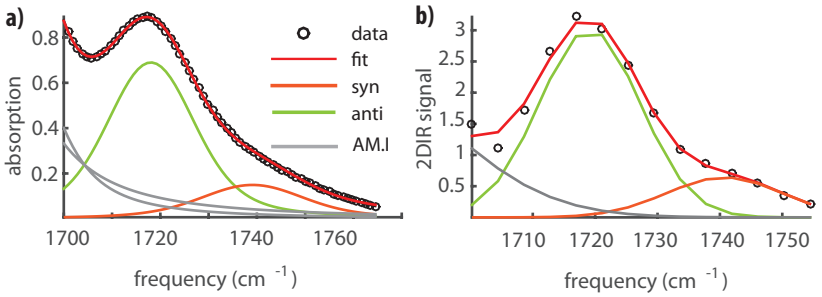

Figure 9.10: Fit of the linear infrared spectrum (a) and 2DIR diagonal slice (b) of N-acetylaspartic acid amide in DMSO solution with two Voigt-shaped bands corresponding to the syn- and anti-conformers. The extracted fraction of the anti-conformer is $20\pm10\%$. The additional Voigt bands (grey) represent the vibrational responses of the two amide groups, which are clearly observed in the linear infrared spectrum.

The relative abundances of the anti- and syn-conformers can be determined from the combination of the linear absorption spectrum and the diagonal 2DIR signal of the carbonyl vibrations. In this determination we make use of the fact that the linear infrared absorption spectrum scales with σ (where σ is the absorption cross-section), while the 2D-IR spectrum scales with σ^2, thus providing an additional relation between the measured signals, cross-sections and concentrations of the conformers. Figure 9.10a-b show the linear spectrum and the diagonal slice of the negative absorption change peaks as a function of pump frequency of N-acetylaspartic acid amide in DMSO. We fit the 2DIR signal by using two Voigt-shaped peaks, which represent the carbonyl stretching vibrations of syn and anti conformers. These two peaks are represented in Figure 9.10 by the green and orange colored peaks, respectively. We find that the *anti* area of the 2DIR signal is $20\pm10\%$, similarly to the linear spectrum, and that the cross-section ratio of the two conformers is 1 ± 0.2.

References

[1] de Grotthuss, C. Memoir on the decomposition of water and of the bodies that it holds in solution by means of galvanic electricity. *Biochimica et Biophysica Acta (BBA) - Bioenergetics* 2006, *1757*, 871–875.

[2] Bernal, J. D.; Fowler, R. H. A Theory of Water and Ionic Solution, with Particular Reference to Hydrogen and Hydroxyl Ions. *The Journal of Chemical Physics* 1933, *1*, 515–548.

[3] Cukierman, S. Et tu, Grotthuss! and other unfinished stories. *Biochimica et Biophysica Acta (BBA)-Bioenergetics* 2006, *1757*, 876–885.

[4] Eigen, M. Methods for investigation of ionic reactions in aqueous solutions with half-times as short as 10–9 sec. Application to neutralization and hydrolysis reactions. *Discussions of the Faraday Society* 1954, *17*, 194–205.

[5] Eigen, M.; De Maeyer, L. Self-dissociation and protonic charge transport in water and ice. *Proceedings of the Royal Society of London. Series A. Mathematical and Physical Sciences* 1958, *247*, 505–533.

[6] Eigen, M. Proton Transfer, Acid-Base Catalysis, and Enzymatic Hydrolysis. Part I: ELEMENTARY PROCESSES. *Angewandte Chemie International Edition in English* 1964, *3*, 1–19.

[7] Zundel, G. Hydration Structure and Intermolecular Interaction in Polyelectrolytes. *Angewandte Chemie International Edition in English* 1969, *8*, 499–509.

[8] Kampschulte-Scheuing, I.; Zundel, G. Tunnel effect, infrared continuum, and solvate structure in aqueous and anhydrous acid solutions. *The Journal of Physical Chemistry* 1970, *74*, 2363–2368.

[9] Agmon, N. The grotthuss mechanism. *Chemical Physics Letters* 1995, *244*, 456–462.

[10] Marx, D.; Tuckerman, M. E.; Hutter, J.; Parrinello, M. The nature of the hydrated excess proton in water. *Nature* 1999, *397*, 601–604.

[11] Markovitch, O.; Chen, H.; Izvekov, S.; Paesani, F.; Voth, G. A.; Agmon, N. Special pair dance and partner selection: Elementary steps in proton transport in liquid water. *The Journal of Physical Chemistry B* 2008, *112*, 9456–9466.

[12] Berkelbach, T. C.; Lee, H.-S.; Tuckerman, M. E. Concerted hydrogen-bond dynamics in the transport mechanism of the hydrated proton: A first-principles molecular dynamics study. *Physical review letters* 2009, *103*, 238302.

[13] Knight, C.; Voth, G. A. The curious case of the hydrated proton. *Accounts of chemical research* 2012, *45*, 101–109.

[14] Tse, Y.-L. S.; Knight, C.; Voth, G. A. An analysis of hydrated proton diffusion in ab initio molecular dynamics. *The Journal of chemical physics* 2015, *142*, 014104.

[15] Xu, J.; Zhang, Y.; Voth, G. A. Infrared spectrum of the hydrated proton in water. *The journal of physical chemistry letters* 2011, *2*, 81–86.

[16] Decka, D.; Schwaab, G.; Havenith, M. A THz/FTIR fingerprint of the solvated proton: evidence for Eigen structure and Zundel dynamics. *Physical Chemistry Chemical Physics* 2015, *17*, 11898–11907.

[17] Śmiechowski, M.; Stangret, J. Proton hydration in aqueous solution: Fourier transform infrared studies of HDO spectra. *The Journal of chemical physics* 2006, *125*, 204508.

[18] Dahms, F.; Fingerhut, B. P.; Nibbering, E. T.; Pines, E.; Elsaesser, T. Large-amplitude transfer motion of hydrated excess protons mapped by ultrafast 2D IR spectroscopy. *Science* 2017, *357*, 491–495.

[19] Izvekov, S.; Voth, G. A. Ab initio molecular-dynamics simulation of aqueous proton solvation and transport revisited. *The Journal of chemical physics* 2005, *123*, 044505.

[20] Woutersen, S.; Bakker, H. J. Ultrafast vibrational and structural dynamics of the proton in liquid water. *Physical review letters* 2006, *96*, 138305.

[21] Stoyanov, E. S.; Stoyanova, I. V.; Reed, C. A. The unique nature of H^+ in water. *Chemical Science* 2011, *2*, 462–472.

[22] Biswas, R.; Carpenter, W.; Fournier, J. A.; Voth, G. A.; Tokmakoff, A. IR spectral assignments for the hydrated excess proton in liquid water. *The Journal of chemical physics* 2017, *146*, 154507.

[23] Fournier, J. A.; Carpenter, W. B.; Lewis, N. H.; Tokmakoff, A. Broadband 2D IR spectroscopy reveals dominant asymmetric H 5 O 2+ proton hydration structures in acid solutions. *Nature chemistry* 2018, *10*, 932–937.

[24] Maupin, C. M.; Aradi, B.; Voth, G. A. The self-consistent charge density functional tight binding method applied to liquid water and the hydrated excess proton: benchmark simulations. *The Journal of Physical Chemistry B* 2010, *114*, 6922–6931.

[25] Carpenter, W. B.; Fournier, J. A.; Lewis, N. H.; Tokmakoff, A. Picosecond proton transfer kinetics in water revealed with ultrafast IR spectroscopy. *The Journal of Physical Chemistry B* 2018, *122*, 2792–2802.

[26] Lapid, H.; Agmon, N.; Petersen, M. K.; Voth, G. A. A bond-order analysis of the mechanism for hydrated proton mobility in liquid water. *The Journal of chemical physics* 2005, *122*, 014506.

[27] Fenn, E. E.; Wong, D. B.; Fayer, M. Water dynamics at neutral and ionic interfaces. *Proceedings of the National Academy of Sciences* 2009, *106*, 15243–15248.

[28] Moilanen, D. E.; Fenn, E. E.; Wong, D.; Fayer, M. D. Water dynamics in large and small reverse micelles: From two ensembles to collective behavior. *The Journal of chemical physics* 2009, *131*, 014704.

[29] Munoz-Santiburcio, D.; Marx, D. Chemistry in nanoconfined water. *Chemical science* 2017, *8*, 3444–3452.

[30] Chowdhary, J.; Ladanyi, B. M. Molecular simulation study of water mobility in aerosol-OT reverse micelles. *The Journal of Physical Chemistry A* 2011, *115*, 6306–6316.

[31] van der Loop, T. H.; Ottosson, N.; Lotze, S.; Kentzinger, E.; Vad, T.; Sager, W. F.; Bakker, H. J.; Woutersen, S. Structure and dynamics of water in nanoscopic spheres and tubes. *The Journal of chemical physics* 2014, *141*, 18C535.

[32] Tielrooij, K. J.; Cox, M. J.; Bakker, H. J. Effect of Confinement on Proton-Transfer Reactions in Water Nanopools. *ChemPhysChem* 2009, *10*, 245–251.

[33] Kim, J.; Schmitt, U. W.; Gruetzmacher, J. A.; Voth, G. A.; Scherer, N. E. The vibrational spectrum of the hydrated proton: Comparison of experiment, simulation, and normal mode analysis. *The Journal of chemical physics* 2002, *116*, 737–746.

[34] Agostini, F.; Vuilleumier, R.; Ciccotti, G. Infrared spectroscopy of small protonated water clusters at room temperature: an effective modes analysis. *The Journal of chemical physics* 2011, *134*, 084302.

[35] Kulig, W.; Agmon, N. A 'clusters-in-liquid'method for calculating infrared spectra identifies the proton-transfer mode in acidic aqueous solutions. *Nature chemistry* 2013, *5*, 29.

[36] Daly Jr, C. A.; Streacker, L. M.; Sun, Y.; Pattenaude, S. R.; Hassanali, A. A.; Petersen, P. B.; Corcelli, S. A.; Ben-Amotz, D. Decomposition of the experimental Raman and infrared spectra of acidic water into proton, special pair, and counterion contributions. *The journal of physical chemistry letters* 2017, *8*, 5246–5252.

[37] Kulig, W.; Agmon, N. Both zundel and eigen isomers contribute to the IR spectrum of the gas-phase H9O4+ cluster. *Journal of Physical Chemistry B* 2014, *118*, 278–286.

[38] Kulig, W.; Agmon, N. Deciphering the infrared spectrum of the protonated water pentamer and the hybrid Eigen-Zundel cation. *Physical Chemistry Chemical Physics* 2014, *16*, 4933–4941.

[39] Wang, H.; Agmon, N. Reinvestigation of the Infrared Spectrum of the Gas-Phase Protonated Water Tetramer. *Journal of Physical Chemistry A* 2017, *121*, 3056–3070.

[40] Samala, N. R.; Agmon, N. The protonated water trimer and its giant Fermi resonances. *Chemical Physics* 2018, *514*, 164–175.

[41] Headrick, J. M.; Diken, E. G.; Walters, R. S.; Hammer, N. I.; Christie, R. A.; Cui, J.; Myshakin, E. M.; Duncan, M. A.; Johnson, M. A.; Jordan, K. D. Spectral signatures of hydrated proton vibrations in water clusters. *Science* 2005, *308*, 1765–1769.

[42] Wolke, C. T.; Fournier, J. A.; Dzugan, L. C.; Fagiani, M. R.; Odbadrakh, T. T.; Knorke, H.; Jordan, K. D.; McCoy, A. B.; Asmis, K. R.; Johnson, M. A. Spectroscopic snapshots of the proton-transfer mechanism in water. *Science* 2016, *354*, 1131–1135.

[43] Fournier, J. A.; Wolke, C. T.; Johnson, C. J.; Johnson, M. A.; Heine, N.; Gewinner, S.; Schöllkopf, W.; Esser, T. K.; Fagiani, M. R.; Knorke, H., et al. Site-specific vibrational spectral signatures of water molecules in the magic H3O+ (H2O) 20 and Cs+ (H2O) 20 clusters. *Proceedings of the National Academy of Sciences* 2014, *111*, 18132–18137.

[44] Fournier, J. A.; Wolke, C. T.; Johnson, M. A.; Odbadrakh, T. T.; Jordan, K. D.; Kathmann, S. M.; Xantheas, S. S. Snapshots of Proton Accommodation at a Microscopic Water Surface: Understanding the Vibrational Spectral Signatures of the Charge Defect in Cryogenically Cooled H+(H2O)n=2-28 Clusters. *Journal of Physical Chemistry A* 2015, *119*, 9425–9440.

[45] Heine, N.; Fagiani, M. R.; Rossi, M.; Wende, T.; Berden, G.; Blum, V.; Asmis, K. R. Isomer-selective detection of hydrogen-bond vibrations in the protonated water hexamer. *Journal of the American Chemical Society* 2013, *135*, 8266–8273.

[46] Agmon, N. Infrared spectroscopy: The acid test for water structure. *Nature chemistry* 2016, *8*, 206.

[47] Thämer, M.; De Marco, L.; Ramasesha, K.; Mandal, A.; Tokmakoff, A. Ultrafast 2D IR spectroscopy of the excess proton in liquid water. *Science* 2015, *350*, 78–82.

[48] Reed, C. A. Myths about the proton. The nature of H^+ in condensed media. *Accounts of chemical research* 2013, *46*, 2567–2575.

[49] Serrano, R. Structure and function of plasma membrane ATPase. *Annual review of plant biology* 1989, *40*, 61–94.

[50] Fang, Y.; Jayaram, H.; Shane, T.; Kolmakova-Partensky, L.; Wu, F.; Williams, C.; Xiong, Y.; Miller, C. Structure of a prokaryotic virtual proton pump at 3.2 Å resolution. *Nature* 2009, *460*, 1040–1043.

[51] Sazanov, L. A. A giant molecular proton pump: structure and mechanism of respiratory complex I. *Nature Reviews Molecular Cell Biology* 2015, *16*, 375–388.

[52] Pedersen, B. P.; Buch-Pedersen, M. J.; Preben Morth, J.; Palmgren, M. G.; Nissen, P. Crystal structure of the plasma membrane proton pump. *Nature* 2007, *450*, 1111–1114.

[53] Abe, K.; Irie, K.; Nakanishi, H.; Suzuki, H.; Fujiyoshi, Y. Crystal structures of the gastric proton pump. *Nature* 2018, *556*, 214–218.

[54] Lanyi, J. K. Bacteriorhodopsin. *Annu. Rev. Physiol.* 2004, *66*, 665–688.

[55] Buch-Pedersen, M. J.; Pedersen, B. P.; Veierskov, B.; Nissen, P.; Palmgren, M. Protons and how they are transported by proton pumps. *Pflügers Archiv-European Journal of Physiology* 2009, *457*, 573.

[56] Morii, M.; Yamauchi, M.; Ichikawa, T.; Fujii, T.; Takahashi, Y.; Asano, S.; Takeguchi, N.; Sakai, H. Involvement of the H3O+-Lys-164-Gln-161-Glu-345 charge transfer pathway in proton transport of gastric H+, K+-ATPase. *Journal of Biological Chemistry* 2008, *283*, 16876–16884.

[57] Luecke, H.; Schobert, B.; Richter, H.-T.; Cartailler, J.-P.; Lanyi, J. K. Structure of bacteriorhodopsin at 1.55 Å resolution. *Journal of molecular biology* 1999, *291*, 899–911.

[58] Pranata, J. Relative basicities of carboxylate lone pairs in aqueous solution. *Journal of Computational Chemistry* 1993, *14*, 685–690.

[59] Sato, H.; Hirata, F. The syn-/anti-conformational equilibrium of acetic acid in water studied by the RISM-SCF/MCSCF method. *Journal of Molecular Structure: THEOCHEM* 1999, *461-462*, 113–120.

[60] Nagy, P. I. The syn–anti equilibrium for the COOH group reinvestigated. Theoretical conformation analysis for acetic acid in the gas phase and in solution. *Computational and Theoretical Chemistry* 2013, *1022*, 59–69.

[61] Boyd, R. W. *Nonlinear optics*; Elsevier, 2003.

[62] Mukamel, S. *Principles of nonlinear optical spectroscopy*; Oxford University Press on Demand, 1999.

[63] Hamm, P. Principles of nonlinear optical spectroscopy: A practical approach or: Mukamel for dummies. *University of Zurich* 2005, *41*, 77.

[64] Rezus, Y., et al. Snapshots of water: orientational dynamics of hydrogen-bonded systems. 2008,

[65] Lotze, S. M., et al. Architecture and dynamics of proteins and aqueous solvation complexes. Ph.D. thesis, 2015.

[66] Lippincott, E. R.; Schroeder, R. One-dimensional model of the hydrogen bond. *The Journal of Chemical Physics* 1955, *23*, 1099–1106.

[67] Chidambaram, R.; Balasubramanian, R.; Ramachandran, G. Potential functions for hydrogen bond interactions I. A modified lippincott-schroeder potential function for NH O interaction between peptide groups. *Biochimica et Biophysica Acta (BBA)-Protein Structure* 1970, *221*, 182–195.

[68] van Der Post, S., et al. *Love and fear of water: Water dynamics around charged and apolar solutes*; Ph. D. thesis, University of Amsterdam, 2014.

[69] Ferreiro, J. J.; de La Fuente, R.; López-Lago, E. Characterization of arbitrarily polarized ultrashort laser pulses by cross-phase modulation. *Optics letters* 2001, *26*, 1025–1027.

[70] Yeremenko, S. Water dynamics explored by femtosecond infrared spectroscopy. Ph.D. thesis, University of Gronningen, 2004.

[71] Lipari, G.; Szabo, A. Effect of librational motion on fluorescence depolarization and nuclear magnetic resonance relaxation in macromolecules and membranes. *Biophysical journal* 1980, *30*, 489.

[72] Dahms, F.; Costard, R.; Pines, E.; Fingerhut, B. P.; Nibbering, E. T.; Elsaesser, T. The hydrated excess proton in the Zundel cation H5O2+: The role of ultrafast solvent fluctuations. *Angewandte Chemie International Edition* 2016, *55*, 10600–10605.

[73] van Dam, E. P.; Giubertoni, G.; Burla, F.; Koenderink, G. H.; Bakker, H. J. Hyaluronan biopolymers release water upon pH-induced gelation. *Physical Chemistry Chemical Physics* 2020,

[74] Selig, O., et al. Ultrasensitive nonlinear vibrational spectroscopy of complex molecular systems. Ph.D. thesis, University of Amsterdam, 2017.

[75] Ando, K.; Hynes, J. T. Molecular mechanism of HF acid ionization in water: An electronic structure- Monte Carlo study. *The Journal of Physical Chemistry A* 1999, *103*, 10398–10408.

[76] Ottosson, N.; Liu, L.; Bakker, H. Vibrational Relaxation of the Aqueous Proton in Acetonitrile: Ultrafast Cluster Cooling and Vibrational Predissociation. *The Journal of Physical Chemistry B* 2016, *120*, 7154–7163.

[77] Liu, L.; Bakker, H. J. Infrared-activated proton transfer in aqueous nafion proton-exchange-membrane nanochannels. *Physical review letters* 2014, *112*, 258301.

[78] Van Der Post, S. T.; Hsieh, C.-S.; Okuno, M.; Nagata, Y.; Bakker, H. J.; Bonn, M.; Hunger, J. Strong frequency dependence of vibrational relaxation in bulk and surface water reveals sub-picosecond structural heterogeneity. *Nature communications* 2015, *6*, 8384.

[79] Ramasesha, K.; De Marco, L.; Mandal, A.; Tokmakoff, A. Water vibrations have strongly mixed intra-and intermolecular character. *Nature chemistry* 2013, *5*, 935–940.

[80] Wallace, V. M.; Dhumal, N. R.; Zehentbauer, F. M.; Kim, H. J.; Kiefer, J. Revisiting the aqueous solutions of dimethyl sulfoxide by spectroscopy in the mid-and near-infrared: Experiments and Car–Parrinello simulations. *The Journal of Physical Chemistry B* 2015, *119*, 14780–14789.

[81] Lotze, S.; Groot, C.; Vennehaug, C.; Bakker, H. Femtosecond Mid-Infrared Study of the Dynamics of Water Molecules in Water–Acetone and Water–Dimethyl Sulfoxide Mixtures. *The Journal of Physical Chemistry B* 2015, *119*, 5228–5239.

[82] Leuchs, M.; Zundel, G. Easily polarizable hydrogen bonds in aqueous solutions of acids. Perchloric acid and trifluoromethane sulphonic acid. *Journal of the Chemical Society, Faraday Transactions 2: Molecular and Chemical Physics* 1978, *74*, 2256–2267.

[83] Rossini, E.; Knapp, E.-W. Proton solvation in protic and aprotic solvents. *Journal of computational chemistry* 2016, *37*, 1082–1091.

[84] Wong, D. B.; Sokolowsky, K. P.; El-Barghouthi, M. I.; Fenn, E. E.; Giammanco, C. H.; Sturlaugson, A. L.; Fayer, M. D. Water dynamics in water/DMSO binary mixtures. *The Journal of Physical Chemistry B* 2012, *116*, 5479–5490.

[85] Lock, A.; Woutersen, S.; Bakker, H. Ultrafast energy equilibration in hydrogen-bonded liquids. *The Journal of Physical Chemistry A* 2001, *105*, 1238–1243.

[86] Rezus, Y. L. A.; Bakker, H. J. Orientational dynamics of isotopically diluted H2O and D2O. *The Journal of Chemical Physics* 2006, *125*, 144512.

[87] Turecek, F. Proton Affinity of Dimethyl Sulfoxide and Relative Stabilities of C 2 H 6 OS Molecules and C 2 H 7 OS + Ions. A Comparative G2(MP2) ab Initio and Density Functional Theory Study. *The Journal of Physical Chemistry A* 1998, *102*, 4703–4713.

[88] Rasul, G.; Prakash, G. K. S.; Olah, G. A. Protonated and Methylated Dimethyl Sulfoxide Cations and Dications. DFT/GIAO-MP2 NMR Studies and Comparison with Experimental Data 1. *The Journal of Organic Chemistry* 2000, *65*, 8786–8789.

[89] Liu, L.; Bakker, H. J. Vibrational Excitation Induced Proton Transfer in Hydrated Nafion Membranes. *The Journal of Physical Chemistry B* 2015, *119*, 2628–2637.

[90] Hammes-Schiffer, S.; Tully, J. C. Vibrationally Enhanced Proton Transfer. *The Journal of Physical Chemistry* 1995, *99*, 5793–5797.

[91] Kreuer, K.-D. Proton conductivity: materials and applications. *Chemistry of materials* 1996, *8*, 610–641.

[92] Garczarek, F.; Gerwert, K. Functional waters in intraprotein proton transfer monitored by FTIR difference spectroscopy. *Nature* 2006, *439*, 109–112.

[93] Voth, G. A. Computer simulation of proton solvation and transport in aqueous and biomolecular systems. *Accounts of chemical research* 2006, *39*, 143–150.

[94] Agmon, N.; Bakker, H. J.; Campen, R. K.; Henchman, R. H.; Pohl, P.; Roke, S.; Thamer, M.; Hassanali, A. Protons and hydroxide ions in aqueous systems. *Chemical reviews* 2016, *116*, 7642–7672.

[95] Fagiani, M. R.; Knorke, H.; Esser, T. K.; Heine, N.; Wolke, C. T.; Gewinner, S.; Schöllkopf, W.; Gaigeot, M.-P.; Spezia, R.; Johnson, M. A., et al. Gas phase vibrational spectroscopy of the protonated water pentamer: the role of isomers and nuclear quantum effects. *Physical Chemistry Chemical Physics* 2016, *18*, 26743–26754.

[96] Markovitch, O.; Agmon, N. Structure and energetics of the hydronium hydration shells. *The Journal of Physical Chemistry A* 2007, *111*, 2253–2256.

[97] Marx, D.; Chandra, A.; Tuckerman, M. E. Aqueous basic solutions: hydroxide solvation, structural diffusion, and comparison to the hydrated proton. *Chemical reviews* 2010, *110*, 2174–2216.

[98] Biswas, R.; Tse, Y.-L. S.; Tokmakoff, A.; Voth, G. A. Role of presolvation and anharmonicity in aqueous phase hydrated proton solvation and transport. *The Journal of Physical Chemistry B* 2016, *120*, 1793–1804.

[99] Nibbering, E. T.; Elsaesser, T. Ultrafast vibrational dynamics of hydrogen bonds in the condensed phase. *Chemical Reviews* 2004, *104*, 1887–1914.

[100] Napoli, J. A.; Marsalek, O.; Markland, T. E. Decoding the spectroscopic features and time scales of aqueous proton defects. *The Journal of chemical physics* 2018, *148*, 222833.

[101] Kalish, N. B.-M.; Shandalov, E.; Kharlanov, V.; Pines, D.; Pines, E. Apparent stoichiometry of water in proton hydration and proton dehydration reactions in CH3CN/H2O solutions. *The Journal of Physical Chemistry A* 2011, *115*, 4063–4075.

[102] Sigalov, M. V.; Kalish, N.; Carmeli, B.; Pines, D.; Pines, E. Probing Small Protonated Water Clusters in Acetonitrile Solutions by 1 H NMR. *Zeitschrift für Physikalische Chemie* 2013, *227*, 983–1007.

[103] Hunger, J.; Liu, L.; Tielrooij, K.-J.; Bonn, M.; Bakker, H. Vibrational and orientational dynamics of water in aqueous hydroxide solutions. *The Journal of chemical physics* 2011, *135*, 124517.

[104] Cringus, D.; Jansen, T. l. C.; Pshenichnikov, M. S.; Wiersma, D. A. Ultrafast anisotropy dynamics of water molecules dissolved in acetonitrile. *The Journal of chemical physics* 2007, *127*, 084507.

[105] Lozada-Hidalgo, M.; Zhang, S.; Hu, S.; Kravets, V. G.; Rodriguez, F. J.; Berdyugin, A.; Grigorenko, A.; Geim, A. K. Giant photoeffect in proton transport through graphene membranes. *Nature nanotechnology* 2018, *13*, 300–303.

[106] Ramaswamy, P.; Wong, N. E.; Shimizu, G. K. MOFs as proton conductors–challenges and opportunities. *Chemical Society Reviews* 2014, *43*, 5913–5932.

[107] Shimizu, G. K.; Taylor, J. M.; Kim, S. Proton conduction with metal-organic frameworks. *Science* 2013, *341*, 354–355.

[108] Thompson, W. H. Solvation dynamics and proton transfer in nanoconfined liquids. *Annual review of physical chemistry* 2011, *62*, 599–619.

[109] Spry, D.; Goun, A.; Glusac, K.; Moilanen, D. E.; Fayer, M. Proton transport and the water environment in nafion fuel cell membranes and AOT reverse micelles. *Journal of the American Chemical Society* 2007, *129*, 8122–8130.

[110] Lawler, C.; Fayer, M. D. Proton transfer in ionic and neutral reverse micelles. *The Journal of Physical Chemistry B* 2015, *119*, 6024–6034.

[111] Cohen, B.; Huppert, D.; Solntsev, K. M.; Tsfadia, Y.; Nachliel, E.; Gutman, M. Excited state proton transfer in reverse micelles. *Journal of the American Chemical Society* 2002, *124*, 7539–7547.

[112] Bardez, E.; Monnier, E.; Valeur, B. Dynamics of excited-state reactions in reversed micelles. 2. Proton transfer involving various fluorescent probes according to their sites of solubilization. *The Journal of Physical Chemistry* 1985, *89*, 5031–5036.

[113] Sedgwick, M.; Cole, R. L.; Rithner, C. D.; Crans, D. C.; Levinger, N. E. Correlating proton transfer dynamics to probe location in confined environments. *Journal of the American Chemical Society* 2012, *134*, 11904–11907.

[114] Dokter, A. M.; Woutersen, S.; Bakker, H. J. Anomalous slowing down of the vibrational relaxation of liquid water upon nanoscale confinement. *Physical review letters* 2005, *94*, 178301.

[115] Dokter, A. M.; Woutersen, S.; Bakker, H. J. Inhomogeneous dynamics in confined water nanodroplets. *Proceedings of the National Academy of Sciences* 2006, *103*, 15355–15358.

[116] Moilanen, D. E.; Levinger, N. E.; Spry, D.; Fayer, M. Confinement or the nature of the interface? Dynamics of nanoscopic water. *Journal of the American Chemical Society* 2007, *129*, 14311–14318.

[117] Rabie, H. R.; Vera, J. H. Counterion binding to ionic reverse micellar aggregates and its effect on water uptake. *The Journal of Physical Chemistry B* 1997, *101*, 10295–10302.

[118] Marques, B. S.; Nucci, N. V.; Dodevski, I.; Wang, K. W.; Athanasoula, E. A.; Jorge, C.; Wand, A. J. Measurement and control of pH in the aqueous interior of reverse micelles. *The Journal of Physical Chemistry B* 2014, *118*, 2020–2031.

[119] Mukherjee, P.; Gupta, S.; Rafiq, S.; Yadav, R.; Jain, V. K.; Raval, J.; Sen, P. Ramping of pH across the water-pool of a reverse micelle. *Langmuir* 2016, *32*, 1693–1699.

[120] Fuglestad, B.; Gupta, K.; Wand, A. J.; Sharp, K. A. Water loading driven size, shape, and composition of cetyltrimethylammonium/hexanol/pentane reverse micelles. *Journal of colloid and interface science* 2019, *540*, 207–217.

[121] Palazzo, G.; Lopez, F.; Giustini, M.; Colafemmina, G.; Ceglie, A. Role of the cosurfactant in the CTAB/water/n-pentanol/n-hexane water-in-oil microemulsion. 1. Pentanol effect on the microstructure. *The Journal of Physical Chemistry B* 2003, *107*, 1924–1931.

[122] Mills, A. J.; Britton, M. M. NMR study of the influence of n-alkanol co-surfactants on reverse micelles in quaternary microemulsions of cetyltrimethylammonium bromide (CTAB). *Magnetic Resonance in Chemistry* 2017, *55*, 425–432.

[123] De Marco, L.; Fournier, J. A.; Thämer, M.; Carpenter, W.; Tokmakoff, A. Anharmonic exciton dynamics and energy dissipation in liquid water from two-dimensional infrared spectroscopy. *The Journal of chemical physics* 2016, *145*, 094501.

[124] Seifert, G.; Patzlaff, T.; Graener, H. Size dependent ultrafast cooling of water droplets in microemulsions by picosecond infrared spectroscopy. *Physical review letters* 2002, *88*, 147402.

[125] Cringus, D.; Bakulin, A.; Lindner, J.; Vöhringer, P.; Pshenichnikov, M. S.; Wiersma, D. A. Ultrafast energy transfer in water- AOT reverse micelles. *The Journal of Physical Chemistry B* 2007, *111*, 14193–14207.

[126] Meiboom, S. Nuclear magnetic resonance study of the proton transfer in water. *The Journal of Chemical Physics* 1961, *34*, 375–388.

[127] Liu, L.; Hunger, J.; Bakker, H. J. Energy relaxation dynamics of the hydration complex of hydroxide. *The Journal of Physical Chemistry A* 2011, *115*, 14593–14598.

[128] Laage, D.; Hynes, J. T. Reorientional dynamics of water molecules in anionic hydration shells. *Proceedings of the National Academy of Sciences* 2007, *104*, 11167–11172.

[129] Laage, D.; Stirnemann, G.; Sterpone, F.; Rey, R.; Hynes, J. T. Reorientation and allied dynamics in water and aqueous solutions. *Annual review of physical chemistry* 2011, *62*, 395–416.

[130] van der Loop, T. H.; Ottosson, N.; Vad, T.; Sager, W. F.; Bakker, H. J.; Woutersen, S. Communication: Slow proton-charge diffusion in nanoconfined water. *The Journal of chemical physics* 2017, *146*, 131101.

[131] Tunuguntla, R. H.; Allen, F. I.; Kim, K.; Belliveau, A.; Noy, A. Ultrafast proton transport in sub-1-nm diameter carbon nanotube porins. *Nature nanotechnology* 2016, *11*, 639.

[132] Gopinadhan, K.; Hu, S.; Esfandiar, A.; Lozada-Hidalgo, M.; Wang, F.; Yang, Q.; Tyurnina, A.; Keerthi, A.; Radha, B.; Geim, A. Complete steric exclusion of ions and proton transport through confined monolayer water. *Science* 2019, *363*, 145–148.

[133] Singh, P. C.; Nihonyanagi, S.; Yamaguchi, S.; Tahara, T. Interfacial water in the vicinity of a positively charged interface studied by steady-state and time-resolved heterodyne-detected vibrational sum frequency generation. *The Journal of chemical physics* 2014, *141*, 18C527.

[134] Nguyen, K. T.; Nguyen, A. V. Suppressing interfacial water signals to assist the peak assignment of the N+–H stretching mode in sum frequency generation vibrational spectroscopy. *Physical Chemistry Chemical Physics* 2015, *17*, 28534–28538.

[135] Nguyen, K. T.; Nguyen, A. V.; Evans, G. M. Interfacial water structure at surfactant concentrations below and above the critical micelle concentration as revealed by sum frequency generation vibrational spectroscopy. *The Journal of Physical Chemistry C* 2015, *119*, 15477–15481.

[136] Agazzi, F. M.; Correa, N. M.; Rodriguez, J. Molecular dynamics simulation of water/BHDC cationic reverse micelles. structural characterization, dynamical properties, and influence of solvent on intermicellar interactions. *Langmuir* 2014, *30*, 9643–9653.

[137] Dokter, A. M.; Woutersen, S.; Bakker, H. J. Ultrafast dynamics of water in cationic micelles. *The Journal of chemical physics* 2007, *126*, 03B624.

[138] van der Loop, T. H.; Panman, M. R.; Lotze, S.; Zhang, J.; Vad, T.; Bakker, H. J.; Sager, W. F.; Woutersen, S. Structure and dynamics of water in nonionic reverse micelles: A combined time-resolved infrared and small angle x-ray scattering study. *The Journal of chemical physics* 2012, *137*, 044503.

[139] Tielrooij, K.; Timmer, R.; Bakker, H.; Bonn, M. Structure dynamics of the proton in liquid water probed with terahertz time-domain spectroscopy. *Physical review letters* 2009, *102*, 198303.

[140] Li, Z.; Voth, G. A. Interfacial solvation and slow transport of hydrated excess protons in non-ionic reverse micelles. *Physical Chemistry Chemical Physics* 2020,

[141] Bankura, A.; Chandra, A. Proton transfer through hydrogen bonds in two-dimensional water layers: A theoretical study based on ab initio and quantum-classical simulations. *The Journal of chemical physics* 2015, *142*, 044701.

[142] Dellago, C.; Naor, M. M.; Hummer, G. Proton transport through water-filled carbon nanotubes. *Physical review letters* 2003, *90*, 105902.

[143] Luzar, A.; Bratko, D. Electric double layer interactions in reverse micellar systems: A Monte Carlo simulation study. *The Journal of chemical physics* 1990, *92*, 642–648.

[144] Yu, J.; Degreve, L.; Lozada-Cassou, M. Charge separation in confined charged fluids. *Physical review letters* 1997, *79*, 3656.

[145] Brown, M. A.; Goel, A.; Abbas, Z. Effect of electrolyte concentration on the stern layer thickness at a charged interface. *Angewandte Chemie International Edition* 2016, *55*, 3790–3794.

[146] Kundu, A.; Dahms, F.; Fingerhut, B. P.; Nibbering, E. T.; Pines, E.; Elsaesser, T. Hydrated Excess Protons in Acetonitrile/Water Mixtures: Solvation Species and Ultrafast Proton Motions. *The journal of physical chemistry letters* 2019, *10*, 2287–2294.

[147] Zhao, X.; Bagwe, R. P.; Tan, W. Development of organic-dye-doped silica nanoparticles in a reverse microemulsion. *Advanced Materials* 2004, *16*, 173–176.

[148] Jafelicci Jr, M.; Davolos, M. R.; dos Santos, F. J.; de Andrade, S. J. Hollow silica particles from microemulsion. *Journal of non-crystalline solids* 1999, *247*, 98–102.

[149] Han, Y.-G.; Kusunose, T.; Sekino, T. One-step reverse micelle polymerization of organic dispersible polyaniline nanoparticles. *Synthetic Metals* 2009, *159*, 123–131.

[150] Fayer, M. D.; Levinger, N. E. Analysis of water in confined geometries and at interfaces. *Annual Review of Analytical Chemistry* 2010, *3*, 89–107.

[151] Sofronov, O. O.; Bakker, H. J. Vibrational Relaxation Dynamics of the Core and Outer Part of Proton-Hydration Clusters. *The Journal of Physical Chemistry B* 2019, *123*, 6222–6228.

[152] Sofronov, O. O.; Bakker, H. J. Energy Relaxation and Structural Dynamics of Protons in Water/DMSO Mixtures. *The Journal of Physical Chemistry B* 2018, *122*, 10005–10013.

[153] Sofronov, O. O.; Bakker, H. J. Slow Proton Transfer in Nanoconfined Water. *ACS Central Science* 2020, *6*, 1150—-1158.

[154] Covington, A. K.; Thompson, R. Ionization of moderately strong acids in aqueous solution. Part III. Methane-, ethane-, and propanesulfonic acids at 25 C. *Journal of Solution Chemistry* 1974, *3*, 603–617.

[155] Telfah, A.; Majer, G.; Kreuer, K.; Schuster, M.; Maier, J. Formation and mobility of protonic charge carriers in methyl sulfonic acid–water mixtures: A model for sulfonic

acid based ionomers at low degree of hydration. *Solid State Ionics* 2010, *181*, 461–465.

[156] Stoyanov, E. S.; Stoyanova, I. V.; Tham, F. S.; Reed, C. A. The nature of the hydrated proton H (aq)+ in organic solvents. *Journal of the American Chemical Society* 2008, *130*, 12128–12138.

[157] Stoyanov, E. S. Composition, structure and IR spectra peculiarities of proton hydratosolvates H+(H 2 O) NL p formed in tributylphosphate solutions of strong acid HFeCl 4. *Journal of the Chemical Society, Faraday Transactions* 1997, *93*, 4165–4175.

[158] Stoyanov, E. S.; Kim, K.-C.; Reed, C. A. A strong acid that does not protonate water. *The Journal of Physical Chemistry A* 2004, *108*, 9310–9315.

[159] Stoyanov, E. S.; Kim, K.-C.; Reed, C. A. The nature of the H3O+ hydronium ion in benzene and chlorinated hydrocarbon solvents. Conditions of existence and reinterpretation of infrared data. *Journal of the American Chemical Society* 2006, *128*, 1948–1958.

[160] Duong, C. H.; Gorlova, O.; Yang, N.; Kelleher, P. J.; Johnson, M. A.; McCoy, A. B.; Yu, Q.; Bowman, J. M. Disentangling the complex vibrational spectrum of the protonated water trimer, H+ (H2O) 3, with two-color IR-IR photodissociation of the bare ion and anharmonic VSCF/VCI theory. *The journal of physical chemistry letters* 2017, *8*, 3782–3789.

[161] Ishimoto, T.; Ogura, T.; Koyama, M. Stability and hydration structure of model perfluorosulfonic acid compound systems, CF3SO3H (H2O) n (n= 1–4), and its isotopomer by the direct treatment of H/D nuclear quantum effects. *Computational and Theoretical Chemistry* 2011, *975*, 92–98.

[162] Paddison, S. The modeling of molecular structure and ion transport in sulfonic acid based ionomer membranes. *Journal of New Materials for Electrochemical Systems* 2001, *4*, 197–208.

[163] Kurniawan, D.; Morita, S.; Kitagawa, K. Hydration structure of trifluoromethanesulfonate studied by quantum chemical calculations. *Computational and Theoretical Chemistry* 2012, *982*, 30–33.

[164] Shimoaka, T.; Wakai, C.; Sakabe, T.; Yamazaki, S.; Hasegawa, T. Hydration structure of strongly bound water on the sulfonic acid group in a Nafion membrane studied by infrared spectroscopy and quantum chemical calculation. *Physical Chemistry Chemical Physics* 2015, *17*, 8843–8849.

[165] Kinugasa, T.; Kondo, A.; Nishimura, S.; Miyauchi, Y.; Nishii, Y.; Watanabe, K.; Takeuchi, H. Estimation for size of reverse micelles formed by AOT and SDEHP based on viscosity measurement. *Colloids and Surfaces A: Physicochemical and Engineering Aspects* 2002, *204*, 193–199.

[166] Seeman, J. I. Effect of conformational change on reactivity in organic chemistry. Evaluations, applications, and extensions of Curtin-Hammett Winstein-Holness kinetics. *Chemical Reviews* 1983, *83*, 83–134.

[167] Taatjes, C. A.; Welz, O.; Eskola, A. J.; Savee, J. D.; Scheer, A. M.; Shallcross, D. E.; Rotavera, B.; Lee, E. P. F.; Dyke, J. M.; Mok, D. K. W.; Osborn, D. L.; Percival, C. J. Direct measurements of conformer-dependent reactivity of the Criegee intermediate CH3CHOO. *Science (New York, N.Y.)* 2013, *340*, 177–80.

[168] Park, S. T.; Kim, S. K.; Kim, M. S. Observation of conformation-specific pathways in the photodissociation of 1-iodopropane ions. *Nature* 2002, *415*, 306–308.

[169] Chang, Y.-P.; Długołęcki, K.; Küpper, J.; Rösch, D.; Wild, D.; Willitsch, S. Specific chemical reactivities of spatially separated 3-aminophenol conformers with cold Ca+ ions. *Science (New York, N.Y.)* 2013, *342*, 98–101.

[170] Kim, M.; Shen, L.; Tao, H.; Martinez, T.; Suits, A. Conformationally Controlled Chemistry: Excited-State Dynamics Dictate Ground-State Reaction. *Science* 2007, *315*, 1561–1565.

[171] Robertson, E. G.; Simons, J. P. Getting into shape: Conforrmational and supramolecular landscapes in small biomolecules and their hydrated clusters. *Physical Chemistry Chemical Physics* 2001, *3*, 1–18.

[172] Fischer, G.; Wittmann-Liebold, B.; Lang, K.; Kiefhaber, T.; Schmid, F. X. Cyclophilin and peptidyl-prolyl cis-trans isomerase are probably identical proteins. *Nature* 1989, *337*, 476–478.

[173] Freedman, R. Folding into the right shape. *Nature* 1987, *329*, 196–197.

[174] Zosel, F.; Mercadante, D.; Nettels, D.; Schuler, B. A proline switch explains kinetic heterogeneity in a coupled folding and binding reaction. *Nature Communications* 2018, *9*, 3332.

[175] Lu, K. P.; Finn, G.; Lee, T. H.; Nicholson, L. K. Prolyl cis-trans isomerization as a molecular timer. *Nature Chemical Biology* 2007, *3*, 619–629.

[176] Evans, P. A.; Dobson, C. M.; Kautz, R. A.; Hatfull, G.; Fox, R. O. Proline isomerism in staphylococcal nuclease characterized by NMR and site-directed mutagenesis. *Nature* 1987, *329*, 266–268.

[177] Ilmain, F.; Tanaka, T.; Kokufuta, E. Volume transition in a gel driven by hydrogen bonding. *Nature* 1991, *349*, 400–401.

[178] Alba, K.; Bingham, R. J.; Gunning, P. A.; Wilde, P. J.; Kontogiorgos, V. Pectin Conformation in Solution. *Journal of Physical Chemistry B* 2018, *122*, 7286–7294.

[179] Fausto, R.; Batista de Carvalho, L. A. E.; Teixeira-Dias, J. J. C.; Ramos, M. N. s-cis and s-trans Conformers of Formic, Thioformic and Dithioformic Acids. *J. Chem. Soc., Faraday Trans. 2* 1989, *85*, 1945–1962.

[180] Hirao, H. Theoretical study of formic acid: A new look at the origin of the planar Z conformation and C-O rotational barrier. *Chemical Physics* 2008, *344*, 213–220.

[181] Pettersson, M.; Maçôas, E. M.; Khriachtchev, L.; Fausto, R.; Räsänen, M. Conformational isomerization of formic acid by vibrational excitation at energies below the torsional barrier. *Journal of the American Chemical Society* 2003, *125*, 4058–4059.

[182] Maçôas, E. M.; Khriachtchev, L.; Fausto, R.; Räsänen, M. Photochemistry and Vibrational Spectroscopy of the Trans and Cis Conformers of Acetic Acid in Solid Ar. *Journal of Physical Chemistry A* 2004, *108*, 3380–3389.

[183] Maçôas, E. M. S.; Khriachtchev, L.; Pettersson, M.; Fausto, R.; Räsänen, M. Internal Rotation in Propionic Acid: Near-Infrared-Induced Isomerization in Solid Argon. *The Journal of Physical Chemistry A* 2005, *109*, 3617–3625.

[184] Marushkevich, K.; Khriachtchev, L.; Lundell, J.; Domanskaya, A. V.; Räsänen, M. Vibrational spectroscopy of trans and cis deuterated formic acid (HCOOD): Anharmonic calculations and experiments in argon and neon matrices. *Journal of Molecular Spectroscopy* 2010, *259*, 105–110.

[185] Marushkevich, K.; Khriachtchev, L.; Lundell, J.; Domanskaya, A.; Räsänen, M. Matrix isolation and ab initio study of trans-trans and trans-cis dimers of formic acid. *Journal of Physical Chemistry A* 2010, *114*, 3495–3502.

[186] Khriachtchev, L.; Domanskaya, A.; Marushkevich, K.; Räsänen, M.; Grigorenko, B.; Ermilov, A.; Andrijchenko, N.; Nemukhin, A. Conformation-dependent chemical reaction of formic acid with an oxygen atom. *Journal of Physical Chemistry A* 2009, *113*, 8143–8146.

[187] Génin, F.; Quilès, F.; Burneau, A. Infrared and Raman spectroscopic study of carboxylic acids in heavy water. *Physical Chemistry Chemical Physics* 2001, *3*, 932–942.

[188] Chen, J.; Brooks, C. L.; Scheraga, H. A. Revisiting the carboxylic acid dimers in aqueous solution: Interplay of hydrogen bonding, hydrophobic interactions and entropy. *Journal of Physical Chemistry B* 2008, *112*, 242–249.

[189] Heyne, K.; Huse, N.; Dreyer, J.; Nibbering, E. T. J.; Elsaesser, T.; Mukamel, S. Coherent low-frequency motions of hydrogen bonded acetic acid dimers in the liquid phase Coherent low-frequency motions of hydrogen bonded acetic acid dimers in the liquid phase. *J. Chem. Phys.* 2012, *902*, 902–913.

[190] Lopes, S.; Domanskaya, A. V.; Fausto, R.; Räsänen, M.; Khriachtchev, L. Formic and acetic acids in a nitrogen matrix: Enhanced stability of the higher-energy conformer. *Journal of Chemical Physics* 2010, *133*, 1–7.

[191] Kovács, A.; Nyerges, B.; Izvekov, V. Vibrational analysis of N-acetyl-alpha-D-glucosamine and beta-D-glucuronic acid. *The journal of physical chemistry. B* 2008, *112*, 5728–35.

[192] Moilanen, D. E.; Fenn, E. E.; Lin, Y.-S.; Skinner, J. L.; Bagchi, B.; Fayer, M. D. Water inertial reorientation: Hydrogen bond strength and the angular potential. *Proceedings of the National Academy of Sciences* 2008, *105*, 5295–5300.

[193] Mwaura, J.; Tao, Z.; James, H.; Albers, T.; Schwartz, A.; Grewer, C. Protonation state of a conserved acidic amino acid involved in Na + binding to the glutamate transporter EAAC1. *ACS Chemical Neuroscience* 2012, *3*, 1073–1083.

[194] Di Nardo, G.; Breitner, M.; Bandino, A.; Ghosh, D.; Jennings, G. K.; Hackett, J. C.; Gilardi, G. Evidence for an Elevated Aspartate pK_a in the Active Site of Human Aromatase. *Journal of Biological Chemistry* 2015, *290*, 1186–1196.

[195] Hanz, S. Z.; Shu, N. S.; Qian, J.; Christman, N.; Kranz, P.; An, M.; Grewer, C.; Qiang, W. Protonation-Driven Membrane Insertion of a pH-Low Insertion Peptide. *Angewandte Chemie - International Edition* 2016, *55*, 12376–12381.

[196] Gunner, M. R.; Alexov, E. A pragmatic approach to structure based calculation of coupled proton and electron transfer in proteins. *Biochimica et Biophysica Acta - Bioenergetics* 63–87.

[197] Davis, C. M.; Dyer, R. B. The Role of Electrostatic Interactions in Folding of β-Proteins. *Journal of the American Chemical Society* 2016, *138*, 1456–1464.

[198] Isom, D. G.; Castañeda, C. A.; Cannon, B. R.; Velu, P. D.; García-Moreno E, B. Charges in the hydrophobic interior of proteins. *Proceedings of the National Academy of Sciences of the United States of America* 16096–100.

[199] Garczarek, F.; Gerwert, K. Functional waters in intraprotein proton transfer monitored by FTIR difference spectroscopy. *Nature* 2006, *439*, 109–112.

[200] Jasti, J.; Furukawa, H.; Gonzales, E. B.; Gouaux, E. Structure of acid-sensing ion channel 1 at 1.9 Å resolution and low pH. *Nature* 2007, *449*, 316–323.

[201] Yoder, N.; Yoshioka, C.; Gouaux, E. Gating mechanisms of acid-sensing ion channels. *Nature* 2018, *555*, 397–401.

[202] Pettersson, M.; Lundell, J.; Khriachtchev, L.; Rasanen, M. IR spectrum of the other rotamer of formic acid, cis-HCOOH. *Journal of the American Chemical Society* 1997, *119*, 11715–11716.

[203] Maçôas, E. M. S.; Khriachtchev, L.; Pettersson, M.; Fausto, R.; Räsänen, M. Rotational isomerization of small carboxylic acids isolated in argon matrices: Tunnelling and quantum yields for the photoinduced processes. *Phys. Chem. Chem. Phys.* 2005, *7*, 743–749.

[204] D'Ascenzo, L.; Auffinger, P. A comprehensive classification and nomenclature of carboxyl–carboxyl(ate) supramolecular motifs and related catemers: implications for biomolecular systems. *Acta Crystallographica Section B Structural Science, Crystal Engineering and Materials* 2015, *71*, 164–175.

[205] Gandour, R. D. On the importance of orientation in general base catalysis by carboxylate. *Bioorganic Chemistry* 1981, *10*, 169–176.

[206] Salmon, M.; Thimmappa, R. B.; Minto, R. E.; Melton, R. E.; Hughes, R. K.; O'maille, P. E.; Hemmings, A. M.; Osbourn, A. A conserved amino acid residue critical for product and substrate specificity in plant triterpene synthases. *Proceedings of the National Academy of Sciences of the United States of America* 2016, *113*, E4407–E4414.

[207] Świderek, K.; Tuñón, I.; Moliner, V.; Bertran, J. Protein Flexibility and Preorganization in the Design of Enzymes. The Kemp Elimination Catalyzed by HG3.17. *ACS Catalysis* 2015, *5*, 2587–2595.

[208] Bahnson, B. J.; Anderson, V. E.; Petsko, G. A. Structural mechanism of enoyl-CoA hydratase: Three atoms from a single water are added in either an E1cb stepwise or concerted fashion. *Biochemistry* 2002, *41*, 2621–2629.

[209] Debler, E. W.; Ito, S.; Seebeck, F. P.; Heine, A.; Hilvert, D.; Wilson, I. A. Structural origins of efficient proton abstraction from carbon by a catalytic antibody. *Proceedings of the National Academy of Sciences* 2005, *102*, 4984–4989.

[210] Eriksson, A.; Kürten, C.; Syrén, P.-O. Protonation-Initiated Cyclization by a Class II Terpene Cyclase Assisted by Tunneling. *ChemBioChem* 2017, *18*, 2301–2305.

[211] Khavrutskii, I. V.; Compton, J. R.; Jurkouich, K. M.; Legler, P. M. Paired Carboxylic Acids in Enzymes and Their Role in Selective Substrate Binding, Catalysis, and Unusually Shifted p K a Values. *Biochemistry* 2019, *58*, 5351–5365.

[212] Gündoğdu, K.; Bandaria, J.; Nydegger, M.; Rock, W.; Cheatum, C. M. Relaxation and anharmonic couplings of the O–H stretching vibration of asymmetric strongly hydrogen-bonded complexes. *The Journal of Chemical Physics* 2007, *127*, 044501.

[213] Stingel, A. M.; Petersen, P. B. Couplings Across the Vibrational Spectrum Caused by Strong Hydrogen Bonds: A Continuum 2D IR Study of the 7-Azaindole-Acetic Acid Heterodimer. *Journal of Physical Chemistry B* 2016, *120*, 10768–10779.

[214] Pal, R.; Reddy, M. B. M.; Dinesh, B.; Venkatesha, M. A.; Grabowsky, S.; Jelsch, C.; Guru Row, T. N. Syn vs Anti Carboxylic Acids in Hybrid Peptides: Experimental and Theoretical Charge Density and Chemical Bonding Analysis. *The Journal of Physical Chemistry A* 2018, *122*, 3665–3679.

[215] Hume, S.; Hithell, G.; Greetham, G. M.; Donaldson, P. M.; Towrie, M.; Parker, A. W.; Baker, M. J.; Hunt, N. T. Measuring proteins in H2O with 2D-IR spectroscopy. *Chemical Science* 2019, *10*, 6448–6456.

[216] Sofronov, O. O.; Giubertoni, G.; Pérez de Alba Ortíz, A.; Ensing, B.; Bakker, H. J. Peptide Side-COOH Groups Have Two Distinct Conformations under Bio-Relevant Conditions. *The Journal of Physical Chemistry Letters 11*.

[217] Peterson, M. R.; Csizmadia, I. G. Determination and analysis of the formic acid conformational hypersurface. *Journal of the American Chemical Society* 1979, *101*, 1076–1079.

[218] Wiberg, K. B.; Laidig, K. E. Barriers to rotation adjacent to double bonds. 3. The carbon-oxygen barrier in formic acid, methyl formate, acetic acid, and methyl acetate. The origin of ester and amide resonance. *Journal of the American Chemical Society* 1987, *109*, 5935–5943.

[219] Hammer, S. C.; Marjanovic, A.; Dominicus, J. M.; Nestl, B. M.; Hauer, B. Squalene hopene cyclases are protonases for stereoselective Brønsted acid catalysis. *Nature Chemical Biology* 2015, *11*, 121–126.

Summary

Protons (H^+) are the most abundant cations in chemical processes. In solutions they usually originate either from the dissociation of Brønsted acids or from the oxidation of hydrogen. Proton itself is a superacid and in solution it always interacts with either with the conjugate base or with the solvent molecules forming complex solvation structures. Particularly interesting is proton solvation in aqueous or water-containing mixed solvents. Water molecules being able to accept and donate proton facilitate a special relay mechanism of proton diffusion. The molecular events of proton transfer occur on picosecond time scale. Thus, to study structure and dynamics of various protonated species we use femtosecond pump-probe and two-dimensional infrared spectroscopy. In these methods we excite the vibrations of the solvated protons with an intense femtosecond pump pulse and measure the time dependent changes in the infrared absorption spectrum using a delayed weak probe pulse. From these spectral changes we can draw conclusions about the dynamics of energy redistribution within the proton solvation structures. In addition, from the dependence of the absorption change on the relative polarization of pump and probe pulses (parallel or perpendicular) we obtain the information about the relative orientation of the transition dipole moments of the vibrations and the molecular groups corresponding to them.

Dynamics of Protons in Water/DMSO Mixtures First, we study the solvation of proton in mixed water/dimethyl sulfoxide (DMSO) solvent. At the concentration ratios we used, water mostly exist as monomers surrounded by DMSO molecules. DMSO being a good hydrogen bond acceptor can solvate water molecules. It creates for the water molecules environment similar to that in neat water, still isolating them from each other, what results in slower vibrational relaxation. We find that in this systems protons are mostly shared between water and DMSO molecules forming $(DMSO\text{-}H)^+$–H_2O clusters. After the excitation of the DMSO-H stretch vibration of this complex we observe an ultrafast contraction of the hydrogen bond between the water molecule and the protonated DMSO cation. Transfer of the excitation energy to this hydrogen bond results in creation of the *local hot state* and partial dissociation of the proton solvation clusters with a water molecule being ejected.

Vibrational Dynamics of the Core and Outer Part of Hydrated Proton We continue studying proton solvation in mixed water containing solvents with experiments on small (2-6 molecules) protonated water clusters embedded in acetonitrile.

Since acetonitrile is much weaker hydrogen bond acceptor than water and DMSO, in this case proton is solvated only by water molecules. In this work we perform the assignment of the OH-stretch absorption spectrum to vibrations in different parts of the hydrated proton. Varying the excitation frequency in our pump-probe experiments, we show that the at frequencies $\leqslant$3100 cm^{-1} mostly the OH-stretch vibrations in the core of the hydrated proton absorb. These OH-groups carry a significant part of the proton positive charge. The OH-vibrations of the outer part of the proton hydration structure mostly absorb at frequencies $\geqslant$3300 cm^{-1}.

Slow Proton Transfer in Nanoconfined Water Proton transfer in nanochannels of biological and artificial membranes is essential for generation and storage of energy. Proton transfer in water involves the rearrangement of many hydrogen bonds, and as such can be strongly affected by nanoconfinement. Using polarization-resolved femtosecond infrared spectroscopy we study dynamics of proton transfer in water nanodroplets of cationic reverse micelles. We find that in bulk water the elementary step of proton transfer - proton hopping between two water molecules - occurs with a time constant T_h=1.6 ps. In nanoconfined water proton hopping occurs much slower: 7 ps in the nanodroplets of diameter 7.4 nm and >10 ps for smaller nanodroplets. This finding indicates that proton hydration structures are highly extended and proton hopping involves rearrangement of multiple hydrogen bonds.

Vibrations of Hydrated Protons in Reverse Micelles The infrared spectrum of hydrated protons in liquid is usually referred as a broad continuous absorption. In our study we focus on the part of the spectrum corresponding to the OH-stretch vibrations (2000-2800 cm^{-1}). With polarization-resolved two-color pump-probe experiments we find that hydrated protons have two distinct OH-stretch vibrations. The high frequency vibration ($\sim$2600 cm^{-1}) is less degenerate and the low frequency vibration ($\sim$2300 cm^{-1}) is more degenerate. In agreement with earlier experiments on small protonated clusters in gas phase, we propose the proton hydration structure is the asymmetric H_3O^+ cation donating two strong hydrogen bonds to water molecules, and a weak hydrogen bond to either a more weakly accepting water molecule or to a counterion. This chapter presents the first detailed study of the OH-stretch spectrum of the hydrated proton in liquid, which provides new information about the proton hydration structure.

Observation of Distinct Carboxylic Acid Conformers in Aqueous Solution An important class of molecules related to proton transfer is carboxylic acids. Carboxyl groups are the most common proton donors in biochemistry and play a central role in proton conduction through the nanochannels of biological membranes. Using two-dimensional infrared spectroscopy we show that in solutions carboxyl groups adopt two conformations: syn and anti. In syn conformation the O-H-group of carboxyl is oriented at $\sim$60° with respect to the C=O-group, and in anti conformation the O-H-group is oriented anti-parallel to the C=O-group. For the simplest carboxylic acid - formic acid -

we show that the anti-conformer is less stable than the syn-conformer. However, fraction of the anti-conformer (20-30%) in solution at room temperature is much more significant than it was expected from theoretical studies.

Conformations of Peptide Side-COOH Groups Under Bio-relevant Conditions In proteins carboxyl groups are usually represented by the acidic side chains of aspartic acid and glutamic acid residues. We continue investigation of conformational isomerism of carboxyl groups using N-acetyl aspartic acid amide as a model peptide. We show that even for such a complex molecule the side chain carboxyl group still adopts syn and anti conformations in aqueous solution at room temperature with the syn/anti ratio 75/25. This finding shows that the syn/anti conformational isomerism is an intrinsic property of carboxyl groups and, thus, should be taken into account when studying complex processes in proteins, such as enzymatic reactions or proton conduction though protein nanochannels.

Samenvatting

Protonen (H^+) zijn de meest voorkomende kationen in chemische processen. In oplossingen ontstaan ze meestal vanuit de dissociatie van Brønsted zuren, of vanuit de oxidatie van waterstof. Proton zelf is een superzuur en in oplossing interacteert het altijd of met de geconjugeerde base, of met de oplosmiddelmoleculen, waarbij het complexe solvatatiestructuren vormt. Proton solvatatie in waterige of waterhoudende gemengde oplosmiddelen is bijzonder interessant. Watermoleculen zijn in staat een proton te accepteren en te doneren, en faciliteren daardoor een speciaal estafette mechanisme van proton diffusie. De moleculaire processen van protonoverdracht vinden plaats op een picosonde tijdschaal. Om de structuur en dynamica van verschillende geprotoneerde moleculen te bestuderen gebruiken we daarom femtoseconde pomp-probe en tweedimensionale infraroodspectroscopie. In deze methoden exciteren we de vibraties van de gesolvateerde protonen met een intense femtoseconde pomp puls, en meten we de tijdsafhankelijke veranderingen in het infrarood absorptiespectrum, door middel van een vertraagde zwakke probe puls. Uit deze spectrale veranderingen kunnen we conclusies trekken over de dynamica van de energieherverdeling binnen de proton solvatatiestructuren. Daarnaast verkrijgen we vanuit de afhankelijkheid van de absorptieverandering van de relatieve polarisatie van de pomp en probe licht pulsen (parallel of loodrecht) informatie over de relatieve ori ëntatie van de transitiedipoolmomenten van de vibraties en de bijbehorende moleculaire groepen.

Dynamica van protonen in water/DMSO mengsels Eerst bestuderen we de solvatatie van protonen in gemengd water/dimethyl sulfoxide (DMSO) oplosmiddel. Bij de concentratieverhoudingen die we gebruikt hebben, bestaan de watermoleculen voornamelijk als monomeren omringd door DMSO-moleculen. Als goede waterstofbrug acceptor is DMSO in staat watermoleculen te solvateren. Het creëert een omgeving die vergelijkbaar is met die in zuiver water, maar isoleert watermoleculen van elkaar. Wij vinden dat in deze systemen, protonen meestal gedeeld worden tussen water en DMSO-moleculen, die $(DMSO\text{-}H)^+$–H_2O clusters vormen. Na de excitatie van de DMSO-H^+ OH-strek vibratie observeren we een ultrasnelle samentrekking van de waterstofbrug tussen het watermolecuul en het geprotoneerde DMSO kation. Overdracht van de excitatie energie naar deze waterstofbrug resulteert in de creatie van de *lokale hete toestand* en gedeeltelijke dissociatie van de proton solvatatieclusters waarbij een watermolecuul wordt uitgestoten.

Vibrationele dynamica van de kern en buitenste deel van gehydra-

TEERD PROTON We vervolgen het bestuderen van protonsolvatatie in water mengsels die oplosmiddelen bevatten met experimenten aan kleine (2-6 moleculen) geprotoneerde water clusters ingebed in acetonitril. Aangezien acetonitril een veel zwakkere waterstofbrug acceptor is dan water en DMSO, worden de protonen alleen gesolvateerd door watermoleculen. In dit werk voeren we de toewijzing uit van het OH-strek absorptiespectrum aan trillingen in verschillende delen van het gehydrateerde proton. Door het variëren van de excitatie frequentie in onze pomp-probe experimenten, tonen we aan dat bij de frequenties $\leqslant$3100 cm^{-1} voornamelijk de OH-strekvibraties in de kern van het gehydrateerde proton absorberen. Deze OH-groepen dragen een significant gedeelte van de proton positieve lading. De OH-vibraties van het buitenste gedeelte van de proton hydratatie structuur absorbeert voornamelijk bij frequenties $\geqslant$3300 cm^{-1}.

LANGZAAM PROTONOVERDRACHT IN NANO-INGEPERKT WATER Protonoverdracht in nanokanalen van biologische en kunstmatige membranen is essentieel voor de opwekking en opslag van energie. Protonoverdracht in water omvat de herschikking van vele waterstofbruggen, en kan als zodanig sterk worden beïnvloed door nano-inperking. Met behulp van polarisatie-opgeloste femtoseconde infraroodspectroscopie bestuderen we de dynamica van protonoverdracht in water nanodruppels van kationische inverse micellen. We vinden dat in bulk water de elementaire stap van protonoverdracht – protonhoppen tussen twee watermoleculen – plaatsvindt met een tijdsconstante T_h=1.6 ps. In nano-ingeperkt water is protonhoppen veel langzamer: 7 ps in de nanodruppels met een diameter van 7.4 nm en $>$10 ps voor kleinere nanodruppels. Deze bevinding geeft aan dat protonhydratatiestructuren sterk uitgebreid zijn en bij protonhoppen een herschikking van meerdere waterstofbruggen plaatsvindt.

VIBRATIES VAN GEHYDRATEERDE PROTONEN IN INVERSE MICELLEN Het infraroodspectrum van gehydrateerde proton in vloeistoffen wordt meestal een brede continue absorptie genoemd. In onze studie focussen we op het gedeelte van het spectrum dat correspondeert met de OH-strekvibraties (2000-2800 cm^{-1}). Met polarisatie-opgeloste twee kleuren pomp-probe experimenten vinden we dat gehydrateerde protonen twee verschillende OH-strekvibraties hebben. Overeenkomend met eerdere experimenten aan kleine geprotoneerde clusters in de gasfase, stellen we voor dat in anionische (AOT) inverse micellen protonen sterk gehecht zijn aan de sulfonaat groep van de surfactant. De protonhydratatiestructuur is het asymmetrische H_3O^+ kation dat twee sterke waterstofbruggen aan watermoleculen doneert, en een zwakkere waterstofbrug aan de sulfonaat groep. In kationische inverse micellen zijn de protonen voornamelijk gelegen in de middelste kern van de water nanodruppel. De meeste protonhydratatiestructuren zijn echter ook asymmetisch.

OBSERVATIE VAN VERSCHILLENDE CARBONZUURCONFORMEREN IN WATERIGE OPLOSSING Een belangrijke klasse moleculen gerelateerd aan protonoverdracht zijn carbonzuren. Carbonzuren zijn de meeste voorkomende proton donoren in de biochemie

en spelen een centrale rol in protongeleiding door de nanokanalen van biologische membranen. Door middel van tweedimensionale infraroodspectroscopie tonen we aan dat in oplossingen carboxylgroepen twee conformaties aannemen: syn en anti. In syn conformatie is de O-H- groep van carboxyl georiënteerd op $\sim 60^{\circ}$ ten opzichte van de C=O groep, en in anti conformatie is de O-H-groep anti-parallel georiënteerd ten opzichte van de C=O groep. Voor het simpelste carbonzuur – methaanzuur – tonen we aan dat de anti-conformeer minder stabiel is dan de syn-conformeer. Echter, de fractie anti-conformeer (20-30%) in oplossing bij kamertemperatuur is significanter dan verwacht werd vanuit theoretische studies.

Conformaties van peptide zij-$COOH$ groepen onder bio-relevante condities In eiwitten zijn carboxylgroepen meestal aanwezig als de zure zijketens van asparaginezuur en glutaminezuur residuen. We vervolgen het onderzoek van de conformationele isomerie van carboxylgroepen door middel van N-acetyl asparaginezuur amide als een model peptide. We tonen aan dat zelfs voor een complex molecuul de zijketen carboxylgroep nog steeds syn en anti conformaties aanneemt in waterige oplossing bij kamertemperatuur, met een syn/anti ratio 75/25. Deze bevinding toont aan dat de syn/anti conformationele isomerie een intrinsieke eigenschap is van carboxylgroepen en dus in overweging moet worden genomen wanneer complexe processen in eiwitten worden bestudeerd, zoals enzymatische reacties of protongeleiding door eiwit nanokanalen.

Publications

Publications covered by this thesis

1. O.O. Sofronov, H.J. Bakker. Energy Relaxation and Structural Dynamics of Protons in Water/DMSO Mixtures. *The Journal of Physical Chemistry B* 2018, *122*, 10005-10013.

2. O.O. Sofronov, H.J. Bakker. Vibrational Relaxation Dynamics of the Core and Outer Part of Proton-Hydration Clusters. *The Journal of Physical Chemistry B* 2019, *123*, 6222-6228.

3. O.O. Sofronov, H.J. Bakker. Slow Proton Transfer in Nanoconfined Water. *ACS Central Science* 2020, *6*, 1150–1158.

4. O.O. Sofronov, H.J. Bakker. Nature of hydrated proton vibrations revealed by nonlinear spectroscopy of acid water nanodroplets. *Physical Chemistry Chemical Physics* 2020, 22, 21334 - 21339.

5. G. Giubertoni, O.O. Sofronov, H.J.Bakker. Observation of Distinct Carboxylic Acid Conformers in Aqueous Solution. *Journal of Physical Chemistry Letters* 2019, *10*, 3217-3222.

6. O.O. Sofronov, G. Giubertoni, A. Pérez de Alba Ortíz, B. Ensing, H.J. Bakker. Peptide side-COOH groups have two distinct conformations under bio-relevant conditions. *Journal of Physical Chemistry Letters* 2020, *11*, 3466-3472.

Other publications from the author

1. G. Giubertoni, O.O. Sofronov, H.J. Bakker. The effect of inter-molecular and intra-molecular interactions on the stability of syn and anti -COOH conformers. *Communications Chemistry* 2020, *3*, 84.

2. F. Lahrouch, O.O. Sofronov, G. Creff, A. Rossberg, C. Hennig, C. Den Auwer, C. Di Giorgio. Polyethyleneimine methylphosphonate: towards the design of a new class of macromolecular actinide chelating agents in the case of human exposition. *Dalton Transactions* 2017, *46*, 13869-13877.

Acknowledgments

There are a lot of people, who helped me to complete this thesis, and I would like to thank them. First of all, I would like to thank all the tax payers of the European Union. My project was supported by European Research Council and it means that every tax payer contributed to this research. Does not matter if you make apps for smartphones or you clean the floor, when you pay taxes you contribute to this science.

I would like to thank my supervisor Huib. You hired me for this job, you gave me freedom in performing the research projects, you discussed with me the results of the research, you asked me what am I eating for lunch, and together we have written some papers. Thank you for that.

I thank Hinco for providing the great solutions for all the technical problems I encountered, and I thank Niels and Dion, who always helped me when Hinco was not there. Thank you Teresa for helping me to talk to Huib and thank you Reshma for all the funny talks we had. I also appreciate all the great job done by people from electronics, software, ICT, HR, purchase and many other departments of AMOLF. I believe that the support you provide for researchers is the thing that makes AMOLF such a great place to work at.

I thank my collaborators Alberto and Bernd, we have made a great paper together. I thank my other collaborators Olivier and Sonia, we did not write a paper together (yet), but it was cool to work with you.

Of course, I want to thank my group members, who helped me throughout these four years. Thank you Jan for bringing to life IRIS even when it was dead and for talks about bike trips at the coffee breaks. Thank you Harmen for your great help in the lab during my first year and for the nights at Veldhoven on separate beds. Thank you Roberto for the endless talks about the local hot state and for that trip to a ghost village in New Zealand. Thank you Rahul for talks about how science works and for trying to understand my jokes. I would like to thank Johannes and Biplab, you are nice guys when you are ~~far away~~ not together. Besides the jokes, you helped me several times, I know. Thank you Eliane for organizing this group, for helping me with Dutch language and for headbanging with me. Many thanks to Carolyn for joining the group and doing the ice project, and thanks for smiling to me at coffee-breaks. Thanks to Balázs for taking into account all the things I said about IRIS, at that point I didn't know that I wouldn't use it anymore, and thanks for accepting the rules of the office 2.16. Thank you Alexandra

for being a milestone in the development of the new 2.16 culture and being my friend. Thank you for understanding me and for the long walks with your bike. I thank another pillar of the office 2.16 - my friend Alexander. Thank you for all the cool stuff that we did together at work and outside of work. Thank you for all the deep conversations we had. You understand me better than anyone in this country. Now you are going to dive into this s...tuff alone, I wish you good luck. Of course, great thanks goes to my friend Giulia. I think you literally did more than anyone else for this thesis. Thank you for asking me once "what can be that second peak?", the question that yielded three papers (of course, we know which paper is "the best") and two chapters of this thesis. We were supervising each other and it definitely helped me to finish my PhD in time. Thank you for believing in me, but I guess my arm will become a gravestone for syn and anti. Also thanks to all the other group members and people whom I met at AMOLF: Yves, Carien, Oleg, Simona, Wilbert, Andrea, Konrad, Marloes, Aditi, Wim, Iarik, Jenny. To all my ultrafast fellas:

Life is barely long enough to get good at one thing.
So be careful what you get good at.
- Rust Cohle

I thank my friend Vitalii, being hundreds kilometers away you helped me to go through this. Even when everything sucked (always) there was a place for Friday skype drinks. And we always had something in common.

Finally, I thank my family. Thanks to my parents Aleksandr and Svetlana who always supported me throughout this PhD with advice, with warmth and, of course, with Ukrainian food. Thanks to my brother Hennadiy. We do not talk much, but I know that you are cool, and I feel your support.

– –

Refer all your questions regarding the thesis to my body.